Novel electrocatalysts for the electrochemical and photoelectrochemical water oxidation reaction

Chaoran Jiang

2019

A thesis submitted for the degree of Doctor of Philosophy at University College London

Department of Chemical Engineering

University College London

Torrington Place

London

`

Declaration

I, Chaoran Jiang confirms that the work presented in this thesis is my own. Where information has been derived from other sources, I confirm that this has been indicated in the thesis.

Signature

Date

I. Acknowledgements

I want to express my sincere gratitude to my primary supervisors, Prof Junwang Tang in University College London (UCL), for his continued guidance and supports to my PhD study. I am also very thankful to my secondary supervisor, Prof Eric Fraga. Many thanks to both for their constructive comments throughout the experimental design, results in analysis/discussion and thesis writing.

I am very thankful for the substantial contribution made from my main collaborators (Prof Huiyun Liu, Prof Aiqin Wang, Prof Tao Zhang, and Dr Jiang Wu) for their expertise and useful feedback in the discussion of the experimental results. Great thanks to all the material characterising technicians at UCL including Mr Martin Vickers, Mr Mark Turmaine, Dr Robert Palgrave, Mr Steve Firth for their tutoring the operation of XRD, SEM/TEM-EDX, XPS and Raman, respectively. Big thanks to the past and present members of the solar energy and advanced materials group at UCL (Dr Savio Moniz, Dr Xiaoqiang An, Dr Mustafa, Dr Yiouwang, Dr Dan Kong, Dr Chiching Lau, Mr Qiushi Ruan, and Mr Jijia Xie) for the discussion of research method and result analysis. I also thank the visiting scholars from other universities (Dr Xu Liu, Prof Nianquan Jiang, Dr Wenjun Luo, Dr Jiefang Sun, Mr Kaiqi Xu), who always give me constructive suggestions and supports. In particular, I appreciate the exchange opportunity and sponsorship to perform catalysis research in Prof Tao Zhang's group based in Dalian Institute of Chemical Physics (DICP), China. During a period of 1.5 years, I expanded my knowledge of catalysis and gained new skills under co-supervisor Prof. Tao Zhang and Prof Aiqin Wang. It was also an excellent opportunity to meet the lovely people with various research backgrounds. I am very grateful to my colleagues in DICP: Dr Xiaochen Zhao, Dr LeiLei Kang, Dr Wenhao Luo, DrJi Yang, Dr Shanshan

Niu, and all the rest of you guys. Many thanks to them for their favour in photo/electrochemical lab set up, electrochemical measurements and material characterisation in DICP. Their expertise and kindness make me more confident about the challenging research project. I also want to thank all the materials characterising technicians at DICP for the training and data analysis including Dr Shuyan Du for XPS, Dr Lin Li for TPR，XRD, Raman, and UV-Vis spectroscopy, Mr Yang Su and Ms Huiming Gong for TEM and SEM microscopy, respectively. I must thank Dr Xiaoyan Liu and Prof Aiqin Wang again for proving me the opportunity to perform X-ray absorption spectroscopy at the Shanghai Synchrotron Radiation Facility (SSRF), China. Their expertise in synchrotron helps me a lot to in-depth understand the materials structure and catalytic mechanisms.

I especially want to acknowledge the PhD studentship from the China Scholarship Council, the visiting research scholarship from Dalian Institute of Chemical Physics, and the early-career conference travel funding from University College London and Royal Society of Chemistry.

Finally, I would like to thank all my family members for their unconditional support and love. In particular, many thanks to my wife, Yingwen Ke, who makes my life so much colourful whenever she is around. Her understanding and encouragements always make me energetic and motivated.

II. Abstract

Chemical energy storage by water splitting, a combination of oxygen evolution (OER) and hydrogen evolution reactions (HER) has emerged as a promising solution for the utilisation of solar energy. Both efficient electrocatalysts and photoelectrodes with long-term stability are indispensable to achieve economic feasibility of solar water splitting. Although the product of interest is hydrogen gas, the thermodynamic and kinetic requirements of the oxygen evolution reaction (OER) are the main limiting factors. The goal of this dissertation was to discover effective strategies for improving the performance of electrocatalytic and photoelectrochemical (PEC) water splitting.

To address the issues for the slow PEC water oxidation kinetics, two typical surface electrocatalysts Co-Pi and Ni-B were firstly synthesised and tested on a reference ZnO photoelectrode. The Ni-B/ZnO exhibited a benchmark photocurrent density (1.22 mA cm^{-2} at 1.0 V vs RHE), resulting into two folds enhancement compared with the unmodified ZnO. The stable photocurrent over a 1 h test period further demonstrated the dual functionality of Ni-B as an efficient OER catalyst and robust surface-protection layer inhibiting photocorrosion, which is much better than Co-Pi. Following the successful strategy used to stabilise of ZnO photoanode, the Ni-B electrocatalyst was introduced onto a very promising p/n junction GaAs by in-situ photoassisted electrodeposition to solve the critical stability issue of GaAs. A monolithic layer of Ni-B/Ga (As)Ox was generated during the Ni-B deposition process, resulting in a Ni-B/Ga (As)Ox/GaAs photoanode structure. Such structure was optimised by varying the GaAs surface architecture, electrolyte pH value and Ni-B deposition time to achieve the optimal photocurrent and best stability. The optimised photoanode, Ni-B/Ga (As)Ox/shallow GaAs exhibited a nearly 22 hour stable photocurrent density of 20

mA/cm^2, while the bare GaAs lost 40% activity in just three hours under identical condition. The remarkable performance in both photocurrent and stability directly addresses the current severe limitation in the application the classic GaAs photoanodes for solar fuel synthesis and could apply to other initially efficient but unstable photoelectrodes.

Although the above studies demonstrated the multi-function of an oxygen evolution reaction (OER) catalyst on the surface of a semiconductor photoanode, e.g. increasing the photocurrent and lifetime, the OER catalysts are still not efficient enough. Therefore, the development of a cost-efficient and long-term stable catalyst for OER is still crucial to produce clean and sustainable H_2 fuels from water. A cobalt vanadium oxide (CoVOx-300) catalyst with high contents of Co^{3+} sites that was manipulated by V^{4+}, was firstly reported as an efficient and durable electrocatalyst. The CoVOx-300 with highest Co^{3+}/Co^{2+} ratio of 1.4 and corresponding highest V^{4+}/ V^{5+} ratio of 1.7 exhibited remarkable OER activity with an overpotential of 330 mV at a current density of 10 mA cm^{-2} (η_{10}), a small Tafel slope of only 46 mV dec^{-1} and a current density of 100 mA cm^{-2} at an overpotential of 380 mV vs RHE, which was 20 time higher than the active CoOx-300 and 1000 time higher than VOx-300. The catalyst also showed excellent stability for 10 hours in alkaline media and a 40 % reduced activation energy to the counterpart, CoOx-300. This study demonstrated that high contents of surface Co^{3+} and V^{4+} species played a crucial role in improving electrocatalytic properties and stability for the water oxidation reaction.

To further improve the OER performance of cobalt-vanadium based electrocatalyst, a series of Cobalt-vanadium (Co-V) bimetallic catalysts were synthesised and tested for the OER. It was found that spinel $Co_{2-x}VO_4$ with Co^{3+}/Co^{2+} ratio of 2.8 and a moderate

crystallinity exhibited the lowest overpotential of 240 mV at 10 mA/cm^2, a smallest Tafel slope of 45 mV dec^{-1} and a current density of 100 mA/cm^2 at an overpotential of 280 mV, where the current density was about 600 times higher than that of CoOOH and 20 times higher than the benchmark commercial RuO_2 electrocatalyst, and it was also much better than the CoOx-300. The cobalt-vanadium based low-crystalline $Co_{2-x}VO_4$ nanoplates with remarkable electrochemical OER performance could be further deposited onto the promising semiconductor photoanodes to enhance the overall OER performance and longevity of the PEC devices.

III. Impact statement

The development of efficient methods for generating clean and renewable fuel is critically important to reduce green house gas emission from burning fossil fuels and to meet the rapid increase in global energy demands. Therefore, considerable research has been conducted, spanning over several decades to find alternative, clean, and efficient energy vectors to replace finite energy sources such as fossil fuels.

Solar water splitting is an attractive approach to meet this target by conversion of solar energy into a storable and transportable form of energy. Splitting of water by direct sunlight into molecular oxygen and hydrogen using a photoelectrochemical (PEC) cell is one such promising method to produce a chemical fuel (hydrogen) that can be utilised in a hydrogen fuel cell or through direct combustion. At present, the development of active and robust surface electrocatalysts turns out to be an effective strategy for the fabrication of highly efficient and stable photoelectrodes for solar water splitting. Therefore, in my research project, Firstly, loading the earth-abundant electrocatalyst of Ni-B by in-situ photoassisted electrodeposition was for the first time reported as a promising approach for improving the efficiency and stabilising ZnO and GaAs photoanodes. Such approach addressed the current severe limitations in the application of narrow bandgap photoanodes for efficient solar fuel synthesis. Moreover, two cobalt based electrocatalysts (CoVOx and $Co_{2-x}VO_4$) with optimal surface composition and crystal structure that can boost oxygen evolution reaction activity and stability are also discovered. My current achievements may help academic researchers from the both academic and industrial community to formulate new highly efficient water splitting catalysts and/or photoelectrochemical devices for H_2 production to eliminate our reliance on rapidly diminishing fossil fuels and to reverse global warming.

Ⅳ. Publications and Conferences

Publications:

1 **C. Jiang,** J. Yang, J. Li, Z. Tian, X. Liu, A. Wang, T. Zhang, J. Tang, Low-crystallinity Co2-xVO4 nanoplates for efficient electrochemical water oxidation, **2019**, in preparation.

2 **C. Jiang,** T. Zhao, X. Liu, A. Wang, T. Zhang, Z.X. Guo, J. Tang, Co^{3+}-O-V^{4+} cluster in CoVOx nanorods for efficient and stable electrochemical oxygen evolution, **2019**, *ACS Catalysis,* in revision.

3 M. Bayazit, **C. Jiang,** S.J.A. Moniz, E. White, M.S.P Shaffer, J. Tang, Defect-free single layer graphene in catalytic water splitting prepared by microwave intensified solid exfoliation*,* **2019**, in preparation.

4 Y. Qiu, Z. Wen, **C. Jiang,** X. Wu, R. Si, J. Bao, Q. Zhang, L. Gu, X. Guo, J. Tang, Rational Design of Atomic Layers of Pt Cluster Anchored on Mo_2C Nanorods for Efficient Hydrogen Evolution over a Wide pH Range, *Small,* **2019,** 15, 1900014.

5 **C. Jiang,** J. Wu, A. Wang, T. Zhang, H. Liu, J. Tang, Stabilization of GaAs photoanodes by in-situ deposition of nickel-borate surface catalyst as hole trapping sites, *Sustainable Energy Fuels*, **2019,** 3, 814-822.

6 **C. Jiang,** S. J. A Moniz, A. Wang, T. Zhang, J. Tang, Photoelectrochemical devices for solar water splitting–materials and challenges*, Chemical Society Reviews*, **2017**, 46, 4645-4660.

7 R Foulkes, **C. Jiang,** J Tang, Devices for Solar-Driven Water Splitting to Hydrogen Fuel and Their Technical and Economic Assessments*, CRC Press, Chapter 2, Solar Fuel Generation,* **2017**.

8 W. Luo, **C. Jiang**, Y. Li, S. A. Shevlin, X. Han, K.Qiu,Y. Cheng, Z.X. Guo,W. Huang, J. Tang, Highly crystallized α-FeOOH for a stable and efficient oxygen evolution reaction, *Journal of Materials Chemistry A*, **2017**, 5, 2021-2028.

9 **C. Jiang**, K Y Lee, C M A Parlett, M K. Bayazit, C C. Lau, Q. Ruan, S J.A. Moniz, A F. Lee, J. Tang, Size-controlled TiO2 nanoparticles on porous hosts for enhanced photocatalytic hydrogen production, *Applied Catalysis A: General*, **2016**, 521, 133-139.

10 J J. Walsh, **C.Jiang**, J. Tang, A J. Cowan, Photochemical CO_2 reduction using structurally controlled g-C_3N_4, *Physical Chemistry Chemical Physics*, **2016**, 18, 24825-24829.

11 K Qiu, G Chai, **C. Jiang,** M Ling, J Tang, Z Guo, Highly efficient oxygen reduction catalysts by the rational synthesis of nanoconfined maghemite in a nitrogen-doped graphene framework, *ACS Catalysis*, **2016**, 6, 3558-3568.

12 **C. Jiang**, S. J. A. Moniz, M. Khraisheh, J. Tang, Earth-abundant Oxygen Evolution Catalysts Coupled onto ZnO Nanowire Arrays for Efficient Photoelectrochemical Water Cleavage, *Chemistry-A European Journal*, **2014**, 20, 12954-12961.

Conferences:

1 **C. Jiang,** Vanadium incorporation into cobalt hydroxide nanorods for efficient electrochemical water oxidation, *The 18th Chinese National Congress on Catalysis, Tianjin, China*, 2017.

2 **C. Jiang,** Photocatalysis and photoelectrochemistry for solar fuel production, *The 5th International Symposium on Solar Fuels and Solar Cells, Dalian, China,* 2016.

3 **C. Jiang,** Stabilization of GaAs photoanode for efficient water oxidation，*Designing New Heterogeneous Catalysis, Designing New Heterogeneous Catalysis: Faraday Discussion, London, England,* 2016.

4 **C. Jiang,** Controllable TiO_2 nanoparticle on porous hosts for efficient H_2 production from solar water splitting, *International Discussion Meeting-Solar Fuels: Moving from Materials to Devices, London, England, 2015.*

5 **C. Jiang,** Photocatalysis and Photoelectrochemistry for Solar Fuel Production. *UCL Materials Hub inauguration symposium, London, UK,* 2015.

6 **C. Jiang, ZnO** nanorods modified with earth-abundant catalysts for efficient and stable photoelectrochemical water cleavage, *The 24th international conference on photochemistry, Berlin, Germany, 2014.*

V. Table of Contents

VI. List of Tables

VII. List of Figures

1. Introduction

1.1 Background

With the technology advances and the ever increasing population in this booming world, the global energy consumption rate is expected to rise by a factor of two, from 15 TW/year today to 27 TW per/year by 2050 and according to this trend, it further increases to 43 TW/year by 2100.[1] At present, the primary energy supply is obtained from fossil fuels, contributing 85 % of the total global energy consumption. [2] However, the upcoming depletion of fossil fuels and linked environmental issues such as pollution and greenhouse gases emission while burning them are the most significant technological challenges encountered by mankind. Therefore, it is imperative to seek alternative energy supplies to cope with the problem of energy issue and climate change. Solar energy, the most abundant, clean and renewable energy resource on the Earth, is a sustainable energy supply for the whole world. Each year, solar energy reaches the Earth surface at the annual rate of 100,000 TW, out of which, 36,000 TW is on land. This means only 1% of the land is needed to be covered with 10 % PEC cells to generate the energy of 36 TW/year, which is sufficient for the annual energy consumption in 2050.[2] Hence, the ability to utilise solar energy is of great importance for humans.

1.2 Motivation

Although solar energy can be harvested by using solar cells, which convert the solar energy to electricity, to store electricity at large scale is at present very challenging. Therefore, solar electricity must be transferred to the grid for immediate usage. By comparison, artificial photosynthesis is a promising technology to achieve not only solar energy harvesting but also storage, which produces energy-rich chemical fuels

such as hydrogen, hydrocarbons or alcohols.[3] Among the various chemical fuels, hydrogen possesses attractive advantages such as environmental friendly and minimum 3-4 folders higher mass energy density compare to other fuels.[4] However, it remains significant challenge to construct an adequately efficient and stable Solar-To–Hydrogen (STH) device, although there are a few possible pathways to produce H_2 by utilizing both water and sunlight including electrolysis of water from solar *photovoltaic* (PV) system,[5] bio-hydrogen routes though reforming of biomass,[6] and photoelectrochemical (PEC) water splitting.[7] Even though the solar-driven water splitting device is available by coupling the photovoltaic (PV) cell and electrolyser with an STH efficiency of 18 %,[8] intensive studies are still concentrating on the development of direct water splitting using PEC cells due to three critical driving forces compared to the above-mentioned indirect water splitting. Firstly, a lower overpotential is required to drive the direct PEC water splitting, but several PV cells are usually used in series to reach the minimum potential (3.0 V), required by electrolyser in an indirect route. Secondly, PEC water splitting requires a much simpler space-saving construction with fewer components (wires, electrodes, glass reactor etc.). Thus the cost of PV-electrolyser system is estimated to be at least US $ 8/kg, but the cost can be reduced to about US $ 3/kg by integrating a light harvesting and water splitting photocatalyst in a single system (PEC cell), which almost reach the target of producing H_2 at the price of US $2-4/kg set by the US Department of Energy (DOE) in order to make it commercially available. [9] In a PEC cell, the key components determining its efficiency are an electrocatalyst (or cocatalyst) and a photoelectrode, the former will be extensively investigated herein.

1.3 Objectives

It is widely accepted within the community that to achieve a sustainable society with an energy mix primarily based on solar energy we need an efficient strategy to convert and store sunlight into chemical fuels. A photoelectrochemical (PEC) device would therefore play a key role in offering the possibility of carbon-neutral solar fuel production through artificial photosynthesis. The past five years have seen a surge in the development of promising semiconductor materials. In addition, low-cost earth-abundant OER catalysts (Co-catalysts) are ubiquitous in their employment in water splitting cells due to the sluggish kinetics of the oxygen evolution reaction (OER).

In general, this thesis aims at developing efficient and stable electrocatalysts that could be coupled to a photoanode for photoelectrochemical water splitting and further understanding the role of surface electrocatalysts for water oxidation reaction. My first goal is to construct a highly efficient and durable PEC device by focusing on a promising semiconducting photoanode. Ideal water splitting photoanode and/or photocathode require semiconductor materials with features including: (i) Low cost and easy fabrication; (ii) Efficient utilisation of solar spectrum; (iii) High chemical stability in the dark and under illumination; (iv) Band edge positions that straddle the water reduction and/or oxidation potentials; (v) High mobility of photo-generated holes and electrons; (vi) Low overpotentials for surface oxygen evolution or hydrogen evolution reactions. However, in practice, the requirements imposed on these semiconductor materials appear to conflict, for example, ZnO exhibits high electron mobility, but the low solar to hydrogen (STH) efficiency due to inefficient utilisation of solar spectrum (UV light only) limits its further application as an efficient photoanode material. Because of this, narrow bandgap materials

such as GaAs could be a good candidate. However, the photocorrosion under illumination results into undesired side reaction (i. e. self- oxidation), rather than water oxidation reaction.

Moreover, efficient OER catalysts for accelerating surface water oxidation reaction of a photoanode is of significance to further decrease the overpotential, increasing the photocurrent, and thus increasing STH efficiency. Therefore, my second goal is the rational design of efficient and robust OER catalysts for water splitting through a cost-effective route.

The objectives of this thesis can be summarised as follows:

(1) Test of the strategy of appropriate co-catalysts to stabilise ZnO and GaAs Photoanodes.
(2) Further demonstration of the strategy of photoelectrodepostion on the very promising GaAs photoanodes by *in-situ* deposition.
(3) Development of high-performance OER electrocatalysts based on non-precious cobalt vanadium oxides.
(4) Fundamental understanding of the active sites during OER by *in-situ* spectroscopies (e.g. *In-situ* Raman and *In-situ* XAFS) and XPS spectroscopies.

1.4 Report outline

There are eight chapters in this thesis, beginning with a brief introduction, describing the motivation and objectives of this investigation (chapter 1). Chapter 2 covered a comprehensive review of the recent progress and challenges of electrochemical and PEC water splitting. The fundamental principles and mechanisms for water splitting

were described and then the novel electrocatalysts and semiconducting photoelectrodes for electrocatalytic and photoelectrocatalytic water splitting were summarised. The strategies for an optimal PEC device were particularly illustrated throughout the whole chapter. Chapter 3 described different techniques used throughout this thesis. The actual research work was reported from chapter 4 to chapter 7.

In chapter 4, ZnO based semiconductor grown on Fluorine doped Tin Oxides (FTO) glass substrates was studied as photoanode material for PEC water oxidation. The strategies such as optimising the length and diameter of the ZnO nanowire and the loading of efficient and robust oxygen evolution catalysts (OER), i.e. Ni-B for improved PEC performance were reported. Furthermore, the effective strategy achieved on ZnO was applied to a narrow bandgap semiconductor (GaAs) that suffered from severe photocorrosion. The as-prepared Ni-B/Ga (As)Ox/ GaAs photoanodes were fully characterised and investigated for PEC water oxidation in chapter 5.

To further develop efficient and robust surface OER catalysts, I have rationally designed two cobalt-vanadium based oxides, which is CoVOx-300 (chapter 6) and low-crystallinity $Co_{2-x}VO_4$ (chapter 7) for boosting OER activity and stability in alkaline conditions. The structure, morphology and chemical states were optimised for the efficient and stable electrocatalytic water oxidation reaction. The mechanisms behind the enhanced OER performance based on Co-V bimetallic oxides were also illustrated throughout these two chapters.

Chapter 8 made an overall conclusion of this thesis and proposed some future work including the strategies for further improving the photoelectrocatalytic/ electrocatalytic water splitting performance and the mechanism insights for water splitting reaction.

2. Literature Review

2.1 Overview

Solar energy is the most abundant, clean and renewable energy resource on the planet. Each year, the amount of solar energy reaching our planet is approximately 100,000 TW, of which approximately 36,000 TW reaches the land.[10] This means that only 1% of the land on the Earth needs to be covered with just 10 % efficient photoelectrochemical (PEC) cells to generate the equivalent of 36 TW/year, which is sufficient for our predicted annual energy consumption in 2050.[2] Hence, the ability to harness and utilize solar energy is of great importance for humans. One of the more attractive options lies in storing this energy as chemical bonds by splitting water into hydrogen and oxygen. Hydrogen exhibits 3-4-fold higher mass energy density compared to gasoline and can be utilised either through direct combustion or in hydrogen fuel cells. Therefore, there is considerable interest in the coupling of solar irradiation to electrochemical water splitting. Two general routes are available for this process: the use of conventional solar panels to run conventional electrolysers (indirect solar to hydrogen production) or the development of a single device that could perform both light absorption and water splitting (direct solar to hydrogen production). The performance of these two approaches highly relies on the development of efficient and stable electrocatalyst for water splitting. In this section, the fundamental aspects of electrochemical and photoelectrochemical water splitting will firstly be described. Then I move to the recent development on electrocatalysts, photoelectrodes and various PEC devices for water splitting. Finally, I will discuss the drive for new electrocatalysts and efficient PEC device.

2.2 Fundamentals of water splitting

Water splitting reaction is an uphill reaction, which requires minimum Gibbs free energy of 237 kJ/mol. In alkaline electrolyte, the following half-reactions occur (Reaction 2-1 and 2-2). However, it is different in an acidic electrolyte (Reaction 2-3 and 2-4).

Alkaline electrolyte:

$4H_2O+4e^- \rightarrow 2H_2+4OH^-$ E_{red} = - 0.828V vs NHE Reaction 2-1

$4OH^- +4h^+ \rightarrow 2H_2O+O_2$ E_{ox} = - 0.401V vs NHE Reaction 2-2

Acidic electrolyte:

$4H^+ + 4e^- \rightarrow 2H_2$ E_{red}= + 0.000V vs NHE Reaction 2-3

$2H_2O+4h^+ \rightarrow 4H^+ +O_2$ E_{ox}= -1.229V vs NHE Reaction 2-4

Therefore, the overall water splitting reaction can be expressed as reaction 2-5, and the potential difference (ΔV) between water oxidation and reduction reaction is 1.23 V.

$2H_2O \rightarrow 2H_2 + O_2$ ΔG= 237kJ/mol Reaction 2-5

2.2.1 Principle of electrochemical water splitting

In the electrolysis process, a direct current is circulated through the water between two electrodes (the anode and the cathode) physically separated by a diaphragm or membrane.[11] A graphical representation of general electrolysis processes is shown in Figure 2-1. The electrodes are submerged in water, often with an electrolyte which increases the ionic conductivity. An oxidation evolution reaction (OER) occurs on the

anode, generating oxygen and leaving electrons to flow to the external circuit resulting in the anode positively charged. The electrons flow to the cathode, negatively polarising the electrode and producing hydrogen through a reduction reaction, which is the hydrogen evolution reaction (HER). The two half-reactions combine to give the overall water splitting reaction. An ion exchange membrane is normally employed in the cell between the two electrodes to transport certain ions in the electrolyte and responsible for the separation of product gases as well.

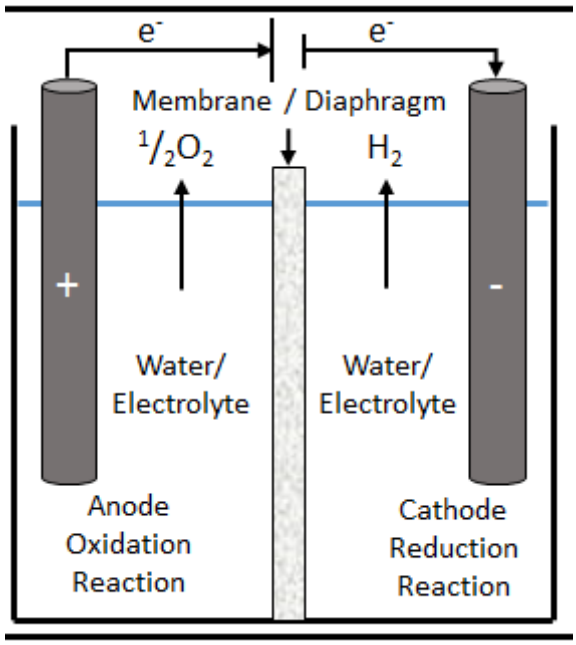

Figure 2-1 : A graphical representation of general electrolysis processes. Reproduced from reference 12.

The minimum theoretical voltage of 1.23 V is required to drive electrochemical water splitting reaction at room temperature. However, the potential required is commonly much higher at 1.23 V in order to overcome the electrodes' kinetic barrier of the reaction. The term 'overpotential' (η) describes how much additional potential

must be applied to achieve a specific current density. The role of electrocatalysts is then to facilitate the electrochemical reactions and reduce this overpotential as much as possible. A lower overpotential (η) of an electrocatalyst in the system indicates the superior electrocatalytic activity of the reaction of interests.

HER is the cathodic part of the overall water splitting, involving the transfer of 2 electrons. The mechanism of the HER process in an acidic electrolyte can be divided into two steps. The first step is known as Volmer reaction (Reaction 2-6), in which a proton (H^+) absorption on the active site (M) of the catalyst is coupled with an electron transfer, yielding an adsorbed hydrogen on the active site ($M\text{-}H_{ads}$). For the second step, two different pathways may occur. One is Tafel reaction (Reaction 2-7), in which an H_2 molecule is released by directly coupling of two adsorbed $M\text{-}H_{ads}$, followed by the desorption from the catalysts surface. The other pathway is Heyrovsky reaction (Reaction 2-8), in which H_2 is formed by the combination of one surface $M\text{-}H_{ads}$ unit with one reduced proton and desorption from the catalyst surface.

Step 1: $M + H^+ + e^- \rightarrow M\text{-}H_{ads}$ (Volmer reaction) Reaction 2-6

Step 2: $M\text{-}H_{ads} + M\text{-}H_{ads} \rightarrow 2M + H_2$ (Tafel reaction) Reaction 2-7

Or

$M\text{-}H_{ads} + H^+ + e^- \rightarrow M + H_2$ (Heyrovsky reaction) Reaction 2-8

The presence of one or another mechanism for H_2 release will depend on the particular system and can be experimentally determined by the use of Tafel slope, which will be discussed in Chapter 3.

The HER exchange current densities for various electrocatalysts can be correlated with the strength of the M-H bonds. This trend was first recorded on metals in 1970 by

Trasatti and the resulted plot is a volcano curve as shown in Figure 2-2.[13] At low M-H strength where the formation of the adsorbed intermediate is the rate determining step (RDS), the plot rises as the M-H bond becomes stronger. At high M-H strength, the H^+ absorption on the active site of the catalysts via Volmer reaction is fast, and the desorption of produced H_2 via Tafel or Heyrovsky steps become RDS. The decrease in the current density after the optimal M-H bonds strength can be interpreted as an overstabilization of the absorbed intermediate. Therefore, a balance is needed between the absorption and desorption process. In 2005, Hinnermann et al. further exploited this relationship using values of free energy for H^+ adsorption (ΔG_H^+) obtained by density functional theory (DFT) calculations.[14] The plot shows a similar volcano plot and the position of the metals also stays the same. It reveals that ΔG_H^+ value is a good descriptor for HER and the maximum catalytic activity is obtained when ΔG_H^+ close to zero.

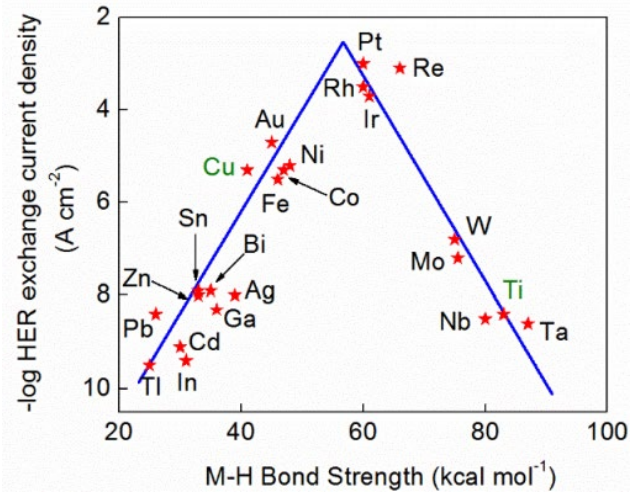

Figure 2-2: Trasatti's HER Volcano plot: exchange current densities for the HER vs the strength of intermediate metal-hydrogen bonds. Modified from reference 15.

OER is a four-electron reaction involving multiple reaction intermediates. Many research groups have proposed mechanisms for oxygen evolution reaction in either an acid or alkaline

condition as described in Figure 2-3 with the blue line and red line, respectively. Here the active site is drawn as M. In general, there are two proposed mechanisms for OER, that is the green route and black route. Both routes involve the formation of the same intermediates such as M-OH and M-O, while the major difference is featured around the reaction that forms oxygen. One pathway involves the creation of MOOH intermediate, which subsequently decomposes to O_2 and the regeneration of the free active sites. The other pathway involves the combination of two-M-O species to release O_2 and M directly. Despite this difference, the common consensus is that the electrocatalysis of OER is a four-electron transfer process, with the main variation being the number of electron or proton transfer in individual steps.

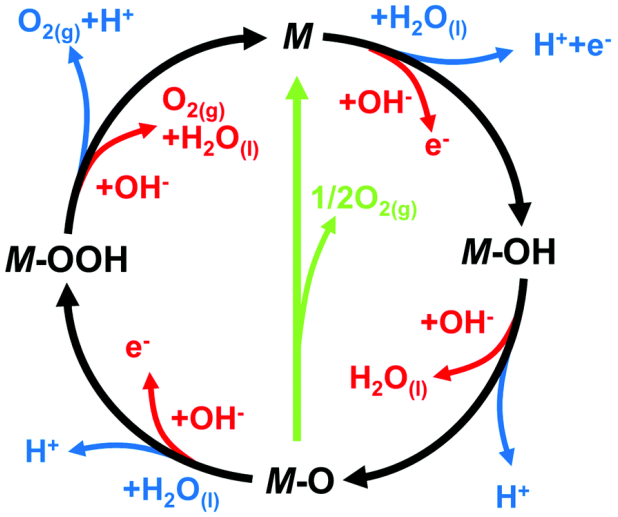

Figure 2-3: The proposed OER mechanism for acid (blue line) and alkaline (red line) conditions. The black line indicates that the oxygen evolution involves the formation of a peroxide (M–OOH) intermediate (black line) while the other route for the direct reaction of two adjacent oxo (M–O) intermediates (green) to produce oxygen is possible as well. Reproduced from reference 16.

2.2.2 Principle of photoelectrochemical water splitting

Water splitting can also be performed by photoelectrolysis in a photoelectrochemical (PEC) cell, whereby the light energy is employed to overcome the required energy barrier to split water. The main components of PEC water splitting devices are two light harvesting semiconductor photoelectrodes, an electrolyte and a separation membrane. In this section, the basic properties of semiconductors will be discussed, followed by a description of the semiconductor-electrolyte interface. Finally, the basic processes and mechanism of PEC water splitting will be described.

2.2.2.1 Properties of semiconductors

According to molecular bonding theory, bonding and anti-bonding levels are formed by the combination of atomic orbitals of several atoms. The closed sets of energy levels constitute a region called energy bands. The valence band (highest occupied molecular orbital; HOMO) and the conduction band (lowest unoccupied molecular orbital; LUMO) are formed which correspond to the bonding and anti-bonding energy levels, respectively. The difference between the two energy bands is termed as the bandgap (E_g) and the bandgap of semiconductors is usually in the range of 1 - 5 eV. At zero Kelvin, the valence band is filled with electrons, whereas the conduction band is mostly empty. Upon excitation by an external energy source, an electron in the valence band is excited to the conduction band which leaves a hole in the valence band. These photo-generated electron-hole pairs play a crucial role in water splitting reactions and will be discussed in more detail in section 2.2.2.4. Since pure semiconductors (intrinsic semiconductors) exhibit poor conductivity, they are usually doped with impurity atoms

(termed extrinsic semiconductors) as either electron donors or acceptors. As illustrated in Figure 2-4, the donor doped semiconductors (e.g. phosphorus into Si) have impurity atoms with greater number of valence electrons than the host atoms, resulting in an electron-rich semiconductor (n-type), whilst acceptor-doped semiconductors have impurity atoms with fewer number of valence electrons than the host atoms, resulting in hole-rich semiconductors (p-type). For the n-type semiconductor, the majority carriers are electrons, whereas in p-type semiconductors these are the holes.

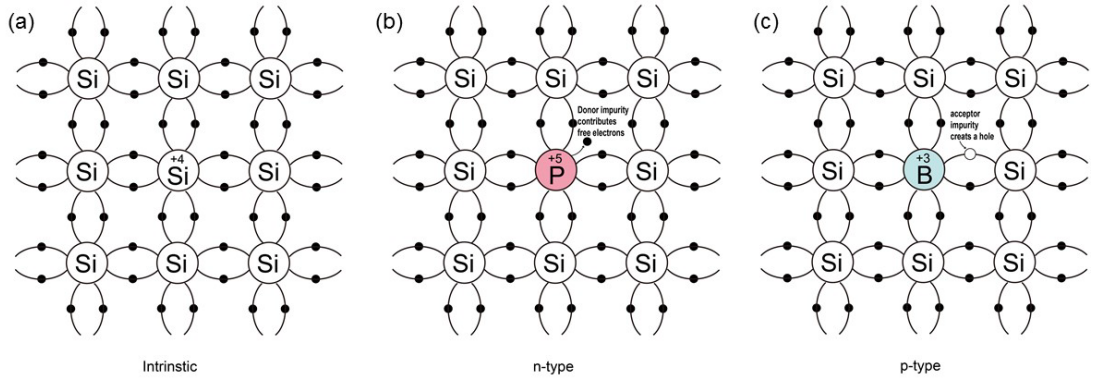

Figure 2-4 : Schematic bond representation for (a) intrinsic silicon; (b) n-type silicon doped with phosphorus and (c) p-type silicon doped with boron.

In metal oxide photoelectrodes, shallow donors and acceptors are always necessary because of the low intrinsic charge carrier mobilities. Not only can conductivity be improved, but also optical absorption, carrier diffusion length and catalytic activity can be promoted. Defects such as vacancies, interstitials or substituents are also usually present in the materials, and the incorporation of dopants in metal oxides and other ionic materials can be described using the Kroger–Fink notation, which represents the overall defect chemistry of the material from the viewpoint of conserving lattice site stoichiometry.[17] A typical example of beneficial doping of compound semiconductors for water splitting is that of Ta-doped α-Fe_2O_3. Here, Ta^{5+} substitutes Fe^{3+}, giving two positive charges at each substituted site. Two electrons are added to conserve the

overall charge; doping with Ta increases the electron density in α-Fe_2O_3. The resultant doped material displayed remarkably improved photoactivity at 420 nm compared to the undoped sample.[18]

2.2.2.2 Semiconductor band-bending and the space charge region

When a semiconductor is immersed in an electrolyte, the electrochemical potential (Fermi level) is disparate across the interface. Equilibration of this interface requires the flow of charge from one phase to the other, and a "band-bending" takes place within the semiconductor. At the semiconductor–liquid junction (SCLJ), the equilibration of the chemical potential of the electrons in the semiconductor (Fermi level) and the oxidation-reduction potential in the electrolyte causes the transfer of electrons across the SCLJ. There is also a characteristic region within the semiconductor within which the charge would have been removed by this equilibration process. Beyond this, the semiconductor is electrically neutral, so this layer is termed as the space charge region (SCR) or depletion layer because the layer is depleted of the majority carriers.[19] One of the key characteristics of a semiconductor used for PEC water splitting is the presence of a built-in electric field in the SCR, where band bending takes place. In devices for solar water splitting, this SCR and the subsequent band-bending aids transfer and separation of the photogenerated electrons and holes, and therefore is of great importance to understand the different types of band-bending exhibited in PEC systems.

Yates et al. have reviewed the phenomena of band-bending in semiconductors and the resultant effects on photochemistry, in particular with respect to photo-generated charge separation and transport.[20] Band bending can be induced by metal/semiconductor contact, surface state, applied bias and molecule absorption,

which results in the formation of a space charge region. In this section, different types of band bending will be discussed in detail.

Metal/semiconductor contact induced band bending

Figure 2-5 describes the principle of band bending which occurs at the metal/n-type semiconductor interface. The work function is defined as the energy difference between the Fermi level and vacuum level. Since the metal and the semiconductor have different Fermi levels (i.e. electropotential), charge carriers are transferred between them until they reach equilibrium. If the work function (ϕ_m) of the metal is larger than the n-type semiconductor(ϕ_s), the electrons will keep flowing from the semiconductor to the metal until equilibrium, whereby the Fermi levels of both materials are located within the same energy level. The electron concentration is thus depleted at the interface in the semiconductor side compared to its bulk, forming a depletion layer. The bands bend upwards due to the repulsion from the negatively charged layer located on the metal surface, termed a Schottky contact, because of the Schottky layer formation at the interface when $\phi_m > \phi_s$. In contrast, in the case of $\phi_m < \phi_s$, an accumulation layer is formed at the interface due to electron transfer from the metal to the semiconductor, resulting in downward band bending. No Schottky layer is formed when $\phi_m < \phi_s$, and therefore it is called an ohmic contact. These two contacts are very useful when designing a junction PEC device for water splitting to enhance the charge separation and transportation at the interface.

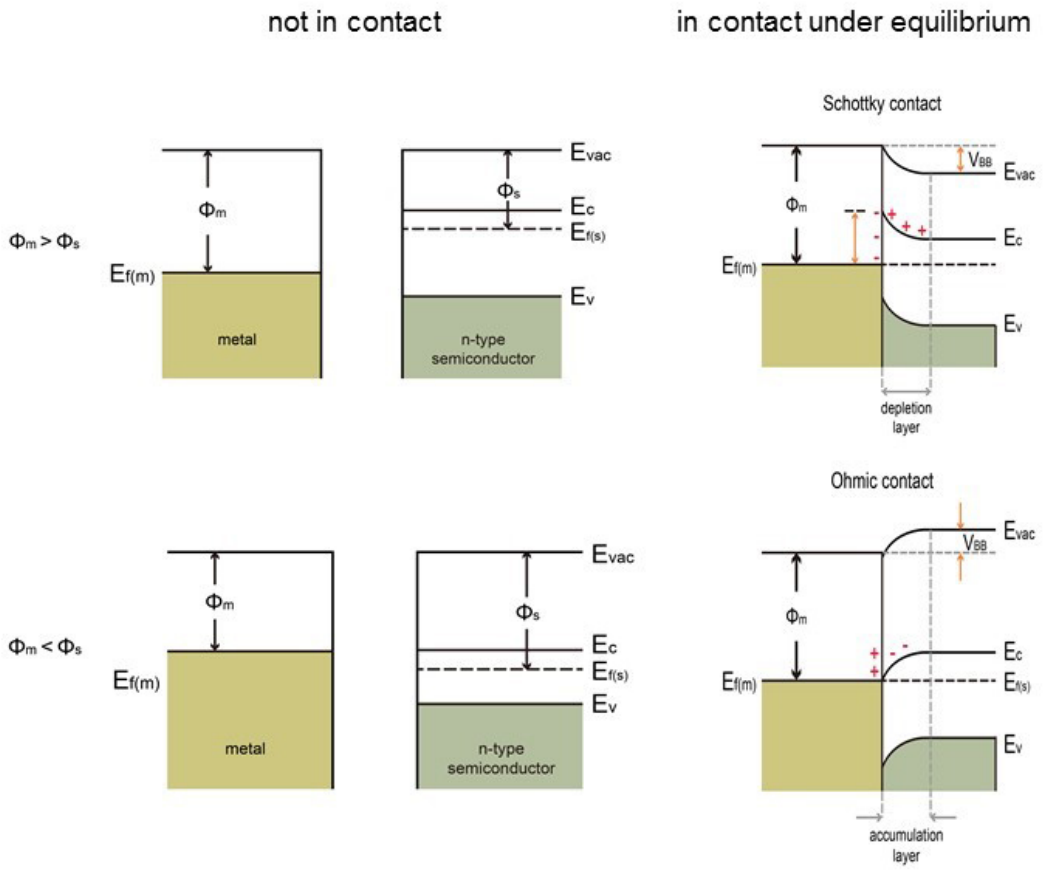

Figure 2-5 : Energy band diagrams of metal and n-type semiconductor contacts, where E_{vac}= vacuum energy; E_c= energy of conduction band minimum; E_v= energy of valence band maximum; $Ef_{(m)}$=fermi level of metal; $Ef_{(s)}$=fermi level of semiconductor; ϕ_m= metal work function; ϕ_s= semiconductor work function; V_{BB}= degree of band bending of the semiconductor at the interface. Modified from reference [20]. In the energy band diagram of metal contacting with a p-type semiconductor, the band bending reverses.

Surface- state induced band bending

Surface states may exist due to the termination of lattice periodicity at the semiconductor surface. For intrinsic semiconductors (undoped), the VB is filled with electrons (100 %), whilst the CB is empty (0%) and thus the Fermi level (E_f) of the semiconductor is located in the middle of the bandgap, as by definition that the Fermi level is where there is a 50 % probability of occupation by electrons at absolute zero

temperature. The Fermi level of the surface state (E_s) is assumed at the mid-energy gap for simplicity. Since the Fermi level of undoped semiconductors is the same as the Fermi level of the surface state, there is no charge transfer between the bulk and surface. However, as shown in Figure 2-6, for surface impurity doped semiconductors, the Fermi level at the surface is shifted close to the CB for n-type semiconductors or close to the VB for p-type semiconductors, respectively. Due to the energy difference, electrons will flow from the bulk to the surface or from the surface to the bulk until the Fermi levels of the semiconductor and surface state become aligned (at equilibrium state), resulting in an upward band bending (depletion layer formation) or downward bending (accumulation layer formation) for n-type and p-type semiconductors respectively.

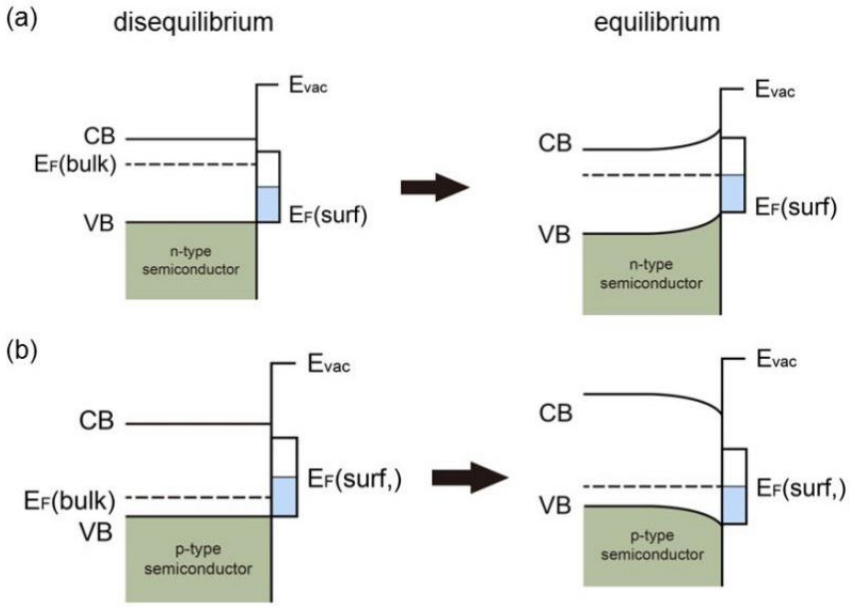

Figure 2-6 : Schematic illustration of a surface state induced band bending: (a) disequilibrium and equilibrium between the bulk and surface for an n-type semiconductor; (b) disequilibrium and equilibrium between the bulk and surface for a p-type semiconductor; Modified from reference 20.

Absorption-induced band bending

When an n-type semiconductor is immersed into an aqueous electrolyte, it will absorb an acceptor molecule (A). As the molecule approaches the semiconductor surface, the LUMO of the acceptor shifts downwards until the equilibrium is established and this leads to electron flow from the semiconductor to the molecule (upward bending, see Figure 2-7). At the same time, a Helmholtz layer, defined as the region between the specifically adsorbed ions and the closest ions in the solution, is formed on the semiconductor surface with a space distance of *d* (ca. 2 - 5 Angstroms). The potential drop across this layer is given by V_H, which changes by -59 mV per unit pH at 25 °C.

Figure 2-7: Schematic diagram shows the adsorption of an acceptor molecule (A) onto a semiconductor surface. Modified from reference 20.

Applied bias-induced band bending

In a PEC cell, band bending can be induced by applying a potential between a working electrode and a reference electrode. The potential difference will be distributed over the space charge layer and the Helmholtz layer. As shown in Figure 2-8 (a), as V_H remains constant, any change in applied bias will fall across the depletion layer of the semiconductor. An increase to the depletion layer will occur when applying a positive bias to an n-type semiconductor, resulting in increased upward band bending (Figure

2-8 (a)). However, by applying a negative bias, the degree of band bending can be reduced or even eliminated when a sufficient negative bias is applied (Figure 2-8 (b)). Similarly, a negative bias is required to be applied between a p-type semiconductor and the reference electrode in order to increase the depletion layer.

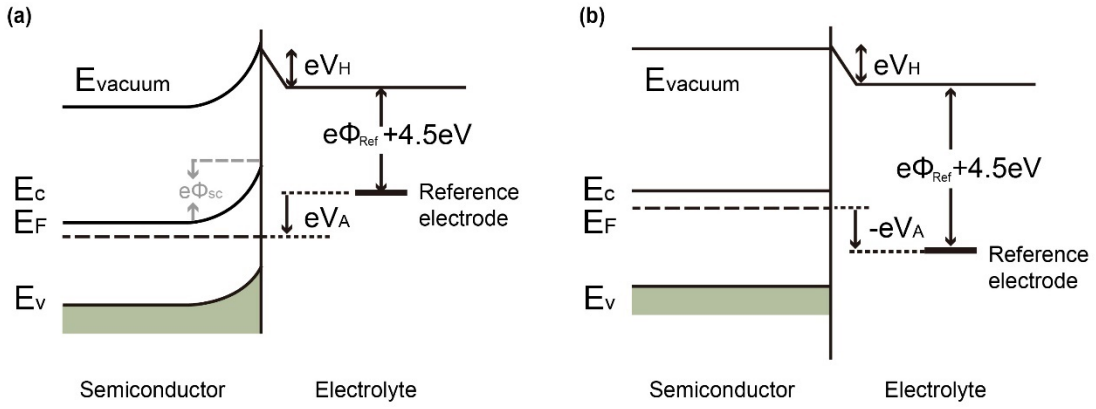

Figure 2-8: Effect of applying a bias voltage (V_A) to an n-type semiconductor photoelectrode. V_H is the potential drop across the Helmholtz layer. Φ_{Ref} is the work function of the reference electrode. Φ_{sc} is the potential drop across the space charge region. A positive potential is applied to the semiconductor in Figure (a) and when a sufficiently negative bias is applied, the band bending can be reduced to zero (Figure b). Reproduced from reference10.

2.2.2.3 Physics of semiconductor/electrolyte contacts

Following on describing the phenomena of semiconductor band-bending and the space charge region, we can draw the band energetics of a semiconductor/electrolyte interface before equilibration between the two phases, after equilibration (under dark conditions) and in quasi-static equilibrium under steady state illumination. As shown in Figure 2-9, when a typical n-type semiconducting photoanode is immersed in an

electrolyte that contains a redox couple (e.g. H_2O/O_2), electron transfer occurs between the semiconductor and the solution until equilibrium is established. After equilibrium, the electrode will have an excess of positive charges, arising from the ionised dopant atoms in the semiconductor, and the solution will have excess negative charges. The positive charge is spread out over the depletion layer with width "W" and the negative charge is spread over a much narrower region (Helmholtz layer) between the electrode and electrolyte (Figure 2-9 a and b). In Figure 2-9 (c), steady-state illumination yields non-equilibrium electron and hole populations, which can be described by the concept of quasi-Fermi level. The quasi-Fermi level is a description of the electrochemical potential of either electrons or holes at a time under non-equilibrium (e.g. illuminated) conditions. The gradient in the quasi-Fermi level results in an electric field near the semiconductor surface and consequently a current and voltage. The voltage generated by the built-in electric field of the semiconductor is termed "photovoltage" or "open - circuit voltage (V_{OC})," which can be obtained experimentally by measuring the potential difference between electron and hole quasi-Fermi levels under no net current flow. The maximum current generated in the built-in electric field is referred to as the short circuit current (J_{SC}) and thus the maximum power point can be obtained by multiplying the V_{OC} by the J_{SC} ($P_{PA}=V_{OC}\times J_{SC}$).

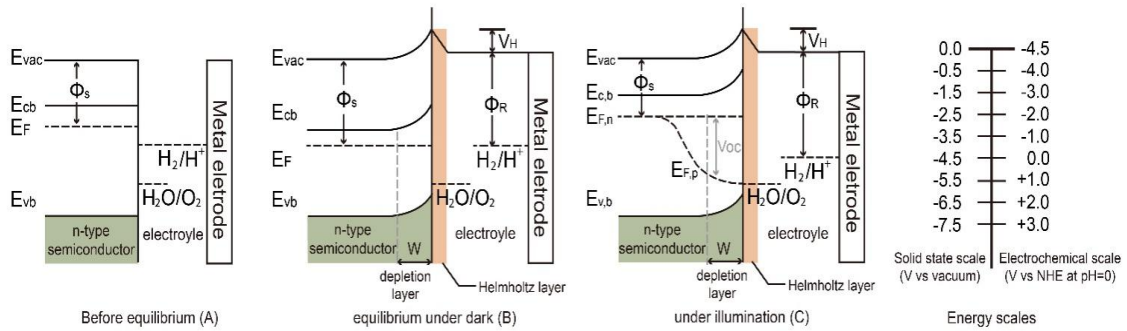

Figure 2-9 : The band energetics of a n- type semiconductor/electrolyte contact showing

the relationships between the electrolyte redox couple (H_2O/O_2 and H_2/H^+), the Helmholtz layer potential drop (VH), and the semiconductor work function (Φs), the electrolyte work function (Φ_R), the electron quasi-Fermi level($E_{F,n}$) and hole quasi-fermi level($E_{F,p}$) in three cases: (A) before equilibration between the two phases; (B) after equilibration under dark conditions; and (C) in quasi-static equilibrium under steady state illumination. The voltage (Voc) generated by the junction under illumination is given by the difference between EF,n and electrochemical potential of the redox couple of interest (H_2O/O_2 for a n-type semiconductor and H_2/H^+ for a p-type).

2.2.2.4 PEC water splitting processes

There are three major physiochemical processes that are involved in a complete PEC water splitting reaction (Figure 2-10). The first process is light absorption from a calibrated light source [e.g. simulated one sun irradiation, 100 mW/cm^2 is often used] by the semiconducting photoelectrode, usually with an n-type semiconductor as the anode and a p-type semiconductor as the cathode. When a semiconductor absorbs photons with energies greater than its band gap energy (E_g), a pair of charge carriers is created: electrons are excited to the conduction band, leaving holes in the valence band (VB). The valence band potential must be more positive than the O_2/H_2O redox potential of 1.23V vs NHE (pH=0) to permit water oxidation, whilst the conduction band (CB) must be more negative than the H^+/H_2 redox potential of (0 V vs NHE) to carry out water reduction. Note that additional energy or overpotential is required to make the reactions proceed at appreciate rates (eg. activation energy). The second process is the separation and transportation of photogenerated electron-hole pairs. During these steps, charge carriers can either recombine in the bulk or at the surface and hence both efficient separation and high mobility of charge carriers are desired. The last process is the surface reaction where the redox reactions for water splitting

occur. Both the potential of the charge carriers and suitable reaction kinetics are crucial for efficient water splitting reaction.

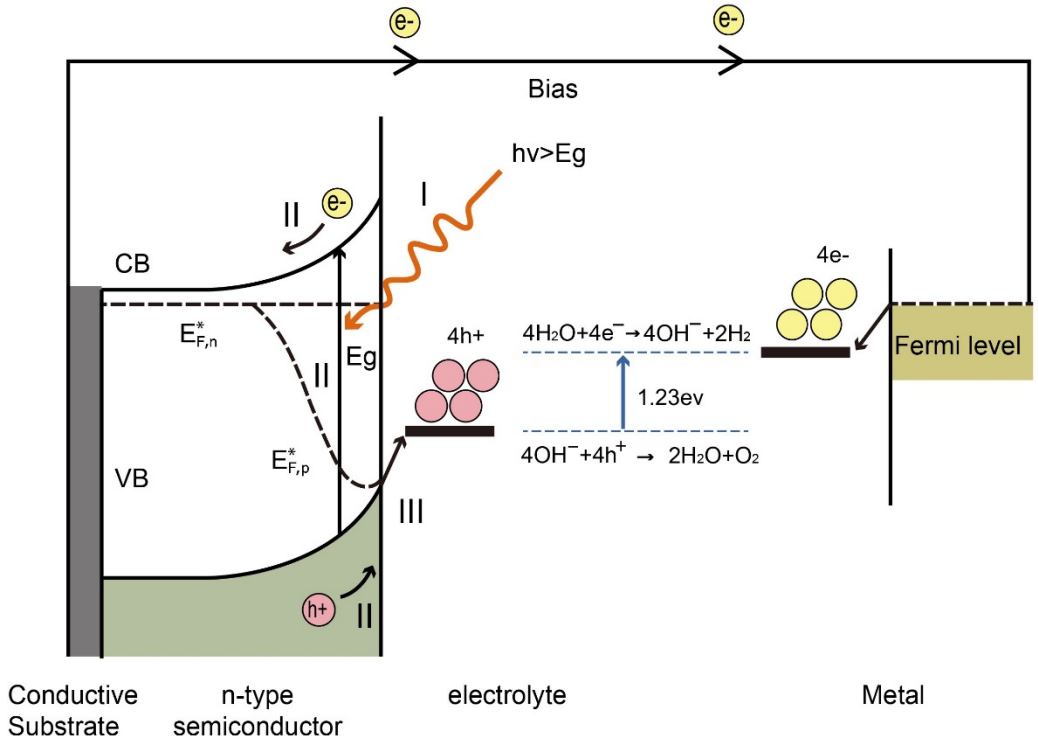

Figure 2-10: Schematic diagram of a simple PEC cell based on an n-type semiconducting photoanode electrically connected to a metal counter electrode under an external bias, performed in alkaline conditions. On the photoanode $4OH^- + 4h^+ \rightarrow 2 H_2O + O_2$ takes place and the bias is required as the position of CB is too positive to drive water reduction. The main processes involve (I) light absorption; (II) charge carrier separation and transportation and (III) surface redox reactions.

2.2.2.5 PEC device configuration

Figure 2-11 summarises the PEC device configurations reported so far (denoted type I-VI devices). Configuration (a), i.e. type I, is the simplest as it contains only one semiconducting light absorber, which we have referred to previously to illustrate the fundamental processes in PEC water splitting. A single semiconductor material can be used either as a photoanode or photocathode to perform water oxidation or reduction.

$SrTiO_3$ (bandgap of 3.2 eV) and $KTaO_3$ (3.5 eV) are widely used as photoanodes for PEC water splitting cells with the aid of an external bias. However, due to their large bandgap, only the UV portion of solar energy can be absorbed, and thus the theoretical maximum STH efficiency is limited to less than 1%. Later in this chapter, promising efficient photoelectrode materials will be further discussed. In most cases, in order to drive the separation of holes from electrons, an external bias is needed for a single light absorber PEC system to function.

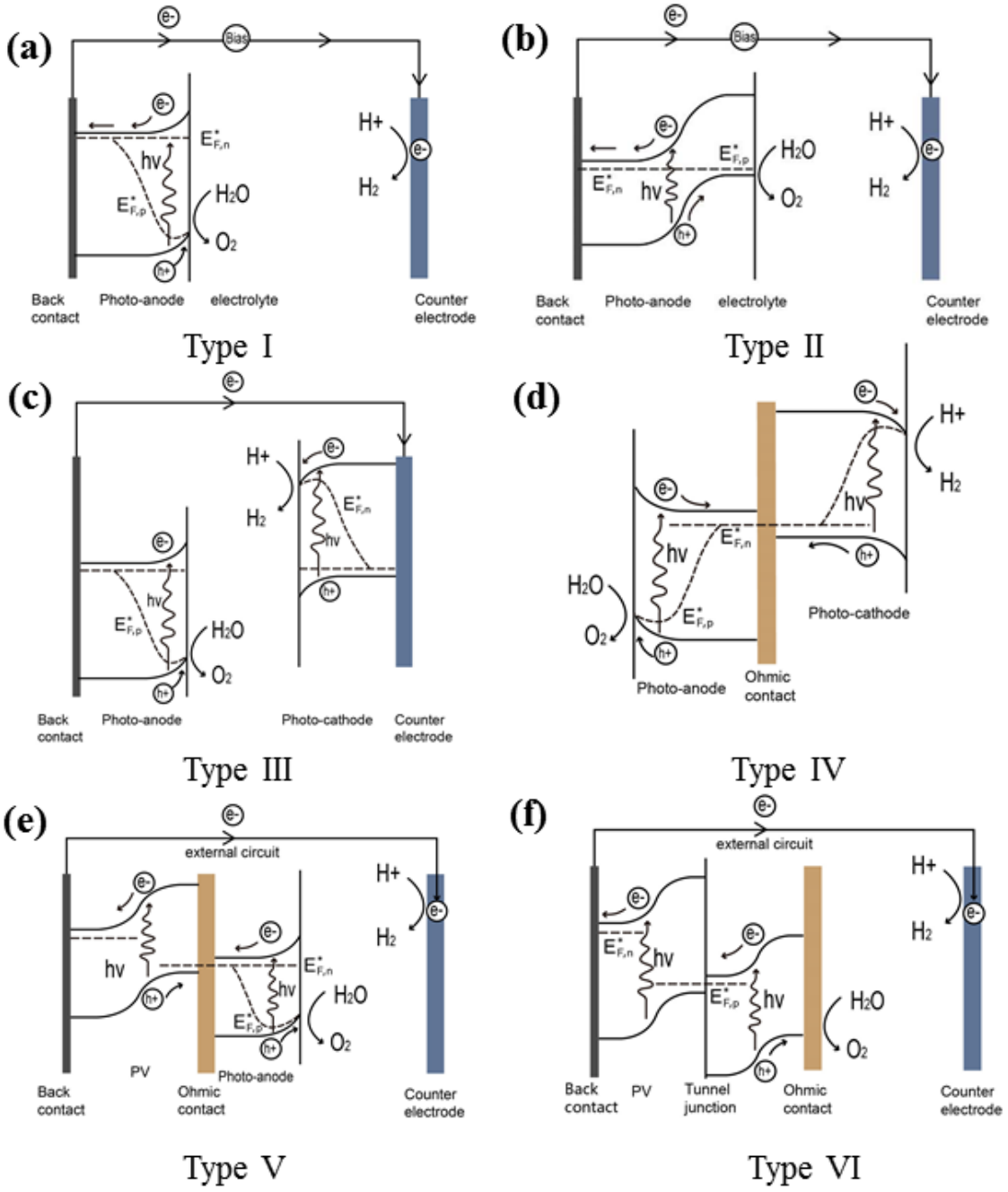

Figure 2-11: Various PEC water splitting device configuration: (a) type I single light absorber; (b) type II heterojunction photoelectrode; (c) type III wired PEC tandem cell; (d) type IV wireless PEC tandem cell; (e) type V PV-PEC tandem cell; (f): type VI PV/electrolyser cell.

Two or more semiconductors are often coupled for better utilisation of the solar spectrum and efficient charge carrier separation. Configuration (b), i.e. Type II, is the

heterojunction photoelectrode PEC device. In these systems, secondary semiconductors are loaded onto the primary absorber to improve light absorption and charge separation.[21] Studies in this area have developed very rapidly within the last 10 years. A recent comprehensive review covering the state-of-the-art visible driven heterojunction photoelectrodes has been conducted by us and readers are directed to this for further examples.[22] An additional PEC-based approach for water splitting is to utilise a series-connected photocathode and photoanode in a tandem configuration. The complete cell contains two light absorbers: a photoanode for water oxidation and photocathode for water reduction. One conductive metal wire can be used for the wired configuration (configuration (c)) or a transparent conductive substrate can be used as an electron-hole recombination layer for the wireless configuration (configuration (d)). In both cases, the conduction band minimum of the photoanode must lie more negative than the valence band maximum of the photocathode to ensure complementary light absorption, whereby photons transmitted through the first material are then absorbed by the second. The main advantages of the PEC tandem cell are the increased photovoltage of the system and additional flexibility in material selection. A critical issue that needs to be addressed in the development of photocathodes and photoanodes in tandem stacks is the high photovoltage generated under illumination, but both sides must maintain a similar current density when no external bias is applied. Another device configuration based on unbiased water splitting is achieved by coupling a PV cell with a semiconductor photoelectrode represented by configuration (e), denoted as Type V. In such a PV-PEC cell, the additional bias is applied to the photoelectrode by the PV material. The PV cell may be composed of single or multiple junctions, based on Si,[23] Group III-V materials,[24] d or hybrid perovskites.[25] Wide bandgap semiconductors are

preferred for the front photoelectrode to enable adequate transmittance for further light harvesting by the PV. In addition, a transparent oxide layer is required between PV and PEC, providing a recombination layer for the photoinduced holes from the PV and electrons from PEC (in the case of a PV-photoanode configuration). Turner et al. demonstrated such a monolithic tandem device based on a photocathode of p-type $GaInP_2$ in combination with a GaAs p–n junction PV, recording a then benchmark STH efficiency of 12.4%. However, the short lifetime and high cost of the device limit its practical use.[24] A device without a photoelectrode containing a shielded PV junction (known as a buried PV cell) is illustrated in configuration (f), denoted as Type VI. Even though there is no semiconductor photoelectrode present, such a device can still be termed a PEC cell because light-driven electrochemical reactions occur within the cell. To date, the highest STH efficiency (30 %) achieved by such a system consists of two polymer electrolyte membrane electrolysers in series with one InGaP/GaAs/GaInNAs(Sb) triple junction solar cell, however this design still suffers from high materials cost amongst other factors.[26]

2.3. Electrocatalysts development

2.3.1 Hydrogen evolution catalysts

The best known heterogenous electrocatalysts for the hydrogen evolution reaction (HER) are based on the platinum (Pt), which sits at the top of the volcano plot with ideal M-H strength or optimal free energy for H^+ adsorption ($\Delta G_{H^+} = 0$). However, their activity highly depends on the mass used and lack of abundance of Pt hinders its large-scale commercialisation.[27] Therefore, considerable efforts have been focused on reducing the Pt amount required or developing alternative catalysts to replace Pt.

The platinum utilisation in traditional Pt-based catalysts is very low, as the active sites only come from Pt atoms on the surface of the catalysts. Therefore, considerable efforts have been devoted to increasing the platinum utilisation as well as to improve the HER activity of Pt-based catalysts.[28, 29] Chen and co-workers showed that Pt monolayer supported on tungsten carbide film (Pt/WC or Pt/W_2C) exhibited nearly identical HER activity to that of bulk Pt foil in acidic media, whereas the low surface area of both Pt/WC and Pt/W_2C limited their application on practical electrolyser devices.[28, 30] For a better mass transfer, the as-prepared HER catalysts are commonly tested on the rotating disc electrodes with glassy carbon as the substrate. Li and co-workers reported that atomic layer deposition deposited 4.4 wt % Pt nanoparticles on Mo_2C supports showed a similar activity to 20 wt % Pt/C with sufficient durability in 0.5 M H_2SO_4 for 48 h.[31] Furthermore, Qiu et al. recently reported atomic layers of Pt clusters modified N-doped Mo_2C (Pt/N-Mo_2C) function as a high-performance and robust catalyst for hydrogen evolution. The optimised 1.08 wt% Pt/N-Mo_2C exhibits 25-fold, 10-fold, and 15‑fold better mass activity than the benchmark 20 wt% Pt/C in neutral, acidic, and alkaline media, respectively with an outstanding long-term operational durability of 120 h.[27] To further increase the Pt utilizing efficiency, the size of Pt was further reduced to a single atom. For example, single Pt atoms immobilized on an MXene (Pt /$Mo_2TiC_2T_x$) exhibited a high catalytic ability with low overpotentials of 30 and 77 mV to achieve 10 and 100 mA/cm^2 and a mass activity about 40 times greater than the commercial Pt/C catalyst.[32] Highly stable single Pt atomic sites are also successfully anchored on aniline-stacked graphene (Pt SASs/AG) with outstanding HER performance. Pt SASs/AG catalyst presents excellent HER activity with 12 mV overpotential at 10 mA/cm^2 and a mass current density of 22400 A/ gram

of Pt at an overpotential of 50 mV, which is 46 times higher than that of commercial 20 wt% Pt/C.[33]

Apart from the widely used Pt, MoS_2 would be a suitable candidate material, which was first confirmed by DFT calculation that the free energy of absorbed H was close to that of the reactant or product ($\Delta G_{H^+} = 0$).[14] However, it was demonstrated only the edges of MoS_2 were highly active for HER in practice.[34, 35] Since this discovery, some rational designs on nanoscale MoS_2 catalysts were conducted for improving their catalytic activity. The first approach was the engineering of the active site by constructing active-site rich nanosheets and creating a porous structure.[36] The second approach was the electronic conductibility engineering by doping suitable heteroatoms (i.e. Co or Ni) and coupling with conductive species, such as carbon nanotubes and graphene.[37]

With the past few years, transition metal-based carbides, borides and phosphides were also reported to exhibit very promising HER activity. Hu's group showed catalysts based on MoB and Mo_2C particles deposited onto carbon-paste electrodes exhibited similar HER activity of -20 mA/cm^2 between -210 and -240 mV overpotential.[38] Moreover, MoB and Mo_2C showed a similar activity at pH 14 in comparison with their activity at pH = 0, highlighting the usage of HER catalysts in a wide pH range that similar to Pt.[38] Popczun et al. first reported hollow nanoparticles of Ni_2P loaded on Ti substrate as an active HER catalysts in an acidic media, which exhibited -20 mA /cm^2 at -130 mV in 0.5 M H_2SO_4. Although Ni-Mo nanopowder on Ti substrate presented a much higher initial activity (-20 mA/cm^2 @ -80 mV), but the activity of Ni-Mo degraded rapidly under acidic conditions.[39] Whereas the Ni-Mo/Ti electrode (1mg/cm^2 mass loading) showed excellent stability for 100 h under alkaline conditions without

loss of their activity (-10 mA/cm^2 @ -100 mV), which was one of the most active, basic-stable, earth-abundant HER electrocatalyst to date.[39] For acid-stable HER catalysts (over 24 h durability in 0.5 M H_2SO_4), CoP nanoparticles on a Ti support (2 mg/cm^2 mass loading) produced a benchmark cathodic current density of 20 mA/ cm^2 at a low overpotential of – 85 mV. [40]

2.3.2 Oxygen evolution catalysts

2.3.2.1 Noble-metal based OER electrocatalysts

Both RuO_2 and IrO_2 are commonly considered as benchmark electrocatalysts for OER owing to their high electrocatalytic activities toward OER in both acidic and alkaline solution.[41, 42] However, it was found that RuO_2 is unstable under high anodic potential. The reason behind is that $(Ru^{4+})O_2$ will transform into the hydrous compound $RuO_2(OH)_2$ and deprotonate into a high oxidation state $(Ru^{8+})O_4$ under anodic conditions,[43] which is not stable in the electrolyte and can be further dissolved into solution, thus leading to the deterioration of RuO_2 catalysts. Although a similar stability issue is present in the OER for IrO_2, where a high oxidation state $(Ir^{6+})O_3$ will be formed under high anodic potential and will be further dissolved in the electrolyte.[44] Many types of research have concluded that the OER performance of IrO_2 is slightly worse but more stable than that of RuO_2.[43, 44] One effective strategy to improve the stability of RuO_2 is to load IrO_2 on RuO_2 surface, constructing a core-shell structure (IrO_2/RuO_2), to minimizing the Ru dissolution during OER.[45, 46] Recent methods to increase the Ru utilising efficiency and stability have focused on synthesising stable isolated single atomic Ru on conductive supports. Li et al. developed an electrocatalyst based on atomically dispersed Ru atoms on platinum-copper alloys

(Ru_1Pt_3Cu), which exhibited an overpotential of 220 mV at 10 mA/cm^2 and nearly ten-folds higher lifetime than pure RuO_2 for acidic OER.[47] Sun et al showed a stable single atomic ruthenium catalyst anchoring on the surface of cobalt iron layered double hydroxides, that was 0.45 wt.% Ru /CoFe- LDHs catalyst, which exhibited a low overpotential of 198 mV to drive 10 mA/cm^2 current and small Tafel slope of 39 mV/dec for OER. The strong electronic coupling between ruthenium and layered double hydroxides also enabled its remarkable stability in alkaline condition (25 hours with 99 % remaining). [48]

Until now, the Ni- and Co-based materials have been intensively investigated as promising non-precious OER electrocatalysts, which will be discussed next.

2.3.2.2. Cobalt-based OER electrocatalysts

In 2008, Nocera and co-workers reported a self-healing amorphous cobalt phosphate (Co-Pi) catalyst, which was *in -situ* formed under the anodic polarisation of an indium tin oxide (ITO) electrode in phosphate-buffered water containing cobalt (II) ions. [49] Further X-ray absorption spectroscopy (XAS) studies suggested that the presence of bis-oxo/hydroxo-bridged Co ions composed of edge-sharing CoO_6 octahedra in the Co-Pi cluster. The proposed structural model of molecular Co-Pi cluster as shown in Figure 2-12 indicated the bridging oxo/hydroxo ligands (Red) and nonbridging oxygen ligands (light red) such as absorbed water, hydroxide and phosphate to complete the octahedral coordination geometry of each peripheral Co ion (Blue).[50]

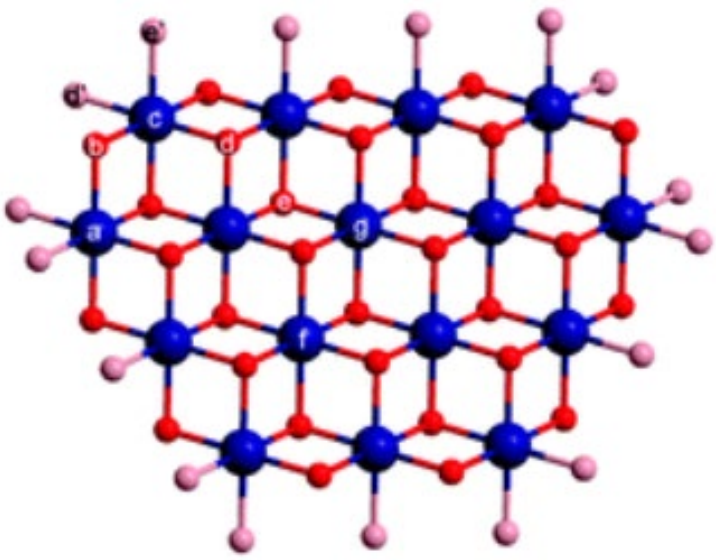

Figure 2-12: A molecular cobaltate cluster model for Co-Pi. Red: bridging oxo/hydroxo ligands; Light red: nonbridging oxygen ligands (including water, hydroxide, and phosphate; Blue: Cobalt ions. Reproduced from reference 50.

Figure 2-13 shows the proposed mechanism involving the catalytic reactions cycle among Co (II), Co (III), and Co (IV)- oxo oxidation states at Co centres during OER. In detail, Co (III) centres in the catalyst undergo oxidation to Co (IV) under anodic bias, and it is these Co (IV) centres that oxidize water to give O_2.[51] At the meantime, the Co (IV) centres are reduced to Co(II), which is further dissolved into solution. However, these Co (II) ions are then rapidly re-oxidised to Co (III) ions under the anodic bias, achieving the self-repair process.[52]

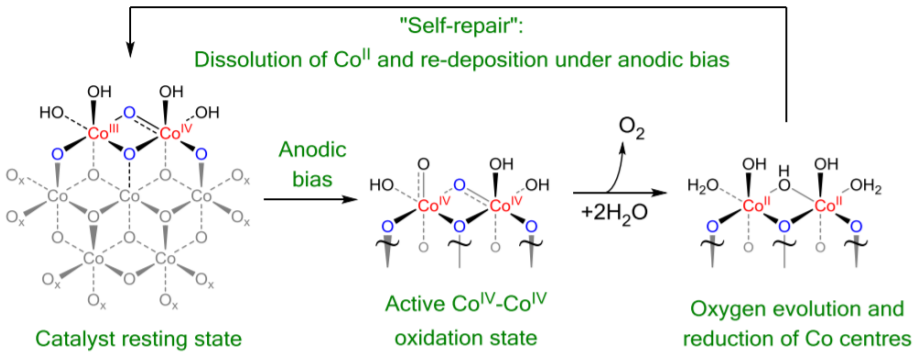

Figure 2-13: the structure and OER mechanism of Nocera's self-repair Co-Pi catalysts. Reproduced from reference 51.

Since the report on Co-Pi catalysts, numerous other groups have focused on developing cobalt based oxides or oxyhydroxides as efficient and stable OER catalysts. Engineering the cobalt electronic states and increasing the surface area are effective strategies.[53, 54] For example, Dai et al. designed an efficient Co_3O_4 nanosheets with proper control of Co^{2+}/Co^{3+} ratio by a plasma- engraving strategy, which also produced high surface area for OER.[55] The plasma-engraved Co_3O_4 nanosheets exhibited 10 times higher current density than that of pristine Co_3O_4.[55] Wei et al. reported that ultrathin γ-CoOOH nanosheets with local structure distortion of the surface CoO_{6-x} octahedron. This greatly enhanced the electrophilicity of H_2O and facilitated the interfacial electron transfer between Co ions and adsorbed -OOH species to form O_2, resulting in the high electrocatalytic activity of layered CoOOH for water oxidation (large mass activity of 66.6 A/g; low overpotential of 300 mV at 10 mA /cm^2, small Tafel slopes of 38 mV/ dec, and 12 hours durability in alkaline medium).[56] Liu et al. showed that the abundant high spin Co^{3+} with spin state of $t_{2g}^4 e_g^2$ on Co_3O_4 greatly improved the intermediates absorption and thus the OER activity (280 mV overpotential at 10 mA/cm^2).[57] Moreover, enhanced performance can be obtained by the incorporation of additional metal ions including V, Fe, Ni, Zn Mn into Co_3O_4 or CoOOH to form mixed spinel-type oxides or layered double hydroxides (LDHs) as summarised in Table 2-1 .[58-64] In particular the benchmark OER activity based on cobalt lies on the Zn-substituted CoOOH reported by Wang et al.[62] The carefully designed catalyst $Zn_{0.2}Co_{0.8}OOH$ with Zn-O-Co-O configuration exhibited an overpotential of 235 mV at 10 mA/cm^2 current density and negligible change of OER potential at 20 mA/cm^2 after 40 hours continuous testing in alkaline environments.[62]

Samples	η@10 mA/cm^2 (mV)	η@100 mA/cm^2 (mV)	Tafel slope (mV/dec)	Substrate	References
Amorphous CoVOx	347	n.a.	51	GC	65
$CoV_{1.5}Fe_{0.5}O_4$	300	~ 350	38	GC	66
CoMoV LDH	270	~ 450	106	NF	67
$Fe_{0.5}$ $V_{0.5}$ sphere	390	n.a.	36.7	GC	68
$Ni_{0.75}$ $V_{0.25}$ -LDH	318	n.a.	50	GC	69
Plasma-engraved Co_3O_4 nanosheets	300	n.a.	68	GC	55
Spin state modulated Co_3O_4 nanowires	280	330	61.4	CC	57
CoOOH ultrathin nanosheets	300	n.a.	38	GC	70
Co (OH)F	313	n.a.	52.8	GC	71
$CuCo_2S_4$	310	n.a.	86	GC	72
$CoS_{4.6}O_{0.6}$	290	n.a.	67	GC	73
3D frame-like CoFe oxides	340	n.a.	57	GC	64
Gelled-FeCoW	223	n.a.	37	GC	74
Fe-CoOOH/Graphene	330	n.a.	37	GC	58
$Co_{0.67}Fe_{0.33}OOH$ porous nanosheets	266	~ 300	30	CC	59
$Zn_{0.2}Co_{0.8}OOH$	235	n.a.	34.7	GC	62
CoMn-LDH	324	n.a.	43	GC	63
Mn_2O_3 hollow nanotube	270	470	85	NF	75
$Mn_3O_4/CoSe_2$ nanocomposite	450	n.a.	49	GC	76
Perovskite $Bi_5CoTi_3O_{15}$	320	n.a.	34	GC	77
NiCo biometal-orgranic framework nanosheets	250	n.a.	42	GC	78
NiCoP	300	n.a.	80	GC	60
NiCoFeP	330	n.a.	n.a.	Au-NF	61
NiFe-LDH	300	n.a.	38	GC	79
NiFe/heteroatom-doped Graphene	~ 310	~ 370	n.a.	GC	80
NiFeCr-6:2:1 LDH	280	n.a.	69	GC	81

Table 2-1: OER performance comparison of recently reported state-of-art transition metal-based electrocatalysts in 1M KOH. GC, CC, NF, and Au-NF stand for glassy carbon, carbon cloth, Nickel foam and Au plated Nickel foam substrates, respectively.

2.3.2.3. Nickel-based OER electrocatalysts

Not long after reporting the Co-Pi self-healing OER catalysts in neutral buffer electrolyte , Nocera and co-workers reported its nickel analogues, that is Ni-Bi catalysts, which exhibited better OER performance in alkaline electrolyte. [82] The Ni-Bi films can be electrodeposited from dilute Ni^{2+} solutions in borate electrolyte at pH 9.2, similar to those of reported Co-Pi electrocatalyst. The active Ni-Bi catalyst films exhibited a short-range ordering structure that similar to γ-NiOOH, which consisted of bis-oxo/hydroxo-bridged nickel centres organized into sheets of edge-sharing NiO_6 octahedra as revealed by the Extended X-ray absorption fine structure reported by Nocera's group.[83] X-ray absorption near-edge structure spectra collected on samples after various amounts of anodization revealed a shift in the average oxidation state of the nickel centres in the catalyst from +3 before any anodization to +3.6 once anodization was complete,[83] indicating that a substantial proportion of Ni (IV) species was formed under anodization condition. In other words, Ni (IV) was the active species in the catalytic cycle, Ni (II)→ inactive Ni (III) → active Ni (IV), at Ni centre as Co (IV) is the active site for Co-Pi water oxidation catalyst described above.[83] It was found that trace amount of irons ions incorporation in nickel oxide or nickel oxyhydroxides would significantly enhance the OER activity.[84] Indeed, Bell and co-workers discovered that electrodeposited $Ni_xFe_{1-x}OOH$ films with 25 % iron in nickel oxides presented up to 500- fold higher OER current density compared to pure Ni and Fe oxyhydroxide films in 0.1 M KOH.[85] Further *in-situ* and operando X-ray absorption spectroscopy (XAS) revealed that the improved OER activity originated from the highly oxidising $Ni^{4+/3+}$ couple, rather than the iron centres, but

Fe doping was proposed to be an effective strategy to promote the access to OER active Ni (IV) species.[86, 87]

2.4 Photoelectrode Materials

2.4.1 Material requirements

In order to reduce energy input in electrocatalytic water splitting, solar energy assisted catalytic water splitting is proposed to drive the reaction, denoted photoelectrochemical (PEC) water splitting. The most important aspect for PEC water splitting is the choice of a suitable photoanode and/or photocathode material. An ideal water splitting photoanode and/or photocathode require semiconductor materials that possess the following characteristics:

(i) **Suitable band gap energy and band positions**. Natural sunlight consists of 5% UV (300–400 nm), 43% visible (400–700 nm), and 52 % infrared radiation (700–2500 nm). Therefore, appreciable light absorption in the visible region is required to increase efficiency, and this in turn depends on the bandgap of the semiconductor. As the proton reduction potential is located at 0 V vs NHE and O_2/H_2O potential at 1.23 V vs NHE (pH = 0), the theoretical minimum bandgap for water splitting requires incident photons with a minimum energy of 1.23 eV, which corresponds to a wavelength of light of ~1100 nm. However, when considering the thermodynamic energy losses (0.3-0.4 eV) occurring during charge carrier transportation and the overpotential requirement for acceptable surface reaction kinetics (0.4-0.6 eV), a minimum bandgap of ~1.8 eV is required, corresponding to light absorption at ca. 700 nm. The upper limit on the

bandgap energy is 3.2 eV because of the rapid drop in the sunlight intensity below 390 nm according to the solar spectrum.

Therefore, for a single semiconductor photoelectrode, a bandgap energy between 1.9 eV and 3.2 eV is desired to obtain sizable photovoltages. Theoretically, a bandgap of *ca.* 2.0 eV is preferred for optimal sunlight utilisation in addition to the thermodynamic band position requirements.[88] However, in practice, it has hardly been achieved because the expected photovoltage could seldom be met. Without high photovoltages (>1.61V), even the highest current density will not solve the problem of unbiased water splitting and thus external bias or tandem devices are needed to provide the extra voltage to split water. Figure 2-14 illustrates the bandgaps and band positions of typical n-type and p-type semiconductors utilised for PEC water splitting at pH=0. It is noteworthy to mention that the band positions of oxide semiconductors vary depending on the pH of the electrolyte since V_H depends on the pH of the solution (by -0.059 V per pH unit) with respect to the redox potential of the electrolyte. Furthermore, according to the Nernst equation, the water reduction and oxidation potentials change in a similar manner to the band positions (i.e. -0.059 V/unit pH). It is generally accepted that the Nernstian dependence indicates that H^+ and OH^- are potential determining ions (PDI) adsorbed on the semiconductor surface within the Helmholtz layer.

Overall the band positions of most semiconductors in particular oxides show the same pH dependence as represented by the Nernst Equation, whereas the band positions are fixed with respect to the water redox potentials. Hence, the relative difference between band positions of an oxide photocatalyst and water redox potential is pH independent.

(ii) **Efficient charge carrier separation and transportation in the semiconductor.** The fast charge recombination is a major factor contributing to low STH efficiencies, and thus a strategy to promote efficient charge carrier separation and transport is required, which depends on both intrinsic properties (hole and electron mobility) and extrinsic properties (crystallinity, nanostructure) of the material.

(iii) **Strong catalytic activity and stability.** Suitably rapid surface reaction kinetics can reduce surface electron-hole recombination due to the rapid electron/hole's consumption on surface by water reduction/oxidation reaction. Photocorrosion is a major problem for many candidate water splitting semiconductors, in particular metal sulphides, and occurs when the photogenerated holes/electrons do not oxidise/reduce water but instead decompose the photocatalyst itself. These photocorrosion reactions depend upon the relative positions of the semiconductor band edges and the respective decomposition potentials. Anodic photocorrosion can occur if the anodic decomposition potential (E_{pd}) is above the valence band potential of the semiconductor. Conversely, cathodic photocorrosion can occur if the cathodic decomposition potential (E_{nd}) is below the conduction band of the semiconductor. Metal oxides such as $BiVO_4$ and ZnO or metal sulphides such as MoS_2 and CdS can easily undergo anodic photocorrosion depending on the pH of the electrolyte since the actual values of the decomposition potentials depend upon the pH value. However, for common photoanode materials such as TiO_2 and Fe_2O_3, even though their anodic decomposition potential is above the valance band potential, they are thermodynamically stable because of the very slow decomposition reaction kinetics.

In addition, the photoelectrode materials should be low-cost and composed of earth-abundant elements for practical applications, which is crucial toward justifying the argument for economical scale-up of solar-to-fuels devices.

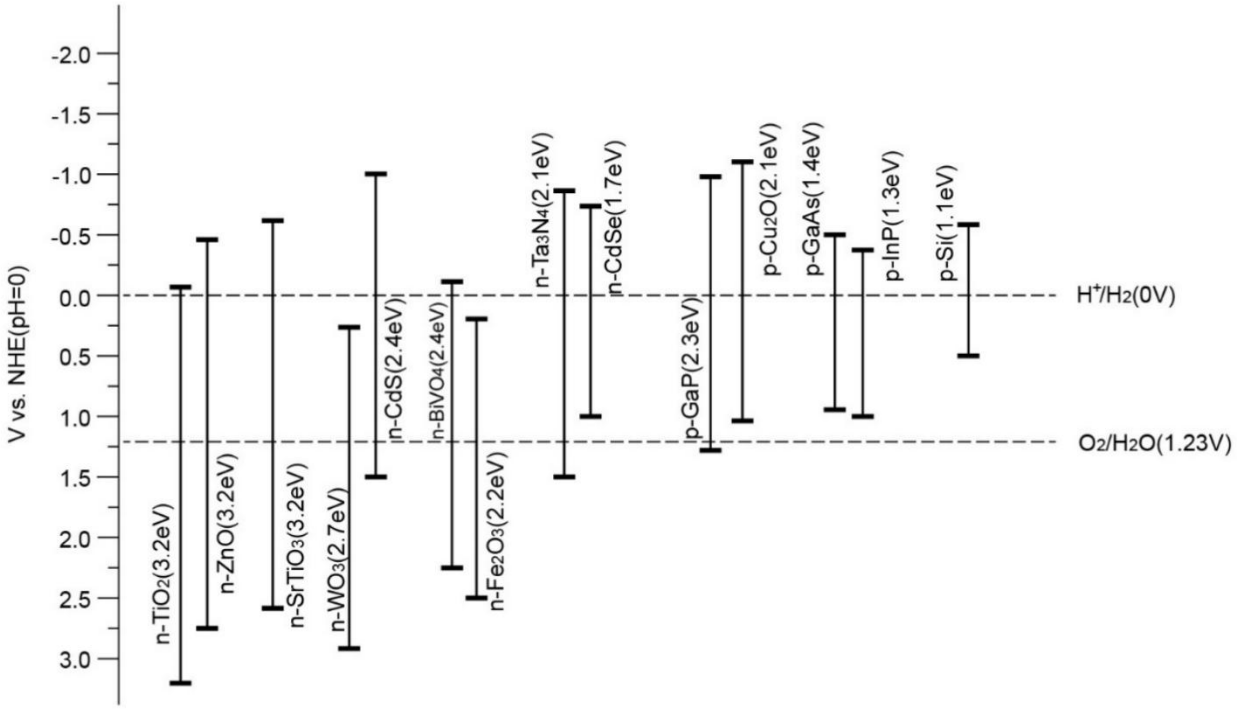

Figure 2-14: Band positions of various semiconductors with respect to the redox potentials of water splitting at pH=0.

2.4.2 Photoanode materials

There are numerous photoanode materials reported for PEC water splitting over the past 10-20 years, reflecting the great amount of research invested in this area. This section summarises the most promising low-cost and efficient photoanodes employed so far and puts forward potential strategies to improve their performance.

(1) TiO_2. TiO_2-based photoelectrodes for water splitting have been intensively investigated since 1972 due to many favourable properties, such as being composed of

earth-abundant, non-toxic elements as well as being photochemically stable under either strongly acidic or basic conditions.[89] However, due to its wide bandgap (3.2 eV for anatase and 3.0 eV for the rutile phase), only 5 % of the solar spectrum (predominantly UV light) can be absorbed, which leads to a very low theoretical STH efficiency (η = 1.3 % for anatase and 2.2 % for rutile TiO_2). During the last decade, many attempts have been made to dope TiO_2 with anions or cations to extend its working range into the visible region in order to improve the overall absorption whilst maintaining its good stability and low-cost. The valence band of TiO_2 can be modified by introducing non-metal species such as carbon, or nitrogen through forming mid-gap states,[90] and the conduction band can be modified by forming donor states below it by doping 3d transition metal ions. However, in most of these examples, because there is no fundamental bandgap change, no substantial enhancement in visible-driven PEC water splitting activity has been recorded by these materials. Although doping can extend its light absorption into the visible, the optical absorption is still very moderate above $\lambda > 450$ nm. Recently, Mao et al. developed a novel strategy to synthesise a disordered nanophase TiO_2 by incorporating a dopant through the hydrogenation of TiO_2 nanocrystals; the as-prepared hydrogenated TiO_2 exhibits a black colour, corresponding to a bandgap energy of 1.0 eV rather than 3.30 eV normally found for pure TiO_2, promising a much higher solar to fuel conversion efficiency.[91]

(2) α-Fe_2O_3. α-Fe_2O_3 (haematite) is a promising photoanode material with good chemical stability, low-toxicity and low-cost due to its high natural abundance. In addition, it has a bandgap value between 1.9-2.32 eV, allowing for visible light absorption which translates to a theoretical 12.9 % STH efficiency.[92] However, haematite possesses a conduction band position significantly more positive than the

proton reduction potential and thus can only be used for PEC water oxidation in the presence of an external bias. In addition, haematite has other drawbacks including: (1) a short charge carrier lifetime on the order of picoseconds, due to the fast charge carrier recombination in the bulk; (2) a relatively low absorption coefficient (order of 10^3 cm^{-1}), requiring at least a 400-500 nm thick film for optimal light absorption, (3) a slow minority charge carrier (hole) mobility (ca. 0.2 cm^2 V^{-1} s^{-1}) which results in a very short diffusion length of 2-4 nm for holes and (4) poor water oxidation kinetics, which leads to a high recombination rate at the surface because of the hole accumulation.[92] To overcome these limitations, several strategies have been applied to improve the activity of haematite-based photoelectrodes. Firstly, high concentration doping by different elements such as Si, Ti and P has shown to improve the conductivity of electrons in hematite.[92] In this regard, Si-doped nanocrystalline haematite films can exhibit a high PEC performance, with photocurrent densities of at least 2.7 mA cm^{-2} at 1.23 V vs RHE under AM 1.5G one sun irradiation. Secondly, nanostructuring of the semiconductor to branched nanorods or core-shells has been reported to overcome the short diffusion length of photoholes and to facilitate efficient hole transportation to the surface.[93] Thirdly, co-catalyst modification, for example, with Co-Pi or FeOOH, has been demonstrated to speed up surface water oxidation kinetics.[94] Furthermore, the addition of thin metal oxide under/overlayers onto α-Fe_2O_3 results in significant improvements in PEC activity, which affects surface state passivation and an increase in charge carrier concentration and mobility.[95]

Nevertheless, the recently reported benchmark photocurrent and STH efficiency for haematite (4.68 mA cm^{-2} at 1.23 V *vs.* RHE, STH of ca. 0.55 %) achieved by a vertically-grown haematite nanosheet film modified with Ag nanoparticles and Co-Pi

co-catalyst suggests much more work is required to improve its STH performance given that the limitations of the material are fairly well understood.[96]

(3) $BiVO_4$ (BVO) is an n-type semiconductor composed of relatively earth-abundant elements. It has a direct bandgap of 2.4 eV with a conduction band position slightly more positive than 0 V vs NHE (pH=0) and a valence band position at *ca*. +2.4 eV vs NHE (pH=0), and was first reported for photocatalytic water oxidation in the presence of sacrificial reagents by Kudo et al.[97] Since this discovery, it has also been employed as a photoanode for PEC water splitting, the progress of which has been reviewed in detail.[98] The theoretical maximum photocurrent and STH efficiency of BVO are 7.4 mA cm^{-2} at 1.23V vs RHE and 9.1% respectively. The efficiency of BVO is limited by several factors. Fast charge carrier recombination is an issue due to its short electron diffusion length (only 10 nm) and the material also exhibits poor surface water oxidation kinetics. The electron diffusion length can be significantly increased up to ~ 300 nm by doping with Mo and W elements. [99] In addition, van de Krol et al. introduced a gradient doping of tungsten, starting from 1 % W at the interface with the back contact to 0% W at the BVO/electrolyte interface, resulting in an enhanced charge carrier-separation efficiency. The charge carrier separation efficiency increases to ~60 % at $1.23V_{RHE}$ compared with ~38 % for homogeneously doped BVO. This enhancement is due to the extension of the band bending region over the entire thickness of the BVO photoanode, and thereby improves the carrier separation. In detail, when W-doped and undoped BVO are brought into contact, the Fermi energy levels equilibrate by electron transfer from the W-doped part to the undoped part of the material. A depletion layer at the interface between W-doped and undoped $BiVO_4$ is then formed.[23]

The poor surface reaction kinetics can be improved by the addition of oxygen evolution co-catalysts such as Co-Pi (cobalt phosphate). For example, a Co-Pi modified junction nanoparticulate $BiVO_4$ / ZnO nanorod exhibited a photocurrent of ca. 3 mA/cm^{-2} at 1.23 V vs RHE; the function of the vertical ZnO nanowires was to trap light and improve electron transfer to counter electrode.[100] Recently, a benchmark photocurrent of 2.73 mA/ cm^{-2} at a potential as low as 0.6 V vs RHE and an ABPE of 1.7% was achieved on a nanoporous BVO photoanode with a dual-layer FeOOH/NiOOH co-catalyst.[101] Furthermore, by assembling a PV-PEC tandem system composed of a silicon solar cell and BVO photoanode, an STH efficiency of 4.6% was achieved.[23] Beyond this, a nanocone Mo:$BiVO_4$/Fe(Ni)OOH photoanode exhibited a record photocurrent of 5.82 mA/cm^{-2} at 1.23 V vs RHE. Together with a single perovskite solar cell, the tandem device exhibited unassisted water splitting with an STH conversion efficiency of 6.2%.[102]

(4) CdS. In theory, photocatalytic H_2 and O_2 evolution under visible light irradiation can be achieved over pure CdS due to its relatively narrow band gap of 2.4 eV and suitable conduction band position of -0.3 V and valence band position of +1.7 V vs NHE (pH=0). Although the material possesses a long charge carrier diffusion length in the micrometre range, its poor water oxidation kinetics leads to the accumulation of photogenerated holes at the surface, resulting in serious anodic photocorrosion. To alleviate this, hole scavengers such as S^{2-} and SO_3^{2-} are commonly employed when utilising CdS for photocatalytic water reduction. Similar to CdS, the related II-VI semiconductors (e.g. CdS, CdTe, CdSe, ZnTe) also require a stabilisation or protection strategy if being utilised as photoanodes for PEC water splitting. Surface passivation layers have been widely used to reduce charge recombination at surface states, increase

the reaction kinetics and protect the semiconductor from chemical corrosion; this has been summarised recently by Yang et al.[103] Using this principle, Lewis et al. reported a 140 nm thick amorphous TiO_2 layer (deposited via atomic layer deposition, [ALD]), together with a thin overlayer consisting of a NiO oxygen-evolution electrocatalyst that enabled CdTe photoanode to run stable photocurrents for four days.[104] CdS photoanodes modified with TiO_2 nanoparticles using organic linkers has also been demonstrated for long-term hydrogen production and a CdS photoanode could also be modified by nano-Nb oxides for efficient and stable photoelectrochemical water splitting.[105] Recently, a TiO_2/CdS/Co-P_i heterojunction exhibited a photocurrent of ca.1 mA cm^{-2} at 1.23 V vs RHE and reasonable stability over 2h irradiation, due to photoelectron injection into TiO_2 from CdS and hole transfer to Co-P_i for water oxidation, which to some extent alleviated the photocorrosion process.[106] Nevertheless, much more work is needed to improve the performance and stability of sulphide-based photoelectrodes.

(5) **Group III-V compounds.** Group III-V compound semiconductors such as GaAs and InP, and related quaternary alloys show some potential to be used in PEC water splitting due to: (1) the possession of ideal and narrow bandgaps for light absorption, (1.42 eV for GaAs and 1.35 eV for InP); and (2) they exhibit extraordinary charge carrier mobilities, e.g. an electron mobility of up to 9200 $cm^2\ V^{-1}\ S^{-1}$ and a hole mobility up to 400 $cm^2\ V^{-1}\ S^{-1}$ for GaAs. One of the first examples of solar-driven water splitting using III-V materials was reported by Turner et al, who fabricated a monolithic PV/PEC device for hydrogen production with an impressive STH efficiency of 12.6% using a tandem cell consisting of a p/n GaAs bottom cell connected to a $GaInP_2$ top cell via a tunnel diode interconnect.[24] However, since reporting this figure

the same group highlighted the quite common problem of little or no standardisation in measuring STH, which manifested itself in a subsequent re-adjustment of the STH efficiency down to 9.3 %. Although high photocurrents and STH efficiencies can theoretically be achieved by III-V materials compared to metal oxides such as TiO_2, Fe_2O_3 and $BiVO_4$, their instability and extremely high cost limit their practical application severely. Recently, Lewis et al. demonstrated that typical GaAs and GaP photoanodes could be stabilised against photo-corrosion by applying a conformal ALD-deposited TiO_2 layer in conjunction with a nickel oxide/hydroxide electrocatalyst.[107] The same group also reported that GaAs, GaP and InP could be protected by a multifunctional layer of NiO_x which acts not only as a protection layer but also an efficient oxygen evolution catalyst.[108] However, these devices use expensive absorbers, advanced overlayer coating technology (ALD) and co-catalyst deposition techniques (sputtering) which would be challenging to apply to large area cells. The widespread use of such complex architectures is not expected in the field of solar-driven fuel synthesis but instead acts as a demonstration to address their stability problems.

2.4.3 Photocathode materials

As shown in Figure 2-13, the conduction band positions of p-type semiconductors such as a cuprous oxide (Cu_2O) and Si are more negative than the redox potential of H^+/H_2, and thus they can be employed as photocathodes for proton reduction. However, in most cases their application is still limited due to their facile cathodic photocorrosion in solution. [109, 110]

(1) Cu_2O. Cuprous oxide (Cu_2O), possesses a direct bandgap of ca. 2 eV and its conduction band position (at roughly -1.1 eV vs NHE) is suitable for light-driven hydrogen evolution from water. An attraction to the use of Cu_2O is its abundance, scalability, low toxicity and high theoretical photocurrent of ~15 mA cm^{-2} together with a potential 18 % STH efficiency under AM 1.5G light illumination.[22] However, one major drawback of Cu_2O is its so far relatively moderate photocurrent due to fast electron-hole recombination. An even more serious drawback is its very poor stability because the redox potentials for the reduction and oxidation of monovalent copper oxide lie within the bandgap.[109] To address these issues, several strategies have been applied, for example, (1) the combination with an n-type semiconductor with a more positive conduction band, which forms a p-n junction to promote the fast transfer of photo-electrons from Cu_2O to the n-type semiconductor, improving not only the efficiency but also the stability. 2) The deposition of a thin protection layer composed of, for example, carbon or a metal oxide. For a stable Cu_2O based PEC electrode, the p−n junction must be contiguous and uniform, the protection layer must be conformal and pinhole-free and the co-catalyst must be robust and uniformly deposited on the electrode surface. Grätzel *et al.* reported a $Cu_2O/ZnO/Al_2O_3/TiO_2/Pt$ hybrid by adopting the strategy mentioned above, which displayed a photocurrent of −7.6 mA cm^{-2} at 0 V *vs* RHE with improved stability due to the protective nature of TiO_2 and the high conductivity of ZnO/Al_2O_3 (AZO).[111] Other similar configurations such as Cu_2O nanowire/AZO/TiO_2/RuO_x and Cu_2O/AZO/TiO_2/MoS_2 have been reported. However, the high cost and limited long-term stability hamper their use in practical solar-to-fuel devices despite a large area cell (50 cm^2) recently produced.

(2) Group IIIA Metal Phosphides

(a) **GaP.** GaP has an indirect bandgap of 2.26 eV, with a conduction band edge located at -0.6V vs NHE at pH=0 and thus could be used for photocatalytic water reduction to produce H_2. Due to its large photovoltage, unbiased overall water splitting can be achieved through coupling with another photoanode material. Although the n-type GaP is unstable in aqueous solution, the p-type GaP is stable for extended periods under water reduction conditions. The overall STH efficiency of GaP is limited by its small minority carrier diffusion length.

(b) InP- based photoanode. InP exhibits a bandgap of 1.35 eV, representing near optimal absorptivity of the solar spectrum. However, the very high cost of InP limits its commercial processibility as a photoelectrode for water splitting. Notten et al fabricated a photocathode composed of InP nanowire arrays with molybdenum sulphide electrocatalysts for H_2 production, with an overall STH of 6.4 % under one sun irradiation. However, the authors claimed the performance of InP-based photoelectrodes was limited by severe photocorrosion.[112] Therefore, amorphous, TiO_2 has been employed as a surface passivation layer to isolate the InP photoelectrode from the electrolyte. One should also note that the large valence band offset between TiO_2 and these metal phosphides can create an energy barrier for holes reaching the surface, reducing recombination at the surface.

It is worth mentioning that Hannappel and co-workers developed an efficient tandem cell based on group III-V materials. The tandem structure consists of a GaInP n-p top cell (Eg=1.78eV) and GaInAs n-i-p bottom cell (Eg=1.26 eV) with Rh electrocatalysts deposited onto the surface. The as-prepared tandem device yields an STH of 14% and 17% for unbiased and potentiostatically assisted water splitting, respectively, which is the present benchmark efficiency for a tandem PEC device. [113]

(3) Silicon (Si). Silicon has a relatively narrow band gap of 1.1eV, which is almost ideal for use in dual bandgap PV-PEC tandem configurations. A recent review summarised the fact that p-Si photocathodes combined with appropriate co-catalysts can efficiently produce H_2 in a PEC cell.[110] Since silicon can easily undergo photocorrosion reactions in aqueous solution under illumination, corrosion–resistant protective layer is required. Ekerdt et al. demonstrated a silicon-based photocathode for water reduction with an epitaxial $SrTiO_3$ protection layer, which was decorated with mesh-like Ti/Pt nanostructured co-catalysts and resulted in a long term (35 h) performance in 0.5M H_2SO_4 with an ABPE of 4.9%.[114] Very recently, stabilisation of silicon photoanodes in alkaline conditions has attracted more attention for integration into a solar driven water splitting device due to the rapid decrease in the cost of commercial silicon. To date, Si-based photoanodes have been experimentally stabilized by several novel strategies including: (i) deposition of a catalytic transition-metal oxide coating (e.g. CoO_x and NiO_x), (ii) deposition of ultrathin metal films (e.g. Ni) on an oxidised Si surface; (iii) ALD deposition of a thin layer of amorphous TiO_2 in-between Si and surface oxygen evolution electrocatalysts.[107] Tandem PEC water-splitting devices based on silicon (p/n Si-PEC) also appear to be very promising due to the potential for unbiased solar-driven water splitting.[23] As such, we recommend more studies to be carried out in this area if the cost of commercial silicon continues to decrease.

2.5 Surface oxygen evolution catalysts (OER catalysts)

Electrolysis requires the application of a potential higher than 1.23V_{RHE} between anode and cathode because of kinetic barriers that are commonly encountered in

performing multielectron reactions. For example, oxygen evolution from water requires four electrons and generates four intermediate species.[115] On most bare semiconductor surfaces, the formation of intermediate species presents a large energy barrier to oxygen/hydrogen evolution and thus an overpotential is necessary to drive the kinetically rate-limiting multistep oxidation/reduction reactions. In the case of photoelectrodes, the electrocatalytic behaviour occurs at the semiconductor/liquid surface and surface co-catalysts (OER catalysts) are often loaded onto these photoelectrodes to reduce the overpotential (activation energy) and suppress surface recombination by acting as electron/hole acceptors.

Typically, these co-catalysts are deposited on the photoelectrode as thin layers or islands (nanoparticles) to minimise their light absorption or scattering. For a well-performing co-catalyst, both a strong overpotential for OER/HER and appreciable stability under the operating conditions are essential. Figure 2-15 shows the qualitative effect of a surface oxygen evolution co-catalyst on photoanode performance. In order to drive a current density of 10 mA cm^{-2}, a 0.6 V overpotential is needed for a poor-performing co-catalyst, whereas only 0.3 V overpotential is needed for a "good" co-catalyst. Since the choice of oxygen evolution catalysts has no effect on the thermodynamics of the reaction, the open-circuit voltage (V_{oc}) should be the same for any co-catalyst. However, the overall water splitting efficiency is kinetically limited by the co-catalyst selection.[116] The choice of the OER catalyst was already discussed in section 2.3 and some state of the art catalyst will be recapped below.

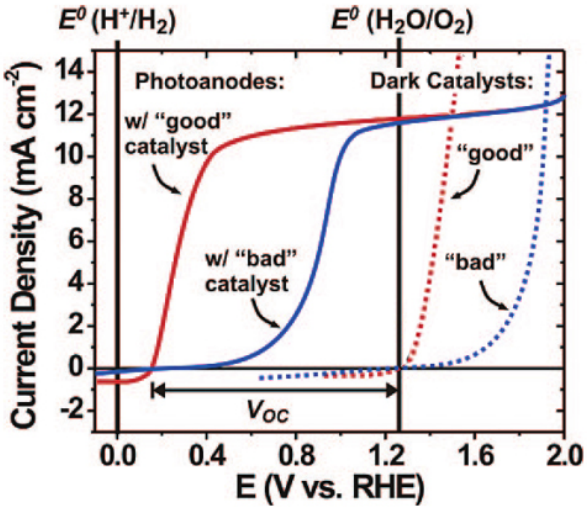

Figure 2-15: Schematic diagram showing the qualitative effect of a surface co-catalyst on photoanode water oxidation performance; the dotted curve represents the dark current with a good or bad co-catalyst; the solid curve represents the photocurrent of a photoanode while coupling a good or bad co-catalyst. Reproduced from reference 116.

Noble metal–based catalysts such as IrO_2 and RuO_2 are among the highest performing OER catalysts but are prohibitively expensive due to their low earth-abundance and therefore in recent years, a great deal of effort has concentrated on developing low-cost first-row transition metal oxide OER catalysts. Jaramillo and co-workers have benchmarked various heterogeneous metal oxide based electrocatalysts for the oxygen evolution reaction based on the overpotential required to achieve a current density of 10 mA cm^{-2}.[117, 118] Among all metal oxide based OER catalysts, cobalt oxide (prepared by electrodeposition) has emerged as a robust, efficient water oxidation co-catalyst and can operate under neutral conditions. Nocera and co-workers prepared cobalt oxide films from cobalt salts in phosphate buffer (Co-P_i) or borate buffer (Co-B_i) solutions at potentials above 1.1 V *vs* NHE.[49] The obtained co-catalyst was amorphous and contained substantial amounts of phosphate or borate anions. The buffer solution was essential for the deposition of highly active films and to maintain

their stability. However, the films were unstable in the electrolyte in the absence of applied bias. The mechanism of Co-Pi films for water oxidation has been investigated by electron paramagnetic resonance (EPR) spectroscopy. During the *in-situ* electrodeposition, changes in the EPR signals were found to correspond to the change of the populations of Co (II) and Co (IV). As the deposition voltage increased into the water oxidation region, the populations of Co(II) decreased while Co(IV) increased, which is evidence for the formation of Co (IV) species during water oxidation at neutral pH.[51] Other co-catalysts such as nickel oxide (NiO_x) have been extensively studied in the literature and have been prepared by various methods. NiO_x films generally convert to either Ni $(OH)_2$ or NiOOH during the water oxidation reaction in alkaline electrolytes (e.g. KOH solution). Yan and co-workers found that highly nanostructured α-$Ni(OH)_2$ nanocrystals were a remarkably active and stable OER catalyst in alkaline media, displaying a current density of 10 mA cm^{-2} at a small overpotential of 331 mV and exhibiting a small Tafel slope of 42 mV/decade.[119] Ni-B_i film prepared with precise thickness control and operating at modest overpotential provided an alternative to the Co-OER catalyst. It was also found that Ni-B_i could undergo self-healing in the proper electrolyte (potassium borate solution), enabling long periods of water oxidation.[82] Very recently, Luo et al. demonstrated that low-cost α -FeOOH film could be fabricated by a facile chemical bath deposition followed by a rapid heat treatment, which guides further development of new low-cost electrocatalysts for hydrogen production *via* water splitting.[120]

These earth-abundant electrocatalysts are also useful to passivate unstable semiconductors such as ZnO and silicon, and thus exhibit additional functionality.[121] Dai and co-workers demonstrated that a thin layer of Ni metal prepared by thermal

evaporation could also have bi-functionality as both an OER catalyst and a passivation layer for silicon photoanodes.[122] In addition, Naldoni et al. demonstrated that a thin layer of photo-deposited amorphous NiOOH coupled onto hematite photoanodes could reduce the overpotential by 150 mV and increase the photocurrent by about 50 % at 1.23 V vs RHE.[123] Furthermore, Mullins and co-workers deposited α-FeOOH onto a Si triple junction solar cell, and the obtained photoanode (α-FeOOH/Si) achieved an STH efficiency of 4.3 % at 0 V vs RHE in a three-electrode configuration with a 4 h lifetime.[124] It is well-known that incorporation of iron species into a nickel hydroxide electrocatalyst forms a NiFe double hydroxide (NiFe-LDH). These Ni-Fe LDH electrocatalysts can be prepared by hydrothermal or photoelectrodeposition directly onto a light absorbing photoelectrodes, such as Ta_3N_5 which can dramatically improve the photocurrent and stability. Recently, Domen demonstrated that nanoworm-like $BiVO_4$ with Ni-Fe-LDH modification exhibited a high STH efficiency (2.25 %) and long-term durability (10 h) in 1 M potassium borate electrolyte (pH= 9.3) under AM 1.5G one sun illumination.[125] More recently, Grätzel et al reported that the hydrothermally-grown Ni-Fe LDH catalyst could be combined with a 17 % efficient $CH_3NH_3PbI_3$ perovskite solar cell to split water with an STH of 12.3 %.[25]

On the other hand, for water reduction, noble metals such as platinum (Pt) are frequently used due to their low overpotential and strong corrosion resistance. However, non-precious hydrogen evolution catalysts including metal disulfides, selenides, carbides, nitrides, phosphides, and heteroatom-doped nanocarbons are essential for economic H_2 production, the majority of which have been summarized in the recent review by Zhang et al.[37] and therefore research should be directed to using these to reduce the overall cost of a PEC device.

Table 2-2 summarises the performance of typical efficient PEC devices that use a combination of efficient photoelectrodes and co-catalysts. PV-based PEC devices (PV-PEC and buried PV) have achieved STH efficiencies >10 %, however their high cost and low stability are still major limiting factors that prevent their commercialisation.

Materials	System	Oxidation co-catalyst	Reduction co-catalyst	Photo anode	Photocathode	Photovoltaic	Life time	Electrolyte	STH (%)	Ref
WO_3 //Si|-Pt	Photoanode/ photocathode	-	Pt	WO_3	Si	----	-	1M HCl	-	126
Co-Pi /$BiVO_4$// Cu_2O/ RuO_2	Photoanode/ photocathode	Co-Pi	RuO_2	$BiVO_4$	Cu_2O	----	2mins 20% current loss	$K_{3-x}H_xPo4$ buffer (pH=6)	0.5%	127
RuO_2/WO_3|2jn Si|-Pt	PV-PEC	RuO_2	Pt	WO_3	------	2jn S	----	0.33M H_3PO_4	3%	128
WO3-|DSSC|-Pt	PV-PEC	---	Pt	WO_3	-----	DSSC	8h	1M $HClO_4$	3.10%	129
Co-Pi|3jn-Si| NiMoZn	PV + electrolyser	Co-Pi	NiMoZn	----	-----	3jn-Si	3h	0.5MK-Bi +1.5M KNO_3	4.7%	130
NiB|3jn-Si|NiMoZn	PV + electrolyser	Ni-B	NiMoZn	----	-----	3 jn-Si	168 h	0.5MKB/0.5M K_2SO_4	9.8%	131

Pt|1jn-GaAs|1jn-$GaInP_2$|-Pt	PV + electrolyser	Pt	Pt	----	---	1jn-GaAs+1jn-$GaInP_2$	9h	2M KOH	16.5%	132
P-Si/SnO_2/Fe_2O_3- Pt	Heterojunction PEC	Pt		-----	p-Si/SnO_2/Fe_2O_3 core /Shell/shell nanowire	---	2h	0.25M Na_2SO_4	-----	133
CoO_x/WO_3/C_3N_4/-Pt	Heterojunction PEC	CoO_x	Pt	WO_3+ C_3N_4	----	----	300s	0.01M Na_2SO4	0.11%	134

Table 2-2: *Overview of the reported efficient PEC cells and the corresponding performance.*
Notation in column 1: (1) cocatalyst/photoelectrode// the other photoelectrode/the other cocatalyst; (2) cocatalyst/photoelectrode|PV cell|-couther electrode; (3) cocatalyst|PV cell|the other cocatalyst; (4) Co-catalysts/ seconductor1/semiconductor2/-counter electrode. Notation in column 7: “jn” stands for junction.

2.6 Summary and Perspective

This chapter first presented the fundamental principles of electrochemical and photoelectrochemical water splitting and focused on an overview of the current materials development of electrocatalysts/photoelectrodes and their scientific challenges. The different kinds of materials based on noble metal and earth-abundant elements highlighting the benchmark activity for HER and OER were reviewed. Among HER catalysts, Pt still showed the best performance in both acidic and alkaline condition, enough though many studies suggested that transition metal-based sulphides, borides, carbides, and phosphides could be the ideal catalysts due to their low cost, abundance, and high efficiency. More importantly, efficient and stable OER electrocatalysts are highly desirable to overcome the sluggish kinetics of OER. As potential alternatives to IrO_2 and RuO_2, recent advances in noble-metal-free electrocatalysts were reviewed with specific attention on Co and Ni-based OER electrocatalysts. The OER mechanisms and strategies including surface electronic structure engineering and structure composition optimisation were also highlighted. Even though considerable progress has been made in the field of fabrication of noble-metal-free OER electrocatalysts, many questions still exist for the practical application. In particular, more attention should be focused to improve the OER performance in two aspects. The first one is the fabrication of more active electrocatalysts and understands the correlations between structure and OER activity, which will help identify the active sites for better catalysts design. Theoretical calculations and *in-situ* characterisations (i.e. *in-situ* X-ray absorption spectroscopy) will definitely play more and more critical roles in correlating the structure-activity relationships. The other is to understand the OER mechanism, which will beneficial for designing the high-performance OER electrocatalysts.

The latter part of this chapter also provided detailed working principles and scientific challenges of PEC water splitting and different device assemblies. Wide bandgap semiconductors such as TiO_2 are inexpensive and stable, but not efficient for sunlight harvesting. Even though α-Fe_2O_3 and $BiVO_4$ exhibit a broader absorption than TiO_2, the achieved photocurrents for these materials fall short of their theoretical maxima, due to the fast charge carrier recombination and poor surface OER kinetics. Narrow bandgap semiconductors, such as CdS, Si, and group III–V compounds, have the potential to achieve high efficiency but suffer from instability over long periods. The ultimate target of the entire solar fuel research field is to design and produce a cost-effective, highly efficient and stable photoanode and/or photocathode for oxygen and/or hydrogen production, either by employing a particulate system or a PEC device. The past decade has witnessed many innovations in combinations of materials, nanoarchitecture design and co-catalyst optimisation, which address the main issues existing in the reported efficient photoelectrodes. Furthermore, the addition of thin surface protection layers by evolving techniques such as ALD has benefitted the field in enhancing the stability and long-term performance of a PEC device. One concern may be the reproducibility in reporting device efficiencies – some degree of standardisation is necessary as the substantial differences in experimental setups and conditions (*e.g.* light sources with/without certification) have led to discrepancies in PEC efficiencies between groups. Several strategies should be adopted to enhance the performance of PEC devices, including (i) combinations of different materials and (ii) materials nanoarchitecture design for charge separation. In parallel, co-catalyst loading is desirable to protect surface photocorrosion and more importantly facilitate the surface chemistry. These are the material design strategies in the PhD project and will be investigated step by step.

3. Methodology

3.1 Material characterisation

3.1.1 UV-Visible spectroscopy

UV-Visible spectroscopy is based on the absorption of light by a sample. UV-Visible spectrophotometers ('UV-Vis') probe through the electromagnetic spectrum from ultraviolet through to the visible range. Molecules often undergo electron transitions at these frequencies, since those molecules in question are semiconductors, which have energy levels corresponding to allowed electron states, one can determine the magnitude and type of bandgap (direct or indirect) by using a Tauc plot based on Equation 3-1[135]:

$$(\alpha h\nu) = A(h\nu - E_{BG})^n \qquad \text{Equation 3-1}$$

Where α is the absorption coefficient, hν is the energy of the incident radiation, A is the constant based on effective masses of electrons and holes, and n can take the values of 0.5 and 2, for a direct or indirect band gap transition. The absorption coefficient can be calculated using the Kubelka-Munk function:

$$\alpha = \frac{(1-R)^2}{2R}$$

The reflectance is related to the absorption by the following equations:

$$1 = T + R + A$$

T is the transmission in %.

$$R = 10^{-A}$$

Often spectrophotometers give the absorbance as a function of a logarithm. If this is to be converted to a percentage, then the following relation can be used:

$$A(\%) = \left(1 - 10^{-A}\right) \times 100$$

The 2nd A is absorbance in log form.

The band gap of a semiconductor is approximately equal to the absorption edge, and so one can also find this from extrapolating towards the x-axis on a plot of wavelength (x-axis) versus absorption ($\log_{10}$ y-axis). Then using the following relation, calculate the band gap:

$$E = \frac{hc}{\lambda} = \frac{1240}{\lambda} \qquad \text{Equation 3-2}$$

It should be noted that the absorption edge can be blue shifted by decreasing the particle size and is often attributed to either a quantum size effect or a direct charge-transfer transition. If the band gap region possesses a long tail and appears to be red shifted, then this would conclude that there are additional sub-bandgap states present. [136]

3.1.2 X-Ray Diffraction (XRD)

The x-ray diffraction patterns are often used to identify the crystalline phases and orientation of crystal materials. Also, it can be used to determine the structural properties of the crystals such as lattice parameters, strain, grain size, preferred orientation and phase composition with detection limits of ~3 %. X-ray diffraction peaks occur when Bragg's equation (Equation 3-3) is satisfied for constructive interference for planes with spacing d.

$$2d\sin\theta = n\lambda \qquad \text{Equation 3-3}$$

Where d is the spacing between different panes, θ is the incident angle, n is an integer, and λ is the wavelength of the X-ray. As shown in Figure 3-1, Bragg's equation is derived by a simple mathematic model.

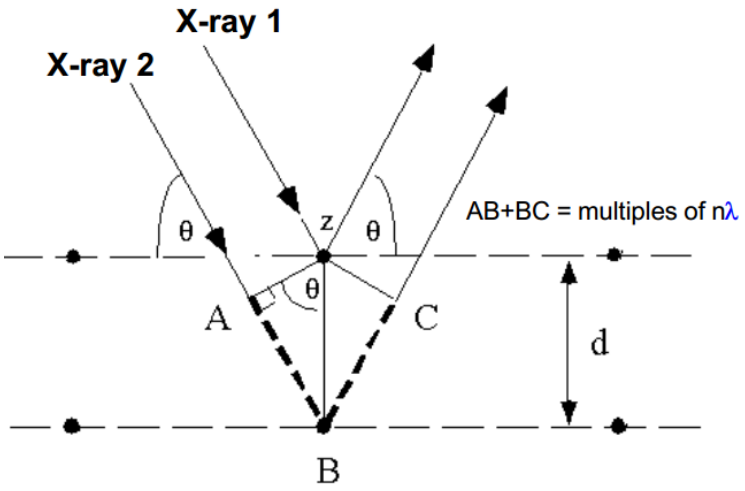

Figure 3-1: Mathematical derivation of Bragg's equation. Reproduced from reference 137.

XRD diffraction patterns can be recorded by an X-ray diffractometer, which consists of an X-ray tube, a sample holder, and an X-ray detector. X-rays of known wavelength are produced in an X-ray tube when electrons bombards to a metal target in the system. The produced X-rays are then sent to the sample in the sample holder. It is diffracted at specific angles with respect to the lattices spacing defined by Bragg's equation. The diffracted beam can then be measured by an x-ray detector, resulting in a plot of diffraction peak intensities versus angle of diffraction. The analysis of acquired data can be accomplished by referring to the databases of known standard patterns to reveal the crystal properties of the sample. [137]

3.1.3 Raman spectroscopy

Raman spectroscopy is frequently employed for the elucidation of the molecular structure of catalysts due to its time-saving and non-destructive features. The spectra show certain bands, i.e., characteristic vibrations, which attributed to the scattering of light by vibrating the molecules. Definite substances can be identified qualitatively and quantitatively by analysing the position, intensity, half-width, and the fine structure of the bands.[138]

Raman spectroscopy is a scattering technique and a change in polarizability during molecular vibration is an essential requirement to obtain a Raman spectrum of the sample.[139] As shown in Figure 3-2, when the sample is illuminated with a monochromatic laser beam with energy of $h\nu_0$, the sample molecules are excited from ground state (E_0) or vibration state (E_1) to the corresponding virtual level ($E_0 + h\nu_0$) or ($E_1 + h\nu_0$). The scattering occurs after the sample molecules recover immediately from the excites states. Much of this scattered radiation has a frequency, which is equal to the frequency of incident radiation and constitutes Rayleigh scattering (elastic scattering). A small fraction of scattered radiation shows a frequency difference compared to that of incident light ($\Delta\nu$), which is also known as Raman shifts, that constitutes Raman scattering (inelastic scattering).[139] When the frequency of incident radiation is higher than frequency of scattered radiation, Stokes lines appear in the Raman spectrum. But when the frequency of incident radiation is lower than frequency of scattered radiation, anti-Stokes lines appear in the Raman spectrum.[140] The vibrational bonds in the sample are identified since each molecule has its own vibrational energy level that exhibiting different Raman shifts.[138, 141] Thus, a Raman spectrum is always presented as a function of Raman Shift (cm^{-1}) versus the intensity.

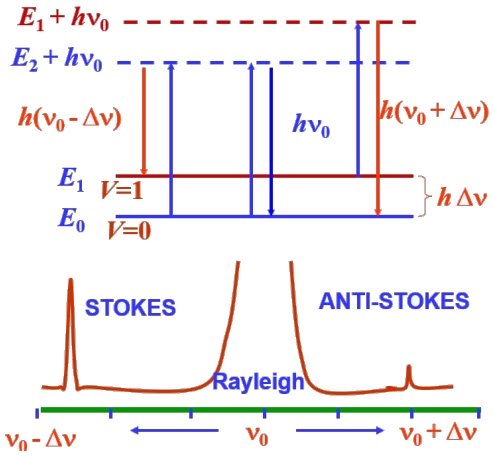

Figure 3-2: Principles of Raleigh and Raman (Stokes/Anti-stokes) scattering. Reproduced from reference 138.

3.1.4 X-ray photoelectron spectroscopy (XPS)

X-ray photoelectron spectroscopy (XPS) is a surface characterisation technique to the semiquantitative analysis of the surface composition, i.e., elemental and chemical states information, which can analyse a sample to a depth of 2 to 5 nm. When treating the sample with etching, the depth can be extended to a few hundred nm. As shown in Figure 3-3, when the sample is illuminated with X-rays monochromatic, a photo (E= hν) is absorbed by an electron. The photoelectron is then emitted from the atom with specific kinetic energy (KE) and can be measured by an energy discriminating electron detector. The measured KE can be used to calculate the binding energy (BE) of a photoelectron by the simple equation; BE = hν-KE-Φ where Φ is the threshold work function. The resulting XPS spectrum is a plot of intensity versus the binding energy. Since electrons at different chemical states exhibit distinct BE, the position and intensity of the peaks in the XPS spectrum can provide the desired chemical state and quantitative information.[142]

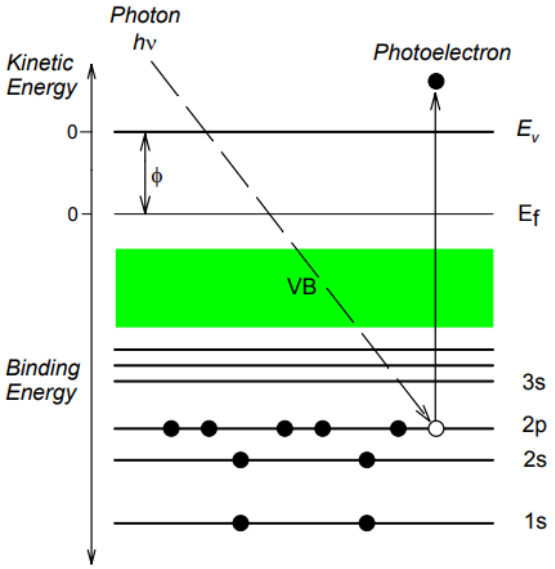

Figure 3-3: Schematic diagram showing the basic principle of XPS. Reproduced from reference 141.

3.1.5 X-ray absorption spectroscopy

X-ray absorption spectroscopy (XAS) is a well-established characterisation technique for providing electronic and structure information of certain elements in material. X-ray intensity is attenuated as passing through a material (Figure 3-4 a), which can be characterized according to Beer-Lambert law: $I_t = I_0 \exp(-\mu(E)t)$, where I_0 is the incident x-ray intensity, I_t is the transmitted x-ray intensity, t is the sample thickness and μ（E）is the absorption coefficient that is dependent on the photon energy.[143] The XAS spectra reflects the correlations between X-ray photon energy and the X-ray absorption coefficient (Figure 3-4 b). In detail, when the X-ray photon energy is lower than the core level binding energies of electron in the element's orbital, the electrons are not excited to the unoccupied electronic state, which leads to the flat region as shown in Figure 3-4b. As core electrons are excited to the unoccupied state with photon energy over the threshold (Figure 3-4c), sharp increases in absorption spectrum occurs at specific x-ray energies, which is known as the X-ray absorption near edge structure (XANES) (Figure 3-4 b). XANES is sensitive to chemical bonding and therefore providing the information about the oxidation state and electronic structure of the detected elements.[144] In general, the absorption edge energy increases with increasing oxidation state, which can be explained as: the higher the oxidation of the element, the more positive the overall charge of the atom, and therefore more energy is required to excite an electron from an orbital, which resulting in XANES spectrum shifting to a higher energy. For photon energies higher than *ca.* 30 eV above the edge, the core electrons are excited to continuum state (Figure 3-4c), forming the outgoing and scattering wave interferences with neighbouring atoms[145] as shown schematically in Figure 3-4 d. The extended X-ray absorption fine structure (EXAFS) modulations, as shown in Figure 3-4 b, are the direct consequence of the wave nature, which

reflects local atomic structure such as the coordination number, bond distances and structural disorder around a particular atomic species.[146]

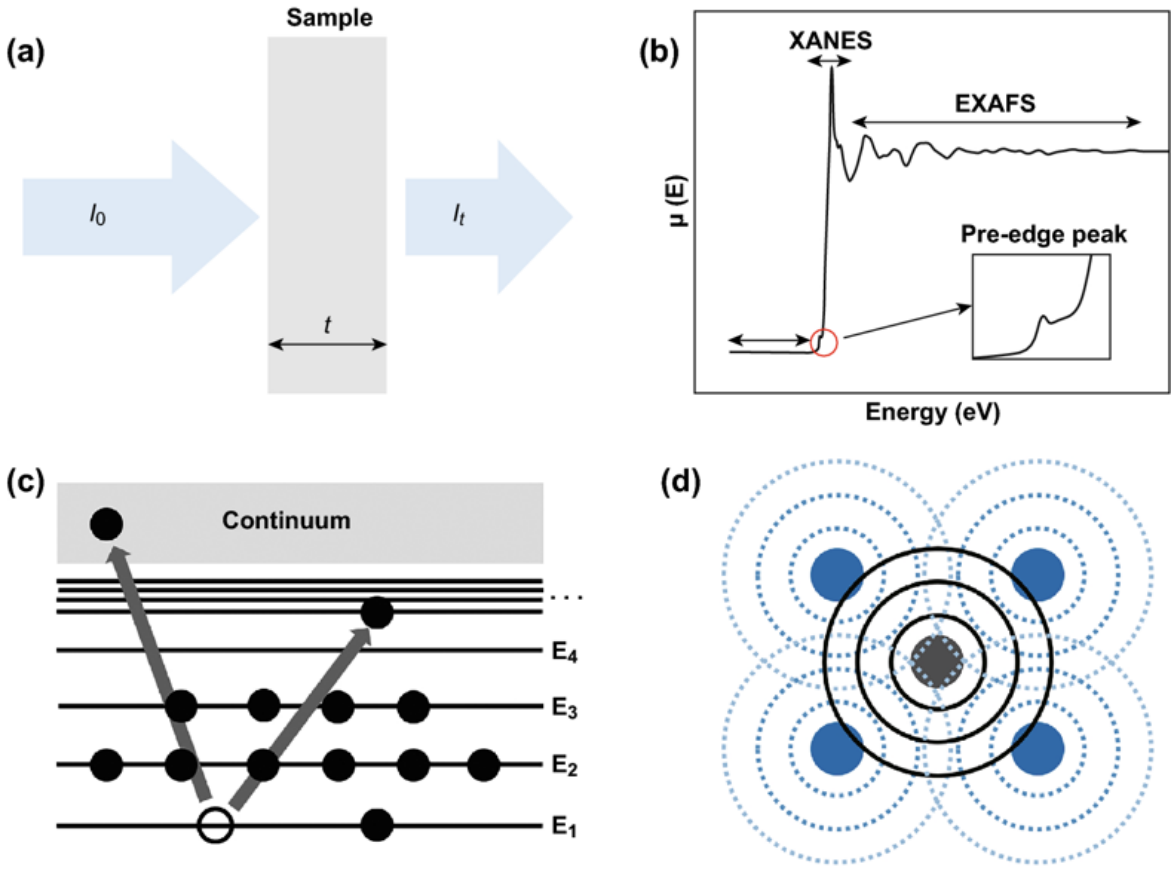

Figure 3-4: (a) Schematic of incident and transmitted X-ray beam. (b) Typical XAS spectra including the pre-edge, XANES and EXAFS regions. (c) Schematic showing the X-ray absorption and electron (black filled circle) excitation process. (d) Schematic of the interference pattern between absorbing atom (grey filled circle) and its first nearest neighbors (blue filled circle). The solid back lines and dashed blue lines shows the outgoing and reflected photoelectron waves, respectively. Reproduced from reference 147.

3.1.6 Microscopes (SEM, TEM & AFM)

Scanning Electron Microscopy (SEM) is a useful technology for imaging the surface features of a semiconductor, surface morphology (shape and particles size which making up the

semiconductor), and the composition of the semiconductor and their relative amount. In order to get the composition information, SEM mush has an Energy Dispersive-X-ray (EDX) attachment. The SEM generates a high energy electron beam by the electron gun that interacts with the semiconductor surface resulting in electrons with different energy ejected from the sample. The standard mode of SEM only collects secondary electrons within a few nanometers from the surface, which has energy as low as 50eV for better three-dimensional imaging (Resolution of 5 nm is achievable). [148]

Transmission Electron Microscopy (TEM) is another critical technology for imaging samples involving the transmission of a high energy electron beam (>100kV) through a thin sample (<100nm). After the interaction between the atoms and electrons, the magnified image is generated by using of optical lens and then projected onto a photographic film or CCD camera. Unlike SEM, TEM images are produced base on transmitted electrons that are directly pointed toward the sample and thus be able to see what inside the surface. Also, TEM produces a two-dimensional image with the resolution as high as 0.5 angstroms. However, it is challenging to prepare thin film samples for TEM since the ultrathin sample is required to allow the transmission of the electron.[149]

Atomic force microscopy (AFM), which use a sharp tip to probe the surface features, can image the height or depth of the surface topography with 1 million magnifications and generate a three-dimensional picture to characterise the surface roughness of the sample.[150]

3.1.7 Electrochemical characterisation

3.1.7.1 Tafel Slope

The Tafel slopes are commonly used to evaluate the reaction mechanism and the catalytic kinetics of electrocatalysts by fitting the Tafel equation:

$$\eta = a + b \log j \qquad \text{Equation 3-4}$$

where η is the overpotential, j is the current density, a and b are called Tafel constants that depending on the properties of the electrode, electrolyte and temperature.

b is also commonly called Tafel slope, which can be defined as how fast the current increases against overpotential (η). In this regard, a smaller Tafel slope (b) indicates that current density can increase faster with smaller overpotential (η) change, which implies faster interfacial reaction kinetics. Moreover, the experimentally observed Tafel slopes can be compared with the theoretically Tafel slopes derived from different rate-determining steps. In a consecutive reaction, a smaller Tafel slope indicates that the ending part of the multiple-electron transfer reaction should be the rate-determine step, which is commonly a sign of better performance of electrocatalyst.[16, 151]

3.1.7.2 Electrochemical Impedance spectroscopy

Electrochemical impedance spectroscopy (EIS) is a powerful technique often used to explore the interfacial behaviour in electrochemical systems as a function of an alternating current (AC) with a variable frequency. The term impedance refers to the frequency dependent resistance to the current flow of a circuit element and thus the impedance (Z_ω) could be expressed as：

$$Z_\omega = E_\omega(t) / I_\omega(t) = E_0 \sin(\omega t) / I_0 \sin(\omega t + \varphi) \qquad \text{Equation 3-5}$$

where $E_\omega(t)$ and I_ω (t) is the frequency – dependent potential and time and current, respectively; E_0 is the amplitude of the signal, ω is the radial frequency and φ is the phase shift.

The impedance may also be written as a complex function:

$$Z_\omega = E/I = Z_0 (\cos \phi + j \sin \phi) \qquad \text{Equation 3-6}$$

Where ϕ is the real number and j is the imaginary unit;

If the real part is plotted on the X-axis and the imaginary part on the Y-axis of a chart, the Nyquist plot can be obtained. The Nyquist plots are based on the equivalent circuits. Figure 3-5 shows a simplified Randles cell and the corresponding Nyquist plot. The electrochemical parameters such as double layer capacity (C_{dl}), polarisation resistance (Rp), and uncompensated (electrolyte) resistance (R_u) are more precisely represented through the use of an analogous electronic circuit which takes into account resistance and capacitance.

In a Randles cell, the electrolyte or uncompensated resistance (R_u) can be obtained by reading the real axis value at the high-frequency intercept, and the semicircle diameter equals to the polarisation resistance (R_p), which indicates the electron charge transfer resistance. One semicircle is characteristic a single time constant. Electrochemical impedance plots often contain one or several time constants, which can be evaluated through the use of one or more equivalent circuits. By fitting the EIS data, it can distinguish the electrical properties of individual contributions of components under investigation.

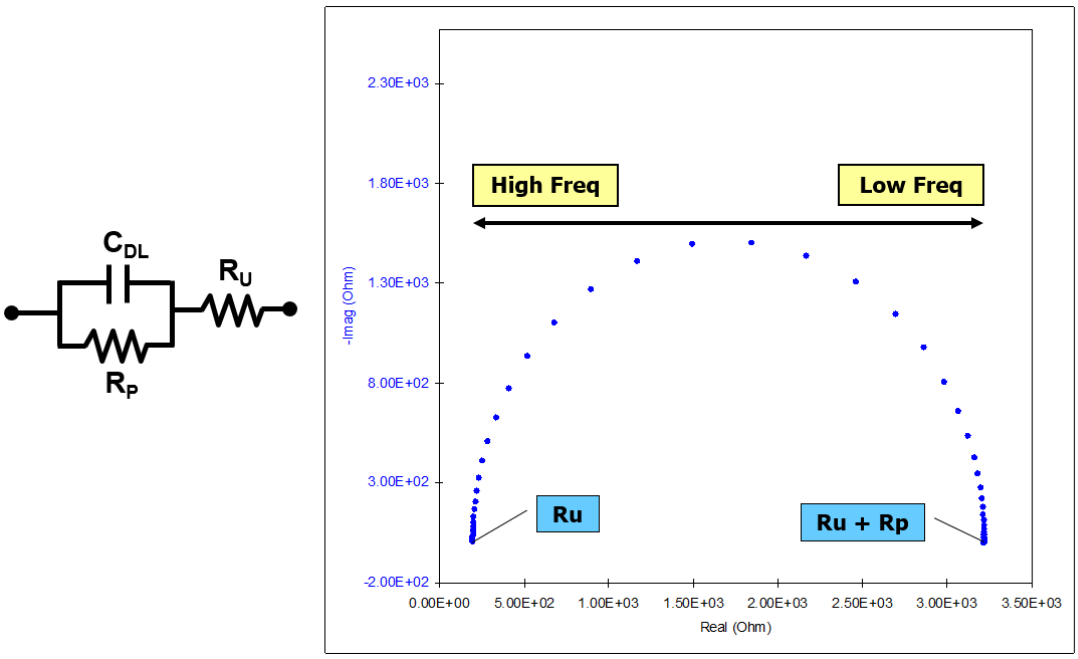

Figure 3-5: A Randles cell consists of double layer capacity (C_{dl}), polarisation resistance (Rp), and uncompensated (electrolyte) resistance (R_u) (Left); and the Nyquist plot based on the equivalent circuits represented in the Randles cell (Right).

3.1.7.3 Flat band potential measurement

The Flat band potential is defined as the applied bias potential needed to reduce the band bending to zero. [150] It is often used to express the band edges of semiconductors with respect to the redox potentials in the electrolyte because the V_{fb} is close to the conduction band of the semiconductor. Therefore, the flat band potential measurement is crucial for semiconductor studies. To date, several techniques have been used to measure the flat band potential. The simplest way is the measurement of the photocurrent onset potential. For example, for an n-type semiconductor, a depletion layer formed when applying a positive bias potential, which enables the separation of photogenerated electrons and holes, and thus photocurrent is produced. However, this is not accurate because of the recombination in the space charge region,[152] hole trapping at surface defects,[153] and poor surface reaction kinetics.[154] The most reliable method is the Mott-Schottky analysis, which has been widely used to determine the flat band potential of metal oxides such as TiO_2,[155] ZnO,[156] $BiVO_4$,[157] WO_3,[158] Fe_2O_3,[159, 160]Cu2O [161]; III-V

semiconductors such as GaAs,[162] InP[22 163] and (3) Si.[164] Based on the Mott-Schottky equation as shown below, V_{fb} can be determined.

$$\frac{1}{C_{sc}^2} = \frac{2}{\varepsilon\varepsilon_0 e N_D A^2}\left(V - V_{fb} - \frac{k_B T}{e}\right)$$

Equation 3-7

Where C and A are the interfacial capacitance and area, respectively; ε_0 is the permittivity of free space; N_D is the number of donors; V is the applied bias potential; V_{fb} is the flat band potential; k_B is the Boltzmann's constant, T is the absolute temperature, and e is the electronic charge. Therefore, a plot of $\frac{1}{C_{sc}^2}$ vs V can be obtained and the V_{fb} can be determined from the intercept on the V axis and N_D can be found from the slope of the plotted straight line.

3.2 Catalytic performance evaluation

3.2.1 Activity and stability measurements

For the photoelectrochemical measurements, a three-electrode configuration under one sun illumination (AM 1.5G, Light intensity = 100 mW/cm^2) is commonly employed to measure the photocurrent density of a photoelectrode. As shown in Figure 3-6 (a), the basic experimental setup for PEC photocurrent measurement in a three-electrode configuration consists of a PEC cell, a light source and a potentiostat. The PEC cell is a glass reactor with a side quartz window consists of a working electrode (WE), a counter electrode (CE), a reference electrode (RE), and the electrolyte for the OER and HER.

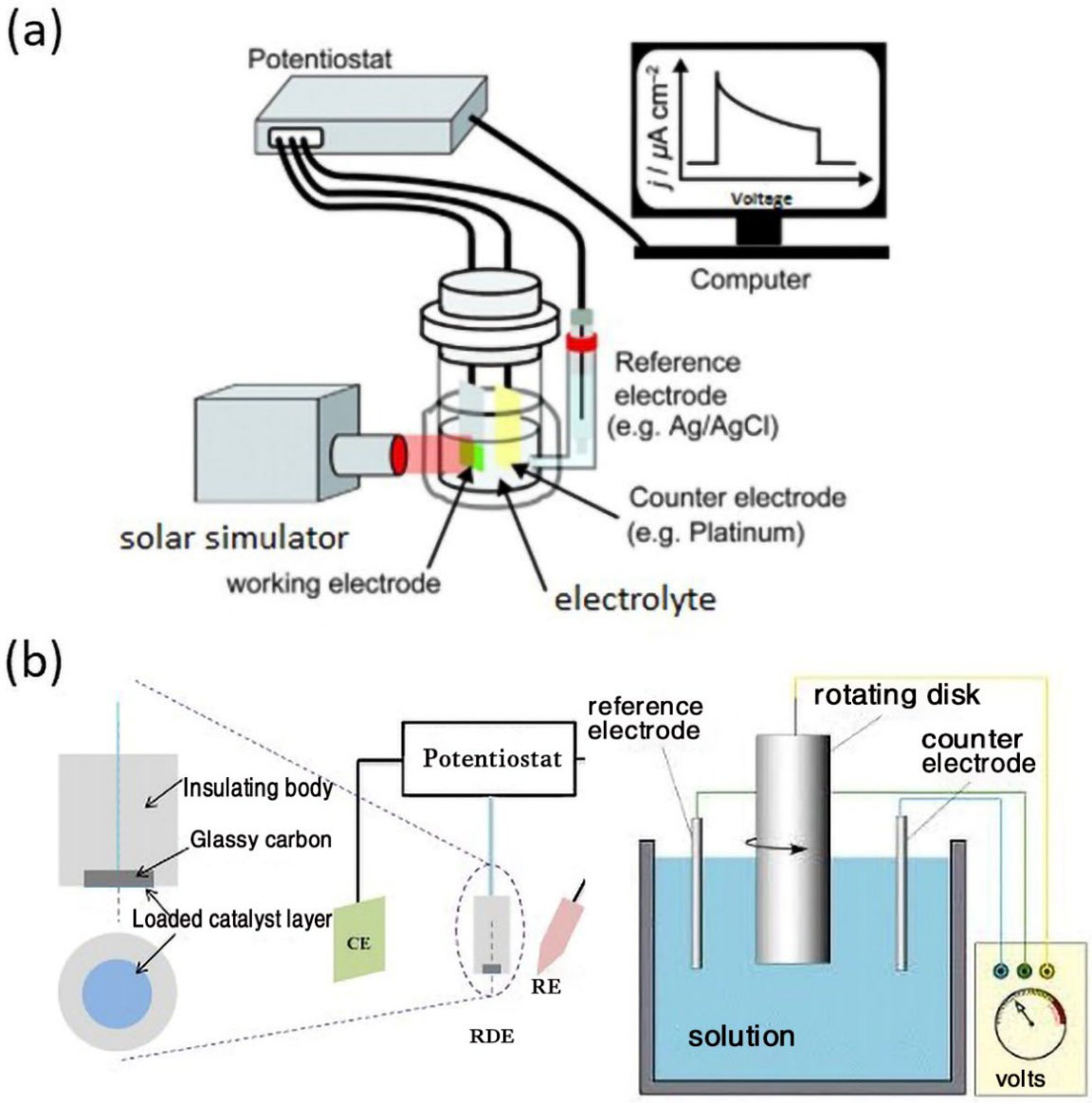

Figure 3-6: The experimental setup for the (a) PEC photocurrent and (b) EC current measurement.

The WE is the photoelectrode sample of interest (semiconductor material), which is deposited on a conductive substrate as the back contact. In order to produce excellent charge transfer at the photoelectrode/substrate interface, ohmic contact between the photoelectrode and substrate is preferred. To form a good ohmic contact, the work function of the substrate must be smaller than that of an n-type photoanode or larger than that of a p-type photocathode. [17 165] Therefore, transparent conductive metal oxides, such as fluorine doped tin oxide (FTO)

and indium tin oxide (ITO) are widely used as conductive substrates for n-type photoanodes and high work function metals, such as gold and platinum, have been used for p-type photocathodes.

The CE provides the reaction site for either water oxidation or water reduction reaction. The most common CE in a PEC cell is Pt mesh, which has a large surface area and fast kinetics.[165]

The RE in a three-electrode configuration is used to ensure that the potential of the WE is applied and measured with respect to a well-defined electrochemical potential scale. Ag/AgCl RE is usually used and the applied potential measured with respect to Ag/AgCl RE is normally converted into the reversible hydrogen electrode (RHE) scale for easy comparison between reported data in the literature by using:

$$E_{(RHE)} = E_{(Ag/AgCl)} + 0.059\ pH + E_{(Ag/AgCl)(ref)}, \text{ where } E_{(Ag/AgCl)(ref)} = +0.199\ V$$

Equation 3-8

The electrolyte should be an aqueous solution with good ionic conductivity and does not undergo electrochemical reactions with electrodes during the measurement. 0.5-1 M solution of KOH and H_2SO_4 is often employed as an alkaline and acidic electrolyte, respectively. For photoelectrodes that require a neural condition, 0.5 M solution of Na_2SO_4 or phosphate buffer is often used.

To perform a photocurrent measurement, the WE, CE, and RE of the PEC cell are connected to the potentiostat, and the WE is illuminated by a light source (a solar simulator or a Xeon lamp with AM1.5G filter). For consistent and accurate photocurrent measurements, a light source with irradiance spatial nonuniformity of < 2 % is necessary. Prior to the PEC measurements, the light source should be warmed up for 30 min to stabilise the system, and the electrolyte should be purged with inert gas for at least 10 min to remove dissolved oxygen.

A silicon reference solar cell is used to calibrate the light intensity to one sun (100 mW/cm^2) in my studies.

Linear sweep voltammetry mode in the potentiostat is employed to measure the photocurrent response versus the applied potential. For a typical current-voltage (J-V) scan, the potential of the WE is linearly swept with respect to the RE with a constant scan rate in the range of 10–100 mV/s and the current flowing between the WE and CE is recorded by the potentiostat. Notably, these measurements should also be performed in the dark condition to obtain the dark current response versus the applied potential, which can be used to confirm that the photocurrent is due to the photon response of the photoelectrode.

The key characteristics of the photoelectrode can be obtained by analysing the J-V curve. First, the conductivity type of the semiconductor photoelectrode can be determined by the sign of the photocurrent (anodic or cathodic). An anodic photocurrent occurs for an n-type semiconductor because of the water oxidation by the minority hole carriers. By contrast, a cathodic photocurrent is generated for a p-type semiconductor due to the water reduction by the minority electron carriers. Second, the photocurrent onset potential (E_{onset}), at which the photocurrent starts to occur with respect to the dark current, can be easily determined from the J-V curve. The photocurrent onset potential (E_{onset}) can be used to estimate the flat band potential (E_{fb}). E_{onset} is considered to be close to E_{fb}, but because of the kinetic overpotential, an offset will be introduced between E_{onset} and E_{fb}.[166, 167] Third, the maximum H_2 or O_2 evolution rate can be obtained through the saturated photocurrent density, which is mainly constrained by the band gap and light absorption efficiency of the semiconductor. [165]

The stability performance of the photoelectrode can be evaluated by plotting the photocurrent density as a function of time at a fixed applied potential (J-t curve). [168] Typically,

the photoelectrode is considered to be stable if the photocurrent density remains constant over a long period. The degree of the photocorrosion of the electrode in the electrolyte can be determined through the J-t curves.

The electrochemical measurements share a similar setup with the photoelectrochemical measurements, which also consist of a three-electrode configuration but without the solar simulator as shown in Figure 3-6 (b). In addition, a typical electrocatalytic test is normally performed by using a rotating disk electrode as the working electrode for excellent mass transfer. The studied electrocatalysts are loaded on the glass carbon surface for the activity and stability test. The activity of the catalysts can be evaluated from the onset potential together with the overpotential at the current density of 10 mA/cm^2 (η_{10}) from the J-V curve and the stability can be evaluated from the J-t or V-t curve, which is a function of current or overpotential over a time constant. The electrocatalysts are considered as the "good" electrocatalysts when exhibiting low onset potential, small overpotential (η_{10}) and stable current/overpotential in a long-term stability measurement.

3.2.2 Energy and Quantum Conversion Efficiencies in a PEC cell

The energy conversion efficiency is the ultimate performance indicator of a PEC cell. The standard solar to hydrogen conversion efficiency (η_{STH}) can be expressed as the ratio between the total energy generated and the total energy input from sunlight irradiation (AM 1.5G, 100 mW/cm^2):

$$\eta_{STH} = \frac{Total\ energy\ \text{generated}}{Total\ \text{energy input}} = \frac{\Delta G \times r_{H_2}}{P_{\text{light}} \times S} \qquad \text{Equation 3-9}$$

Where ΔG is the Gibbs free energy (237 KJ/mol), r_{H_2} is the rate of hydrogen production in moles/second; P_{light} is the incident light intensity (100 mW/cm^2) and S is the illuminated area of the photoelectrode (cm^2).

When an external bias is applied to the PEC system, the electrical energy must be subtracted and thus the applied bias photon-to-current efficiency (ABPE) is frequently used.

$$ABPE = \frac{P_{out} - P_{in}}{P_{light}} = \frac{J_{ph}(V_{redox} - V_{bias})}{P_{light}}$$ Equation 3-10

Where V_{redox} is the redox potential for water splitting (1.23V vs NHE); V_{bias} refers to the actual potential difference between the working and counter electrode (not the bias with respect to a reference electrode); P_{light} is the light intensity (100 mW/cm^2) and J_{ph} is the generated photocurrent density.

Faradaic efficiency is the most useful method to verify that the generated photocurrent is in fact due to water splitting and not photo-corrosion of the electrodes or other side reactions. It is defined as the ratio of the experimentally evolved gas divided by the theoretically evolved gas based on the measured photocurrent.

$$\text{Faradaic efficiency} = \frac{\text{Experimental gas evolution}}{\text{Theoretical gas evolution}} = \frac{\text{Oxygen evolution measured}}{\text{Gas evolution based on the photocurrent}}$$

$$= \frac{\text{Oxygen evolution measured}}{(\frac{J_{photo} \times A \times T}{e} / 4) / N_A} \times 100\%$$

Equation 3-11

The unit of gas evolution is moles; J_{photo} is the photocurrent density (A/cm^2) generated during the measurement time T (seconds); A is the illumination area of photoelectrode (cm^2); e is the charge of an electron (1.602 ×10^{-19} C) and N_A is the Avogadro constant (6.02×10^{23} mol^{-1}). The

amounts of evolved gases can be analyzed by gas chromatography (GC) or, in the case of oxygen, by using a suitable oxygen electrode or fluorescence detector.

Quantum efficiencies such as the incident photon to current efficiency (IPCE) measured at fixed incident wavelengths are often used to evaluate performance of a photoelectrode for water splitting. The IPCE is defined as the number of photogenerated charge carriers contributing to the photocurrent per incident photon, which can be represented by the following equation:

$$IPCE(\lambda) = \frac{Total \text{ energy of converted electrons}}{Total \text{ energy of incident photons}} = \frac{(\frac{J_{photo}(\lambda)}{e}) \times (\frac{hc}{\lambda})}{P(\lambda)} \times 100\%$$

Equation 3-12

Where J_{photo} is the photocurrent density at that particular wavelength of incident light (mA/cm^2); e is the charge of an electron (1.602×10^{-19} C); h is Planck's constant (6.626×10^{-34} J·S); C is the speed of light ($3.0 \times 10^8 \times 10^9$ nm/s); λ is the wavelength of the incident light (nm); P (λ) is the incident light intensity at that specific wavelength (mW/cm^2).

It is noticeable that the value of IPCE is related to the wavelength of the incident light, the photocurrent and the incident light intensity, where absorbed, reflected and transmitted light are included. Thus, IPCE is also named as external quantum efficiency. The internal quantum efficiency is often termed as the absorbed photon-to-current conversion efficiency (APCE). The APCE is defined as the number of photogenerated charge carriers contributing to the photocurrent per absorbed photon and can be expressed using the following equation:

$$APCE(\lambda) = \frac{IPCE(\lambda)}{A(\lambda)} = \frac{IPCE(\lambda)}{1 - R - T} \times 100\% \qquad \text{Equation 3-13}$$

Where A, R, T are the optical absorption, reflection, and transmission, respectively.

3.2.3 Product analysis

The amount of oxygen and hydrogen gases produced in a PEC cell can be detected by a Gas Chromatography (GC). GC is frequently used as a robust technique with a high resolution to both qualitatively and quantitatively analysis of the gas within a sealed cell. Figure 3-7 shows a schematic diagram of GC. A gas sample is injected through the injector port firstly. The individual gas in the mixture gas (mobile phase) sample can be separated by a column (stationary phase). Since different gas has different retention time in the column, individual gas can be detected by a detector, followed by a signal generation through a data recorder.

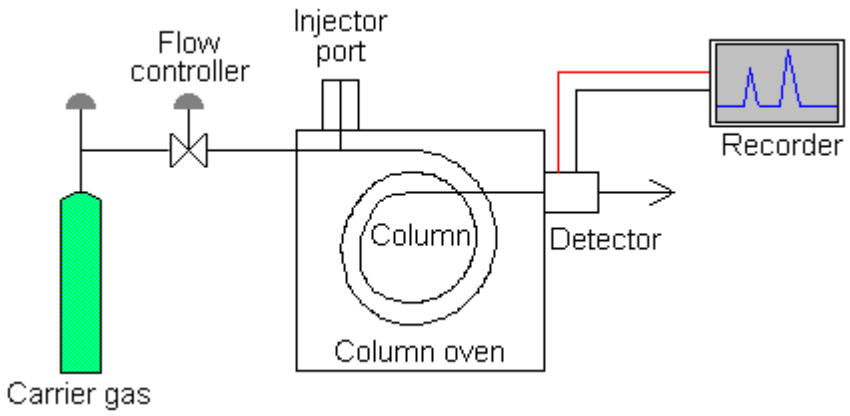

Figure 3-7 : schematic diagram of a gas chromatograph.

The detector used in a GC usually is either a Thermal Conductivity Detector (TCD),[169] or a Flame Ionisation Detector (FID).[170] However, only TCD is suitable for the detection of gases such as H_2, O_2 and N_2. This detector senses changes in the thermal conductivity with respect to the different gases. By comparison with a reference flow of carrier gas (helium or argon), a detectable signal is produced. Argon is much favourable than helium in our system because the thermal conductivity of Argon is much larger than H_2, O_2 and N_2, [171] as well as the low cost, compared to Helium.

The GC data represents as a graph of retention time (x-axis) and detector response (y-axis). The amount of each Gas can be calculated when using the corresponding peak area, followed by a comparison with a calibration curve, which can be obtained using standard gas with known concentration.

4 Efficient and robust oxygen evolution catalysts on 1D ZnO nanowires for PEC water oxidation

4.1 Introduction

Since the discovery of TiO_2 as a stable photoanode for photoelectrochemical water cleavage by Honda and Fujishima in 1972,[172] considerable efforts have been made to seek an efficient and stable photoanode for water oxidation. Studies have focused on semiconductor metal oxides such as TiO_2,[173] ZnO,[174] WO_3,[175] $BiVO_4$,[176] and Fe_2O_3.[177] However overcoming their poor stabilities and/or poor utilisation of solar energy still remain significant challenges. Furthermore, the efficiency of these semiconductor photocatalysts is seriously limited by factors including, but not limited to, low charge carrier mobility, poor conductivity, low surface reaction rates and high charge carrier recombination. Studies have shown that photogenerated electrons and holes recombine fast on the scale of nanoseconds for TiO_2 colloid,[178, 179] and on the order of picoseconds for α-Fe_2O_3.[93] Despite this, carrier recombination could be alleviated by applying a small external bias to the light-absorbing photoanode to provide sufficient overpotential to transfer electrons to the counter electrode in a PEC cell.

Zinc oxide (ZnO), with a band gap energy of 3.2 eV, has been reported to be a suitable model semiconductor for solar water oxidation due to its low onset potential[174] and high electron mobility; several orders of magnitude higher than that of TiO_2 and thus its electrical resistance is lower and the electron-transfer efficiency higher.[180, 181] However, the drawbacks of utilising ZnO include a low hole mobility[182] and slow kinetics at the ZnO/electrolyte interface, which results in fast electron-hole recombination and thus limits the overall applied bias photon-to-current efficiency (ABPE). Additionally, the extremely poor photostability of ZnO in aqueous solution limits the performance of a ZnO-based photoanode significantly,

which has restricted its widespread employment in commercial devices.[183] To date, numerous strategies have been developed to overcome its poor activity, including (a) fabricating a multi-semiconductor system (e.g. Si/ZnO core-shell nanowires) to reduce the hole-electron recombination,[184] (b) constructing one dimensional (1D) nanostructured ZnO-based electrodes with various morphologies (e.g. nanotubes,[185] nanorods/nanowires)[186, 187] for increased surface area and improved charge transport and light trapping, and (c) the loading of oxygen evolution catalysts (e.g. Co-Pi) to improve the electron-hole separation and O_2 evolution kinetics.[188] To address the issue of poor stability, it has been demonstrated that a thin layer of SnO_2 can act as a partial passivating layer for ZnO nanowires.[189] However, in all cases the ABPE(η) and incident-photon-to-current conversion efficiency (IPCE) are still moderate, for example, nitrogen-doped ZnO (η =0.35 %; IPCE=35 % at 350 nm),[184] and Si/ZnO core-shell nanowires (η=0.38 %).[184] The poor stability of the photoanode still remains a significant challenge.

For my material design strategy, employing a 1-D nanostructured morphology for ZnO offers the potential advantage of improved charge transport over a flat surface, whilst simultaneously suppressing light scattering due to the light trapping effect.[180, 190] Furthermore, the optimisation of their length and diameter will maximise light absorption and provide a short charge carrier diffusion length. Furthermore, the use of cheap, earth-abundant oxygen evolution catalysts on the surface of ZnO nanowires could improve the photoanodic performance by acting as hole trapping sites for water oxidation and *in-situ* charge separation. It is also expected that employing high surface area ZnO nanowires would result in significantly increased co-catalyst deposition on the ZnO surface compared to flat ZnO films. Therefore, to directly address the aforementioned challenges in the employment of ZnO photoanodes, I herein reported the morphology optimisation of well-aligned 1D ZnO nanowire arrays. The loading of water oxidation catalysts (Co-Pi and Ni-B) on ZnO for efficient photoelectrochemical water

splitting were investigated. Finally, the highest IPCE recorded for ZnO-based photoelectrodes and unprecedented stability have been achieved.

4.2 Experimental section

4.2.1 Photoanodes preparation

ZnO nanowire arrays were fabricated on FTO glass substrates from ZnO seeds by a hydrothermal (hydrolysis-condensation) method described by Greene *et al.*[191, 192] Firstly, ZnO seed crystals were deposited onto FTO glass (TEC 15, Pilkington NSG) *via* spray pyrolysis (nozzle size 2 cm^2, at a distance of 15 cm) from a solution containing 0.005M Zinc acetate dihydrate (98 %, Aldrich) in ethanol followed by an annealing process in air at 350 ℃ for 20 mins. This procedure was repeated twice to obtain uniform coverage of ZnO seed crystals with density and size similar to those already reported.[192] Secondly, a precursor solution with 0.025M Zinc nitrate hexahydrate [$Zn(NO)_3 \cdot 6H_2O$] (98%, Sigma) and Hexamethylenetetramine (HMT) (≥99.5%, Sigma) was heated in an open water bath at 90 ℃. In our optimized procedure, ZnO films were synthesized by varying the growth time from 0.5 h to 5h, and then by varying the concentration of the precursor solution from 0.025M to 0.01M at intervals of 0.025M. The concentration ratio of [$Zn (NO)_3 \cdot 6H_2O$] and HMT was kept constant at 1:1 whilst varying the concentration of precursor (pH = 3.5)

Both Co-Pi and Ni-B catalysts were deposited onto optimised ZnO films by photo-assisted electrodeposition.[193, 194] A three-electrode system with as-prepared ZnO films as the working electrode, Ag/AgCl as the reference electrode and a Pt mesh as the counter electrode were used for the photo-assisted electrodeposition process. Co-Pi/ZnO and Ni-B/ZnO junctions were synthesized by applying a constant potential of 0.4V (*vs* Ag/AgCl) in a solution of 0.5 mM cobalt nitrate containing 0.1 M potassium phosphate buffer at pH 7 and a solution of 0.1 M

potassium borate at pH 9.2 containing 1 mM Ni $(NO_3)_2$, respectively, for 600 seconds under AM 1.5G light (100 mW/cm^2) illumination.

4.2.2 Photoelectrode characterisation

X-ray diffraction (XRD) was carried out on a Bruker D8 Advance X-ray Diffractometer (40 kV, 30 mA) with Cu-K_α radiation (λ= 1.54 Å) equipped with a PSD LynxEye silicon strip detector. UV-vis spectra were obtained on a Shimadzu UV-2550 UV-Visible spectrometer. The band gap energy was estimated using equation 3-1. The morphologies of the samples were obtained on a Jeol JSM-7401F Scanning Electron Microscope. High-resolution X-ray photoelectron spectroscopy (XPS) was performed using a Thermo Scientific K-alpha photoelectron spectrometer using monochromatic Al-Kα radiation; peak positions were calibrated to carbon (284.5 eV) and plotted using the CasaXPS software.

4.2.3 PEC Measurements for ZnO -based photoanodes

The PEC measurements were conducted in a three-electrode cell equipped with a quartz window and potentiostat (IVIUM technology). As-prepared films were used as the working electrode. A Pt mesh and Ag/AgCl was used as a counter electrode and a reference electrode, respectively. The scan speed was 20 mV/s between -0.4 V and 1.0 V (*vs* Ag/AgCl); while all measurements were carried out using an Ag/AgCl (3 M KCl) reference electrode, results reported in this study were presented against the reversible hydrogen electrode (RHE) for ease of comparison with the H_2 and O_2 redox levels and with other literature reports that used electrolytes with different pH. Thus, electrode potentials were converted to the RHE scale using equation 3-8. The electrolyte was 0.2 M Na_2SO_4 aqueous solution with 0.1 M phosphate buffer

(pH=7) or 0.1 M potassium borate solution (pH=9.2). All electrolytes were purged with argon for 10 mins to remove dissolved O_2 before PEC measurement. A 150 W Xenon lamp (Newport, USA) equipped with an AM1.5G filter was used to irradiate the ZnO electrodes from the front side which was calibrated to one sun illumination (100 mW/cm^2) using a photodiode.

As for Incident Photon to Charge Carrier Efficiency (IPCE) measurements, monochromatic light was generated using a monochromator and the resultant photocurrent was recorded for wavelengths between 350 nm and 440 nm. The light intensity was measured using a silicon photodiode and a Newport Optical Meter (Model 1918-R). IPCE was calculated using equation 3-12. The absorbed photon-to-current conversion efficiency (APCE, η) was estimated using equation 3-13.

4.3 Results and discussion

4.3.1 Morphology optimisation of ZnO nanowires

The effect of deposition time and the concentration of precursor were investigated for growth of bare ZnO nanowire arrays. The X-ray diffraction (XRD) (Figure 4-1 a) revealed that prepared ZnO films possessed a hexagonal wurtzite structure (space group: $P6_3mc$; a=b=3.25 Å, c = 5.21 Å), which is composed of tetrahedrally coordinated O^{2-} and Zn^{2+} ions stacked alternatively along the c-axis as shown in Figure 4-1a insert. The much higher intensity of (002) diffraction peak provides further evidence that all ZnO nanorods are highly oriented in the c-axis direction. [191, 192]

The UV-Vis transmittance spectra and SEM images of bare ZnO films prepared under different reaction times are shown in Figure 4-2 and 4-3. All films exhibited good transparency

in the visible range (380-500 nm), for example, the sample grown for 1 hour displayed close to 90 % transmittance in this wavelength range. The bandgap energy of ZnO nanowires was estimated to be ~3.3 eV from the UV-Vis absorption spectra (Figure 4-2 insert), and as expected, did not vary with reaction time. From the SEM images obtained for bare ZnO nanowires synthesised by varying deposition time (Figure 4-3), it is clearly seen that all nanowires possess an average diameter of ~50 nm independent of deposition time, whereas their lengths increase with time, similar to previous reports.[191] However, a little increase in length is observed when the reaction time increases to 5 h, which indicates the dissolution-precipitation equilibrium was obtained.[195] Figure 4-4 displays the I-V curves for ZnO films prepared with 0.025M precursor at 90°C as a function of growth time in 0.2 M Na_2SO_4 with phosphate buffer (pH=7) electrolyte under 100 mW/cm^2 illumination. The dark current was negligible over the entire potential range from 0.2 V to 1.6 V (*vs* RHE). It can clearly be observed that the maximum photocurrent is strongly dependent on the length of nanowires. Longer nanowires maximize the light absorption and provide more reaction sites, and thus higher photocurrent. ZnO nanowires prepared at 4 h and 5 h (having similar length ~1300 nm) both result in similarly high photocurrents.

Next, the effect of precursor concentration was investigated when keeping the reaction time fixed (4h). Table 4-1 summarises the effect of precursor concentration on the length and diameter of the nanowires. Both the average length and diameters increased as a function of precursor concentration - from 1300 nm (0.025M) to 1800 nm (0.075M) and the diameter increased from ~50 nm to ~110 nm (Figure 2). However, SEM images of ZnO nanowires grown using a concentration of 0.1M zinc nitrate represent a significant morphology change to a mixture of nanowires and nanoflakes, resulting into a condensed structure (1500 nm length).

The UV-Vis transmittance spectra of ZnO films prepared as a function of precursor concentration are shown in Figure 4-1 b. As a reference, the transmittance spectrum of an uncoated FTO glass substrate was recorded (Figure 4-1b insert). As expected, all ZnO films showed closed to zero transmittance in the UV range and exhibited no variation in bandgap (~3.3 eV). I-V curves of ZnO nanowires prepared at 90°C for 4 h with various precursor concentrations (Figure 4-6) indicate the dramatic effect of the nanowires' parameters (length and diameter) on photocurrents. Since ZnO-based semiconductors have high electron mobility, (*ca.* 400cm^2/Vs at 300K), [196] but low hole mobility (1-15 cm^2/Vs at 300K), [197-199] the efficient charge carriers' separation and activity are highly dependent upon the hole diffusion length. Although longer and wider nanowires can absorb more photons as indicated in UV-Vis absorption spectra, and likely provide a larger surface area, a larger diameter also leads to a longer hole diffusion length. In other words, the distance for transporting photogenerated electron-hole pairs from bulk to surface is increased with increased nanorods' diameter, which may further increase the possibility of charge carriers' recombination and then lower reaction activity. Therefore, the best-performing ZnO nanowire arrays should have the optimised length and diameter in order to balance these key factors related to photoreaction.

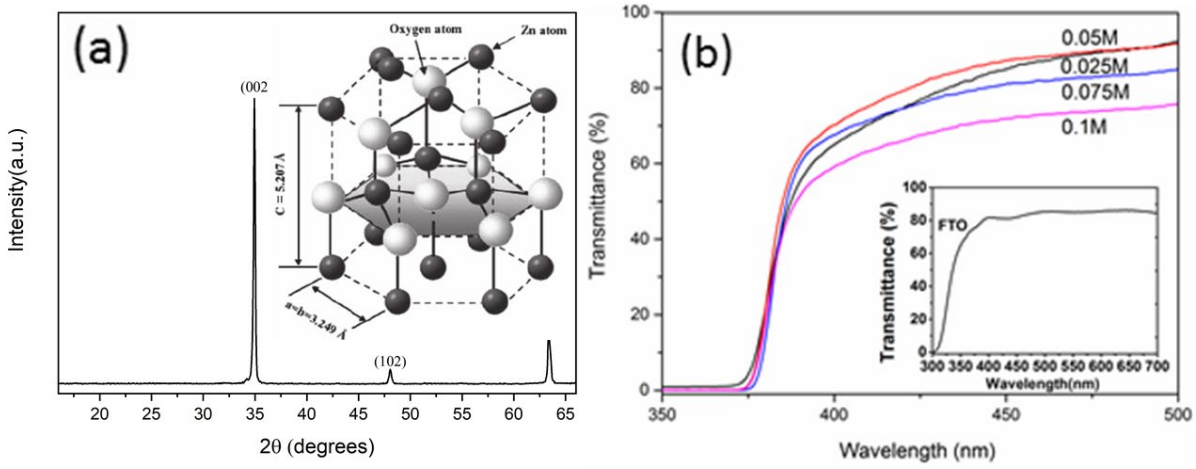

Figure 4-1 (a): XRD pattern of ZnO nanowire arrays grown on FTO glass substrate at 90 °C

for 4 h; Insert image shows the hexagonal wurtzite structure model of ZnO (White spheres : O atoms; Brown spheres: Zn atoms). (b) UV-Vis Transmittance spectra of ZnO films fabricated at 90 °C for 4 h as a function of precursor concentration; Insert image shows the transmittance spectra of a bare FTO glass substrate.

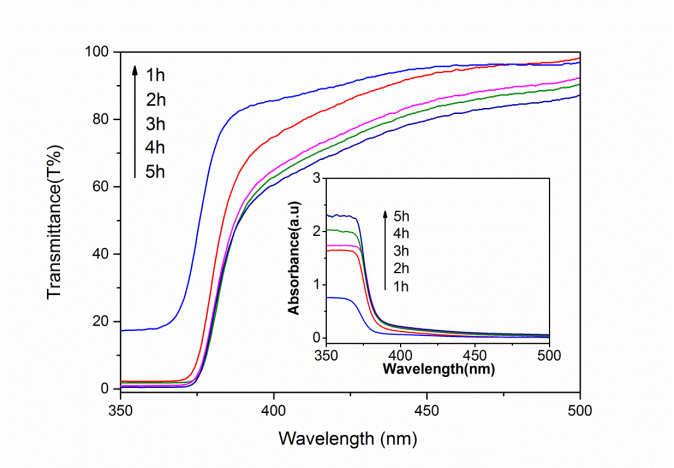

Figure 4-2: UV-Vis transmittance spectra of ZnO nanowires grown at 90°C (0.025M precursor concentration) as a function of reaction time. (Insert shows the corresponding UV-Vis absorption spectra).

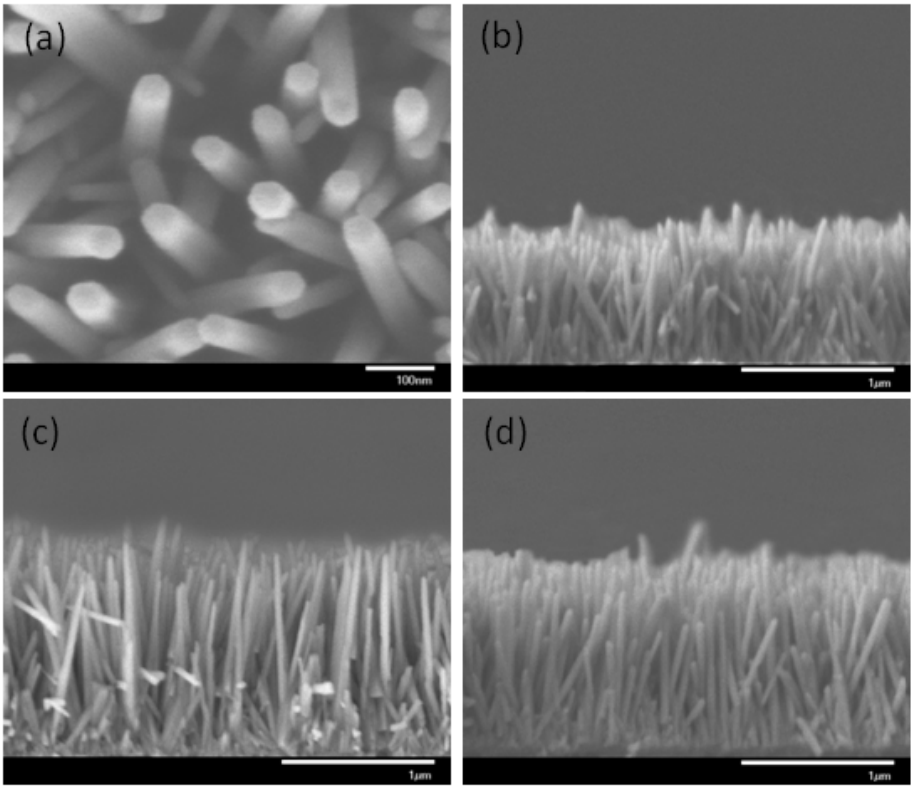

Figure 4-3: SEM images of ZnO nanowire arrays grown by hydrolysis-condensation reaction with 0.025M precursor concentration at 90°C for different growth times (a) Top view of ZnO

wires with a reaction time of 4h; (b-d): Side-on view of 3h, 4h, 5h grown ZnO nanowires, which results in the ZnO nanowires' length of *ca.* 900 nm, 1300 nm, 1300 nm, respectively.

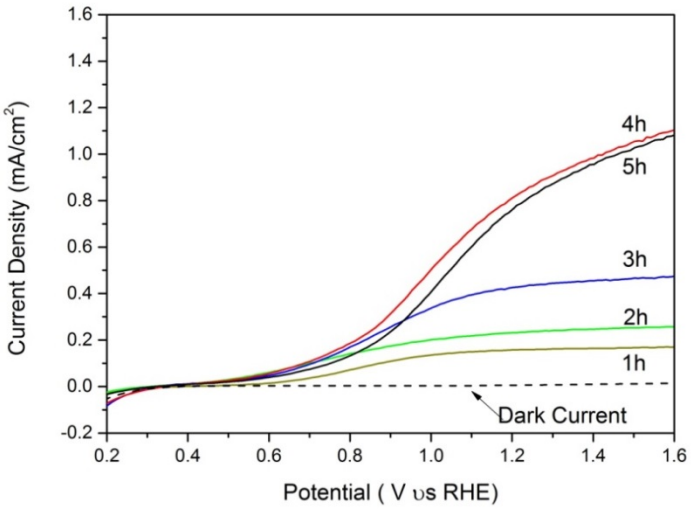

Figure 4-4: I-V curves measured in a 0.2 M Na_2SO_4 solution with phosphate buffer (pH=7) for ZnO films prepared at 90 °C with 0.025 M precursor concentration for varying reaction time; Dark Scan was indicted by the dashed line.

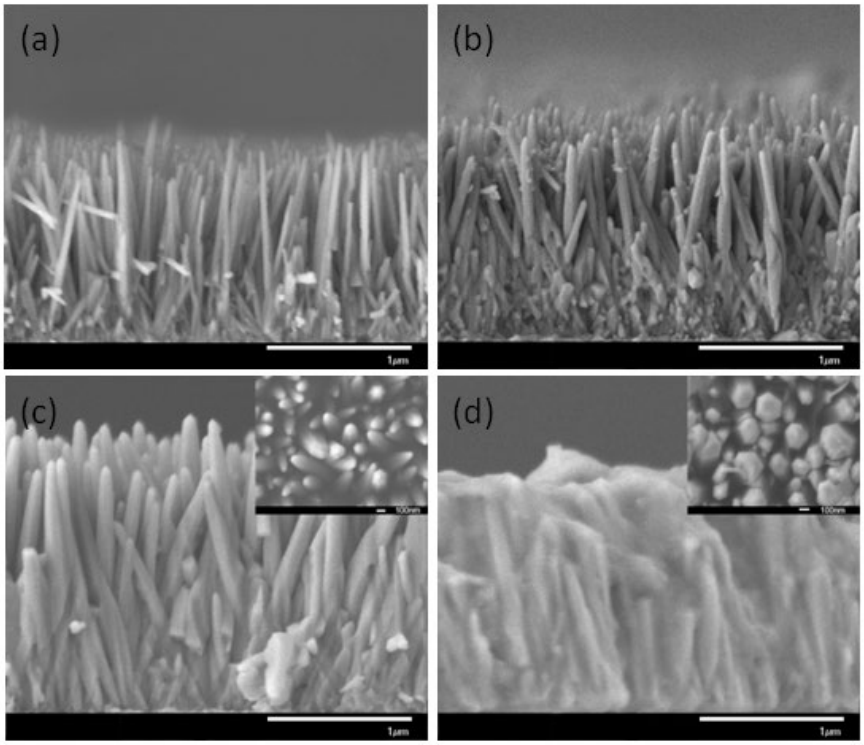

Figure 4-5 : SEM images of ZnO nanowire arrays grown by hydrolysis-condensation reaction at 90 °C for 4 h as a function of precursor concentration: (a) 0.025 M; (b) 0.05 M; (c) 0.075 M (d) 0.1 M. (Insert shows the top view SEM images).

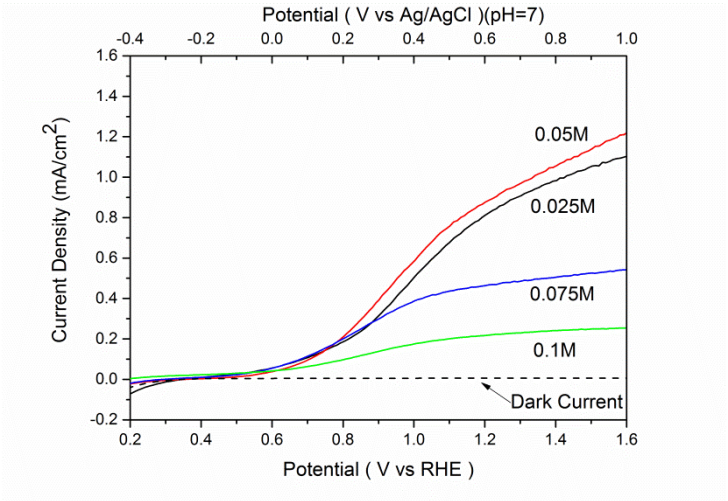

Figure 4-6: I-V curves measured in a 0.2 M Na_2SO_4 solution with phosphate buffer (pH=7) for ZnO films synthesised at 90 °C for 4 h with varying precursor concentration.

Precursor Concentration (mol/L)	Length (nm)	Diameter (nm)
0.025	1300 ±20	50±3
0.05	1400±30	70±5
0.075	1800±80	110±10
0.1	1500±100	250±30

Table 4-1: The effect of precursor concentration on the length and diameter of the ZnO nanowires

In total, as a result of my optimisation procedure, the ZnO films with length of *ca.*1400 nm and diameter of *ca.* 70 nm prepared with 0.05 M precursor concentration at 90 °C for 4 h result in a photocurrent of 0.62 mA/cm^2 at 1V (*vs* RHE) and highest photocurrent of 1.2 mA/cm^2 at 1.6V (*vs* RHE) due to its optimised surface area, light absorption and hole diffusion length, which is much higher than the photocurrent of bare ZnO nanowires reported recently (0.4 mA/cm^2 at 1.0V *vs* RHE).[200]

4.3.2 Surface oxygen evolution catalysts modification of ZnO nanowires

In order to improve the kinetics for water oxidation and holes separation from electrons due to their low mobility mentioned above, oxygen evolution catalysts cobalt phosphate (Co-Pi) and nickel borate (Ni-B) were deposited onto the optimised ZnO nanowire arrays through a simple photo-assisted electrodeposition procedure.[193,194] Figure 4-7 shows the typical SEM images of Co-Pi/ZnO film and Ni-B/ZnO film before PEC tests, compared with a bare ZnO film (Figure 4-7 e), prepared with 0.05 M precursor concentration at 90°C for 4h). Deposition of Co-Pi or Ni-B onto the ZnO surface reveals uniform coverage along the entire length of the nanowires. In addition, compared with bare ZnO nanowires, the average length of Co-Pi/ZnO and Ni-B/ZnO junction is maintained, however their average diameter increased slightly from 70 nm for bare ZnO to 120 nm and 100 nm for Co-Pi/ZnO and Ni-B/ZnO nanowires respectively, attributed to addition of the catalyst layer and indicates a catalyst/ZnO core-shell type array.

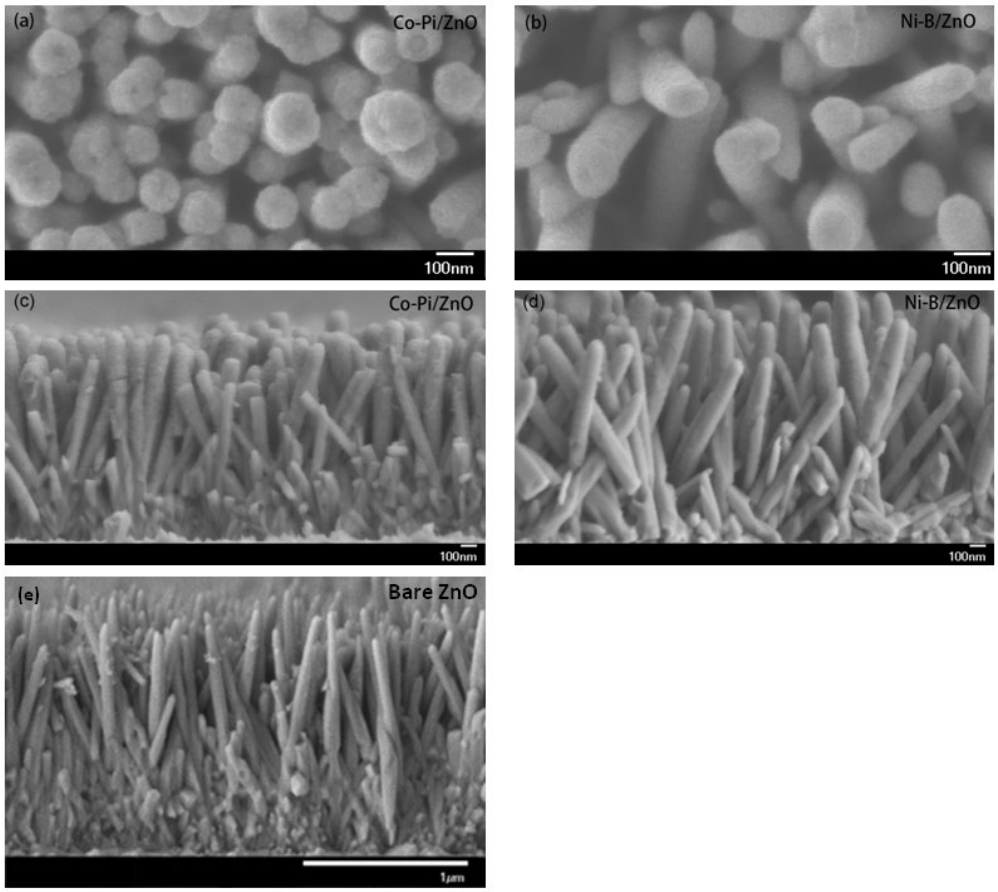

Figure 4-7: Typical SEM images of ZnO nanowires before PEC measurement: (a)Top-view Co-Pi/ZnO; (b) Top-view Ni-B /ZnO; (c) Side-on Co-Pi/ZnO; (d) Side –on Ni-B/ZnO; (e) Side-on bare ZnO.

The UV-Vis transmittance spectra of optimised bare ZnO and co-catalyst modified ZnO films are shown in Figure 4-8. All ZnO-based films exhibited good transparency in the visible range but almost zero transmittance and good absorption in the UV range. The bandgap (E_g) of as-prepared ZnO films was estimated from the absorption spectra. (Figure 4-8 insert).[195] As expected, the band gaps were calculated to be ~3.3 eV for both bare ZnO and co-catalyst modified ZnO films, thus revealing that the addition of co-catalysts did not alter the band gap or light absorption of ZnO significantly.

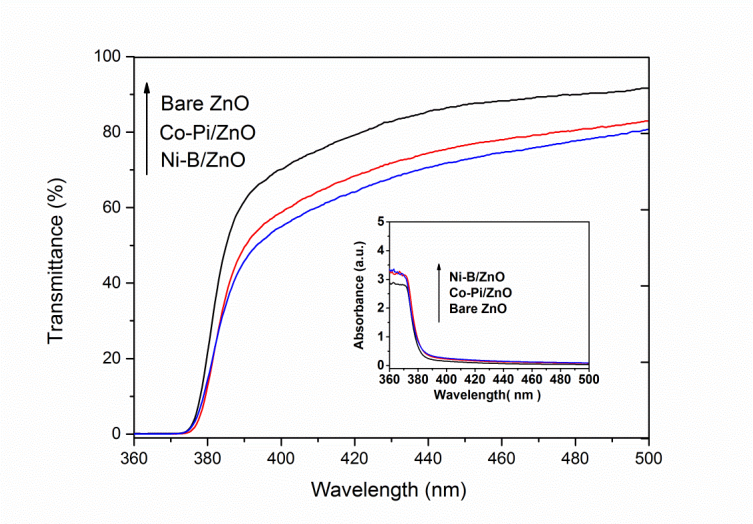

Figure 4-8: UV-Vis transmittance spectra of bare ZnO, Co-Pi/ZnO and Ni-B/ZnO. Inset figure shows the corresponding absorption spectra.

High-resolution XPS was used in order to ascertain the presence and exact valence states of co-catalyst-loaded ZnO nanowire arrays. In all cases the Zn 2p peaks are seen at 1022 and 1045 eV as a result of Zn^{2+} (Figure 4-9). For Co-Pi loaded ZnO, Co 2p peaks at 781.1 and 796.3 eV confirm the presence of the Co^{2+} in Co-Pi surface oxygen evolution catalysts, in good agreement with those previously reported for Co-Pi loaded on the surface of semiconductors (Figure 4-10 a).[201] Furthermore, the phosphorus 2p peak is observed at 133.4 eV due to phosphate in the electrodeposited Co-Pi confirming the formation of Co-Pi on the ZnO surface,[49] but in addition to this, another phosphorus environment is observed at 140.1 eV (marked with *) which is characteristic of phosphorus absorption on ZnO surface but is not part of the oxygen evolution catalyst (Figure 4-10 b).[202] For Ni-B loaded ZnO, two clear Ni 2p peaks are observed at 855.2 and 872.8 eV that are likely to correspond to either Ni^{2+} or Ni^{3+}, but as the binding energies of these two states suffer from a high degree of overlap it is difficult to distinguish the exact nature of Ni with confidence (Figure 4-10 c).[203] The two corresponding Ni 2p satellite peaks (marked with *) are also found at 860.7 and 878.6 eV respectively. For

boron, the expected singlet peak is found at 191.1 eV, indicative of a B^{3+} environment and in agreement with XPS spectra of Ni-B catalysts recently reported (Figure 4-10 d).[194]

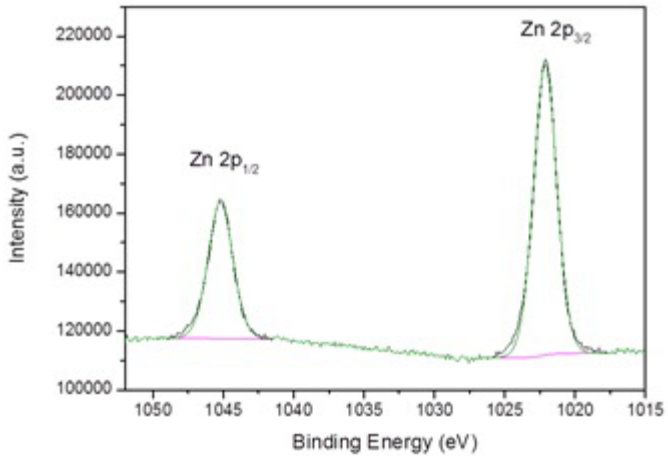

Figure 4-9: XPS spectrum of Zn 2p for ZnO nanowires.

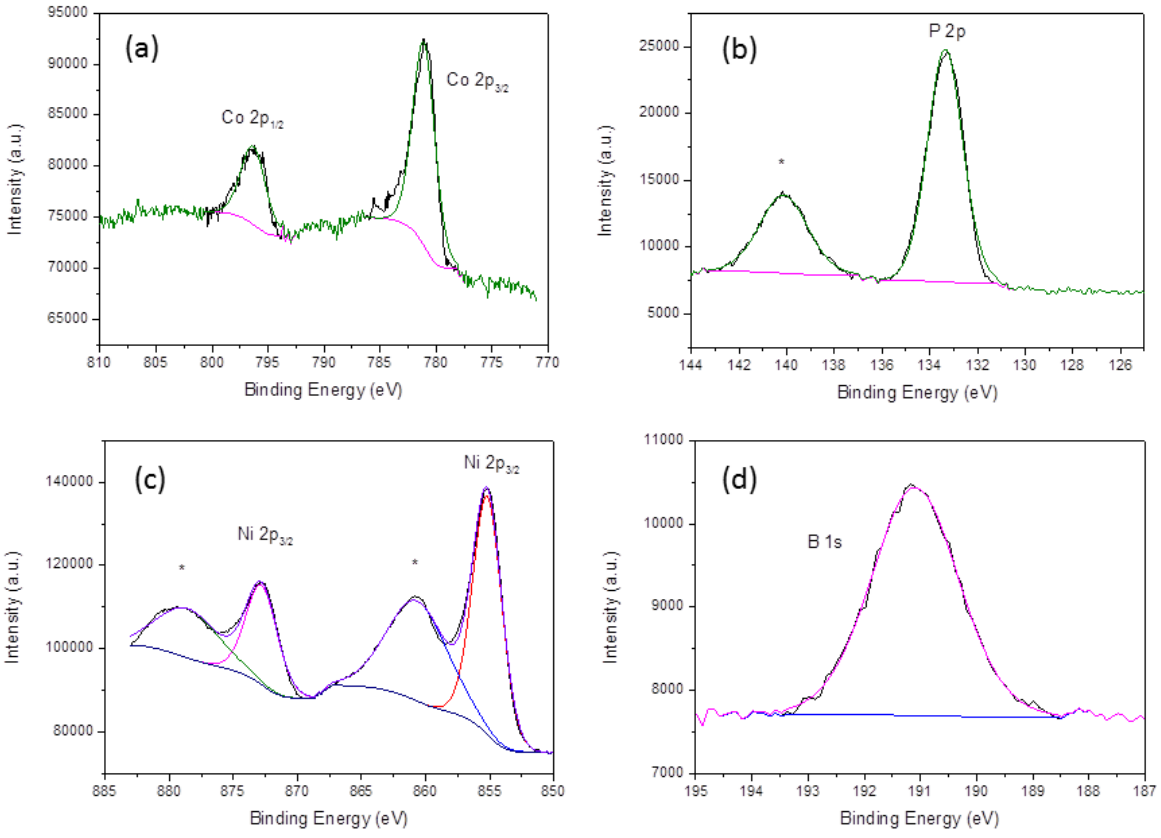

Figure 4-10: XPS spectra of (a): Co 2p; (b): P 2p; (c): Ni 2p; (d): B1s.

Figure 4-11 displays the I-V curves of optimised ZnO nanowires (length 1400 nm, diameter 70 nm), Co-Pi/ZnO and Ni-B/ZnO junction photoelectrodes measured in either sodium sulphate or potassium borate electrolytes. In comparison with bare ZnO, which has an onset potential of 0.5 V (*vs* RHE), the photocurrent onset is cathodically shifted by ~0.1V (*vs* RHE) for Co-Pi modified ZnO, attributed to the Co-Pi catalyst mitigating the hole-electron recombination by acting as a hole trapping site to increase charge separation efficiency. Surprisingly, the onset potential for Ni-B/ZnO is observed to shift cathodically as much as 0.2 V over bare ZnO to *ca.* 0.3V (*vs* RHE). A low onset potential is crucial for widening the operating window and therefore achieving a high ABPE. Similar to the function of Co-Pi co-catalyst, Ni-B also appears to act as a hole trapping site, which can facilitate the hole transfer on the semiconductor surface, thus decreasing electron-hole recombination. The overall photocurrent also increases by loading Co-Pi and Ni-B onto ZnO, resulting in a photocurrent of 0.72 mA/cm^2 and 1.22 mA/cm^2 at 1.0V (*vs* RHE) for Co-Pi/ZnO and Ni-B/ZnO, respectively. More interestingly, the saturated photocurrent of *ca.* 1.1 mA/cm^2 has been achieved at 0.9 V (*vs* RHE) by Ni-B/ZnO instead of 1.6 V (*vs* RHE) by both bare ZnO and Co-Pi/ZnO nanowires.

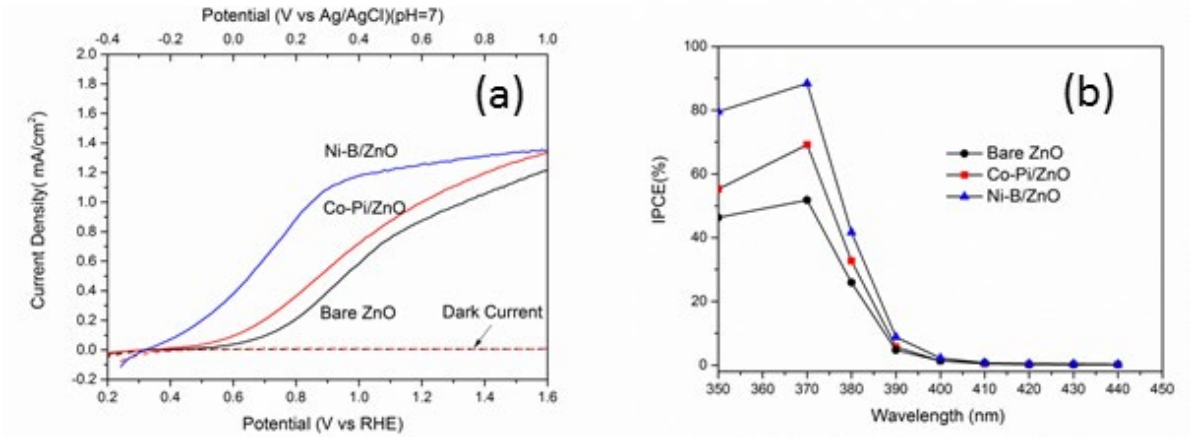

Figure 4-11: (a) Current vs potential curve of bare ZnO, Co-Pi/ZnO and Ni-B/ZnO films; (b) IPCE spectra for bare ZnO, Co-Pi /ZnO and Ni-B/ZnO. ZnO nanowires with the length of *ca.* 1400 nm and diameter of *ca.*70 nm is employed for Co-Pi and Ni-B loading.

Recent studies have reported that the incorporation of cobalt-phosphate oxygen evolution catalyst (Co-Pi OEC) onto n-type semiconductors such as Fe_2O_3,[193, 204, 205] $BiVO_4$,[99, 206] WO_3,[207] n-Si[208] and ZnO[202] could enhance the PEC performance under neutral conditions because the Co-Pi complex functions as a hole trapping site for *in-situ* charge separation, thus reducing surface recombination and improving the kinetics for water oxidation. For example, Zhong *et al.* reported a simple photo-assisted electrodeposition strategy to deposit Co-Pi OEC on α-Fe_2O_3 (hematite) photoanodes in an aqueous, neutral phosphate medium containing Co^{2+} ions.[193] In this process, photogenerated holes from hematite are used to oxidise Co^{2+} to Co^{3+}, resulting in Co-Pi deposition on the surface of the semiconductor. Ni-B shares a similar catalytic mechanism for water oxidation to Co-Pi. The electron-hole pairs generated by the light-absorbing semiconductor are separated by an internal electric field; [193] conduction band (CB) electrons move towards to the back contact (FTO substrate), through the external circuit to the Pt counter electrode under external bias (for hydrogen evolution). Photogenerated holes migrate to the Ni-B surface and oxidise Ni from 2+ to 3+, and then O_2 evolution occurs by the withdrawal of electrons from water, accompanied by a change in Ni oxidation state back to 2+. On the other hand, it has recently been reported that the active site in the Ni-B catalyst possesses an intermediate oxidation state of 3.6, indicating the Ni centre to be in formal oxidation of 4+.[83]

In order to compare the light conversion efficiency of bare ZnO and co-catalyst modified ZnO, incident-photon-to-current conversion efficiency (IPCE) was measured for all samples (Figure 4-11 b). The IPCE spectra of optimized bare ZnO nanowires (1400 nm length) is, as expected, near zero in the visible region (400-440 nm) but increases rapidly to *ca.* 52 % at 370 nm, which is consistent with its corresponding UV-Vis spectrum and high photocurrent, and is subsequently much higher than that recorded for ZnO nanowire arrays reported in the literature (~40 %).[174, 200, 209] Both Co-Pi and Ni-B deposition onto ZnO result in a sharp increase in their

respective IPCE; the IPCE of Co-Pi/ZnO increases dramatically to *ca.*72% at 370 nm and for Ni-B/ZnO, an even larger increase to *ca*. 90 % at 370 nm is observed, which represents a near 75% increase compared to the bare ZnO film. This observation provides further explanation for the somewhat early saturated photocurrent achieved (1.1 mA/cm^2 at *ca.* 0.9 V *vs* RHE) observed in Figure 4-11 (a). In general, the process of efficient water splitting is highly dependent on three factors: efficient light absorption by the photocatalyst, efficient charge carrier separation and efficient surface reaction (charge utilisation). The saturated photocurrent is observed for Ni-B/ZnO at an early stage due to efficient hole trapping and subsequent faster surface reaction compared to both Co-Pi/ZnO junction and bare ZnO. ZnO has an intrinsically high electron mobility[196] but very low hole mobility,[197-199] leading to fast recombination and therefore, bare ZnO requires a higher electrical bias to obtain a saturated photocurrent. As the early saturated photocurrent is observed for Ni-B/ZnO rather than Co-Pi/ZnO, it strongly indicates that Ni-B is a much more efficient surface co-catalyst and hole acceptor than Co-Pi. The high IPCE of Ni-B/ZnO can be attributed to increased light trapping by ZnO nanowires, efficient separation of photogenerated electrons and holes through the loading of an improved oxygen evolution surface catalyst, fast rectifying electron transport through 1-D ZnO nanowires to the counter electrode and efficient surface catalysis. Furthermore the ABPE (η) for Ni-B/ZnO was measured to be 0.4 %, which is considerably higher than recently reported values for nitrogen doped ZnO nanowires (0.15 %),[174] Si/ZnO core-shell nanowires (0.38%)[184] and even some visible-driven semiconductor-based photoanodes, such as WO_3 /C_3N_4/CoO_x ,[210] However, it is lower than the recently reported benchmark Co-Pi/W:$BiVO_4$ – photoelectrode.[23] Therefore a new visible driven junction based on 1-D ZnO is underway in order to more efficiently utilizing solar energy.

An important consideration in the employment of photoanodes for water cleavage on a commercial scale is their stability under prolonged illumination in aqueous solution, which is extremely serious for ZnO based photoanodes. Therefore the stabilities of bare ZnO, Co-Pi/ZnO, and Ni-B/ZnO junctions were investigated and measured at a potential of 1.0V (*vs* RHE) for 1h (Figure 4-12 a). For bare ZnO nanowires, very poor stability is observed with continuous decay of photocurrent; only 34% residual photocurrent remains at the end of the experiment. A slight improvement in stability is observed for Co-Pi/ZnO junction as Co-Pi itself appears to have some short-term stability in solution, followed by a relatively stable stage (65 % photocurrent remaining at end of the experiment). It is most likely to be due to the facile exchange of cobalt and phosphorus ions directly between the film and solution.[211] Most significantly, Ni-B/ZnO junction exhibited unprecedented retention in photocurrent over the 1 hour time period, which, to the best of our knowledge, is the first such observation for ZnO photoelectrodes. Similarly, a very recent report also mentioned that a nickel film deposited by electron beam evaporation on an otherwise poorly stable n-type silicon (n-Si) photoanode results in an unprecedented improvement in stability during PEC measurements in aqueous solution and a significant shift in onset potential when immersed in potassium borate electrolyte.[203]

To confirm the improved stability of our Ni-B/ZnO junction, the morphologies of these ZnO-based photoelectrodes were examined using SEM after our prolonged PEC testing (Figure 4-12 b-d). In agreement with the stability test, no photocorrosion is observed for the Ni-B/ZnO junction, however the images of the bare ZnO and Co-Pi/ZnO electrodes reveal a significant alteration in structure into a dense, compact film with very few distinct features and significantly, they no longer resemble nanowire arrays. The side-on views of these samples before and after PEC testing clearly show the effect of photocorrosion on their morphologies.

Only Ni-B/ZnO retains the vertically aligned nanowire morphology (Figure 4-7 and Figure 4-n12 b-d). Furthermore, no significant change is observed in diffraction patterns before and after one-hour photoelectrochemical water oxidation reaction for Ni-B/ZnO photoelectrodes (Figure 4-13), which suggests the maintained crystal structure after reaction.[212] Similarly, high resolution XPS analysis of Ni-B/ZnO photoelectrodes reveal that no obvious change in positions and intensities of Ni and B peaks, which is also in agreement with the recently reported stability enhancement of Ni-protected n-Si photoelectrodes.[213, 214, 203] Overall this study demonstrates the application of Ni-B not only as an efficient surface water oxidation catalyst but also as an effective passivation layer for semiconductor electrodes.

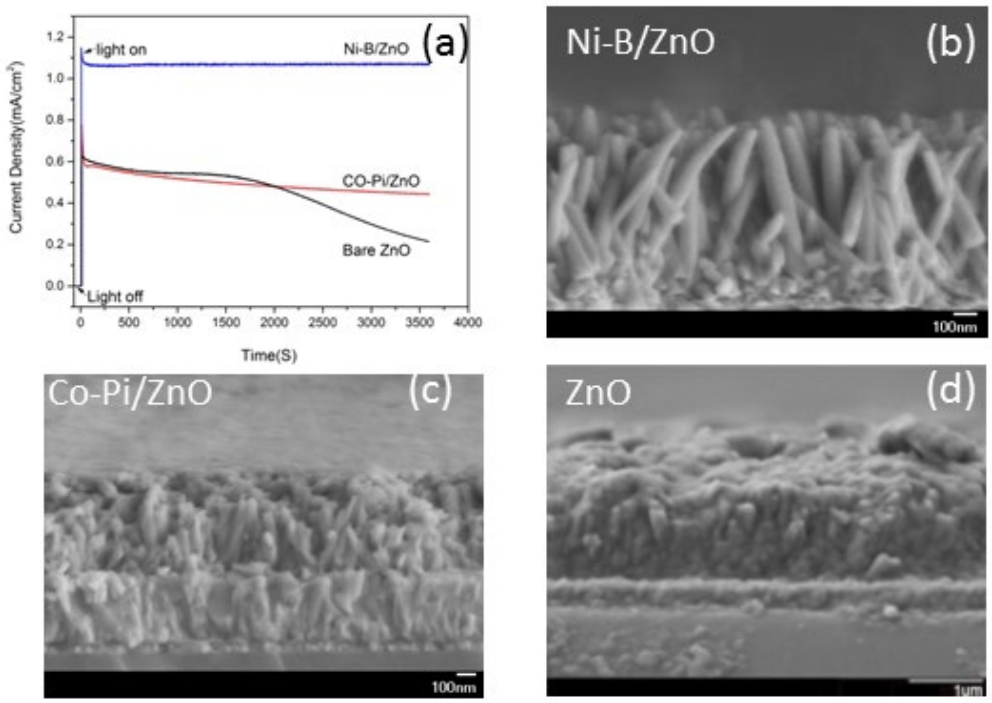

Figure 4-12: (a) Current-time curves of bare ZnO, Co-Pi/ZnO and Ni-B/ZnO photoelectrodes measured at 1.0 V (vs RHE) for a 1 hour period; (b-d) typical side-on SEM images of ZnO nanowires after 1 hour of PEC measurements - (b) Ni-B/ZnO; (c) Co-Pi/ZnO; (d) bare ZnO.

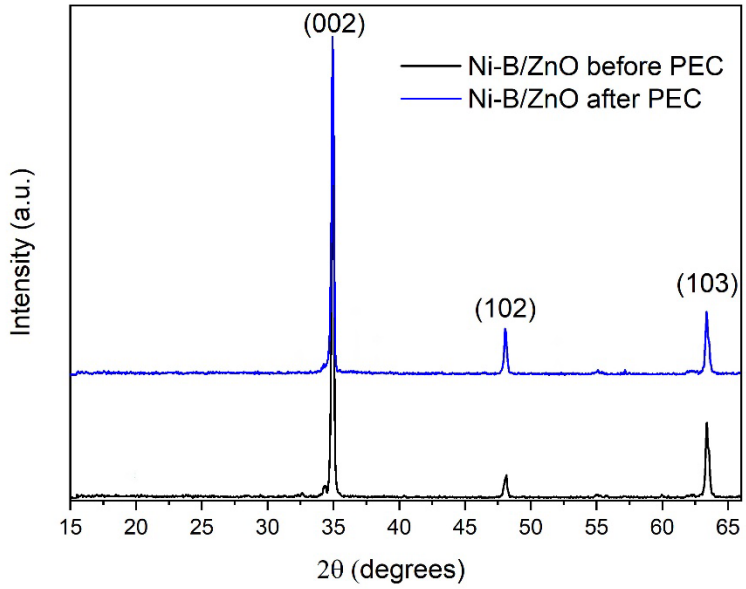

Figure 4-13: XRD patterns of Ni-B/ZnO photoelectrodes before and after 1h PEC measurement.

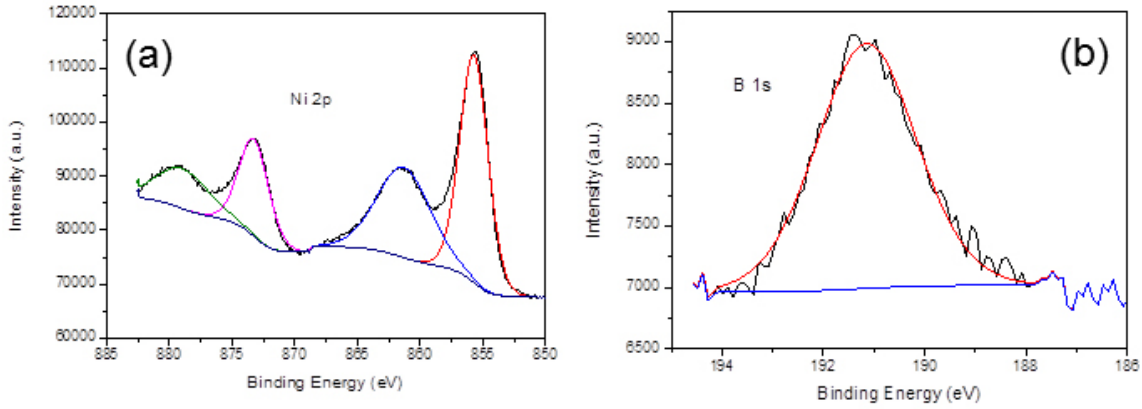

Figure 4-14 : XPS spectra of Ni-B/ZnO photoelectrodes after one-hour PEC measurements: (a) Ni 2p and (b) B 1s regions.

4.4 Conclusion

In this study, a mild and efficient method was reported to significantly improve the photoelectrochemical performance of 1-D ZnO nanowire arrays through optimisation of their length and diameter followed by surface modification with noble metal free co-catalysts. Optimized bare ZnO nanowires (1400 nm length, 70 nm diameter) exhibited a photocurrent of

0.62 mA/cm^2 at 1.0 V and 1.2 mA/cm^2 at 1.6 V (*vs* RHE) under 1 sun illumination. Co-catalysts Co-Pi and Ni-B were successfully loaded onto the surface of these optimised ZnO nanowires *via* photo-assisted electrodeposition, resulting in a higher steady-state photocurrent (0.75 mA/cm^2 at 1.0 V *vs* RHE) and improved IPCE (72 % at 370 nm) for Co-Pi/ZnO compared to bare ZnO. Furthermore, the Ni-B/ZnO junction exhibited two times higher steady-state photocurrent (1.22 mA/cm^2 at 1.0V *vs* RHE) compared to unmodified ZnO, resulting in an IPCE of ~90 % at 370 nm. More importantly, a significant cathodic shift in onset potential (by 0.2V) and potential for saturated photocurrent (by nearly 0.7 V) are observed after Ni-B modification. The stability of ZnO has been improved significantly with the introduction of these surface oxidation catalysts, with the Ni-B/ZnO junction exhibiting an unprecedented zero loss in photocurrent over the 1 hour test period, thus proving its dual functionality as a benign water oxidation catalyst and robust surface protection layer that can inhibit photocorrosion. The overall mechanism for the enhancement in current is due to efficient hole trapping by the surface co-catalyst and its catalytic effect. Next, fast electron transfer along highly charge mobile, well-aligned ZnO wires to the counter electrode also plays an important role.

In total, this simple junction strategy has dramatically improved the efficiency and stability of ZnO, proving the importance of an electrocatalyst (cocatalyst). However, the drawback of low STH conversion efficacy still remains due to its inherent wide band gap. By applying an efficient electrocatalyst to other narrow bandgap semiconductors (e.g. GaAs, BiVO4, α-Fe_2O_3,) to form a junction strategy would further increase the STH efficiency of the narrow band semiconductor photoelectrodes. More importantly, by using a photo-assisted electrodepostion method, Ni-B catalyst could be successfully loaded onto ZnO surface and acted as a protection layer against the photocorrosion. Therefore, Ni-B catalyst would be coupled onto those visible-driven semiconductors (e.g. GaAs or InP) which have the potential to exhibit high STH efficacy

(>10 %), but poor stability. In order to improve the overall performance of a water splitting device for practical application, a potential heterojunction architecture would likely involve the coupling Ni-B catalyst to a narrow bandgap semiconductor to achieve efficient and prolonged photocatalytic water cleavage.

5 Nickel-borate surface catalyst stabilised GaAs photoanodes

5.1 Introduction

In a PEC water splitting system, oxygen evolution is the rate determining step. Among the typical III-V materials, such as InGaP, GaAs, InP, GaAs could be an ideal material for PEC water oxidation due to its intrinsically small band-gap (1.42 eV), and appropriate band positions, promising a high theoretical solar energy conversion efficiency of 33%.[215] Therefore there is substantial interest in using group III-V materials, in particular GaAs, as a photoanode for PEC water splitting. However the stability of III-V materials is one of the major challenges for their application in PEC cell due to the fast photocorrosion at the interface between III-V materials and electrolyte.[216 217]

One of the first works reporting GaAs photoanodes for solar fuel synthesis was by Zhou et al.[162] The as-synthesized GaAs nanowire arrays exhibited a solar energy conversion efficiency of 8.1 % without a co-catalyst. However, the hydrogen production was not affordable due to the electrode instability (50 % current loss in one hour). Basically, the surface dissolves during the photoelectrochemical reaction and this fast surface etching results in H_2 gas generation is limited to approximately one hour. This etching is caused by generated holes which are not used for the oxidation of water at the GaAs surface while accumulated to oxidise the GaAs layer. This is partly because the consumption rate of holes for O_2 generation on the GaAs surface is much lower than that of electrons on the counter electrode because four holes are required to produce an O_2 molecule while only two electrons are necessary for the generation of an H_2 molecule.

Nocera et al. have developed an earth-abundant oxygen-evolving catalyst (Cobalt Phosphate, Co-Pi) to improve the hole utilisation efficiency for the oxidation reaction of water.[49] The devices consisting of a Co-Pi modified silicon-based photoanode for oxygen evolution and NiMoZn catalyst for hydrogen evolution exhibited relatively good stability (10 h) for water splitting with a solar to hydrogen conversion efficiency of 4.7 % for a wired configuration and 2.5 % for a wireless configuration.[130] An efficiency of 12.3 % was also reported using a perovskite photovoltaic together with a bifunctional earth-abundant catalyst, but authors underlined its poor stability.[25]

Various coating strategies have been explored to stabilise narrow gap semiconductors in a PEC cell. Horn et al. reported an n/p-GaAs (001) photocathode that operated in neural pH, stabilised by an epitaxial $SrTiO_3$ surface layer to deliver photocurrents of 3.1 mA /cm^2 at 0.18 V with 24 h stability.[218] Lewis et al. coated a GaAs electrode with a conformal amorphous TiO_2 as a protection layer alongside a thin layer of Ni metal as a co-catalyst. The prepared photoanodes exhibited a photocurrent of 15 mA/cm^2 at -0.2 V (vs SCE) in 0.1 M KOH with almost one-day constant operation.[219] The same group also fabricated NiO_x film on p^+n-InP photoanodes as both a protection layer and a surface oxygen evolution catalyst via sputtering to achieve 48 hours solar driven water oxidation.[220] In fact, both the protection layer and surface catalyst are significant for high and stable photocurrent. Lewis et al. also demonstrated that n-cadmium telluride photoanodes could be stabilised for water oxidation by using amorphous TiO_2 films formed by atomic layer deposition.[104]

In chapter 4, an earth-abundant catalyst, nickel borate (Ni-B) was successfully coupled onto ZnO photoanodes to dramatically enhance the holes' efficiency for water oxidation reaction and also improve the ZnO stability.[121] Herein, in order to fabricate a

stable and efficient device for solar fuel synthesis, this chapter moved forward to focus on the Ni-B surface catalyst as hole trapping sites on top of GaAs to suppress the photocorrosion reaction caused by accumulated holes on GaAs surface and to facilitate charge separation. The p-n GaAs junction was designed firstly to facilitate a hole transfer pathway while maintaining a good light absorption. *In-situ* photoassisted electrodeposition of Ni-B onto p-n GaAs photoanode was able to generate a monolithic layer of Ni-B/Ga (As)Ox on GaAs, which acts as a catalytic and passivation layer to protect GaAs against photocorrosion. Such a procedure resulted in a stable photocurrent and the surface treatment for the loading of water oxidation catalysts (Ni-B) on GaAs was also discussed in detail.

5.2 Experimental section

5.2.1 Photoanodes fabrication

(1) P/n junction GaAs growth

The GaAs photoanodes were grown by a Veeco Gen 930 molecular beam epitaxy system. Before loading the substrate into the epitaxy system, the GaAs substrate was thermally degassed to remove contaminants. The GaAs photoelectrodes were homoepitaxially grown on an n-type GaAs substrate (650 μm thickness). A thin layer of native oxide was thermally removed by holding the substrate at high temperatures (600 °C) under the protection of arsenic flux for eight minutes. The GaAs growth temperature was 580 °C. An n-type GaAs buffer layer of 200 nm was first grown on the substrate. After the buffer layer, a p-type GaAs layer of 2000 nm was grown. The doping density was 2×10^{18} cm^{-3}. The growth rate was ~1 monolayer per second, controlled by adjusting the Ga source temperature. The temperature variation was very small within ± 0.1 °C controlled by a PID controller, thus enabling a high

reproducibility of the GaAs photoelectrodes synthesis. Doping of the GaAs layers to make p or n-type semiconductor was achieved in-situ during epitaxy growth, where Si and Be were used as n-type and p-type dopant, respectively. The growth was monitored with a reflection high-energy electron diffraction system, which includes a high energy electron gun, phosphor screen, and CCD camera.

(2) Pre-treatment of GaAs surface

As-prepared p/n junction GaAs samples were either etched or polished to promote attachment with surface catalysts Ni-B. For etched GaAs samples, a thin Ni layer (2 nm) was deposited on the sample surface by evaporation followed by thermal annealing at 500 ˚C to form surface Ni nanodots. The sample was then chemically etched by using the Ni nanodots as a mask. To further increase the surface roughness, samples were polished using 1-micron grinding papers by a mechanical polisher. After polishing, the samples were washed by the solution with the mixture of H_3PO_4/H_2O_2/HCl in 1:1:1 ratio and dried for use.

(3) Preparation of bare and Ni-B modified GaAs photoanodes

Ohmic contacts to the GaAs photoanodes were formed by evaporation of Ni/AuGe/Ni/Au metals on the back of the substrate and rapid thermal annealing at preferred temperatures at 400 °C. The GaAs electrodes were then wired by soldering a Cu wire to the alloyed metal contact. The samples were encapsulated by using epoxy (Sigma, Resin: hardener = 1:1). Ni-B catalyst was deposited onto the GaAs samples by photoassisted deposition in a three-electrode system with GaAs samples as working

electrodes, Ag/AgCl as a reference electrode, and a Pt mesh as a counter electrode. Before loading Ni-B on the pre-treated GaAs surface, it was immersed into methanol solution for 60s, followed by 1:1 volume ratio of HCl and deionised (DI) water for another 60s, and then rinsed with a large amount of DI water and dried under the stream of Argon to make a clean surface. The photoassisted electrodeposition of Ni-B on GaAs was carried out by applying a constant bias of 0.5 V (vs Ag/AgCl) in a solution of 0.1 M potassium borate containing 1 mM Ni $(NO_3)_2$ with varying deposition times under AM 1.5 G light illumination (100mW/cm^2).

5.2.2 Photoanodes characterisation

SEM images were obtained by Jeol JSM-7401F scanning electron microscope with EDX detector. High-resolution XPS was performed by using a Thermo Scientific K-alpha photoelectron spectrometer with monochromatic $Al_{k\alpha}$ radiation; peak positions were calibrated to carbon (284.5 eV) and plotted with the CasaXPS software. Atomic force microscopy (AFM) images of the surface morphology were obtained using a Veeco Nanoscope atomic force microscope. The X-ray diffraction (XRD) patterns were performed by using a Jordan Valley Bede D1 system.

5.2.3 Photoelectrochemical measurements

The photoelectrochemical measurements were carried out in a gas-tight cell equipped with a quartz window. The prepared GaAs samples were used as the working electrodes. A Pt mesh and Ag/AgCl (3M KCl) were used as the counter electrode and reference electrode, respectively. The electrolyte containing 0.1 M KOH (pH=14) in deionised

water, which was purged by argon gas prior to use for 20 mins to remove dissolved oxygen. The light source was a 150 W xenon lamp (Newport) equipped with a standard AM 1.5G filter. The light intensity was calibrated to 100 mW/cm^2 using a silicon photodiode, together with a hand-held optical meter (Newport, 1918-R). A potentiostat (Ivium technology) was used to apply the bias at a scan rate of 20 mV/s between -1.5 and 1.0 V (vs Ag/AgCl). The electrochemical impedance spectroscopy (EIS) data were carried out through the same electrochemical measurement system under an AM 1.5-light illumination at an applied bias of -0.6 V (vs Ag/AgCl) in 0.1 M potassium hydroxide solution with a frequency range of 100,000 and 1 Hz of a sinusoidal perturbation with 10 mV amplitude.

Gas Evolution Analysis: a gas-tight three-electrode one compartment PEC cell with an Ag/AgCl reference electrode, a Pt mesh counter electrode and a gas chromatograph (Varian 430- GC, TCD detector, argon carrier gas 99.999%) was used for the analysis of gas evolved from electrodes. Before the measurement, the PEC cell was purged with Ar flow until no nitrogen and oxygen gases were detected by the gas chromatograph. The photoelectrode was constantly biased at -0.6 V (vs Ag/AgCl) and illuminated by a 150 W xenon lamp (AM 1.5 G ,100 mW/cm^2). The photoanode current was recorded by a potentiostat (Ivium technology) and simultaneously the produced amount of O_2 and H_2 in the closed cell were measured by injecting the headspace gas into gas chromatograph. Then the Faraday efficiency based on the oxygen evolution could be calculated by equation 3-11. The solar to hydrogen conversion efficiency (η) was estimated by using equation 3-9.

5.3 Results and Discussion

5.3.1 Photoanode design and characterisation

P/n junction GaAs samples were fabricated by using commercial n-type GaAs (001) as the substrate for the epitaxial growth of 2000 nm p-type GaAs. The GaAs surface was treated before loading of Ni-B in order to increase the roughness of GaAs surface for better attachment of Ni-B catalyst, which would improve the stability of the photoanode and catalyse the water oxidation reaction. The surface of the GaAs samples was either textured by etching or polished by a mechanical polisher, annotated as textured (etched), shallow (moderately polished) or deep GaAs (deep polished) photoanodes based on the surface roughness while the untreated was named flat photoanode. Figure 5-1shows the AFM images for the surface treated GaAs before loading of Ni-B. The root mean square (RMS) roughness of the as-grown GaAs (flat GaAs) photoanode is about 0.25 nm. The RMS roughness of textured GaAs change to 1.94 nm and the average peak to valley height is ~10 nm. The RMS roughness increases after surface treatment by the mechanical polisher, resulting in shallow and deep dents on the surface. Measured RMS roughness is 8 nm and 39.2 nm for shallow and deep treated GaAs surface, respectively and the average peak to valley height is increased by an order of five from shallow to deep treated GaAs photoanode.

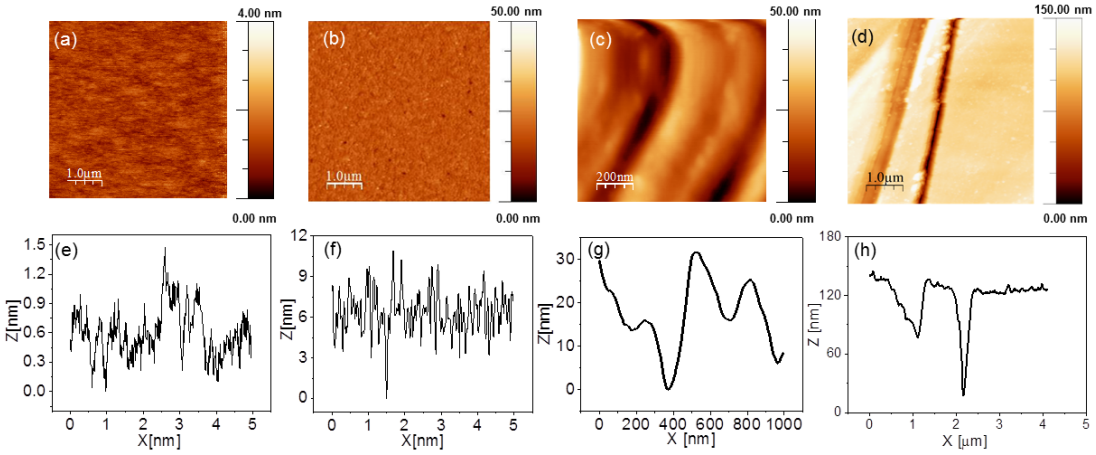

Figure 5-1 ： AFM images and the corresponding Width-Height plot for various GaAs films; (a)&(e): Flat GaAs; (b)&(f): Textured GaAs; (c)&(g): Shallow GaAs; (d)&(h): Deep GaAs.

Figure 5-2 shows the AFM image and the corresponding width-height plot of Ni-B/Ga (As)Ox/textured GaAs photoanodes with 0.5 h Ni-B photoassisted electrodeposition. After Ni-B loading, the RMS roughness of textured GaAs surface increases from 1.94 nm to 30 nm and the peak to valley height of textured GaAs surface increases from 10 nm to 15 nm, which indicates the change of GaAs surface roughness after Ni-B modification.

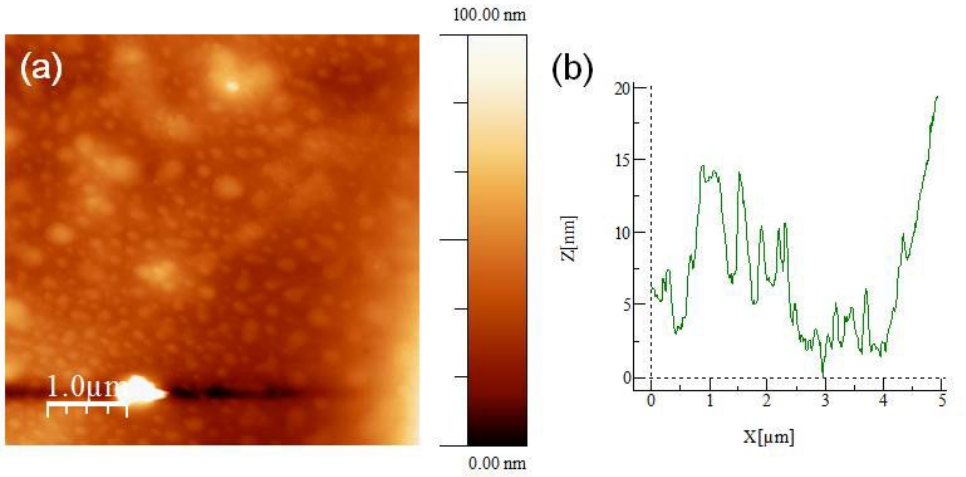

Figure 5-2 : (a) AFM image and (b) Width-height plot of Ni-B/Ga (As)Ox/textured

GaAs photoanodes with 0.5h Ni-B photoassisted electrodeposition.

X-ray photoelectron spectroscopy measurements (XPS) were carried out to monitor the valence change of the components in the fabricated photoanodes. The XPS spectra of 0.5 h photoassisted electrodeposited Ni-B onto shallow GaAs electrodes are shown in Figure 5-3. Three Ga-based 3d peaks are observed. The peak at 19.1 eV corresponds to the GaAs substrate. The gallium oxides (GaOx) are composed of a mixture of Ga_2O (Ga^{1+}) and Ga_2O_3 (Ga^{3+}) at binding energy of 19.7 eV and 20.7 eV, respectively. The O 2s signal originates from gallium oxide formation during the photoassisted electrodeposition process. These values well match with the literature.[221] The As 3d spectrum also confirms the presence of As-Ga substrate (41.2eV). The arsenic oxides (AsOx) are composed of a mixture of As_2O_3(44.1eV), As^{3+} native oxide (45.0 eV) and As_2O_5(45.9 eV).[222] Two Ni 2p peaks are observed at 855.2 and 872.8 eV, which likely corresponds to Ni^{2+} or Ni^{3+}. As the binding energies of these two states suffer from a high degree of overlap, it is difficult to distinguish the exact nature of Ni with confidence.[122] For boron, the expected singlet peak is found at 191.1eV, indicative of a B^{3+} environment and in agreement with literature.[121, 223] Also, the surface residual potassium species from the potassium borate electrolyte are confirmed by XPS of K 2p spectra as shown in Figure 5-4. Such samples are denoted as Ni-B/Ga (As)Ox/shallow GaAs. Moreover, the X-ray diffraction patterns of Ni-B/Ga(As)Ox/shallow GaAs reveals a highly crystallised GaAs substrate with (001) orientation while amorphous nature of Ni-B (Figure 5-5).[224-226]

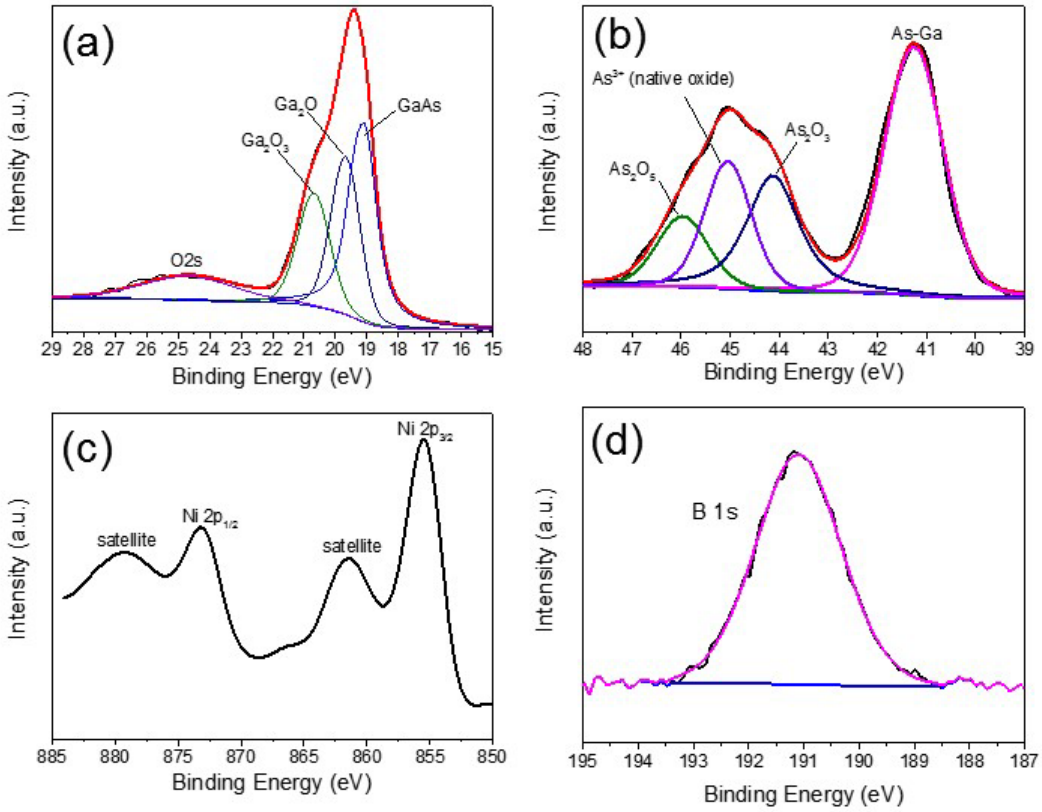

Figure 5-3*: XPS spectra of Ga 3d, As 3d, Ni 2p and B1s of Ni-B/Ga (As)Ox/shallow GaAs photoanode with 0.5 h photoassisted electrodeposited Ni-B catalyst.*

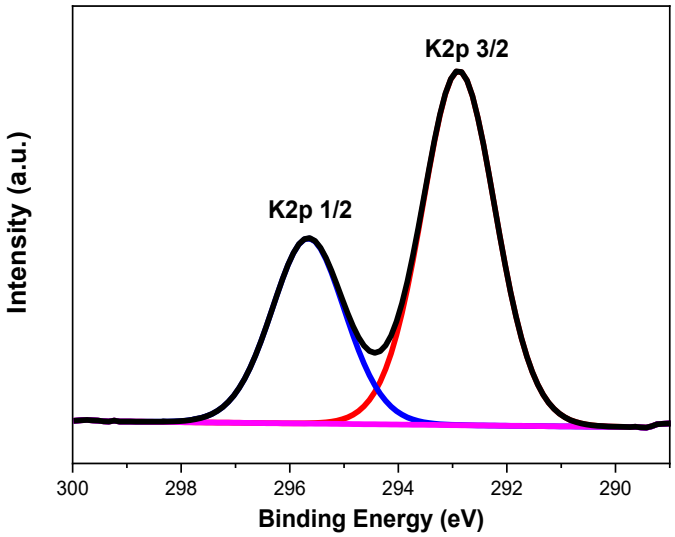

Figure 5-4 : XPS spectra of K 2p of Ni-B/Ga (As)Ox/shallow GaAs photoanode with 0.5 h photoassisted electrodeposited Ni-B catalyst.

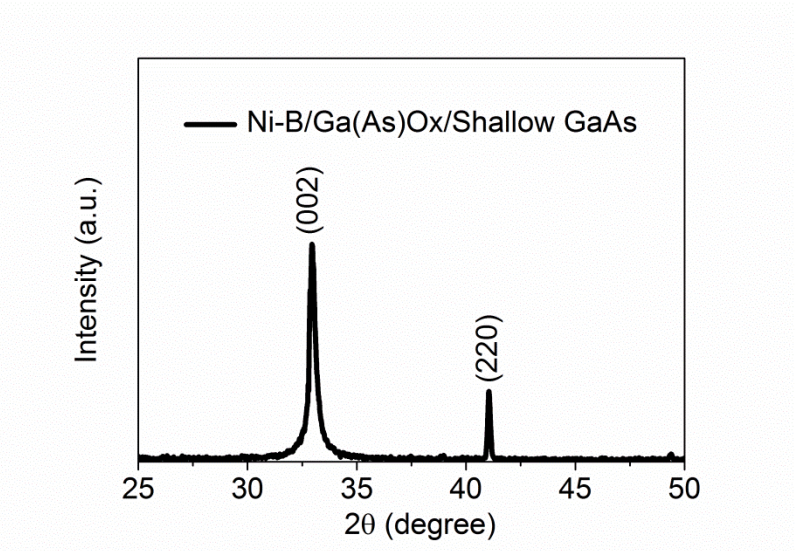

Figure 5-5 : XRD patterns of Ni-B/Ga (As)Ox/shallow GaAs.

SEM image of a shallow GaAs surface is shown in Figure 5-6a, which indicates uncorroded GaAs electrode before photoelectrochemical reaction. Figure 5-7a, b shows the cross-sectional and top-down morphology of shallow GaAs decorated by a Ni-B catalyst with 0.5 h deposition time, respectively. The cross-sectional SEM image in Figure 5-7a displays a layer of Ni-B/Ga (As)Ox with a thickness of *ca.* 900 nm on top of GaAs surface. The monolithic Ni-B/Ga (As)Ox layered structure might be resulted from Ni-B loading and Ga (As)Ox passivation layer formation during the photoassisted simultaneous electrodeposition. The line analysis using SEM-EDX (Figure 5-7b) throughout the Ni-B/GaAs layer indicates the co-existence of Ni, Ga, As and O in the top 900 nm while more Ni and O exist in the top 550 nm likely in the form of NiOx. B is only observed on the surface (Figure 5-7e), suggesting Ni-B is only formed on the surface. The top-down SEM image (Figure 5-7c) and the corresponding elemental mapping images (Figure 7 d-h) further provide the evidence of a Ni-B/Ga (As)O_x layer formation on top of GaAs and furthermore, evenly distributed Ni elements are observed.

This observation illustrates the in-situ formation of Ga (As)Ox layer from loading Ni-B catalyst on GaAs substrate, which is consistent with XPS results.

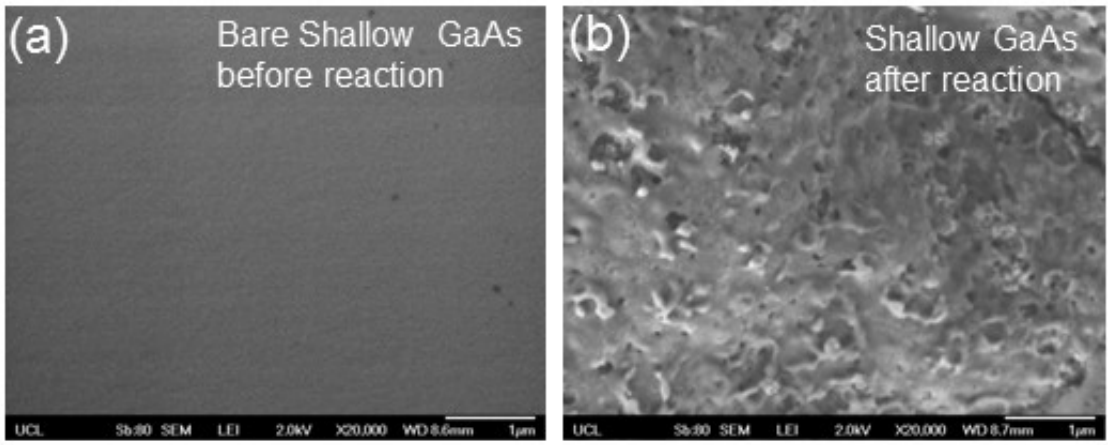

Figure 5-6: Typical SEM images of bare shallow GaAs photoanodes: (a) before and (b) after 6h photoelectrochemical reaction in 0.1M potassium hydroxide under one sun illumination with a constant applied potential of -0.6 V (vs Ag/AgCl).

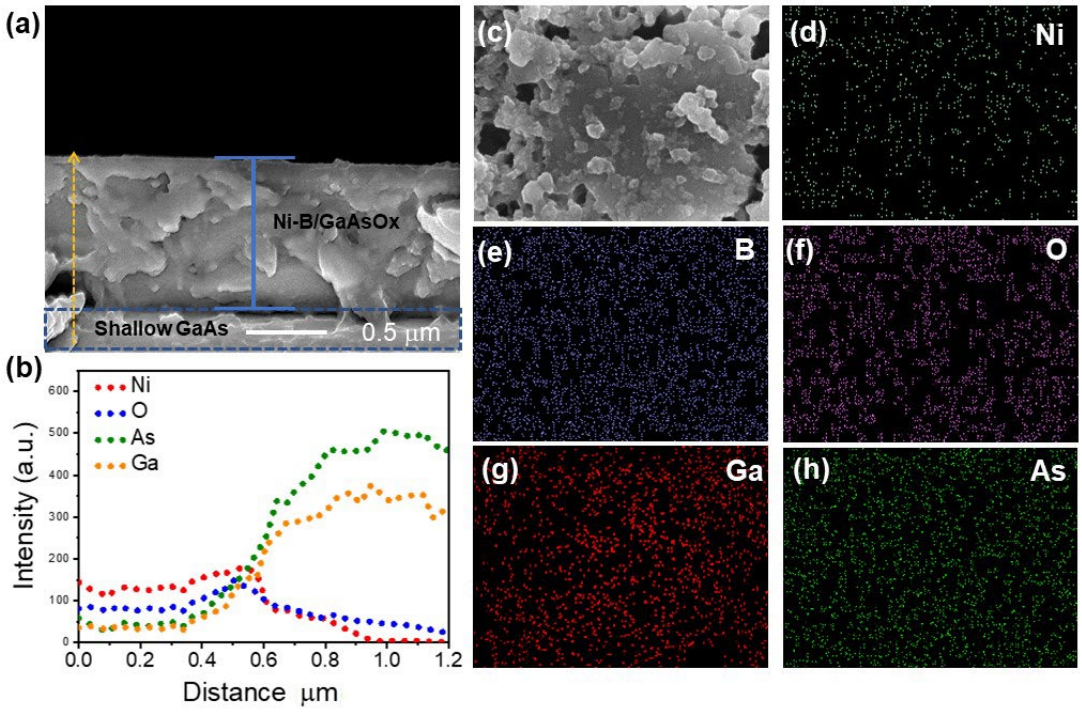

Figure 5-7: Ni-B/Ga (As) Ox/shallow GaAs electrode: (a) Cross-sectional SEM image and (b) line analysis throughout the cross-section. (c) Top-down SEM images. (d-h) SEM-EDX micrograph and maps of the distribution of elements on the electrode surface for Gallium (Ga), oxygen (O), arsenide (As), nickel (Ni), and boron (B).

5.3.2 PEC performance measurements of as-prepared GaAs based photoanodes

The PEC performance of as-prepared GaAs based photoanodes was investigated in a three-electrode configuration. Initially, the effect of Ni-B surface catalysts on PEC water oxidation performance was investigated. Figure 5-8 shows the photocurrent density as a function of applied voltage under one sun illumination (100 mW/cm^2) and dark current for both bare shallow GaAs and Ni-B/Ga (As)Ox/GaAs photoanodes in 0.1 M potassium hydroxide electrolyte (pH = 14). In comparison with bare shallow GaAs, which has a dark current onset potential of 0.5 V (vs Ag/AgCl), the dark current onset is cathodically shifted to 0.25 V (vs Ag/AgCl) for the Ni-B/Ga (As)Ox/Shallow GaAs photoanode (Figure 5-8b). This significant shift in onset potential for dark current (by 0.25 V) after Ni-B loading indicates the catalytic effect and improved water oxidation kinetics by Ni-B. However, no significant photocurrent onset potential shift is observed between bare shallow GaAs and Ni-B/Ga (As)Ox/Shallow GaAs photoanodes (Figure 5-8a). The flat band position of the Ni-B/GaAsOx/shallow GaAs was determined by Mott-Schottky measurements to be -1.6 V vs Ag/AgCl at pH=14 (Figure 5-9), consistent with previously reported GaAs.[22] The conduction band is believed to approximate to -1.6 V vs Ag/AgCl. Based on the band gap of *ca.* 1.4 eV, the valence band of GaAs is *ca.* -0.2 V relative to Ag/AgCl. Taking into account that the potential for water oxidation, E (O_2/H_2O) is about 0.19 V (vs Ag/AgCl) at pH=14,[10, 219] the onset potential should be about -1.2 V (vs Ag/AgCl), which is almost consistent

with our experimental observation. The saturated photocurrent is observed when the bias is above -0.6 V (vs Ag/AgCl), which is due to the increased water oxidation by simultaneously reducing photocorrosion by the Ni-B catalyst. The overall photocurrent density also increases by loading the Ni-B catalyst onto GaAs, resulting in a photocurrent density rising from 10 to 20 mA/cm^2 at -0.6 V (vs Ag/AgCl). Furthermore, the oxygen evolution on both the GaAs and Ni-B/Ga (As)Ox/GaAs photoanodes was analysed at the photocurrent of 20 mA/cm^2, as shown in Figure 5-8c. One can see there is no oxygen gas produced at all on the bare GaAs photoanode. However, linear oxygen evolution is observed with time on the Ni-B/Ga (As)Ox/GaAs photoanode, proving the enhanced photocurrent is due to water oxidation by the Ni-B catalyst. Therefore, I attribute such an enhancement in photocurrent to the catalytic effect of the Ni-B catalyst while loading on GaAs. In addition, the Ni-B catalysts could mitigate hole-electron recombination by acting as a hole-trapping site under sufficient bias applied (above -0.6 V vs Ag/AgCl (pH=14)) to increase charge separation efficiency as proved previously.[121]

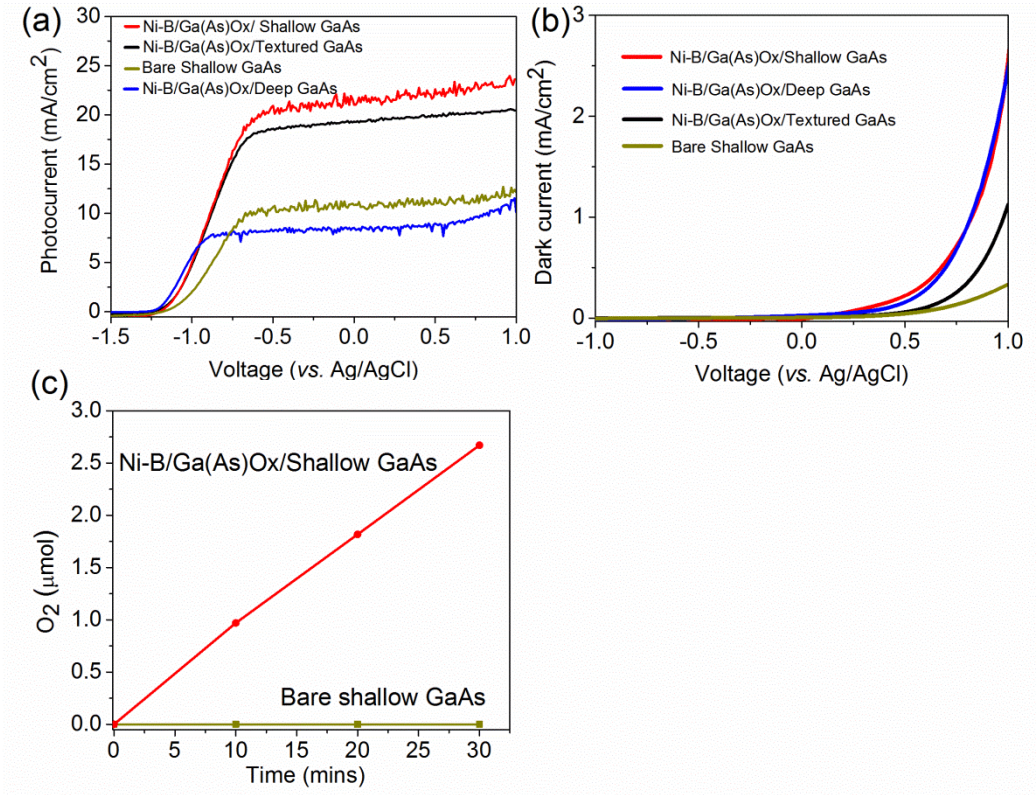

Figure 5-8: Photocurrent (a) and dark current (b) of Ni-B/Ga(As)Ox/GaAs photoelectrodes with 0.5h Ni-B photoassisted electrodeposition and various GaAs surface architecture by using a bare shallow GaAs as a control sample. All photoelectrodes are measured in 0.1M potassium hydroxide electrolyte under one sun illumination (100 mW/cm^2). (c) Time profile of O_2 generation during photoelectrochemical water splitting reaction in a gas-tight three electrodes cell at constantly applied potential of -0.6 vs Ag/AgCl using photoanode of Ni-B/Ga (As)Ox/ Shallow GaAs and bare shallow GaAs (Counter electrode: Pt mesh; Reference electrode: Ag/AgCl; electrolyte: 0.1 M potassium hydroxide; light source: AM 1.5 light irradiation ,100 mW/cm^2).

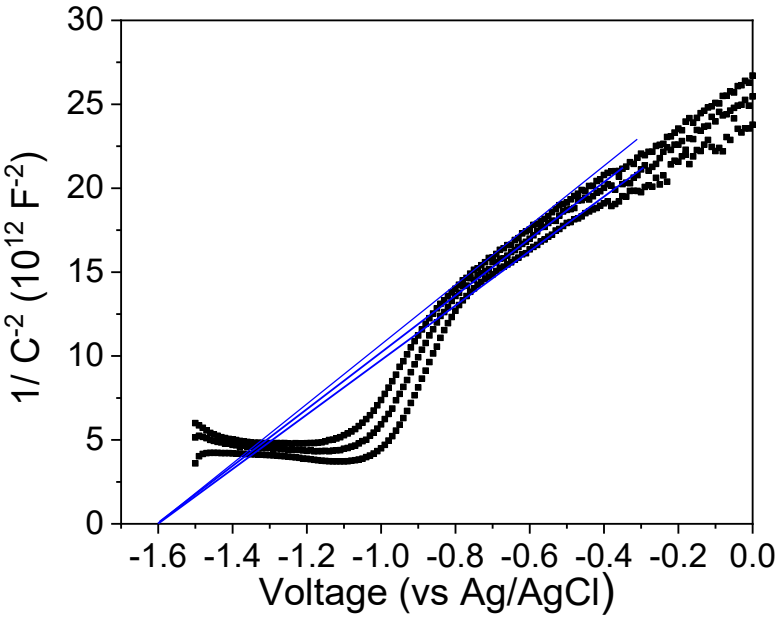

Figure 5-9: Mott–Schottky plots of Ni-B/GaAsOx/shallow GaAs at 500, 1000 and 2000 Hz in 0.1M KOH solution under dark condition.

Furthermore, we optimised the Ni-B/Ga (As)Ox/GaAs electrodes for PEC water oxidation performance based on three factors including 1) GaAs surface architecture; 2) electrolyte pH value; 3) Ni-B surface catalyst deposition time.

(1) <u>Effect of GaAs surface architecture</u>

Surface architecture and roughness of GaAs substrate are believed to affect the loading profile of the catalyst Ni-B, which was then studied by using textured, shallow, and deep GaAs samples. The current-voltage curves in Figure 5-8a show the photocurrent of as-treated GaAs photoanodes with Ni-B loading, which is strongly dependent on surface roughness. The deep GaAs surface likely has a thicker Ni-B/ Ga (As)Ox layer than the textured and shallow GaAs surface while keeping other deposition parameters constant due to the larger surface area generated. The thickness

of Ni-B/Ga (As)Ox monolithic layer deposited on shallow and deep GaAs surface is measured to be 900 nm (Figure 5-7 a) and 1200 nm (Figure 5-10), respectively. Thick Ni-B/Ga (As)Ox layer on the GaAs photoanode surface not only result in light loss due to Ni-B absorption but also a high possibility of charge carrier recombination in the bulk due to the long diffusion length of photo-generated holes to the reaction sites.[23] The deep GaAs surface treated by the mechanical polisher may also have larger surface recombination centres. Consequently, in comparison with Ni-B/Ga (As)Ox/deep GaAs with 0.5 h Ni-B loading by photoelectrochemistry, which exhibits a photocurrent of 8 mA/cm^2 at -0.6 V (vs Ag/AgCl), the photocurrent of Ni-B/Ga(As)Ox/shallow GaAs and Ni-B/Ga(As)Ox/textured GaAs photoanodes increases to 20 mA/cm^2 and 18 mA /cm^2 at -0.6 V (vs Ag/AgCl) under one sun illumination, respectively (Figure 5-8a) . The noisy photocurrent as shown is due to the bubbles generated on electrodes as well as the vigorous stirring during the photocurrent measurements. Because of the high photocurrents achieved on both shallow and textured samples, they were used for the subsequent studies.

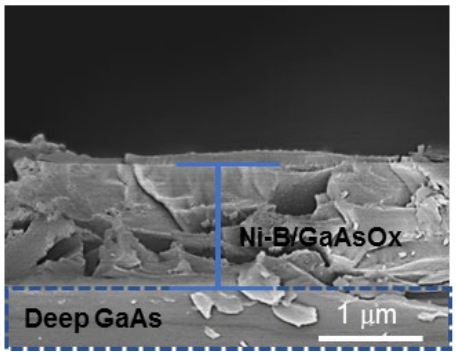

Figure 5-10 : Typical cross-sectional SEM image of Ni-B/Ga (As)Ox/Deep GaAs photoelectrode.

(2) Effect of electrolyte pH value

Next, the effect of electrolyte pH on the PEC activity of Ni-B/Ga (As)Ox/textured GaAs photoanodes was investigated. As shown in Figure 5-11, the photocurrent onset potential shifts to more negative potential (0.059 V per pH unit) while pH value increases. For the Ni-B/Ga (As)Ox/textured GaAs photoanodes measured in 0.1 M potassium borate (pH=9.2), photoinduced holes accumulate rapidly on the surface due to efficient electron-hole separation when applying a bias higher than -0.4 V (vs Ag/AgCl). Whereas there are not enough OH^- groups in the electrolyte to be oxidised by accumulated holes, and thus the surface electron-hole recombination occurs, resulting in a large current drop at high applied bias. This also proves the high efficiency of the catalyst Ni-B for water oxidation in part. When increasing the concentration of OH^- ions in the electrolyte (pH=10.2), no current drop is observed and upon further increasing the pH value to 14, the highest photocurrent of 18mA/cm^2 was obtained. Therefore, the electrolyte was fixed as 0.1 M KOH solution (pH=14) for further PEC measurements.

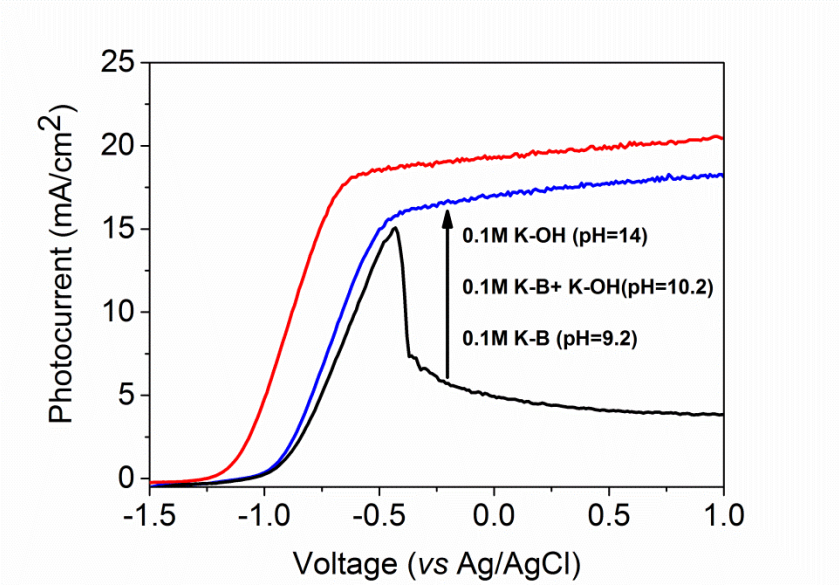

Figure 5-11 : Effect of pH value on current-voltage curve on Ni-B/Ga (As)Ox/ textured GaAs photoanodes with 0.5h Ni-B deposition time.

(3) Effect of Ni-B surface catalyst deposition time.

The loading amount of Ni-B by photoelectrochemisty not only depends on the surface architecture of GaAs electrodes but also the loading time. Since the Ni-B loading amount on GaAs surface dominates the stability and activity of the photoanode, various Ni-B/Ga (As)Ox/GaAs photoanodes were prepared by photoelectrodeposition with the electrolyte, applied potential and light intensity fixed, but varying deposition times from 0 h to 1 h for further study. Figure 5-12 (a) and the insert show the photocurrent and dark current of the Ni-B/Ga (As)Ox/shallow GaAs photoanodes, respectively. The Ni-B/Ga (As)Ox/shallow GaAs photoanode with 1 h Ni-B loading time exhibits the lowest onset potential under dark condition, which is cathodically shifted by about 0.3 V compared to bare shallow GaAs and Ni-B/Ga (As)Ox/shallow GaAs photoanode with 0.5 h Ni-B loading time. This observation proves the excellent catalytic effect of Ni-B with long deposition time. However, this photoanode does not exhibit the highest photocurrent under illumination. According to the Nyquist plots (Figure 5-12 b), the electrodes exhibit semicircles with different radii. The fittings for the semicircles indicate that bare shallow GaAs has an interfacial charge transfer resistance (Rct) of 15 kΩ under light irradiation. The Rct of the Ni-B/Ga (As)Ox/shallow GaAs photoanode with 0.5 h Ni-B loading time is significantly reduced by a factor of 10 (1.5 kΩ) compared to bare shallow GaAs. Hence the charge transfer should be enhanced by Ni-B surface catalyst, which may result in the enhanced hole transfer to surface Ni states. However, while increasing the photo-assisted electrodeposition time to 1 h, dense Ga (As)Ox layer is formatted together with Ni-B deposition on GaAs surface and thus results in increased resistance (4 kΩ). Meanwhile, dense Ga (As)Ox may cause poor light absorption. Therefore, it is crucial to control the

Ni-B photo electrodeposition time. Ni-B/Ga (As)Ox/shallow GaAs photoanode with 0.5 h Ni-B deposition time exhibits a saturated photocurrent of 20 mV/cm^2 at -0.6 V (vs Ag/AgCl), which is two-fold higher than bare shallow GaAs (10 mA/cm^2 at -0.6 V (vs. Ag/AgCl)). I also investigated the current-voltage characteristic of textured GaAs with varying Ni-B photo-assisted electrodeposition time. The photocurrent (Figure 5-13 a) and dark current (Figure 5-13 b) of Ni-B/Ga (As)Ox/textured GaAs exhibits a current-voltage characteristic analogous to Ni-B/Ga(As)Ox/shallow GaAs photoanodes. The Ni-B/Ga (As)Ox/textured GaAs with 1 h Ni-B loading time still shows the lowest onset potential (0.2 V vs Ag/AgCl) under dark condition and the Ni-B/Ga (As)Ox/textured GaAs with 0.5 h Ni-B loading time exhibits the highest photocurrent (18 mA/cm^2 at -0.6 V vs Ag/AgCl). The photocurrent of GaAs photoanodes increases dramatically after Ni-B loading because the Ni-B complex functions as a hole trapping site for in-situ charge separation, thus reducing surface recombination and improving the water oxidation kinetics.[24, 25] During the photoelectrochemical process, the electron-hole pairs generated by the light-absorbing semiconductor are separated by an internal electrical field. Photogenerated electrons move towards to the Pt counter electrode through the external circuit under external bias (for H_2 evolution) and photogenerated holes migrate to the Ni-B surface and oxidise Ni from 2^+ to 3^+, and then O_2 evolution occurs by the withdrawal of electrons from water, accompanied by a change in Ni oxidation state back to 2^+.[121]

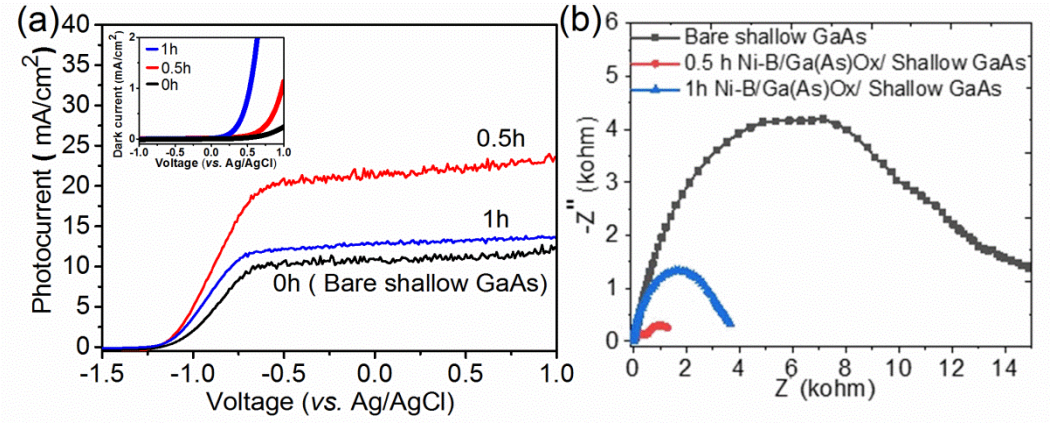

Figure 5-12 : (a) Photocurrent and dark current (Insert) of Ni-B/Ga(As)Ox/shallow GaAs photoanode with varying deposition time; (b) Impedance analysis (Nyquist plots) for bare shallow GaAs and Ni-B/ Ga（As）Ox/Shallow GaAs electrodes; All photoanodes were measured in 0.1M potassium hydroxide (pH=14) under one sun illumination (100 mW/cm^2).

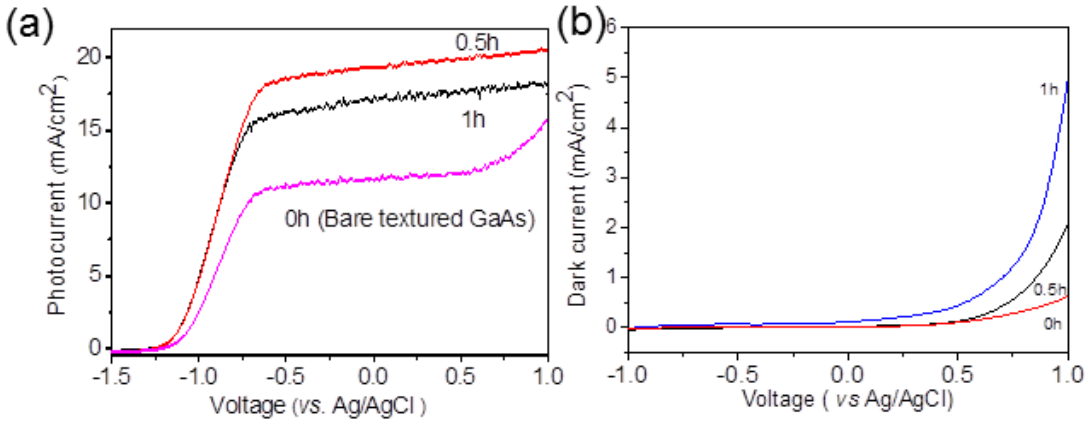

Figure 5-13: (a) Photocurrent and (b) dark current of Ni-B/Ga(As)Ox/textured GaAs photoanode with varying deposition time; All photoanodes were measured in 0.1M potassium hydroxide (pH=14) under one sun illumination (100 mW/cm^2)

Altogether, the Ni-B loading amount, which can be controlled by GaAs surface texture and deposition time by photoassisted electrodeposition, has a significant effect on the PEC performance of Ni-B/Ga (As)Ox/GaAs photoanodes. Therefore, the best performing photoanode with the highest photocurrent is Ni-B/Ga(As)Ox/shallow GaAs with 0.5 h photoelectrochemical Ni-B catalyst deposition, which exhibits a saturated photocurrent of 20 mA/cm^2 at a potential of -0.6 V (vs Ag/AgCl) in 0.1 M KOH

electrolyte under one sun illumination, in comparison these are 6, 18, 8 mA/cm^2 at -0.6 V (vs Ag/AgCl) on the flat, textured and deep GaAs photoanodes, respectively.

The stability of a photoelectrode under prolonged illumination in aqueous solution is one of the major criteria for its commercial application, which is a critical issue for GaAs-based electrodes as discussed in the introduction.[26] Therefore, the stability of both the bare shallow GaAs and Ni-B/Ga(As)Ox/shallow GaAs photoanodes were monitored in 0.1 M potassium hydroxide solution (pH=14) at a constant applied potential of -0.6 V (vs Ag/AgCl) under one sun illumination, see Figure 5-14a. The photocurrent of the bare shallow GaAs photoanode decays very sharply during the first three hours irradiation, resulting in 60 % photocurrent loss caused by the rapid etching of GaAs surface by surface accumulated holes. After that it shows a relatively stable photocurrent of *ca.* 6 mA/cm^2 because of a dense oxide protection layer formed (Figure 5-15b). In contrast, the optimised photoanode of Ni-B/Ga (As)Ox/shallow GaAs with 0.5 h Ni-B deposition time shows excellent stability (zero photocurrent loss within 22 h) when measured in 0.1 M KOH electrolytes with continuous argon purge and electrolyte replacement every 12 hours. It has been reported that glass corrodes in an alkaline solution and the produced contaminants, such as lead and silica, can influence the electrochemical activity on Pt-electrodes.[27] This effect exhibits in gradually decreasing of photocurrent during the first 12 hours, but recovering after the replacement of a fresh electrolyte. To minimise such contamination at the solid-liquid interface, the electrolyte was replaced with a fresh one after 12 hours. The photoelectrochemical stability of Ni-B/Ga(As)Ox/shallow GaAs is comparable with GaAs photoanodes protected by atomic-layer-deposited amorphous TiO_2 in combination with a thin layer of Ni metal surface catalysts, exhibiting a saturated photocurrent of 15 mA/cm^2 with 24 h durability under

identical experimental conditions. The morphology of the obtained GaAs based electrodes after 6 hours PEC reaction was revealed by the SEM images as shown in Figure 5-15. Typically, a 4 μm thick Ga (As)Ox passivation layer is formed on bare shallow GaAs surface due to the photooxidation of GaAs (Figure 5-15b). As expected, after 6 hours PEC reaction, the Ni-B/Ga (As)Ox/shallow GaAs with 0.5 h Ni-B deposition time has the same Ni-B/Ga (As)Ox layer thickness of *ca.* 900 nm as the fresh prepared Ni-B/Ga (As)Ox/shallow GaAs (Figure 5-7a and Figure 5-15a). In addition, as shown in Figure 5-16, the Ni 2p spectra of Ni-B/Ga (As)Ox/shallow GaAs after PEC measurements reveal no apparent changes in chemical states, which is also in good agreement with the previous reported enhanced stability of Ni-B protected ZnO and BiVO4 photoelectrodes.[14, 18]

The Faradic efficiency of O_2 and H_2 generation by employing Ni-B/Ga (As)Ox/Shallow GaAs photoanode together with Pt counter electrode is calculated to be 36 % and 75 %, respectively. In detail, the total running charge during the 30 min photoelectroncatalytic experiment is 9 C for the Ni-B/Ga (As)Ox/Shallow GaAs. The total H_2 gas generated is 35 μmol (Figure 5-17) and thus 6.7 C was used for H_2 generation. Therefore, the Faradic efficiency of H_2 production is 75 %, indicating 25 % of electrons was used to reduce other species, very likely O_2 in this study which was produced by the photoanode as a single compartment cell was used for the gas measurement. Based on O_2 amount generated (2.67 μmol in 30 mins as shown in Figure 5-17) and taking account of the oxygen reduced in the one-compartment cell, the Faradic efficiency of O_2 generation is about 36 %. In comparison, no oxygen was detected at all for bare shallow GaAs photoanode during the identical measurement (Figure 5-8c), which further proves Ni-B surface co-catalyst acts as hole trapping sites on GaAs

surface to promote water oxidation reaction and prevent photocorrosion of the photoanode in part although it is not ideal at present. This low Faradic efficiency of O_2 generation indicates that holes generated by the photocatalytic reaction are partially used for other reactions. One possibility is the oxidation of some organic matters originated from the epoxy resin or its surface.

In contrast, the Faradaic efficiency of O_2 production on bare shallow GaAs photoanode is almost zero during the identical measurement (Figure 5-8c), proving Ni-B surface cocatalyst acts as hole trapping sites on GaAs surface to promote water oxidation reaction and prevent photocorrosion of the photoanode in part although it is not ideal at present, which we believe is due to voids formed in the top Ni-B/Ga(As)Ox layer as shown in Figure 5-7b. However such facile strategy has been successfully demonstrated and the synthesis of a denser top layer free of voids is underway.

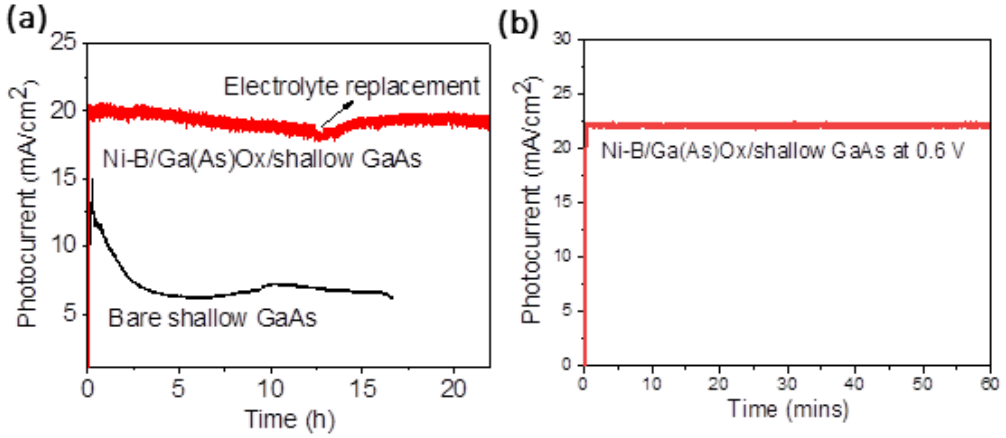

Figure 5-14: Current–time plot of Ni-B/Ga(As)Ox/shallow GaAs with continuous argon purge and electrolyte replacement every 12 hours in 0.1 M potassium hydroxide electrolyte (pH=14): (a) measured in a three-electrode system with a constant applied potential of -0.6 V (vs Ag/AgCl) by using a bare shallow GaAs as a control sample and (b) two-electrode system when the bias is 0.6 V.

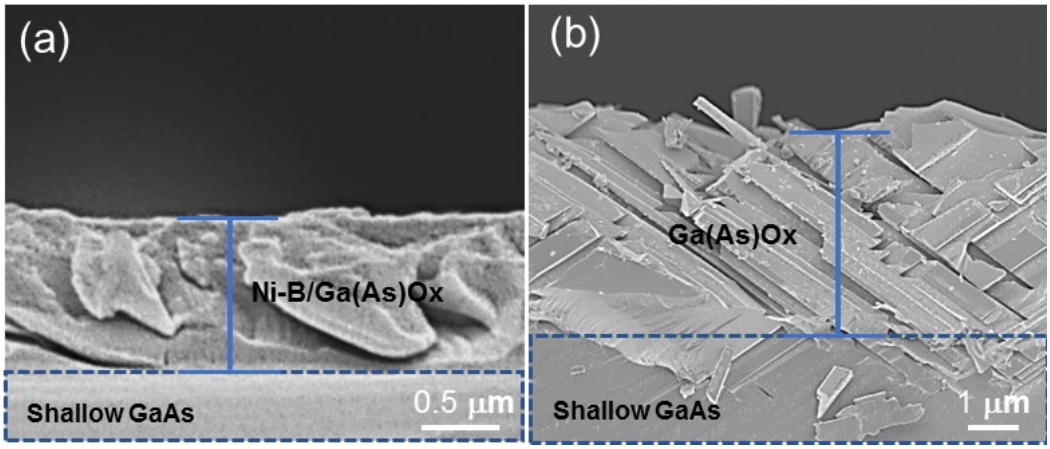

Figure 5-15: Typical cross-sectional morphology of (a) bare shallow GaAs and (b) Ni-B/Ga(As)Ox/shallow GaAs electrodes after 6 h photoelectrochemical water splitting reaction in 0.1 M potassium hydroxide solution under AM 1.5 light irradiation.

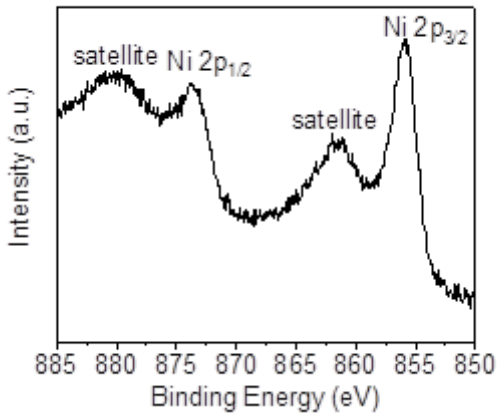

Figure 5-16: *XPS spectra of Ni 2p for Ni-B/Ga (As)Ox shallow GaAs sample with 0.5 h photoassisted electrodeposition after 6 h PEC reaction in 0.1 M potassium hydroxide (pH=14).*

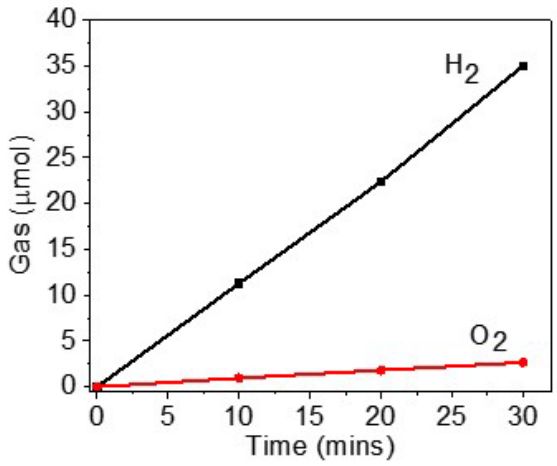

Figure 5-17: Time profile of gas generation (H_2 and O_2) during photoelectrochemical water splitting reaction in a gas-tight three electrodes one-compartment cell at constantly applied potential of -0.6 vs Ag/AgCl (Photoanode: Ni-B/Ga(As)Ox/ Shallow GaAs photoanodes; counter electrode: Pt mesh; Reference electrode: Ag/AgCl; electrolyte: 0.1 M potassium hydroxide; light source: AM 1.5 light irradiation ,100 mW/cm^2). The total running charge during 30 mins photocatalytic experiment was 9 C.

The high activity and stability of Ni-B/Ga (As)Ox/shallow GaAs photoanode is attributed to i) the surface protection layer of Ga (As)Ox, which is deposited in-situ on the GaAs surface during photoassisted electrodeposition of Ni-B and more importantly ii) the efficient catalytic effect of Ni-B for water oxidation. Without Ni-B modification, all holes generated in GaAs are consumed for GaAs oxidation, which is the typical photocorrosion process of GaAs. Whereas surface Ni-B catalysts can efficiently trap the photogenerated holes and speed up water oxidation reaction, and thus suppress the GaAs self-oxidation reaction. The deposited porous Ni-B/Ga (As) layer allows the direct water attack of the substrate, which is the reason why the Faradic efficiency of O_2 production is smaller than H_2. In addition, conducting PEC measurements in potassium hydroxide (KOH) electrolyte not only yields higher photocurrents but also has little effect on the photoelectrode stability. The energy conversion efficiency, i.e., conversion efficiency from incident light energy to stored H_2 chemical energy, was

calculated as *ca.* 15 % based on the observed photocurrent and H_2 faraday efficiency. Furthermore, the photocurrent was measured in a two-electrode system for Ni-B/Ga (As)Ox/shallow GaAs (Figure 5-14 b), indicating its photostability again. These results demonstrate a promising strategy, comprised of the in-situ formation of Ni-B/Ga (As)Ox protection layer on GaAs substrate, which ultimately leads to a stable and efficient photoanode for solar energy conversion.

5.4 Conclusion

Overall, I have demonstrated a novel strategy to achieve a very high and more importantly stable photocurrent by GaAs photoanodes using a reproducible and robust method. The as-prepared photoanodes were characterised by AFM, SEM with EDX mapping, and XPS, which suggested in situ formation of a Ni-B/Ga (As)Ox layer during Ni-B photo-assisted electrodeposition. This Ga (As)Ox acts as a passivation layer which not only prevents the GaAs substrate from photocorrosion in part but also does not block photogenerated hole transfer to the Ni-B surface catalyst. The Ni-B on p-n GaAs substrate plays a key role in reducing the photocorrosion (photooxidation of GaAs) from the continuous operation and enhancing water oxidation kinetics of the surface catalyst. The optimized photoanode with the highest photocurrent is Ni-B/Ga (As)Ox/shallow GaAs with 0.5 h photoassisted electrochemical loaded Ni-B catalyst, which exhibits a saturated photocurrent of 20 mA/cm^2 under one sun illumination compared with 10 mA/cm^2 of bare shallow GaAs photoanode at an identical potential of -0.6 V (vs Ag/AgCl) in 0.1 M KOH electrolyte. In addition, the photocurrent can be maintained for at least 22 hours without decay under continuous operation while the bare GaAs exhibits 60 % photocurrent loss after three hours. Therefore, the current

system demonstrates strong potential for scale-up to produce a device capable of efficient H_2 synthesis and the novel strategy may be applicable to other unstable group III-V based photoelectrodes. To further improve the activity of the classic narrow band photoanode, a more robust and efficient electrocatalyst is desired.

6 Synthesis of Co^{3+} and V^{4+} enriched CoVOx nanorods for efficient and stable water oxidation

6.1 Introduction

As illustrated in Chapter 4 and 5, one can see that the surface OER electrocatalysts play a vital role in the fabrication of not only highly efficient but also quite stable photoanodes for PEC water oxidation reaction. OER electrocatalysts are well-known to accelerate the sluggish kinetics of the electrochemical oxygen evolution reaction by reducing the required overpotentials. Therefore the integration of OER electrocatalysts with semiconductor-based photoabsorbers enables not only the boosting of PEC activity by providing active sites for interfacial reactions with reducing overpotentials, but also improving the PEC stability by rapidly consuming the photogenerated carriers and/or physical separation of semiconductor materials against the electrolyte. Although Ni-B has been demonstrated an effective surface OER catalyst for boosting and stabilizing the ZnO and GaAs photoanodes, the current lifetime and efficiency are still quite limited so far, which means more efficient and robust OER catalysts need to be developed.

State of the art OER catalysts, based on precious metals such as IrO_2 and RuO_2, can perform the OER with an overpotential close to 370 mV at a current density of 10 mA/cm^2.[227] However, the scarcity and cost of those metals limit their large-scale applications. The use of low-cost catalysts, especially the 3d metal (V, Mn, Fe, Co, Ni) compounds, has shown great potential to replace the highly active but scarce noble metal oxides (*e.g.*, IrO_2 and RuO_2).

Cobalt-based electrocatalysts have been studied as promising OER candidates because of their excellent charge transport properties.[228] Previous studies have demonstrated that the proper control of the Co^{3+} amount in the Co_3O_4 could lead to significant modifications on its electrocatalytic properties.[55] Sun et al. found that the surface Co^{3+} species of Co_3O_4 crystal were the active sites of OER,[229] which was further proved by Dai et al. through X-ray absorption near-edge spectrum (XANES) observations.[230] The higher Co^{3+}/Co^{2+} ratio is favourable for creating more targeted $^*OOH$ intermediates, which is beneficial for boosting OER activity.[231] Therefore, diverse approaches were developed to achieve a high concentration of Co^{3+}, such as high-temperature calcination,[232] coatings with an oxidant, meal ion insertion[233], and introducing highly electronegative support.[234] On the other hand, through Ar plasma[55] or $NaBH_4$[235] solution treatment, the lower atomic ratio of Co^{3+}/Co^{2+} in Co_3O_4 could be achieved, which was believed to be indicative of relatively more oxygen vacancies.[236] These oxygen vacancies near the Co^{3+} could improve electronic conductivity and facilitate adsorption of H_2O onto nearby Co^{3+} sites.[236]

To understand the two conflicting conclusions, this work attempted to manipulate the Co^{3+}/Co^{2+} ratio on the surface of cobalt oxides while more or less maintaining the level of oxygen vacancies. To date, tuning the surface Co^{3+}/Co^{2+} ratio or electronic structure through doping other transition-metal elements such as Ni, Fe, Mo, Mn, Zn and, Al, into cobalt based material to form bimetallic oxide/hydroxide catalyst has proved to be an effective way for efficient water splitting.[237, 238] In particular, Yan et al. found that Co^{3+}/Co^{2+} ratio of $Co_{3-x}Al_xO_4$ could be controlled by varying Al^{3+} dopant concentration[239] and Xing et al. reported the high stability of zinc-doped $NiCo_2O_4$ electrode resulted from the stabilisation of Co^{3+} in the presence of Zn.[240] Moreover,

vanadium (V^{3+} and V^{4+}) dopant level has been shown to have a substantial effect on Fe^{3+}/Fe^{2+} ratio in the magnetite for water gas shift reaction,[241] and very recently Sun et al has proved that vanadium incorporation into iron oxyhydroxide could effectively lower the overpotential of water oxidation due to the excellent conductivity, facile electron transfer and abundant active sites of oxyhydroxide.[242]

Inspired by these findings, for the first time, a reproducible strategy of incorporating vanadium into CoOx nanorods and subsequent rapid heat treatment to produce high concentration of Co^{3+} and V^{4+} in the CoVOx nanorod catalysts (noted as CoVOx-300) was reported herein. In combination with various characterisations, the synergistic effect between Co^{3+} and V^{4+} for efficient water oxidation was discovered, which was achieved by controlling the ratio of V^{4+} to V^{5+} on CoVOx-300 surface, leading to 20 times higher current than CoOx-300 without V^{4+} at the identical overpotential of 0.38 V. Such understanding of the structure-activity relationship for electrocatalytic reactions demonstrated on CoVOx-based catalysts could be applied to other candidate electrocatalysts.

6.2 Experimental section

6.2.1 Preparation of electrocatalysts

A one-step hydrothermal method was employed to synthesise the CoVOx, CoOx and VOx. In brief, the solution with different Co/V mole ratios (1:0, 5:1, 3:1, 1:1, 1:3 and 0:1) was obtained by mixing $CoCl_2$ and VCl_3 in 40 ml H_2O, while the total amount of metal ions (Co^{2+}+V^{3+}) was kept to 1.6 mmol. Afterwards, 0.15 g of urea was added and the above mixture solution was transferred to an 80ml stainless-steel Teflon-lined

autoclave and heated in an oven at 120 ℃ for 12 h. After cooling the autoclave to room temperature, the resulting powder was washed by deionised water and ethanol three times, collected and then freeze-dried overnight. The obtained materials were evaluated for OER on a glassy carbon electrode firstly to find out the optimised composition. The optimised CoVOx catalyst (Co:V=3:1) was further treated in a muffle furnace with an air atmosphere at 300 ℃ for 5 mins, 600 ℃ for 5 mins or 300℃ for 2 hours, noted as CoVOx-300, CoVOx-600 or CoVOx-300-2h, respectively. The control samples (CoOx or VOx) after rapid heat treatment at 300℃ for 5 mins were noted as CoOx-300 or VOx-300.

6.2.2 Electrode preparation

5 mg of the obtained powders were dispersed in the mixture solution of 1 ml H_2O, 250 ul 2-propanol and 10 ul 5 % Nafion by sonication for 1 h. The 2.5 ul of the above suspension was uniformly drop-casted to a pre-polished GC electrode (diameter: 3 mm) with the loading of ~0.14 mg cm^{-2} and dried under an infrared lamp for 5 mins to evaporate the solvent.

6.2.3 Structure and surface characterisation

X-ray diffraction (XRD) measurements were carried out on Bruker X-ray diffraction diffractometer with Mo Kα radiation (wavelength = 0.7093 Å). Mo X-ray radiation was used instead of the more common Cu X-ray radiation to avoid fluorescence from Co in the sample. Raman spectra were recorded on a Horiba Raman spectrometer in a back scattered confocal configuration using 543 nm laser excitation.

Transmission electron microscope (TEM) images were taken on JEOL JEM2100 TEM with an Oxford instrument EDX detector and scanning electron microscopy (SEM) images were obtained by a field-emission JSM-7800F microscope. X-ray photoelectron spectroscopy (XPS) measurements were conducted by using a Thermo Scientific K-alpha photoelectron spectrometer with monochromatic $Al_{K\alpha}$ radiation; peak positions were calibrated to carbon (284.6 eV) and plotted with the XPS peak software. H_2-TPR was carried out with a Micromeritics AutoChem II 2920 System. 0.02 g sample was loaded in a quartz reactor, heated in He flow at 150℃ for one hour with a ramp of 10 ℃ min^{-1}, and then cooled down to 25 °C. The reactor was flushed with 10 % H_2/He to reach a stable background. The consumption of H_2 was carried out from 80 °C to 800 °C at a ramp of 10 °C pre mins.

6.2.4 Electrochemical measurements

The OER activity and stability were measured by liner scan voltammetry (LSV) and chronopotentiometry using a Metrohrm Autolab potentiostat in a polytetrafluoroethylene cell with a standard three-electrode configuration, which was composed of working electrode (samples deposited on Glassy carbon (GC) electrodes), a counter electrode (Pt sheet) and a reference electrode (Ag/AgCl). The GC ramping rate is 1600 rpm. The electrolyte was 1 M KOH, and the applied potentials were converted to the reversible hydrogen electrode (RHE) by using the following equation 3-8.

Before all the electrochemical measurements, a cyclic voltammetry (CV) activation scan from 0.2 to -0.8 V (vs Ag/AgCl with a scan rate of 10mV/s in O_2 saturated 1 M

KOH solution) was performed until stable. Then LSV were measured from 0.2 to 0.7 V versus Ag/AgCl with a slow scan rate of 2 mV/s in 1M KOH. By plotting overpotential Z against log (J) from LSV curves, Tafel slopes can be obtained. The electrochemical impedance spectroscopy (EIS) data were carried out through the same electrochemical measurement system at applied bias of 0.58 V (vs RHE) in 1 M potassium hydroxide solution with a frequency range of 100,000 and 0.1 Hz of a sinusoidal perturbation with 10 mV amplitude. The resistivity of the solution was determined using the iR compensation feature of the epsilon software and all currents presented were corrected against the ohmic potential drop according to equation 6-1.

$$E_{RHE} = E_{Ag/AgCl} + 0.197 + 0.059 \times pH - iR \qquad \text{Equation 6-1}$$

6.3 Results and Discussion

6.3.1 Structure of CoVOx catalysts

The hydrothermal synthesis was used to produce CoOx, VO_x and CoVOx catalysts. The as-synthesized samples were further processed by rapid heat treatment in air at 300 ℃ for 5 mins, and these were noted as CoOx-300, VOx-300 and CoVOx-300, respectively. The composition and crystallinity of all the samples were analysed by XRD (Figure 6-1 and 6-2). As shown in Figure 6-1a, all the diffraction peaks of the three samples of CoOx, CoVOx and CoVOx-300 can be well indexed to a pure cobalt hydroxide carbonate phase with orthorhombic structure ($Co_2(OH)_2CO_3$, JSPDS 48-0083).[243] In comparison with CoVOx-300, the cobalt phases of CoOx-300 is partially crystallised to cubic-phase spinel Co_3O_4 (JCPDS card no.43-1003),[244] which results in a mixed cobalt phase ($Co_2(OH)_2CO_3$ and Co_3O_4). This suggests the strong interaction between cobalt and vanadium suppresses structure change of CoVOx, and thus CoVOx-

300 could preserve the crystal orthorhombic structure. The diffraction peaks of VOx and VOx-300 can be assigned to $VO(OH)_2$ (JCPDS 11-0209) and V_2O_5 (JCPDS card no. 001-0359), respectively, according to previous literature (Figure 6-2a).[69] Noticed that no VOx species could be identified in the sample of CoVOx and CoVOx-300, suggesting the possibilities that vanadium incorporation into CoVOx or CoVOx-300. Furthermore, the enlarged XRD patterns of the above samples (Figure 6-1b) show that there is a slight shift in (231) diffraction peak toward lower two-theta value when introducing vanadium into CoOx lattice as vanadium ions have a larger diameter than cobalt ions. The shift is much more apparent when comparing CoVOx-300 and CoOx-300, which indicates that the rapid heat treatment somehow promotes the vanadium incorporation. However, upon the heat treatment of CoVOx sample at either high temperature for a short period (600 °C/5mins) or low temperature for an extended period (300 °C/2 h), the CoVOx samples were oxidized to cubic-phase spinel Co_3O_4 (JCPDS card no.43-1003),[244] which were noted as CoVOx-600 and CoVOx-300 (2h) in Figure 6-2b, respectively.

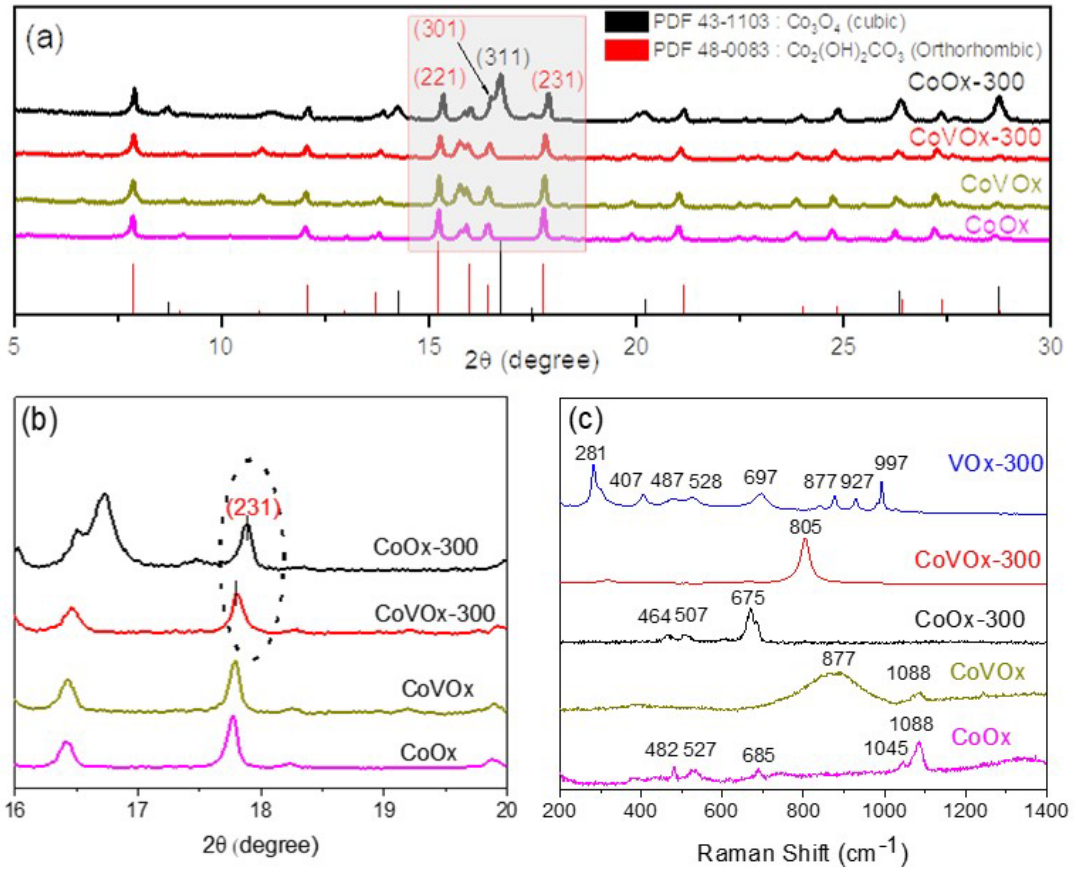

Figure 6-1: (a) XRD patterns of CoOx, CoVOx, CoOx-300 and CoVOx-300 with standard JCPDS card number 48-0083 and 43-1003; (b) Enlarged view of the corresponding XRD patterns at the range of 2θ between 16 and 20 degree; (c) Raman spectra of CoOx, CoVOx, VOx-300, CoOx-300 and CoVOx-300.

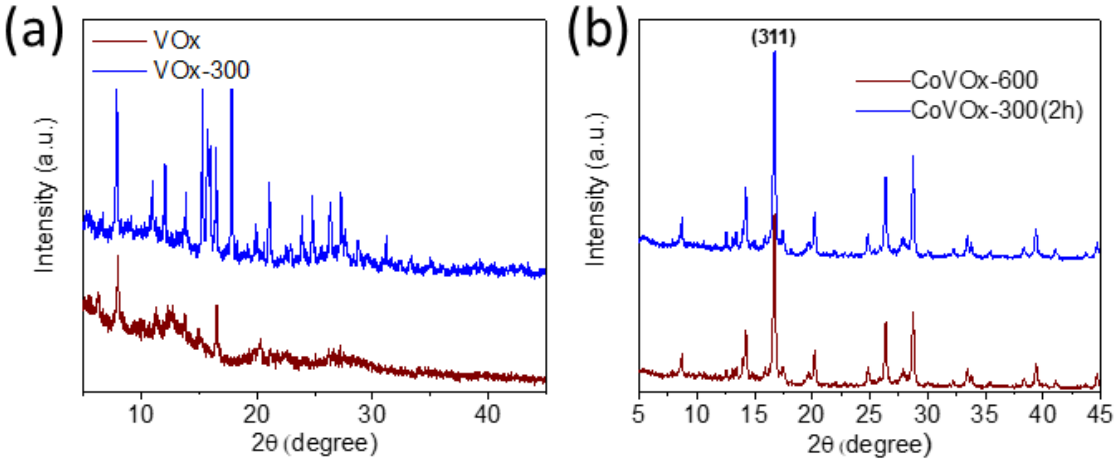

Figure 6-2: XRD pattern of (a) VOx and VOx-300 samples; (b) CoVOx with heat treatment at 600°Cfor 5mins (CoVOx-600) or 300°Cfor 2h (CoVOx-300 (2h)).

Figure 6-1c shows Raman spectra of CoOx, CoVOx, VOx, CoOx-300 and CoVOx-300 and VOx-300. CoOx sample can be identified as cobalt hydroxy carbonate in the 800 –1400 cm^{-1} region, which is characterised by an intense sharp peak at 1088 cm^{-1}. This band is assigned to the ν_1 CO_3^{2-} symmetric stretching mode. The shoulder at 1045 cm^{-1} is assigned to a hydroxyl deformation mode.[245] Other Raman bands observed at 482, 527 and 685 are attributed to Co-O Eg, F_{2g} and A_{1g} variation modes, respectively. Whereas, upon rapid heat treatment at 300 °C for 5 min, CoOx-300 exhibits four characteristic peaks located at 464, 507, 606, and 675 cm^{-1}, which correspond to E_g, F_{2g}^1, F_{2g}^2, and A_g^1 modes of the Co_3O_4 crystal.[246] VOx-300 exhibits four distinct peaks located at 281,407,697 and 997 cm^{-1}, similar to the characteristic peaks of reported lepidocrocite VOOH sphere.[247] In detail, the first two peak at 281 and 407 cm^{-1} are assigned to the bending vibration of the V = O bonds.[248] The peak at 697 cm^{-1} is assigned to the doubly coordinated oxygen (V_2–O) stretching mode, which results from corner-shared oxygens.[248] The relative sharp peak at 997 cm^{-1} corresponds to the stretching mode of vanadyl oxygen (V-O).[248] The two weak peaks at 487 and 528 cm^{-1} are assigned to the bending vibrations of bridging V-O-V (double coordinated oxygen) and triple coordinated oxygen (**V_3**–O) stretching mode, respectively.[248] Also, there is a peak at 927 cm^{-1}, which can be assigned to V^{4+}= O bond.[249] The peak at 877 cm^{-1} is assigned to the ν_1 symmetric stretching mode of VO_4.[250] The CoVOx sample preserves the ν_1 CO_3^{2-} symmetric stretching mode at 1088 cm^{-1} and exhibits a broad peak centred at 877 cm^{-1}, which could be tentatively explained in terms of stretching mode of VO_4 tetrahedral with A_1. The cobalt cations may be bonded with each oxygen atom of a VO_4 tetrahedral to form Co-O-V-O species. This may introduce some asymmetry in the VO_4 unit without disturbing the overall cubic symmetry of the

elementary unit cell.[251] Similar features of Raman modes are observed on reported $LiCoVO_4$.[251] However, Raman bands corresponding to either V-O or Co-O vibration modes are not observed in CoVOx-300 sample. The sharp peak at 805 cm^{-1} situated between Co-O A_g^1 (675 cm^{-1}) and VO_4 A1 mode, is very likely due to the variation mode of Co-O-V. Further, the strong peak at 1088 cm^{-1} disappears due to the decomposition of carbonates after rapid heat treatment. The Raman result indicates the rapid heat treatment not only increases the crystallinity of the CoVOx but also induce strong interaction between Co and V through oxo-bridge. Co-O-V species, probably due to the intense interaction between cobalt and vanadium, supported by the H_2- TPR profile (Figure 6-3), which was used to observe the reducibility of catalysts. There are three peaks (at 320, 390, and 415℃) in the H_2-TPR profile of CoOx-300. The first peak at 320 ℃ can be assigned to the transformation from the $Co_2(OH)_2CO_3$ phase to Co_3O_4.[252] This further reveals the existence of mixed cobalt phases in CoOx-300, as detected by XRD. The second at 390 ℃ is due to the Co_3O_4 to CoO (Co^{2+}),[252] and the third at 415 ℃ is attributed to the reduction of CoO to Co metal (Co^0).[252] The H_2-TPR profile of the VOx-300 catalyst entails a single reduction peak with the maximum at 560 ℃ due to the reduction of V^{5+}/ V^{4+} to V^{3+} in the bulk of VOx-300.[253] The CoVOx-300 TPR shows all typical reduction peaks Co^{3+} to Co metal and V^{5+}/V^{4+} to V^{3+}, while both cobalt and vanadium ions reduction peaks shift to higher temperature except the transformation of $Co_2(OH)_2CO_3$) to Co_3O_4. In other words, the cobalt and vanadium ions are extremely difficult to reduce in CoVOx-300 sample, indicating that Co^{3+} is dominated after V doping and strong interaction between cobalt and vanadium ions .[254]

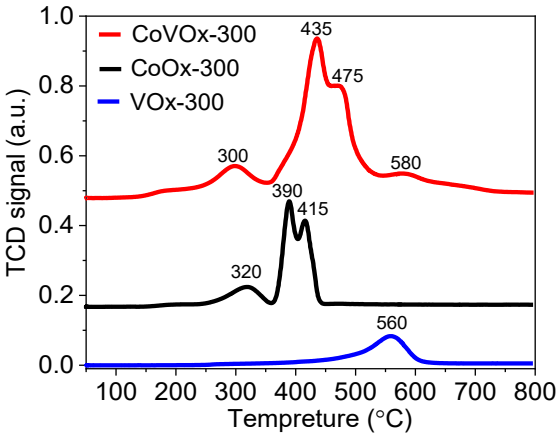

Figure 6-3: H_2-TPR profile of CoOx-300, VOx-300 and CoVOx-300.

6.3.2 Surface composition analysis of CoVOx catalysts

X-ray photoelectron spectroscopy (XPS) was used to analyse the electronic structure and the surface composition of the constituents. The core level spectra of the two samples before rapid heat treatment (CoOx and CoVOx) show only the characteristic peak of Co^{2+} at a binding energy of 781.2 eV (Figure 6-4 a and b). After rapid heat treatment, both CoOx-300 and CoVOx-300 display two major peaks with binding energy at 779.5 and 781.2 eV corresponding to Co^{3+} and Co^{2+}, respectively (Figure 6-5 a and c), suggesting the coexistence of Co^{3+} and Co^{2+}.[237, 255] It should be noted that the surface atomic ratio of Co^{3+}/Co^{2+} for CoOx-300 is 0.4. The Co^{3+}/Co^{2+} ratio is further increased to 1.4 after *in-situ* electrochemical activation (Figure 6-5c). To investigate the effect of V in CoVOx-300 sample, the XPS spectra of V 2p 3/2 for as-prepared and after *in-situ* electrochemical activation CoVOx-300 samples are compared (Figure 6-5d). The as-prepared CoVOx-300 exhibit two characteristic peaks corresponding to V^{5+} (516.7 eV) and V^{4+}(515.8eV),[256] respectively, with a V^{4+}/V^{5+} ratio of 0.7. The V^{4+}/V^{5+} ratio is increased from 0.7 to 1.7 after *in-situ* electrochemical activation. The increased Co^{3+}/Co^{2+} well matches with the decreased V^{5+}/V^{4+},

suggesting that the valance states of surface vanadium species in CoVOx-300 play a key role for manipulating the surface Co^{3+}/Co^{2+} ratio. Therefore, one can conclude that the higher ratio of V^{4+}/V^{5+} is favourable for a higher concentration of Co^{3+} and consequently only Co^{2+} is observed when the V^{4+}/V^{5+} ratio is as low as 0.3 for CoVOx (Figure 6-4).

Moreover, the XPS depth profile analysis of the surface and bulk (50 nm) composition of CoVOx-300 presents that the ratio of Co^{3+}/Co^{2+} varying from 1.0 on the surface to 0.6 in bulk, which indicates a Co^{3+} enriched surface for CoVOx-300 (Figure 6-6). Frost et al. have shown that high spin cobalt(II) compounds have intense satellite bands associated with both these lines, while satellite lines for the low spin cobalt(III) compounds are either weak or missing.[257, 258] As shown in Figure 6-7, much weaker satellite bands appear in the Co 2p spectra on the surface compared to the bulk, further indicating that the high concentration of low spin Co^{3+} on the surface and high spin Co^{2+} in bulk, respectively. In the V 2p 3/2 spectra, V^{5+} (516.7 eV) and V^{4+}(515.8 eV) coexist on the surface , whereas V^{3+} (514.4 eV) and V^{4+} (515.8 eV) coexist in bulk (Figure 6-6b), suggesting that the vanadium ions were partially oxidized to $V^{4+}$and V^{5+}on surface when rapid treatment at 300 °C.[256]

Furthermore, it was found that the Co/V ratio changes from 2.9 on CoVOx-300 surface to 4.5 in bulk referring to the XPS survey spectra (Figure 6-8), which means that vanadium atoms are extremely rich on the surface of CoVOx-300. Such V^{4+}/V^{5+} rich surface guarantees the high concertation of Co^{3+} on the surface, which would boost OER activity.[259] The O1s core level spectra of CoVOx-300 could be fitted and deconvoluted into four characteristic peaks of oxygen atoms bound to metals (529.5 eV for O1), defect sites (531.1 eV for O2), hydroxyl species (532.0 eV for O3) and

absorbed molecular water (533.0 eV for O4).[236] Of note, the same level of defect sites or oxygen vacancies was observed on CoVOx-300, CoOx-300 and CoVOx (Figure 6-9).

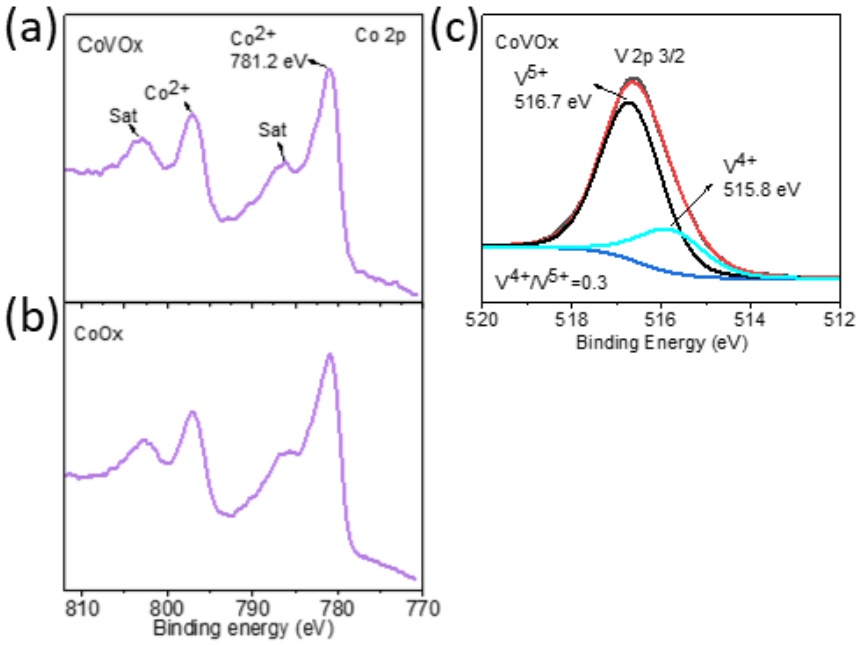

Figure 6-4: XPS spectra for (a) Co 2p of CoVOx; (b) Co 2p of CoOx and (c) V 2p 3/2 of CoVOx.

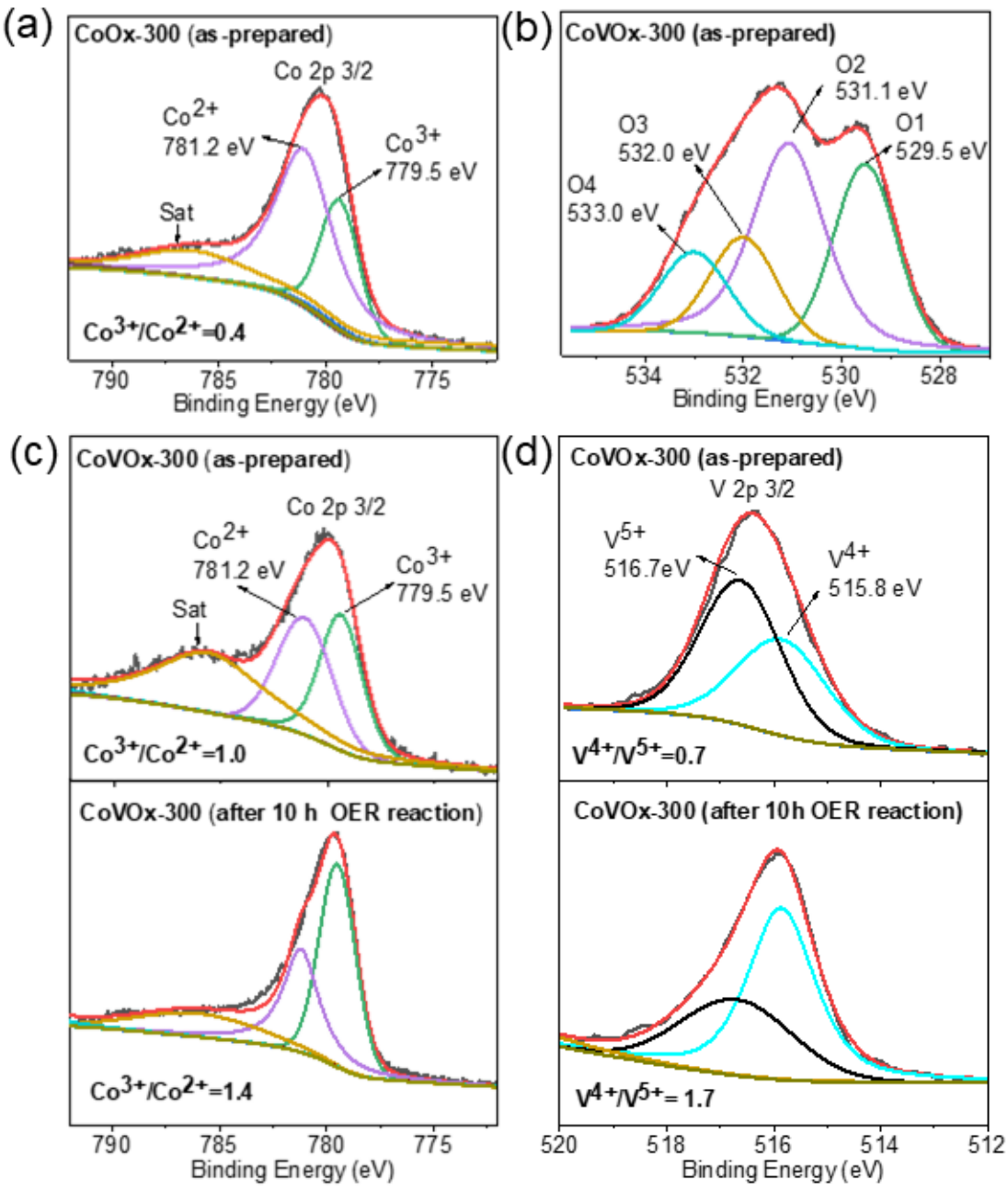

Figure 6-5: (a): XPS spectra of Co 2p 3/2 for CoOx-300; (b-d) XPS spectra of CoVOx-300: (b) O1s; (c) Co 2p 3/2 for the as-prepared samples and after activation; (d) V 2p 3/2 for the as-prepared samples and after activation. O1, O2, O3 and O4 corresponds to the oxygen atoms bound to metals (529.5 eV), defect sites (531.1 eV), hydroxyl species (532.0 eV) and absorbed molecular water (533.0 eV), respectively.

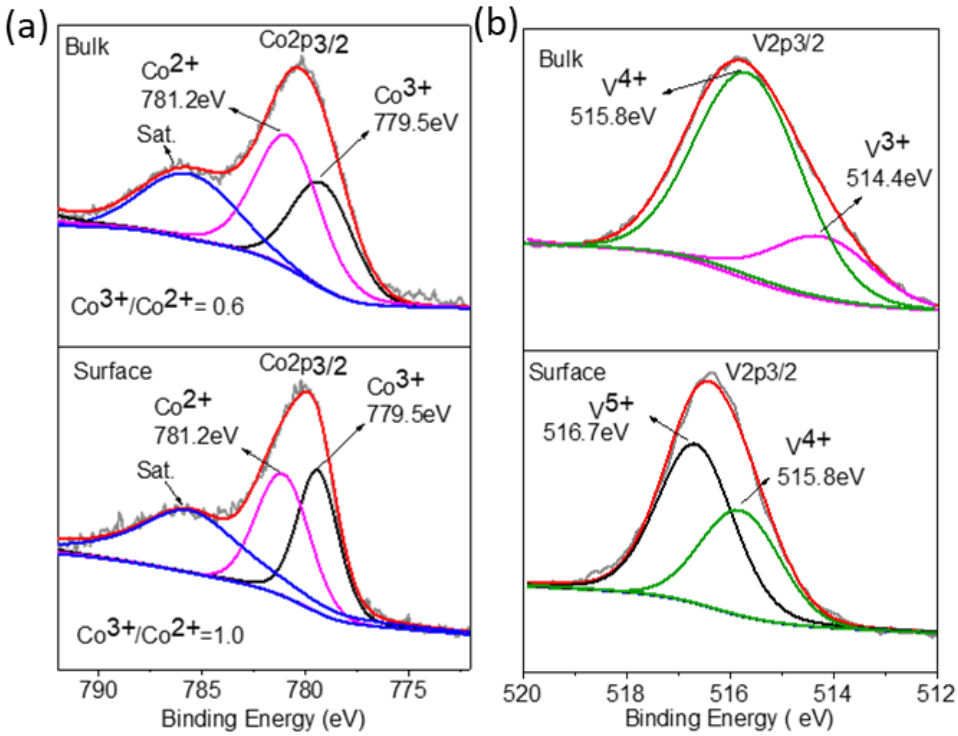

Figure 6-6 : XPS depth profile analysis of surface and bulk (50 nm) composition of CoVOx-300 for (a) Co 2p 3/2 and (b) V 2p 3/2.

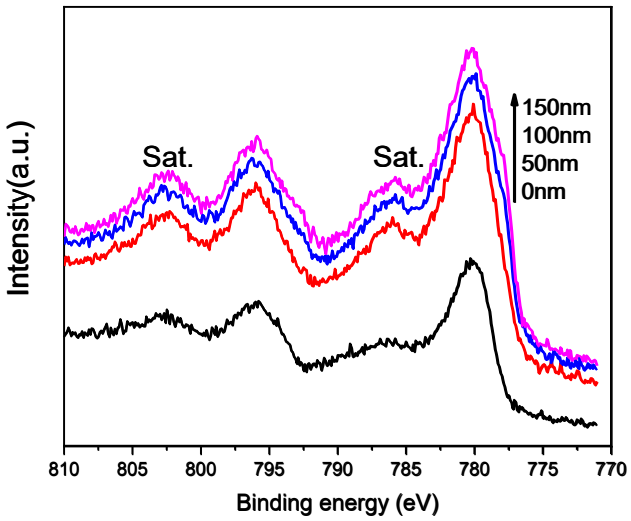

Figure 6-7: Depth profile XPS spectra from the surface to bulk of Co 2p for CoVOx-300 catalyst.

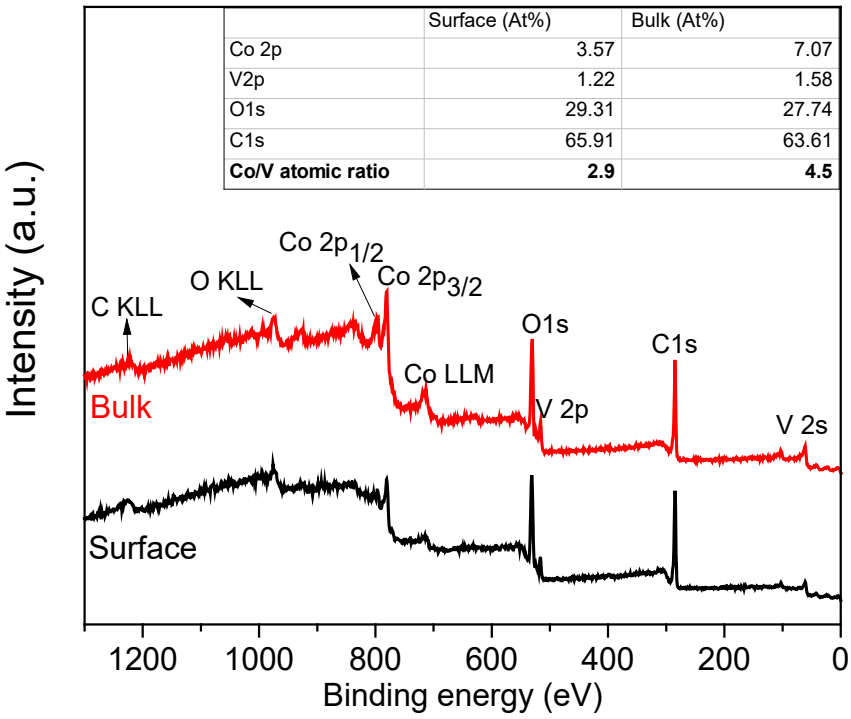

Figure 6-8: XPS survey spectra of surface and bulk (50 nm) forCoVOx-300.

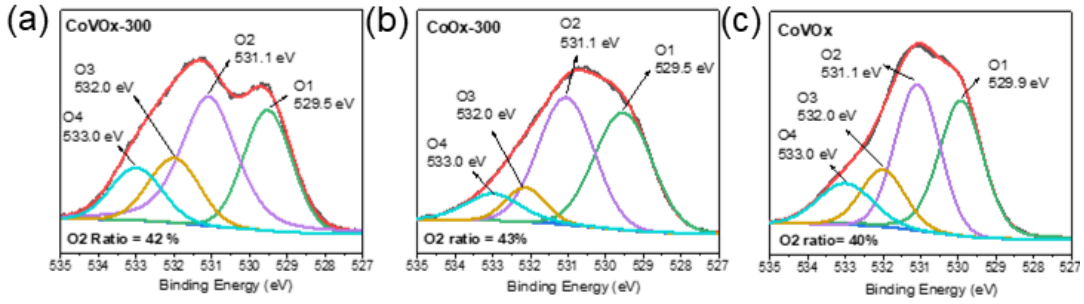

Figure 6-9: XPS spectra of O 1s for CoVOx-300, CoOx-300 and CoVOx. O1, O2, O3 and O4 corresponds to the oxygen atoms bound to metals (529.5 eV), oxygen vacancy sites (531.1 eV), hydroxyl species (532.0 eV) and absorbed molecular water (533.0 eV), respectively.

6.3.3 Morphology of CoVOx catalysts

Typical scanning electron microscopy (SEM) and transmission electron microscopy (TEM) of the CoVOx-300 show nanorod morphology of CoVOx-300 sample (Figure 6-10). The average diameter of the nanorods is measured to be 80 nm from the TEM image and the cobalt and vanadium species are uniformly distributed over the entire catalyst according to the corresponding EDX elemental mapping images.

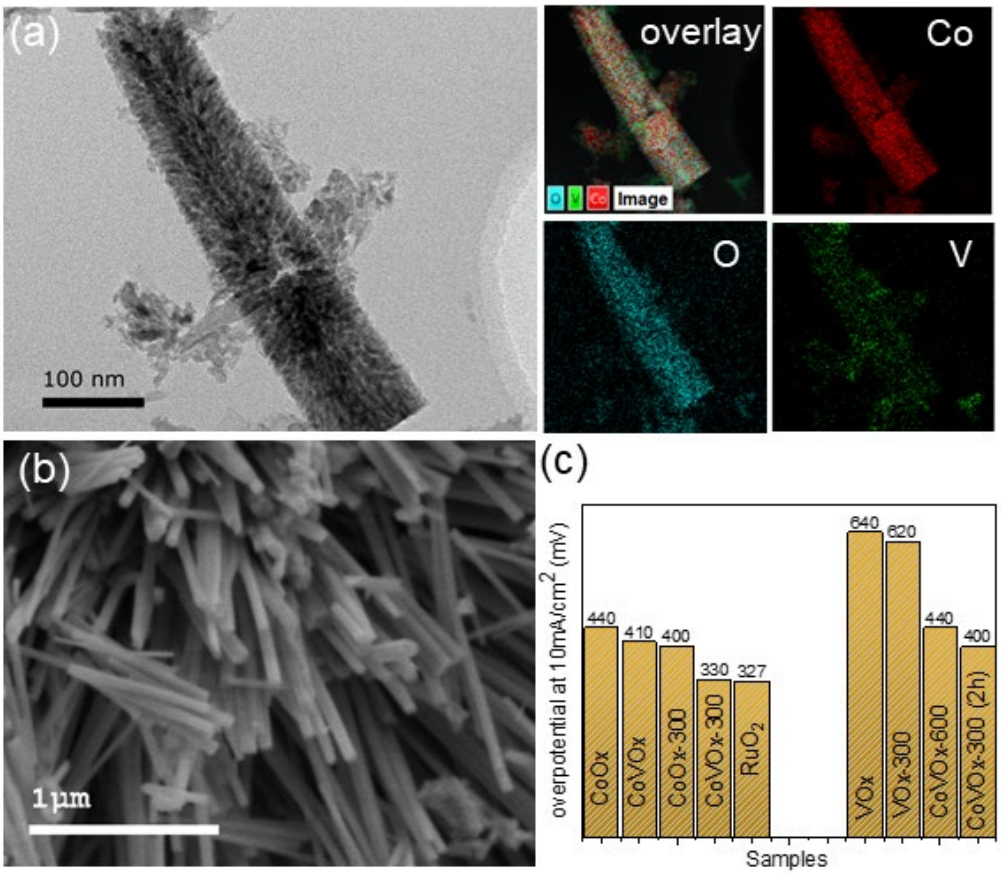

Figure 6-10: (a): Typical TEM images of CoVOx-300 and the corresponding EDX elemental mapping of cobalt, vanadium and oxygen; (b): Typical SEM image of CoVOx-300 nanorods; (c) The overpotential graph of all studied catalysts.

6.3.4 Electrochemical characterisation and activity measurements

The water oxidation activities of CoVOx prepared with different molar ratios (5:1, 3:1, 1:1, 1:3 and 1:5) of cobalt and vanadium in the precursors were assessed in O_2-saturate 1M KOH on a glassy carbon electrode (see experimental details). All the measurements were carried out with ohmic-drop correction and all the amount of the catalyst loadings on GC electrodes were identical at 0.14 mg cm^{-2} for comparison. The electrocatalytic activities are strongly related to the Co/V ratio in CoVOx and increasing Co or decreasing V in the precursors leads to an increase of current (Figure 6-11a). The best water oxidation performance has been achieved when the molar ratio of Co/V is 3:1. Further increasing the Co reduces the performance likely due to the reduced synergy between Co and V effects. Of note, the influence of the cobalt precursors on the electrocatalytic activity of the CoVOx catalysts with the optimum ratio of Co to V is relatively small (Figure 6-11b) and $CoCl_2$ was employed in our subsequent studies as it is the best one. The CoVOx (molar ratio of Co/V = 3/1) exhibits a relatively good performance for OER with the overpotential of 410 mV at current density of 10 mA/cm^2 (η_{10} = 410 mV), while the bare VOx (η_{10} = 640 mV) and CoOx (η_{10} = 440 mV) display poor performance for OER in Figure 6-11c and 6-12a, respectively, which is attributed to the synergy between Co and V ions. Interestingly, electrocatalytic activity of both CoVOx and CoOx can be dramatically enhanced by rapid heat treatment in air at 300 ^{0}C for 5 mins (noted as CoVOx-300 and CoOx-300 in Figure 6-12a). The CoOx-300 catalyst requires an overpotential of 400 mV at j =10 mA/cm^2 while it is 330 mV for CoVOx-300 due to increasing Co^{3+} in the two samples (Figure 6-12f), which is also considerably smaller than 410 mV for untreated CoVOx and 620 mV for VOx-300 (Figure 6-12a and 6-11c). Furthermore, it is found that to

control the temperature and time is important during the heat treatment of CoVOx. Either rapid heat treatment at 600 ^{0}C for 5mins (CoVOx-600) or annealing at 300 ^{0}C for 2 hours (CoVOx-300-2h) would dramatically decrease the catalytic activity and the required overpotentials are 425 mV and 385 mV to drive current of 10 mA/cm^2, respectively (Figure 6-11d). This may be attributed to the phase change from CoVOx hydroxide to Co_3O_4, supported by the XRD pattern in Figure 6-2. Previous studies have concluded that oxygen electrocatalysis on meal oxides began with protonation of the surface metal centres to form M-OH.[260-262] The higher performance of CoVOx-300 than both CoVOx-600 and CoVOx-300-2 h could possibly due to the fast OER kinetics of M-OH than M-O.[263] The lowest η value at 10 mA/cm^2 (η_{10} = 330 mV) highlights the high OER catalytic activity of CoVOx-300, which is comparable with the commercial RuO_2 (Figure 6-12a) and superior to other six cobalt/vanadium based catalysts investigated here (Figure 6-10c). Additionally, the overpotential for CoVOx-300 is smaller than other cobalt-based catalysts reported, such as $Co_2V_2O_7$ (η_{10} = 340 mV),[264] $Co_3V_2O_8$ (η_{10} = 359 mV),[265] $Co_3V_2O_8$ nanoroses (η_{10} = 391 mV),[266] and recently reported amorphous CoVOx (η_{10} = 347 mV)[65] tested on a flat glassy carbon electrode in 1M KOH electrolyte.

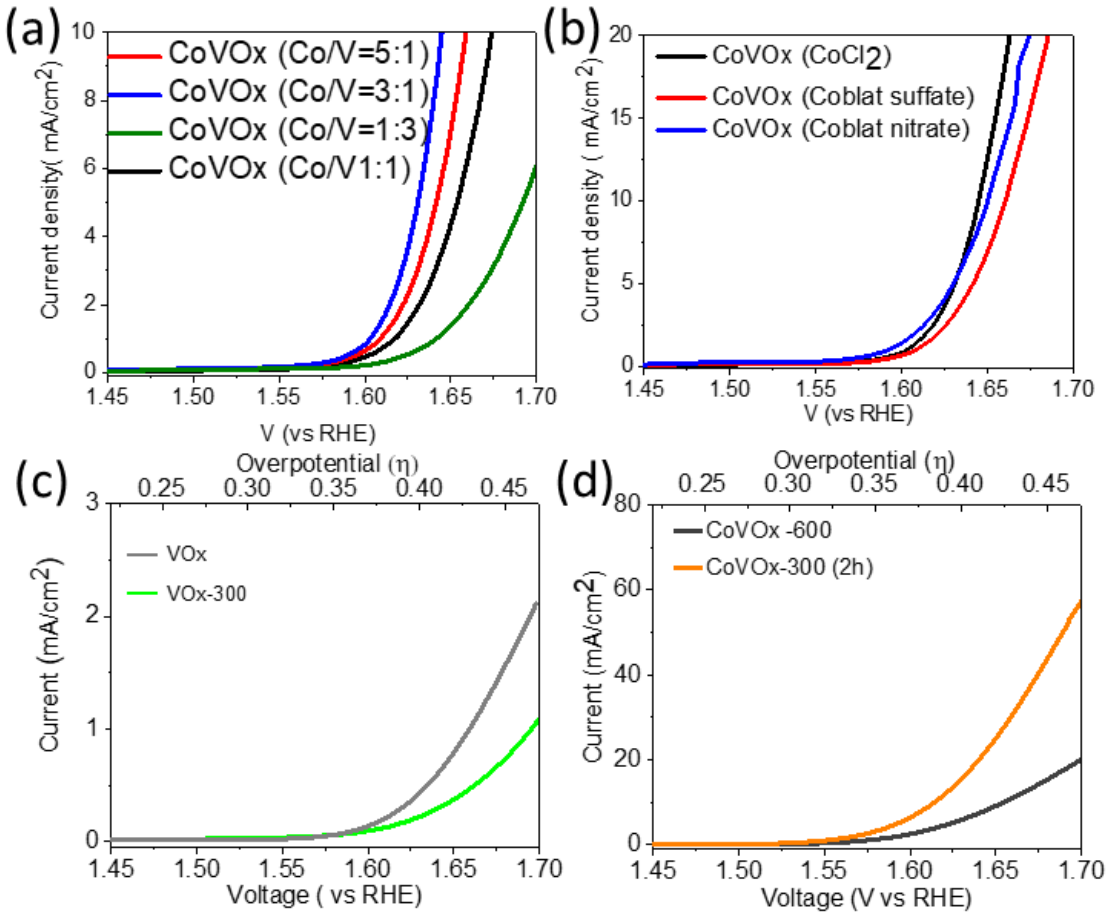

Figure 6-11: LSV curves of (a) CoVOx with different Co/V molar ratio; (b) CoVOx with optimized Co/V ratio (3:1) synthesized with different cobalt precursor; (c)LSV curves of VOx and VOx-300 catalysts; ;(d) CoVOx (Co:V=3:1) with different heat treatment conditions.

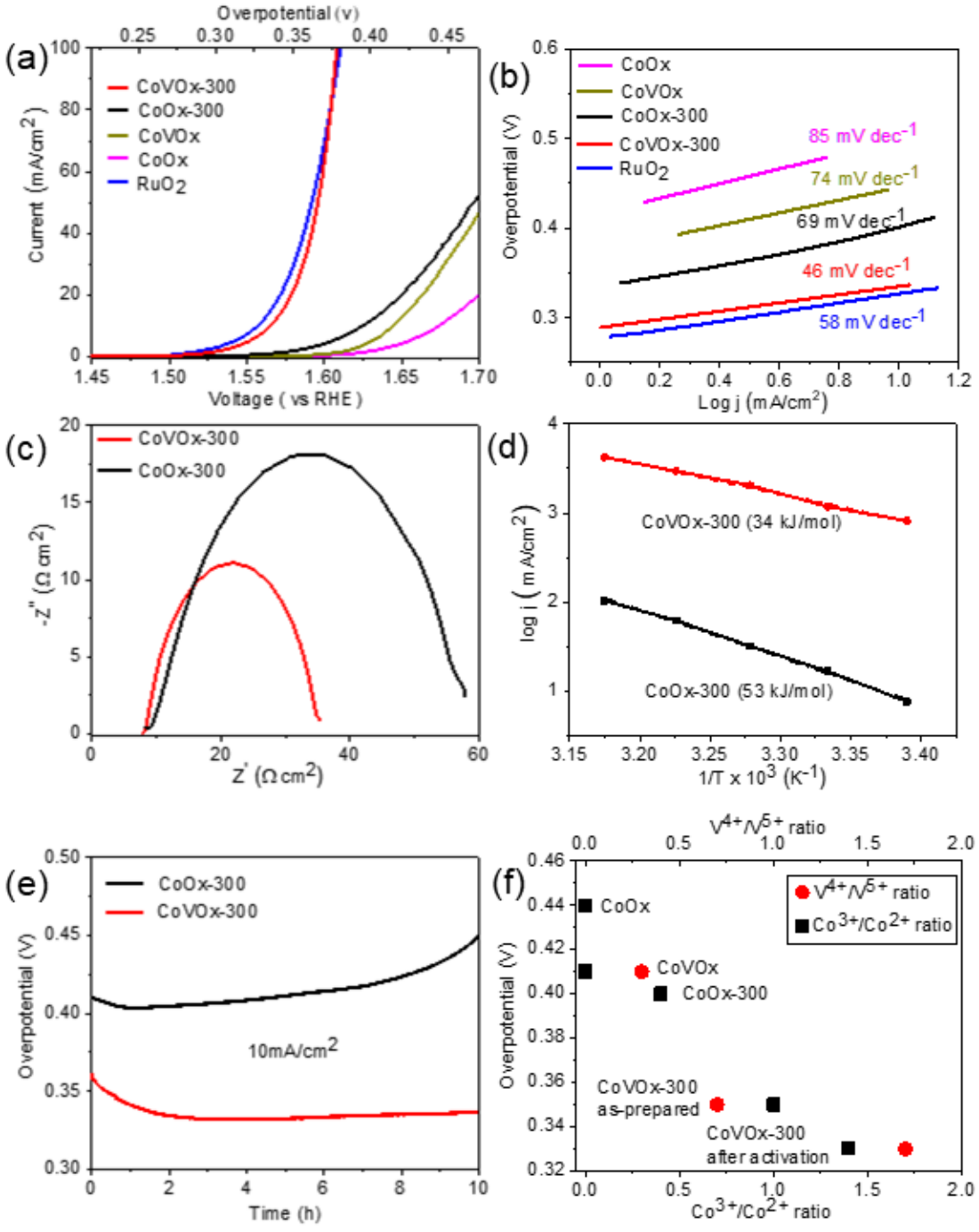

Figure 6-12 : (a): IR corrected LSV curves of CoOx, CoVOx, CoOx-300, CoVOx-300 and commercial RuO_2 at 2 mV/s and 1600 rmp in 1M KOH at 300 K; (b) Tafel plots derived from the polarization curves; (c) Electrochemical impedance spectra measured at an overpotential of 350 mV at 300K; (d) Arrhenius plots of the exchange current density J against the inverse temperature 1/T of CoOx-300 and CoVOx-300 at the overpotential of 350 mV; (e) Chronopotentiometric measurements at j = 10mA/cm2 in 1M KOH for CoVOx-300 and CoOx-300; (f) the trend of overpotentials at j = 10 mA/cm2 with increasing Co^{3+}/Co^{2+} and matched V^{4+}/V^{5+} ratio.

It has been widely reported that the valence of cobalt ions plays a crucial role in OER catalytic activities and Co^{3+} atoms with intermediate spin in the octahedral and square pyramidal symmetry could be considered as the active sites for OER due to its lower coordination number and large adsorption energy for H_2O molecules, [233, 267, 268] thus promoting to deprotonation of the OOH species to form O_2.[269, 270] In addition, Co^{3+} species can enhance the electrophilicity of materials, promoting the OER process.[234, 269] Moreover, it has been reported that the OER activity of cobalt hydroxide nanosheets can be improved through doping Fe atoms.[271] This improvement can be attributed to a change in the OH^- absorption energy difference (ΔG_O-ΔG_{OH}) at the Co sites, and can be rationalized by the difference in electron affinity between Co and Fe ions. Furthermore, Sun's group demonstrated that doping V into FeOOH could dramatically increase the binding energy of $^*OH$ and $^*OOH$, leading to a decreased overpotential for OER.[19] Similarly, in our system, the doping of V atoms may also lead to a change in ΔG_{OH} and ΔG_O-ΔG_{OH} at the Co sites, and facilitate the formation of OH^- and O^{2-} on the surface Co^{3+}, promoting the oxidation of Co^{3+} to Co^{4+}. As discussed above (Figure 6-5), it is shown that higher Co^{3+}/Co^{2+} ratio exists on the surface of CoVOx-300 than that of CoOx-300 catalyst. The results suggest that the vanadium incorporation into CoOx and rapid heat treatment could effectively promote the high concentration of Co^{3+} as the active sites, leading to high OER performance.

The Tafel plot is an inherent method of measuring the catalytic kinetics for the comparative catalysts by fitting the Tafel equation (equation 3-4). Figure 6-12b manifests that the Tafel slope of CoVOx-300 (46 mV dec^{-1}) is considerably smaller than that of CoOx-300 (69 mV dec^{-1}), CoVOx (74 mV dec^{-1}), CoOx (85 mV dec^{-1}) and even commercial RuO_2 (58 mV dec^{-1}) when using the same amount catalyst on the

electrode. The smallest Tafel slope of CoVOx-300 indicates that the synergetic effect of Co^{3+} and V^{4+} plays a vital role in facilitating the kinetics of OER and enhancing the intrinsic activity.

The kinetics of electrode interface reactions were also studied by the Electrochemical Impedance Spectroscopy (EIS) for all the relevant samples (Figure 6-12c). EIS study of the as-prepared electrodes was carried out in a three-electrode configuration cell in 1M KOH at 300 K with the overpotential of 350 mV. The Nyquist diagrams of all catalysts show an apparent semicircle, which could be mainly associated with charge transfer resistance (R_{ct}) of the prepared catalysts. CoVOx-300 exhibits lower R_{ct} of 37 Ω cm^2, which is nearly half value of CoOx-300 (60 Ω cm^2), suggesting its superior conductivity and efficient charge transfer. As known, the Ni or Co hydroxide is close to the insulator,[272, 273] resulting in slow kinetics during the OER process. Considering the partially filled d-orbitals of vanadium cations (V^{5+}: $t_{2g}^0 e_g^0$, V^{4+}: $t_{2g}^1 e_g^0$ and V^{3+}: $t_{2g}^2 e_g^0$) which may behave like electron acceptor sites, it provides states to accept electrons from the interacting molecules such as CoOx in our case.[274] The high valence vanadium ions incorporation into CoOx lattice facilitates the charge transfer process, which accounts for the improved conductivity, in good agreement with lower Tafel slop in Fig 6-12b. This is also consistent with the reported V doped Ni(oxy)hydroxide systems, where the V doping induced finite DOS for the spin-down state near the Fermi Level and thus help improve the electrical conductivity of the material.[275]

The apparent activation energy is also a crucial electronic property influencing the water oxidation catalytic activity. From the Arrhenius plot as shown in Figure 6-12d, the apparent activation energy of CoVOx-300 is calculated to be 34 kJ mol^{-1}, *ca*. 40 % smaller than that of CoOx-300 (53 kJ mol^{-1}). It is suggested that V doping results in the

creation of new active sites with lower activation energy for OER. The apparent activation energy value of 34 kJ mol^{-1} for CoVOx-300 compares favourably to other Co-based catalysts such as Fe doped CoP (39.6 kJ mol^{-1}) . [276]

The long-term performance or stability is another important criterion to evaluate an electrocatalyst, especially for commercial applications. To assess the durability of the CoVOx-300 in an alkaline environment, long-term chronopotentiometric experiments at a constant current density *j* of 10 mA/cm^2 was performed in O_2-saturated 1M KOH solution at 300 K for 10 h. As shown in Figure 6-12e, at the initial stage of two hours, the overpotential continues decreasing, owing to an increase of Co^{3+} concentration during the *in-situ* electrochemical activation of the CoVOx-300 electrocatalyst as proved by Figure 6-5c and d. After that the activation stage, the overpotential remains almost constant towards the end of measurements (10 h), suggesting the excellent stability.

In contrast, apart from the initial activation stage, the counterpart CoOx-300 exhibits worse stability as the overpotential keeps increasing toward up to 450 mV after 10 h OER reaction. The outstanding physical and chemical stability of CoVOx-300 is also confirmed by STEM images and the corresponding mapping images (Figure 6-13). As shown in the images, the nanorods morphology of the CoVOx-300 is well preserved, and the Co, V and O elements remain evenly distributed throughout the whole nanorod with some K residue from the electrolyte. This again proves the synergy between Co^{3+} and V^{4+} is the core for the excellent stability and efficient activity.

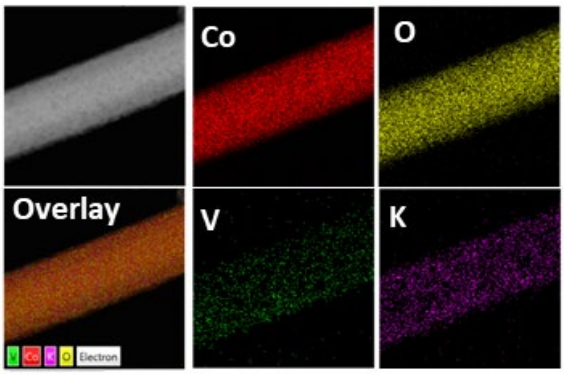

Figure 6-13: TEM images of CoVOx-300 after 10 h in-situ electrochemical activation and the corresponding EDX elemental mapping of cobalt, vanadium and oxygen.

The trend of overpotentials at j = 10 mA/cm^2 with changing Co^{3+}/Co^{2+} and corresponding V^{4+}/V^{5+} ratio on all catalysts was further investigated. As shown in Figure 6-12f, the Co^{3+}/Co^{2+} ratio could be easily manipulated by introducing the V^{4+}/V^{5+}couple. With increasing Co^{3+}/Co^{2+} ratio, V^{4+}/V^{5+} ratio increases and then the overpotential decreases. The outstanding activity and stability of CoVOx-300 under alkaline condition thus results from the stabilisation of Co^{3+} active sites by the presence of V^{4+}.

6.4 Conclusion

In summary, a high-performance cobalt vanadium oxide (CoVOx-300) electrocatalyst towards OER has been developed through a two-step method. The vanadium can be homogeneously doped at the surface of cobalt oxides via a reproducible hydrothermal method followed by rapid heat treatment. The Co^{3+}/Co^{2+} ratio can be tuned by controlling the V^{4+}/V^{5+} ratio. My study reveals that increasing V^{4+}/V^{5+} ratio matches with the increased Co^{3+}/Co^{2+} ratio, keeping an overall balanced charge at the surface of the new catalyst, resulting in the highest Co^{3+}/Co^{2+} ratio of 1.4 when the V^{4+}/V^{5+} ratio is tuned up to 1.7 for the CoVOx-300 catalyst. Further studies confirm that the excellent performance of CoVOx-300 is well related to the population of Co^{3+} on the surface, leading to good conductivity and easy electron transfer in the CoVOx-300 catalyst. On a flat glassy carbon electrode, the catalyst reaches 10 mA cm^{-2} at an overpotential of 330 mV in 1M KOH electrolyte with a Tafel slop as low as 46 mV dec^{-1}, 20 % lower than the benchmark commercial electrocatalyst RuO_2. A high content of Co^{3+} and V^{4+} formed on the surface of CoVOx-300 is believed to be beneficial for boosting electrocatalytic activity of water oxidation and reduce the activation energy for OER by *ca*. 40 % to the CoOx-300 catalyst. The comprehensive investigation of the surface structure-activity relationships for OER paves the way for the design of other transition metal oxides as the low-cost, efficient and stable electrocatalysts for the advanced electrochemical application.

7 Low-crystallinity $Co_{2-x}VO_4$ nanoplates for efficient electrochemical water oxidation

7.1 Introduction

Electrochemical water splitting offers a feasible way to store sustainable energy in the form of hydrogen.[277] However, the oxidative half reaction of water splitting, oxygen evolution reaction (OER) is kinetically extremely sluggish due to the proton-coupled four electron transfer process, which limits the overall efficiency of water splitting.[16, 48] RuO_2 and IrO_2 are considered as the benchmark OER catalysts with low overpotentials, of typically *ca.* 300 mV at the current density of 10 mA/cm^2, whereas the high cost and/or instability of these catalysts limit their large-scale applications.[41, 42] In the last few years, substantial effort has been devoted to exploring cost-effective, robust and highly efficient OER catalysts. With comparable activities to precious metal-based catalysts, earth-abundant cobalt-based oxides (perovskites or spinels), hydroxides and layered double hydroxides (LDH) have become increasingly attractive.[53, 233, 278] For example, thin-film of perovskite-based strontium cobaltite (SrCoOx) with optimised oxygen vacancy concentration displayed catalytic performance of OER commensurate with noble-metal electrodes such as IrO_2;[279] Low-temperature prepared spinel-type lithium cobalt oxide (LT-$LiCoO_2$) was reported as an efficient OER catalysts with slightly higher activity than IrO_2;[268] CoOOH nanosheets with partial iron substitution ($Co_{0.67}Fe_{0.33}OOH$) exhibited about 24 mV lower overpotential at 10 mV/cm^2 compared to IrO_2.[59]

In Chapter 6, it was found that the increase of Co^{3+} concentration in CoVOx catalysts would be an effective strategy to enhance the OER activity. The importance of Co^{3+} for active OER was also recognised for other cobalt-based materials such as Co_3O_4,[229] CoSe,[255] and $Co_3(PO4)_2$.[280] Co^{3+} was prevalently believed to be able to enhance the electrophilicity of materials and facilitate the formation of $^*OOH$ intermediates and thus O_2.[231]

On the other hand, there is an ongoing contradictory factor on the importance of structural disorder or degree of crystallinity on the catalytic activity of cobalt-based oxides and hydroxides, which is generally related to the defects or vacancies, and the spin states or electronic configuration. In particular, Yamauchi et al. reported the superior catalytic activity of OER and stability of mesoporous cobalt phosphate with crystallised walls, which offered a large number of active sites and better mass transportation at the electrolyte-catalyst interface.[281] Thus, cobalt-based oxides with high crystallinity have been regarded as more stable than those amorphous ones during OER process due to the strong crystal lattice constraint. On the other hand, recent work widely reported that the electrocatalysts at amorphous states exhibited better activity than those of crystalline states.[282, 283] It has been further demonstrated that the activity of the cobalt-based oxides could be dramatically increased by introducing oxygen vacancies in high-crystallinity cobalt oxides. For example, Liu et al. found that lattice distortion of spinel Co_3O_4 led to the massive high-spin Co^{3+} in octahedron sites, accompanied by rich oxygen vacancies, which would facilitate the OER activity by significantly enhancing the overlap of the e_g orbital of cobalt with the oxygen adsorbates.[57] However, Shi et al. found that largely increasing oxygen vacancies in the double perovskite $PrBaCo_2O_{6-\delta}$ would lead to cobalt ions spin state transition from

high-spin to low-spin, resulting significant reduction in the intrinsic OER activity.[284] Xie et al further proved that the optimal spin state of cobalt or e_g electron filling in perovskite $LaCoO_3$ achieved by optimising the degree of distortion of the CoO_6 octahedron would dramatically lower the adsorption free energy of oxygen intermediates, which resulted in 6 times higher mass activity than the counterpart.[285] Moreover, Zou et al. found that well crystallised Co-OER electrocatalyst performed water oxidation on the crystal surface with no ions penetrating the bulk, leading to low catalytic efficiency.[282] Therefore, they tuned crystallinity of spinel $CoGa_2O_4$ and found that low-crystallinity $CoGa_2O_4$ could achieve a stable and efficient bulk electrocatalysis.[282] Du et al further demonstrated the spin state of cobalt nickel oxide could be remarkably affected by the lattice distortion, which was inversely related to the crystallinity.[286]

According to these very informative studies, one can conclude that not only Co^{3+} concentration but also the degree of disorder or the crystallinity affects the electrocatalytic activity of cobalt-based electrocatalysts. The work in this chapter targeted to control the crystallinity as well as maintain the high concentration of Co^{3+} by synthesising a class of cobalt-vanadium (Co-V) bimetallic electrocatalysts via a one-step coprecipitation method. The components and crystallinity of Co-V bimetallic electrocatalysts could be readily controlled by varying the VO_4 amounts introduced. The relatively low-crystallinity $Co_{2-x}VO_4$ showed both stable and efficient water oxidation, resulting in an overpotential of 240 mV at 10 mA/cm^2 and stable for 8 hours, much better than the commercial benchmark catalyst RuO_2 in both overpotential and stability. The reason behind this novel property has been proved due to the controlled CoO_{6-x} distortion with rich Co^{3+}-O-V^{4+}catalytic active sites. This approach is believed

to be applied to other types of cobalt-based oxides or hydroxides and open new opportunities to achieve efficient electrocatalysts.

7.2 Experimental section

7.2.1 Catalysts synthesis

All the chemical agents used in the present work were of analytical grade and used without further purification. Typically, $CoCl_2$ and VCl_3 with different ratios (1:0, 3:1, 1:1, 1:3 and 0:1 mmol) were first dissolved in 40 mL deionized water to form a homogeneous solution (denoted as solution A). Secondly, 40 mmol NaOH and 4 mmol anhydrous Na_2CO_3 were dispersed in 40 mL deionised water to form a homogeneous solution (denoted as solution B). Solutions A and B were stirred vigorously for 1 h, respectively. Then, the solution B was added to the solution A dropwise with a 50 ℃ water bath with vigorously stirring. After ageing for 4 h, the precipitate was centrifuged and washed three times with water and dried for 12 h at 60 °C. The as-prepared samples were denoted as CoOOH, $Co_{2-x}VO_4$/CoOOH, LC-$Co_{2-x}VO_4$, A-$Co_{2-x}VO_4$, V(OH)x when solution A with Co/V molar ratio of 1:0, 3:1, 1:1, 1:3 and 0:1, respectively. The LC-$Co_{2-x}VO_4$ sample was further treated at 300 ℃ for 2 h in Muffle furnace with air atmosphere, denoted as HC-$Co_{2-x}VO_4$.

7.2.2 Catalysts characterisations

The XRD diffraction patterns were obtained by using a STOE StadiP spectrometer (Mo $K\alpha_1$ (using 50kV and 30mA; λ=0.71 Å) and analysed by using Jade 6.5 software

(Materials Data, Inc). The Raman spectra were collected on a Horiba Jobin-Yvon LabRAM HR800 spectrometer with a 532 nm laser source with 10 s integral time (0.1 mW laser power). The Raman spectrometer was calibrated by a Si wafer at Raman band of 520 cm^{-1} before data collection. X-ray photoelectron spectroscopy (XPS) data were acquired by a Thermo Scientific K-alpha photoelectron spectrometer with monochromatic $Al_{K\alpha}$ radiation. Peak positions were calibrated to carbon (284.8 eV) and then peaks were fitted with the XPSPEAK41 software. The SEM and TEM images were taken on a field-emission JSM-7800F and a JEOL JEM2100 microscope coupled with an Oxford instrument EDX detector. The X-ray absorption spectra (XAS) including X-ray absorption near-edge structure (XANES) and extended X-ray absorption fine structure (EXAFS) of the samples at Co or V K-edge were collected at the BL 14W1 of Shanghai Synchrotron Radiation Facility (SSRF), China. A double Si (311)- crystal monochromator was used for energy selection. Co or V foil was employed to calibrate the energy. The spectra were collected at transmission mode at room temperature. The i*n-situ* XANES spectra were collected at fluorescence mode *with* applied bias fixed at 1.5 V *vs.* RHE for *in-situ* OER measurements in 1M KOH. The *in-situ* electrochemical X-ray absorption spectroscopy (XAS) was carried out by using a custom-made polyethene cell as shown in Figure 7-1 and XAS data was analysed by ATHENA software.

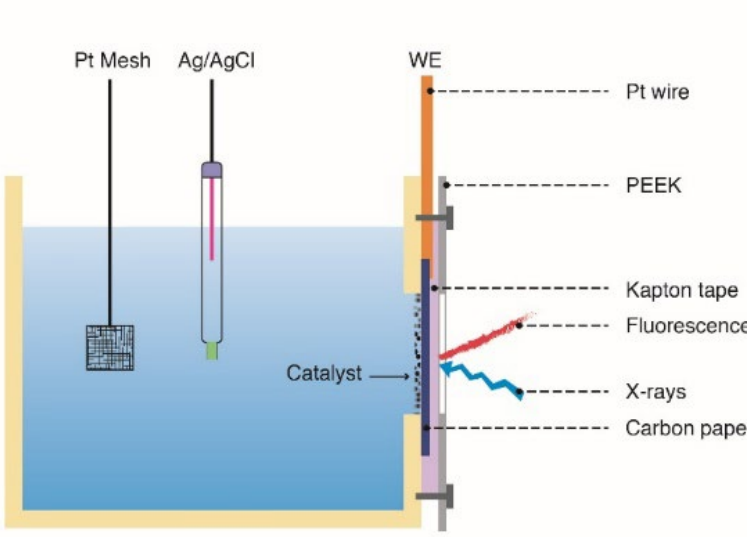

Figure 7-1: The electrochemical cell for *in-situ* electrochemical XAS measurements.

7.2.3 Electrode preparation

5 mg of the obtained powder were dispersed in the mixture solution of 1 ml H_2O, 250 ul 2-propanol and 10 ul 5% Nafion by sonication for 1 h. The 2.5 ul of the above suspension was uniformly drop-casted to a pre-polished glassy carbon electrode (diameter: 3 mm) with the loading of *ca.* 0.14 mg cm^{-2} and dried under an infrared lamp for 5 mins to evaporate the solvent.

7.2.4 Electrochemical measurements

The OER activity and stability were measured by liner scan voltammetry (LSV) and chronopotentiometry using a Metrohrm Autolab potentiostat in a polytetrafluoroethylene cell with a standard three-electrode configuration, which was composed of a working electrode (samples deposited on GC electrodes), a counter electrode (Pt sheet) and a reference electrode (Ag/AgCl). The GC ramping rate was 1600 rpm. The electrolyte was 1 M KOH, and the applied potentials were converted to

the reversible hydrogen electrode (RHE) according to equation 1-8 and the overpotential $\eta = E_{RHE}-1.23V$. Before all the electrochemical measurements, a chronopotentiometry electrochemical activation at a fixed current of 10 mA/cm^2 was performed until a stable phase was achieved. Then LSV were measured from 0.2 to 0.7 V versus Ag/AgCl with a slow scan rate of 2 mV/s in 1M KOH. By plotting overpotential Z against log (J) from LSV curves, Tafel slopes could be obtained. The electrochemical impedance spectroscopy (EIS) data were carried out through the same electrochemical measurement system at applied bias of 0.5 V (vs RHE) in 1 M potassium hydroxide solution with a frequency range of 100,000 and 0.1 Hz of a sinusoidal perturbation with 10 mV amplitude.

7.3 Results and discussions

7.3.1 Materials characterisation

The Co-V bimetallic oxides, that is $Co_{2-x}VO_4$/CoOOH composite ($Co_{2-x}VO_4$/CoOOH), Low-crystallinity $Co_{2-x}VO_4$ sample (LC-$Co_{2-x}VO_4$), Amorphous $Co_{2-x}VO_4$ (A-$Co_{2-x}VO_4$) and counterparts (CoOOH and V (OH)x) were synthesized at 50 ℃ in a water bath by dropping an alkaline solution into a solution containing cobalt chloride and/or vanadium chloride. (see the experimental section for details). Typical high-crystalline $Co_{2-x}VO_4$ (HC-$Co_{2-x}VO_4$) was obtained through annealing low-crystalline $Co_{2-x}VO_4$ at 300 ℃ in the air for 2 h. The Co/V ratio in the synthesis can affect the component and crystallinity as shown in the X-ray diffraction (XRD) patterns of the as-prepared materials. As shown in Figure 7-2a, without vanadium incorporation, the diffraction peaks can be indexed to highly crystallised CoOOH with pure

heterogenite phase. While introducing some vanadium species (Co/V molar ratio =3/1), a composite material of $Co_{2-x}VO_4$/CoOOH was obtained due to the over-dose of cobalt feedstock. Further increasing the vanadium content to a proper concentration, i.e. 50 % (Co/V= 1/1), a pure spinel Co_2VO_4-like material with relatively low crystallinity (denoted as LC-$Co_{2-x}VO_4$) is obtained. The crystallinity was further reduced when the vanadium contents up to 75 % (Co/V = 1/3), which resulted in an amorphous structure (denoted as A-$Co_{2-x}VO_4$). One can conclude that the vanadium doping concentration could readily modulate the components and crystallinity. Further annealing treatment of LC-$Co_{2-x}VO_4$ will dramatically increase the crystallinity, resulting in highly crystallised spinel Co_2VO_4-like material (denoted as HC- $Co_{2-x}VO_4$). The chemical environment of as-prepared catalysts was further investigated by Raman spectroscopy (Figure 7-2b). The CoOOH displays a single intense band at 503 cm^{-1}, which can be assigned to the Eg vibration mode of CoOOH.[287-289] V(OH)x exhibits four distinct bands located at 281 cm^{-1}, 407 cm^{-1}, 697 cm^{-1} and 997 cm^{-1}, in agreement with the characteristic peaks of reported lepidocrocite VOOH.[247] In detail, the first two peak at 281 and 407 cm^{-1} are assigned to the bending vibration of the V =O bonds.[248] The peak at 697 cm^{-1} is assigned to the doubly coordinated oxygen (V_2–O) stretching mode which results from corner-shared oxygens.[248] The relatively sharp peak at 997 cm^{-1} corresponds to the stretching mode of terminal oxygen (V=O).[290] For Co-V bimetallic oxides ($Co_{2-x}VO_4$/CoOOH, LC-$Co_{2-x}VO_4$ and A-$Co_{2-x}VO_4$), new additional bands are observed in the 750 -900 cm^{-1} region, which can be attributed to the stretching vibrations of the VO_4 tetrahedron with A_1 symmetry.[291, 292] The cobalt cations may be bonded with each oxygen atom of a VO_4 tetrahedral to form Co-O-V-O species. This may introduce some asymmetry in the VO_4 unit without disturbing the overall

symmetry of the elementary unit cell.[251] Moreover, a clear shift toward higher wavenumber in the 750 -900 cm^{-1} band is also observed with increasing vanadium content or in other words, decreasing the crystallinity which is very likely due to the local distortion caused by vanadium substitution in Co-V bimetallic oxides. Such feature of Raman bands shift was also observed on $CoCr_{2-x}V_xO_4$.[293] The Raman spectrum of HC-$Co_{2-x}VO_4$ shows a narrow peak at 805 cm^{-1} in comparison with LC-$Co_{2-x}VO_4$, indicating the crystallinity enhancement after annealing, as proved in XRD as well (Figure 7-2a).

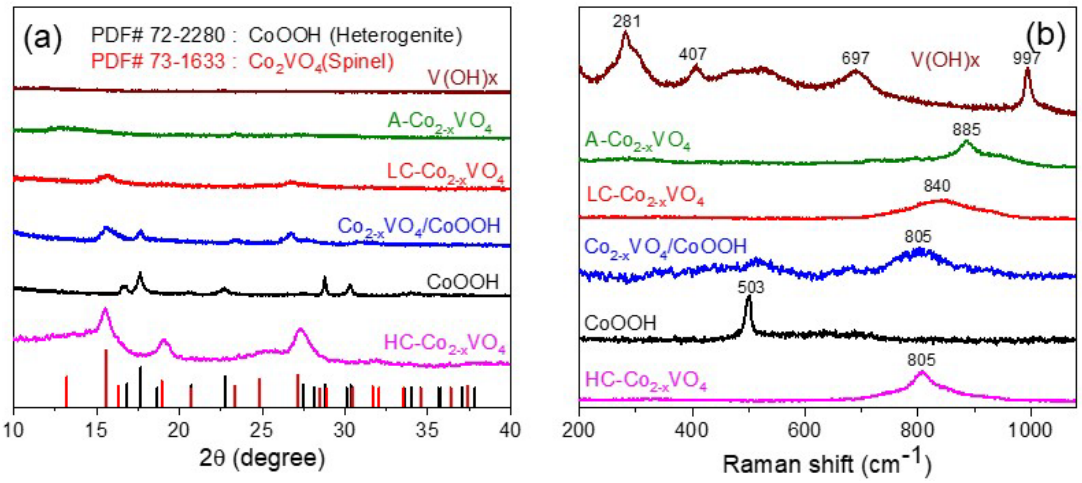

Figure 7-2： Catalysts characterisation： (a) The XRD patterns and (b) Raman spectra of CoOOH, $Co_{2-x}VO_4$/CoOOH composite, LC-$Co_{2-x}VO_4$, A-$Co_{2-x}VO_4$, V(OH)x and HC-$Co_{2-x}VO_4$.

The 2D nanoplate-like morphology of as-synthesized LC-$Co_{2-x}VO_4$ can be observed by transmission electron microscopy (TEM) and scanning electron microscopy (TEM) images (Figure 7-3 a and b). The thickness of these vertical nanoplates is found to be *ca.* 5 nm. Notably, the Co/V ratio in the synthesis can affect the morphology of the as-prepared materials as well. As shown in Figure 7-4, when low vanadium concentration in Co-V bimetallic oxides, $Co_{2-x}VO_4$/CoOOH composite and

LC-$Co_{2-x}VO_4$ has similar morphology of nanoplates, but thinner than CoOOH. However, the nanoplate morphology is destroyed when further increasing the vanadium content, where A-$Co_{2-x}VO_4$ and V(OH)x catalysts were obtained. The TEM elemental mappings of the LC-$Co_{2-x}VO_4$ (Figure 7-3 c-f) indicate the elements Co, V, and O are dispersed uniformly throughout the nanoplates. XPS spectra of Co 2p and V 2p further reveals the mix chemical states of Co^{3+}, Co^{2+}, V^{5+} and V^{4+} on LC-$Co_{2-x}VO_4$ surface, also confirmed by X-ray absorption near edge spectroscopy (XANES) (See detailed description in Figure 7-8 for XANES and Figure 7-9 for XPS). In addition, as shown in Figure 7-5, the XPS survey spectra of LC-$Co_{2-x}VO_4$ shows a Co/V molar ratio of 1.7 on the surface, close to the results indicated from SEM-EDX (1.8).

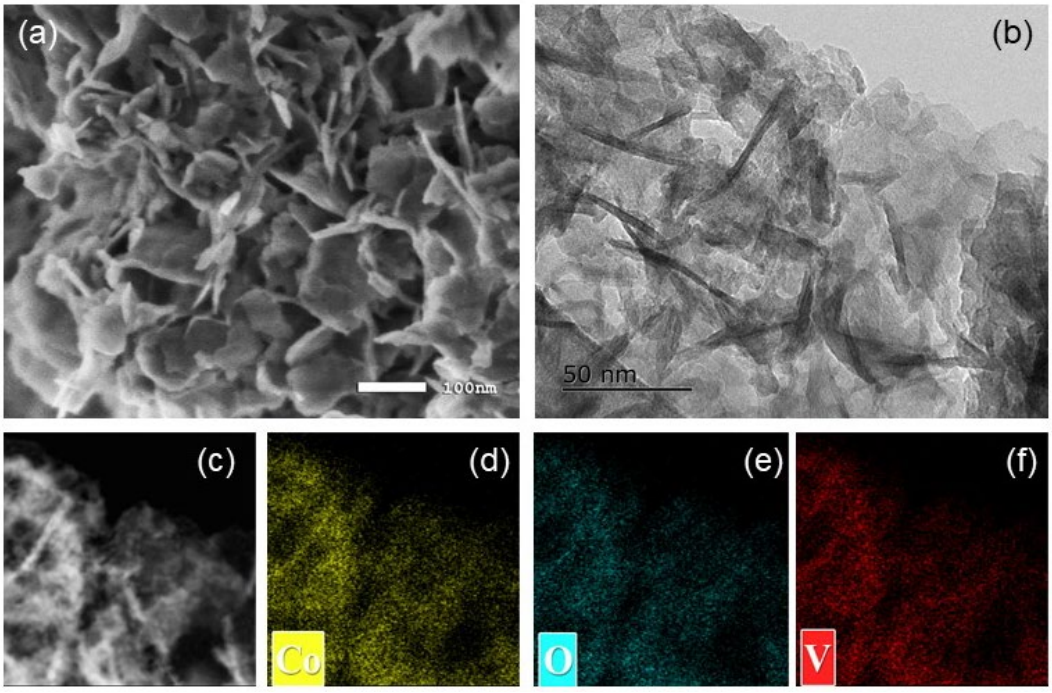

Figure 7-3: (a) SEM and (b) TEM image of LC-$Co_{2-x}VO_4$. (c)-(f): The STEM image of LC-$Co_{2-x}VO_4$ and the corresponding elemental mapping for Co, O and V.

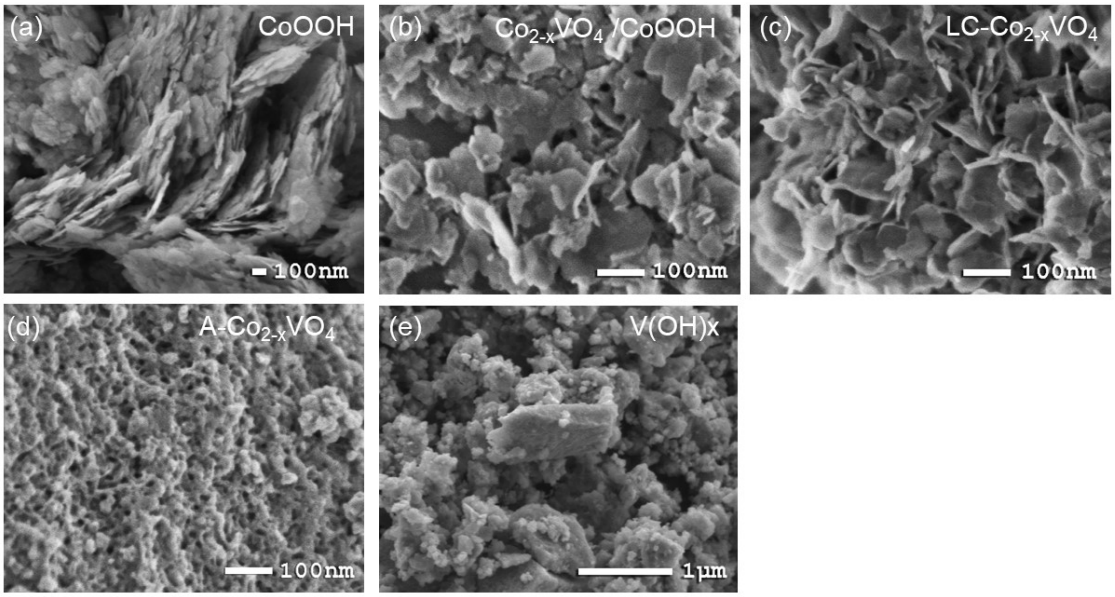

Figure 7-4: SEM images of CoOOH, V(OH)x and the Co-V bimetallic oxides ($Co_{2-x}VO_4$/CoOOH, LC-$Co_{2-x}VO_4$ and A- $Co_{2-x}VO_4$).

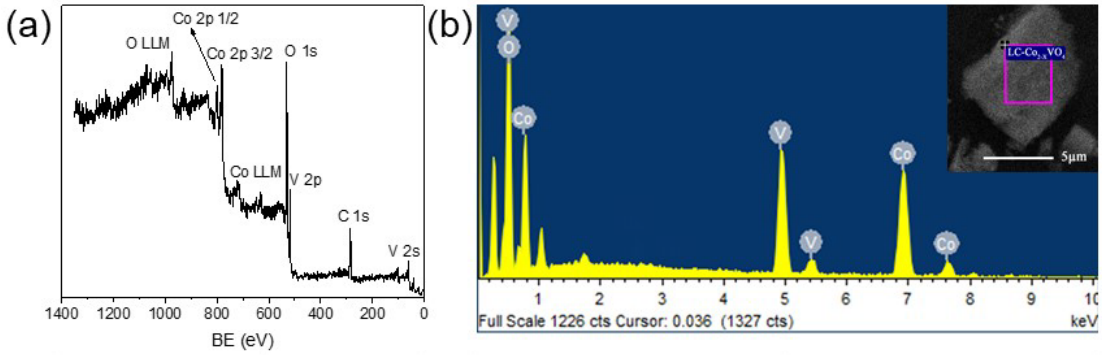

Name	Atomic
Co 2p	13.83 %
O 1s	77.99 %
V 2p	8.18 %
Co/V atomic ratio	1.7

Name	Atomic
Co	23.97 %
V	13.03 %
O	63 %
Co/V atomic ratio	1.8

Figure 7-5：(a) The XPS survey spectrum and the relevant analysis results of LC-$Co_{2-x}VO_4$ sample. (b) The SEM-EDX spectrum of LC-$Co_{2-x}VO_4$ sample and the relevant analysis results. The inset shows the SEM image to perform EDX.

7.3.2 Catalytic performance test

Figure 7-6 compares the catalytic performance of Co-V bimetallic oxides with the counterparts CoOOH, V (OH)x and commercial RuO_2 for the OER. As displayed in Figure 7-6a, the commercial widely used RuO_2 requires an overpotential of 300 mV to reach the 10 mA/cm^2 current, consistent with the reported value.[41, 42] The reference sample CoOOH is a bit less active, resulting into an overpotential of 360 mV to obtain the 10 mA/cm^2 current, which is also consistent with previous studies,[62, 74] while the V (OH)x exhibits negligible electrocatalytic activity for OER. After incorporating vanadium into the Co-based catalysts, the overpotentials (η@10 mA/cm^2) are significantly decreased to 280, 240 and 310 mV for $Co_{2-x}VO_4$/CoOOH composite, LC-$Co_{2-x}VO_4$, and A-$Co_{2-x}VO_4$, respectively, indicating vanadium doping is an efficient way to improve the electrocatalytic performance of the Co-based catalyst. However, further increasing the crystallinity of the LC-$Co_{2-x}VO_4$ unfavourably downgrades its OER activity, and thus an additional 45 mV overpotential is required to drive the 10 mA/cm^2 current for HC-$Co_{2-x}VO_4$. The smallest overpotentials (η) of LC-$Co_{2-x}VO_4$, reflects its remarkable OER activity. At the current density of j = 10 mA/cm^2, the LC-$Co_{2-x}VO_4$, (η = 240 mV) shows 60 mV lower overpotential in comparison with the widely used commercial catalyst RuO_2 (η = 300 mV). It further exhibits a considerably low overpotential of 280 mV even at j = 100 mA/cm^2, 70 mV lower than the benchmark commercial RuO_2 catalyst (η = 350 mV @100 mA/cm^2). In other words, the current density at η = 280 mV is 100 mA/cm^2 for the optimised LC-$Co_{2-x}VO_4$, nearly 600-folds as high as that of CoOOH (0.175 mA/cm^2), and 20 times better than the commercial RuO_2 (4.8 mA/cm^2), respectively. The OER kinetics of the as-prepared electrocatalysts was also investigated by the corresponding Tafel slopes as depicted in Figure 7-6b. As

expected , the LC-$Co_{2-x}VO_4$ exhibits the lowest Tafel slope of 45 mV dec^{-1}, indicative of the superior reaction kinetics towards OER process,[67] which is comparable to the performance of the state-of-the-art electrocatalysts reported very recently under identical experimental conditions as shown in Figure 7-7, while the overpotential at 10 mA/cm^2 of my catalyst is the champion among these highly efficient catalysts reported.

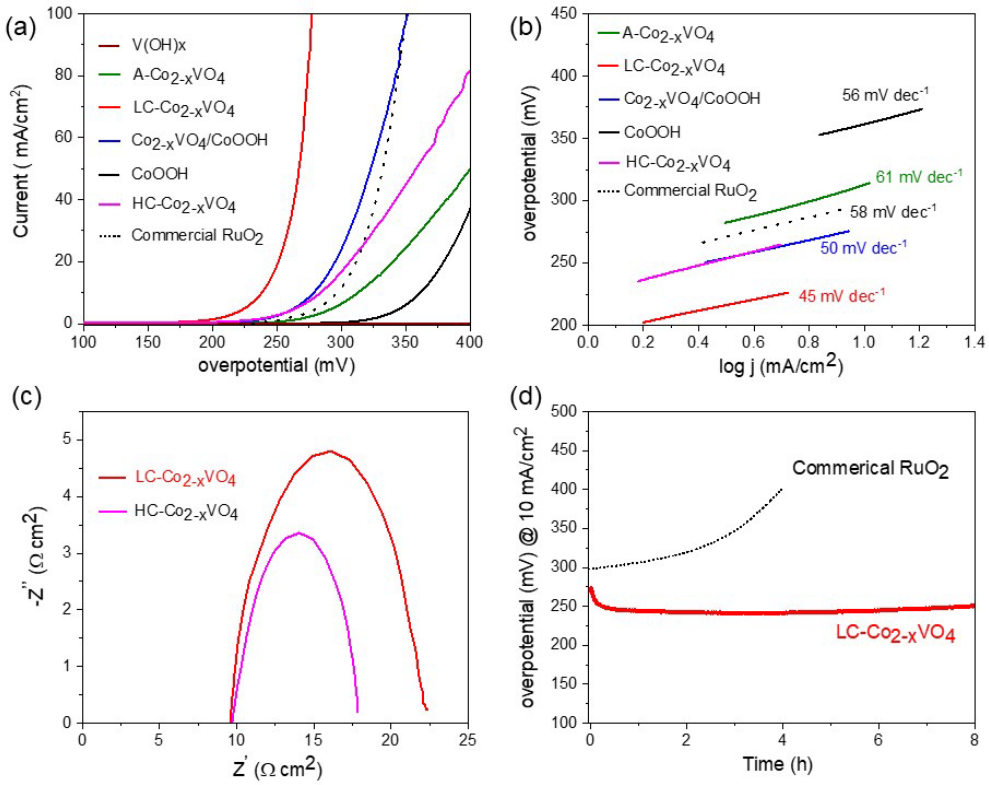

Figure 7-6: Electrochemical performance for OER in 1 M KOH solution. (a) iR-corrected OER polarization curves. (b) Tafel slope of CoOOH, $Co_{2-x}VO_4$/CoOOH composite, LC-$Co_{2-x}VO_4$, A-$Co_{2-x}VO_4$, HC-$Co_{2-x}VO_4$.and commercial RuO_2. (c) Electrochemical impedance spectra measured at an overpotential of 270 mV in 1 M KOH for LC-$Co_{2-x}VO_4$ and HC-$Co_{2-x}VO_4$. (d) Chronoamperometric response of LC-$Co_{2-x}VO_4$ and commercial RuO_2 at j = 10 mA/cm^2.

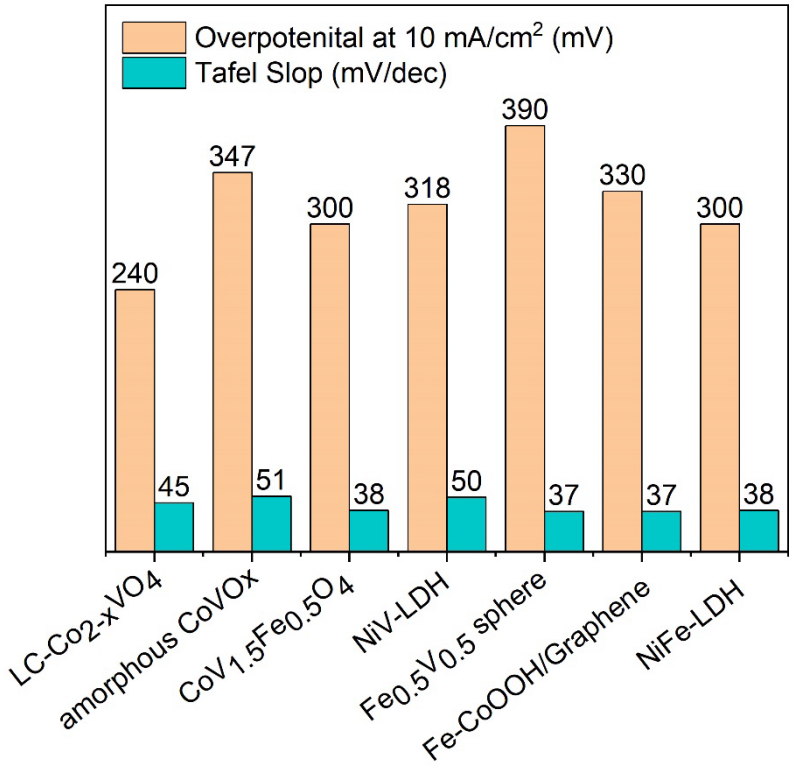

Figure 7-7: The OER performance comparison between LC-$Co_{2-x}VO_4$ and very recent nonprecious electrocatalyst including amorphous CoVOx,[65] $CoV_{1.5}Fe_{0.5}O_4$,[66] Fe-CoOOH/Graphene,[58] $Fe_{0.5}$ $V_{0.5}$ hollow sphere,[68] NiV-LDH, [69] and NiFe-LDH.[79]

The kinetics of electrode interface reactions were also studied by the Electrochemical Impedance Spectroscopy (EIS) for both the LC-$Co_{2-x}VO_4$ and HC-$Co_{2-x}VO_4$ (Figure 7-6c). HC-$Co_{2-x}VO_4$ exhibits lower charge transfer resistance (R_{ct}) than LC-$Co_{2-x}VO_4$, as obtained from the diameter of the semicircle in Nyquist diagrams, suggesting its superior conductivity and efficient charge transfer. To further characterise the activity stability of the LC-$Co_{2-x}VO_4$ catalyst, long-term durability measurement was performed as shown in Figure 7-6d, which shows the time-dependent overpotential required to reach 10 mA/cm^2 current for LC-$Co_{2-x}VO_4$ and the commercial RuO_2 electrocatalysts. For the LC-$Co_{2-x}VO_4$ electrocatalyst, the

overpotential decreases in the first one hour, which is likely to due to the activation period, in agreement with the behaviour observed on others reported previously.[63] Then the LC-$Co_{2-x}VO_4$ catalyst presents a very stable behaviour until the end of the study period (8 h). In contrast, RuO_2 exhibits nearly 40 % overpotential increase for driving 10 mA/cm^2 current in the first 4 h measurement under identical conditions, which might be due to the oxidation of RuO_2 into a higher valence state that is more easily dissolved into the alkaline electrolyte.[41, 294]

7.3.3 Mechanism insight

In-situ synchrotron radiation X-ray absorption spectroscopy (XAS) were undertaken to give an in-depth understanding of the atomic structure of the excellent catalyst LC-$Co_{2-x}VO_4$. The oxidation states of Co and V can be confirmed by X-ray absorption near edge spectroscopy (XANES). As shown in Figure 7-8a, the Co K-edge position of fresh LC-$Co_{2-x}VO_4$ is very close to that of Co $(OH)_2$, indicative of the Co oxidation state of +2. Notably, a right-shifted white line peak is observed for LC-$Co_{2-x}VO_4$ in comparison with $Co(OH)_2$, implying the incongruity in the coordination environment of the former.[295] Figure 7-8b shows that the V K-edge position of fresh LC-$Co_{2-x}VO_4$ is located between VO_2 and V_2O_5 while closer to the latter, suggesting the estimated V valence state of *ca.* +5. The pre-edge peak for the V K-edge XANES of the fresh sample is more intense than those of V_2O_5 and VO_2, indicating that vanadium species in LC-$Co_{2-x}VO_4$ are likely located in a VO_4 tetrahedron, different from those of VO_5 or VO_6 in V_2O_5 and VO_2, respectively.[296] The VO_4 tetrahedron can also be verified by Raman spectra as discussed in Figure 7-2b. In addition, the *in-situ* XANES was employed to probe the dynamic behaviour and real active phase of LC-

$Co_{2-x}VO_4$ during the OER process. As shown by the red dotted line in Figure 7-8a and 7-8b, after running in-situ experiment for 5 mins at a potential of 1.5 V *vs.* RHE (or 270 mV of overpotential) in 1 M KOH , the absorption edge of Co in LC-$Co_{2-x}VO_4$ is conspicuously shifted to a higher energy position that close to that of CoOOH, which could be attributed to the oxidation of Co sites from Co^{2+} to Co^{3+}. In contrast, The V edge for LC-$Co_{2-x}VO_4$ slightly shifts to lower energy close to V^{4+}. The decrease of the valence state for the V species may be due to the charge transfer from cobalt to vanadium caused by strong interaction between them.[66, 74] This indicates that Co^{2+} can be readily oxidised to Co^{3+} for water oxidation as observed in the *in-situ* measurement, which is further stabilised by V^{4+}, thus such presence of V^{4+} is favourable for highly active Co^{3+} generation that is very active during OER process.[57] Therefore, the improved OER performance for LC-$Co_{2-x}VO_4$ is owing to the high valence V^{4+}/V^{5+} ions, which could draw electrons to keep valence of neighbouring Co ions in a high-valence state for accelerating the OER process.[67] The higher valence cobalt species not only supply high conductivity, as proved by EIS results in Figure 7-6c, but also act as real active sites in OER catalysis, in agreement with previous work.[70]

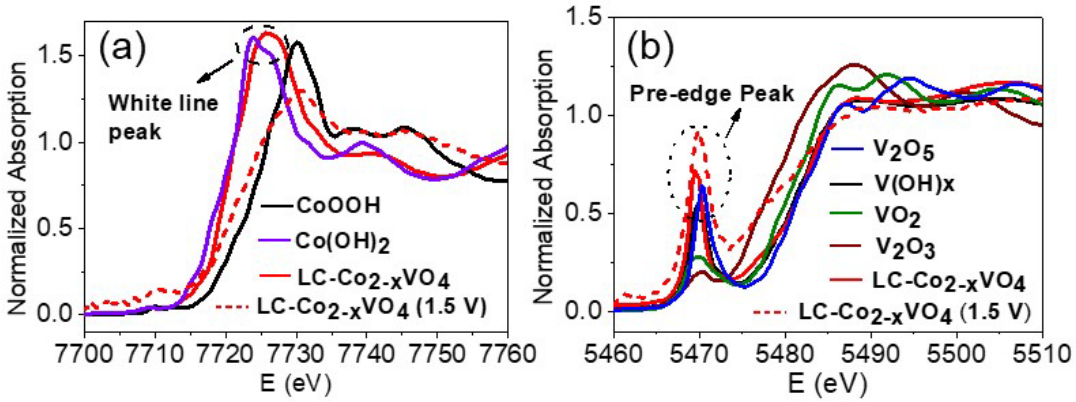

Figure 7-8: (a) Co K-edge and (b) V K-edge X-ray absorption near edge structures (XANES) measurements performed at the initial stage and in-situ OER stage of LC-$Co_{2-x}VO_4$ with CoOOH, Co (OH)2, V_2O_3, VO_2, V_2O_5 and V(OH)x as reference samples. The in-situ measurements were carried out during the OER at an applied potential of 1.5 V vs RHE in 1 M KOH.

The surface Co and V chemical states of LC-$Co_{2-x}VO_4$ were further studied by high-resolution XPS before and during OER (Figure 7-9). Since $2p_{3/2}$ and $2p_{1/2}$ of cobalt and vanadium qualitatively contain the same chemical information,[297] therefore, in this study, only the higher intensity Co $2p_{3/2}$ and V $2p_{3/2}$ were curve-fitted, as shown in Figure 7-9. In Figure 7-9a, two peaks at 780. 2 eV and 781.6 eV are observed for Co 2p 3/2, corresponding to Co^{3+} and Co^{2+}, respectively. The fresh sample contains more Co^{2+} than Co^{3+} while the activated sample has reverse amount, in good agreement with the *in-situ* XANES measurement.[237, 298] The ratio of Co^{3+}/Co^{2+} (2.84) for LC-$Co_{2-x}VO_4$ after 1 h OER exhibits an apparent increase compared to the fresh sample (1.12), implying that Co^{3+} is *in-situ* generated and is advantageous for activating the OER. Meanwhile, the Co^{3+}/Co^{2+} ratio keep nearly constant after 1 h OER towards the end of the reaction (8 h), further suggesting the excellent stability of LC-$Co_{2-x}VO_4$, as observed from the stability measurements illustrated in Figure 7-6d. On the other hand, in Figure 7-9b, the V 2p3/2 can be fitted into two constituent peaks corresponding to V^{4+} (516.6 eV) and V^{5+} (517.6 eV) for both fresh and activated OER samples.[68] The

reduced V^{5+}/V^{4+} ratio is observed for LC-$Co_{2-x}VO_4$ after the one hour, which exactly matches with the increased Co^{3+}/Co^{2+} ratio. As expected, no noticeable change of V^{5+}/V^{4+} ratio while comparing the sample after OER at 1 h and 8 h reaction time.

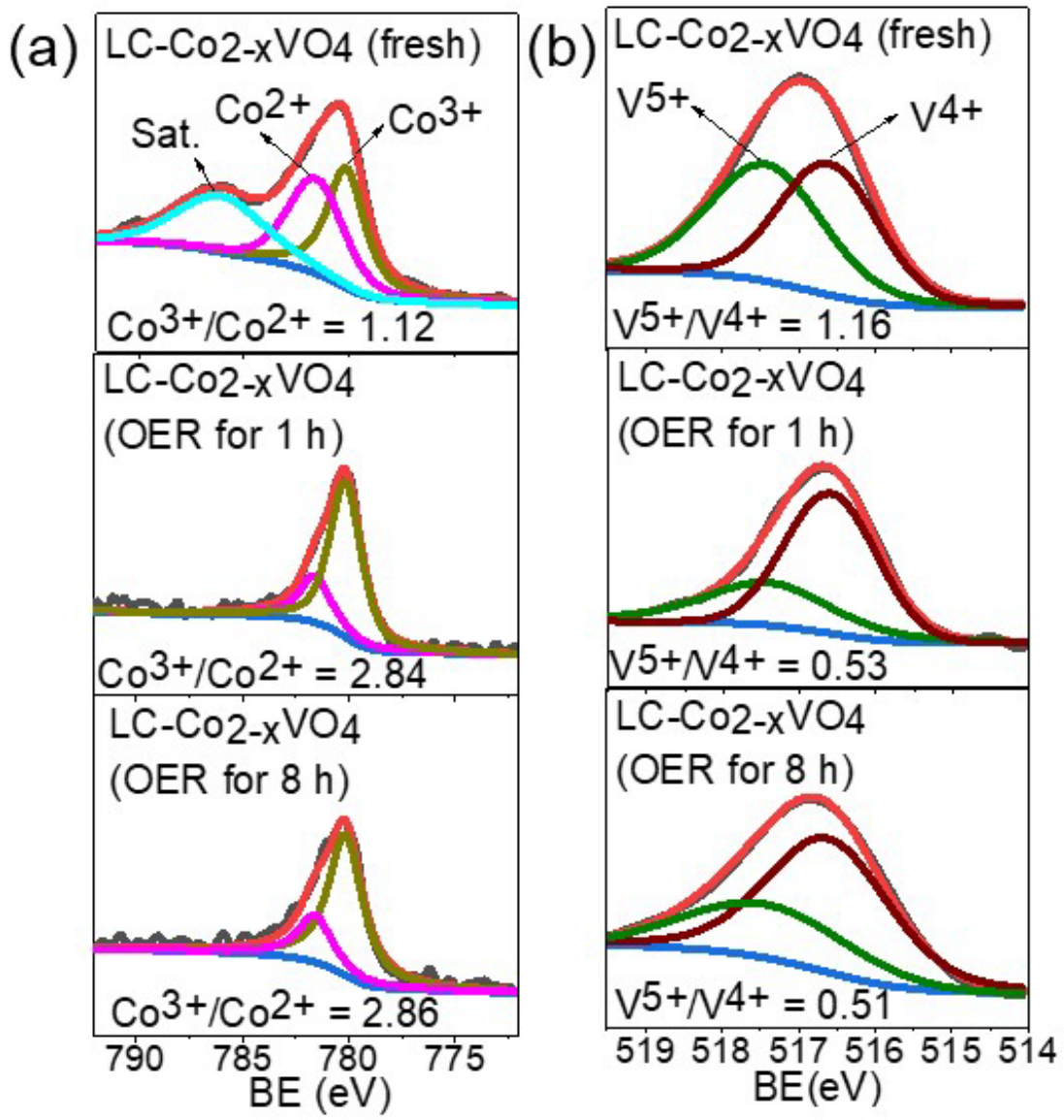

Figure 7-9: (a) and (b) XPS high-resolution spectra of Co 2p3/2 and V 2p3/2 of the LC-$Co_{2-x}VO_4$ catalyst at fresh, after 1 h OER, after 8 h OER states, respectively.

Furthermore, in Figure 7-10 of the extended X-ray absorption fine structure (EXAFS) in the R-space of LC-$Co_{2-x}VO_4$, a scattering length of 1.5 Å is assigned to the Co-O, which is longer comparing with Co-O in CoOOH (1.4 Å). The elongation of Co-O bonds may lower the absorption energy of H_2O and thus improve OER performance according to the previous study.[299] It is worth highlighting that the vanadium incorporation also lowers the coordination numbers of the Co-O clusters, signifying the general lattice distortion and coordination deficiency (*i.e.* CoO_{6-x}) occurs in LC-$Co_{2-x}VO_4$ (Figure 7-10a). In contrast, the LC-$Co_{2-x}VO_4$ exhibits higher V-O coordination number in comparison with V(OH)x (Figure 7-10b), which matches well with the better crystallinity than the amorphous V(OH)x. All these spectroscopic results draw an important conclusion that vanadium incorporation leads to CoO_{6-x} octahedra and VO_4 tetrahedra. These results from both *in-situ* XANES and XPS confirm the oxidisation of Co and reduction of V ions during the OER For spinel Co_2VO_4-like catalyst, it is very interesting to conclude that the active reaction sites are Co^{3+}-O-V^{4+} species which was *in-situ* yield herein.[296]

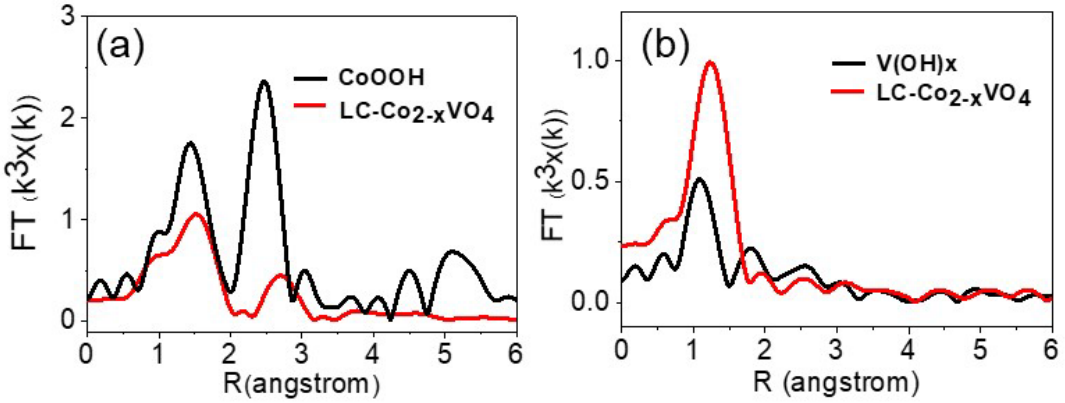

Figure 7-10：Fourier transforms curves of EXAFS spectra in R space for (a) cobalt and (b) vanadium

The previous experimental and theoretical study established a strong evidence that structural distortion of the CoO_{6-x} octahedra would enhance the electrophilicity of H_2O and facilitate the interfacial electron transfer between Co ions and adsorbed *OOH intermediates to form O_2, resulting in enhanced OER activity for CoOOH.[70] On the other hand, increasing the crystallinity of $Co_{2-x}VO_4$ to form lower degree of distorted CoO_{6-x} configuration would lead to a lower charge transfer resistance according to both EIS result in Figure 7-6c and in agreement with reported Co_3O_4 films.[284] When adding V to CoOOH, distortion of CoO_6 octahedron (CoO_{6-x}) occurs in $Co_{2-x}VO_4$ and the degree of the distortion depends on the vanadium amount introduced. Although CoO_{6-x} is beneficial for OER, too much distortion may also dramatically lead to excess oxygen vacancies, resulting in a significant reduction in the intrinsic OER activity as reported before.[284] Herein, the as-developed vanadium doping strategy not only adjusted the crystallinity of Co-V bimetallic oxides to the optimal CoO_{6-x} configuration but also led to the formation of Co^{3+}-O-V^{4+} active species under in-situ OER condition. The synergistic effect of the optimal CoO_{6-x} configuration and surface Co^{3+}-O-V^{4+}

species resulted in a superior electrocatalyst for OER.

7.4 Conclusions

In summary, I have discovered a simple route to fabricate the Co-V bimetallic oxides by controlling the molar ratio between cobalt and vanadium precursor solution during the co-precipitation process. The component, crystallinity and morphology could be regulated by the Co/V ratio in the synthesis. It was found the relative low crystallinity of $Co_{2-x}VO_4$ catalyst shows much higher activity than the amorphous or crystalline analogues due to the controlled distortion degree of CoO_6 apart from the high concentration of Co^{3+}. In combination with *in-situ* XANES and XPS analysis, the real active species of Co^{3+}-O-V^{4+} during the OER was identify for low-crystallinity of $Co_{2-x}VO_4$, which displayed the smallest overpotential of 240 mV at 10 mA/cm^2, 8 hours durability for OER in 1 M KOH and the Tafel slope of 45 mV dec^{-1}. The overpotential is nearly 130 mV lower than the widely reported CoOOH catalyst and also outperformed the commercial RuO_2. This will open up opportunities to advance the electrochemical performance of non-precious OER electrocatalysts by V doping and precisely manipulating crystallinity.

8 Conclusions and future work

In general, the performance of a photoelectrode for water splitting to produce H_2 fuel is determined by a few parameters including light absorption efficiency, charge carrier's mobility, and surface OER/HER kinetics. Substantial approach has been achieved based on the strategies of bandgap engineering, materials architecture design and surface modification by electrocatalysts. However, it is still very challenging to balance efficiency and durability. Most of the metal oxides based photoanodes displayed relatively stable photocurrent in contrast to III-V materials, but limited STH efficiency (< 10 %). III-V materials such as GaAs was able to achieve the > 10 % STH efficiency, but the bad stability slowed it down from moving forward to the commercial market.

Initially, ZnO nanorods decorated with surface OER catalysts (Co-Pi & Ni-B) were prepared by a hydrothermal method to address the issues of ZnO based photoanodes such as the fast charge-carrier recombination, poor stability in aqueous solution, and slow kinetics of surface water oxidation reaction. Bare ZnO nanowires were optimised by varying the reaction time, temperature and precursor concentration to achieve the optimal photoelectrochemical performance. Optimised bare ZnO nanowires (1400 nm length, 70 nm diameter) exhibited a photocurrent of 0.62 mA/cm^2 at 1.0 V (*vs* RHE) under 1 sun illumination. The addition of earth-abundant nickel borate (Ni-B) oxygen evolution catalysts onto ZnO nanowires (Ni-B/ZnO) resulted in substantial cathodic shifts in onset potential to as low as about 0.3 V versus the reversible hydrogen electrode (RHE), and a maximum photocurrent density of 1.22 mA cm^{-2} at 1.0 V (vs RHE) was achieved, two folds higher than unmodified ZnO. Besides, an unprecedented near-unity incident photo-to-current efficiency at 370 nm was achieved for Ni-B/ZnO.

Furthermore, the potential required for saturated photocurrent was dramatically reduced from 1.6 to 0.9 V versus RHE with Ni-B loading. The stability of these ZnO nanorods was significantly enhanced by using Ni-B compared to Co-Pi due to its superior chemical robustness, which presented an unprecedented zero loss in photocurrent over one-hour test period and it thus showed additional functionality as a stable protecting layer on the ZnO surface. However, due to the wide bandgap of ZnO, only UV light could be absorbed, as-synthesized ZnO based PEC devices achieved only 0.4 % STH efficiency.

To further increase the STH efficiency of a PEC device, GaAs was employed as a promising photoanode due to its near-ideal bandgap energy, appropriate band-edge alignment, as well as superior mobility of photogenerated carriers. Despite such compelling advantages and high theoretical STH efficiency (33 %), the limited stability of GaAs photoanodes in highly alkaline electrolytes prohibited their practical application in a PEC device. To address this challenge, a stabilising strategy that can *in-situ* deposit nickel- borate (Ni-B) OER electrocatalysts on GaAs as hole trapping sites to mitigate GaAs self-photooxidation under illumination was presented. A monolithic layer of Ni–B/Ga (As)O_x was generated during the Ni–B photoassisted electrodeposition process, resulting in a Ni–B/Ga (As)O_x/GaAs photoanode structure. By optimising the GaAs surface architecture, electrolyte pH value and Ni–B deposition time, the optimized photoanode Ni–B/Ga(As)O_x/shallow GaAs with 0.5 h Ni–B deposition time (∼ 900 nm thickness of the Ni–B/Ga(As)O_x layer) exhibited a very high photocurrent, leading to a nearly 22 hour stable photocurrent density of 20 mA cm^{-2}, while bare GaAs exhibited 60 % photocurrent loss after three hours under continuous one sun illumination (100 mW cm^{-2}) in alkaline media (pH = 14). Furthermore, faradaic efficiency of O_2

increased from 0 % to 36 % in the presence of *ca.* 900 nm thick layer of Ni–B/Ga (As)O_x on GaAs substrate. The faradic efficiency could be further improved by synthesising of more conformal catalytic layers based on efficient and robust surface OER electrocatalysts. Therefore, following this, extensive research effort has been made towards discovering more promising OER electrocatalysts in alkaline condition.

The as-prepared cobalt vanadium oxides (CoVOx-300) displayed superior electrocatalytic performance for the oxygen evolution reaction including i) low overpotential, that was 330 and 380 mV for driving 10 and 100 mA/cm^2 current density, respectively. The overpotential at 10 mA/cm^2 for CoVOx-300 showed nearly 70 and 80 mV lower than the corresponding CoOx-300 and CoVOx catalysts, respectively; ii) small Tafel slope of 46 mV/dec, which was 20 % lower than the commercial RuO_2 electrocatalyst for OER; iii) low activation energy (34 kJ /mol), which was 40 % lower than the counterpart, CoOx300; and iV) the excellent durability of 10 h in alkaline electrolyte. Raman, TPR, SEM/TEM, and XPS analysis demonstrated that the surface Co^{3+} and V^{4+} species were responsible for this excellent electrocatalytic activity and stability. The vanadium incorporation and rapid heat treatment of CoVOx brought more surface Co^{3+} without altering its crystal structure, as confirmed by XRD results. In-depth XPS analysis further revealed the highest Co^{3+}/Co^{2+} ratio (1.4) was manipulated by the highest V^{4+}/ V^{5+} ratio (1.7) in CoVOx-300 after OER. Therefore, the present results suggested that this novel CoVOx-300 catalyst with a high density of Co^{3+} and V^{4+} on the surface was supposed to be the real active and stable species for OER.

Despite the substantial progress achieved on CoVOx-300 OER catalyst, the overpotential for driving 10 mA/cm^2 was still over 300 mV. To further reduce the overpotential for OER, more active OER catalysts are required. I then developed a

simple route toward the Co-V bimetallic oxides by the low temperature co-precipitation of cobalt chloride and vanadium chloride precursors. The components and structure of the catalysts could be readily tuned by regulating the composition of the feedstock materials. As a result, the $Co_{2-x}VO_4$/CoOOH composite, low-crystallinity $Co_{2-x}VO_4$, amorphous $Co_{2-x}VO_4$ could be selectively obtained by fixing the cobalt/vanadium ratio in the precursor material to 3:1, 1:1, and 1:3, respectively. The catalysts exhibited good structure-related performance for OER. In particular, low-crystallinity $Co_{2-x}VO_4$ presented the lowest overpotential of 240 mV at 10 mA/cm^2, a smallest Tafel slope of 45 mV/dec and a high current density of 100 mA/cm^2 at a low overpotential of 280 mV, where the current density is nearly 600 times higher than that of pure CoOOH and 50 times higher than high-crystallinity $Co_{2-x}VO_4$ prepared by calcination of the as-prepared low-crystalline $Co_{2-x}VO_4$. The low-crystallinity $Co_{2-x}VO_4$ also held the superior activity (240 mV) and durability (8 h) that outperformed the commercial benchmark RuO_2, which typically required at least 300 mV to drive 10 mA/cm^2 current density while rapidly degraded in alkaline condition. The *in-situ* X-ray absorption spectroscopy was further employed to investigate the dynamic behaviour and real active phase of low-crystallinity in the OER process. *In-situ* x-ray absorption near edge spectra revealed that the Co^{2+} could be oxidised to Co^{3+}during the water oxidation, along with the partially V^{5+} reduced to V^{4+}, which was consistent with the XPS analysis by comparing the surface chemical states before and after OER. Such an efficient catalyst was attributed to the extremely high concentration of Co^{3+} (Co^{3+}/ Co^{2+} (2.84), nearly double the Co^{3+} concentration in the previous CoVOx-300. Extended x-ray absorption spectra further confirmed the structure distortion of CoO_{6-x} and VO_4 structure for the

low-crystallinity $Co_{2-x}VO_4$ catalyst, which would also beneficial for the high OER performance.

Although my current research work achieved the main goals set out, including efficient surface OER electrocatalyst design and stabilised photoanodes configuration, several things still need to be considered for efficient and stable operations:

First of all, coupling the current developed Co-V based OER catalysts with a good photoanode deserves extensive study, which would generate H_2 fuel at a very high efficacy driven by solar light. The *in-situ* electrocatalyst assembling techniques such as electrodeposition or photoassisted electrodeposition, chemical vapour deposition method may be applied to make a well contact between the electrocatalysts and the underlying photoabsorber. The management of the incident irradiation, interface engineering, and the exposure active site density on the surface should be considered together to form a transparent, dense and efficient catalytic layer to against the photocorrosion while maintaining the high STH efficiency.

Next the OER mechanism in alkaline electrolyte needs to be clarified further by o*perando* characterisation techniques, since they can disclose more key information regarding the intermediate and active sites, therefore guiding subsequent catalyst design. Some techniques such as *operando* Raman spectroscopy, *operando* X-ray absorption spectroscopy and *in-situ* ambient pressure X-ray photoelectron spectroscopy may have the potential to realise the purpose of *in situ* characterisation.

Finally, the performance of current cobalt-vanadium based catalysts could be further improved by optimising the composition, material preparation/processing, and morphology, which are responsible for the electrochemical activity, current selectivity and

stability of oxygen evolution catalysts. The longevity and durability at varying temperatures should also be tested, which will provide useful information for the real commercial application.

9 Bibliography

1. N. S. Lewis and D. G. Nocera, *Proceedings of the National Academy of Sciences*, 2006, **103**, 15729-15735.
2. J. Barber, *Chemical Society Reviews*, 2009, **38**, 185-196.
3. M. Barroso, S. R. Pendlebury, A. J. Cowan and J. R. Durrant, *Chemical Science*, 2013, **4**, 2724-2734.
4. R. Van de Krol and M. Grätzel , *Photoelectrochemical hydrogen production* , Springer, Switzerland, 2012.
5. R. Clarke, S. Giddey, F. Ciacchi, S. Badwal, B. Paul and J. Andrews, *International Journal of Hydrogen Energy*, 2009, **34**, 2531-2542.
6. G. Lauermann, P. Häussinger, R. Lohmüller and A. M. Watson, *Ullmann's Encyclopedia of Industrial Chemistry*, Wiley-VCH Verlag GmbH & Co. KGaA, Germany, 2000.
7. T. Minegishi, N. Nishimura, J. Kubota and K. Domen, *Chemical Science*, 2013, **4**, 1120.
8. S. Licht, B. Wang, S. Mukerji, T. Soga, M. Umeno and H. Tributsch, *International Journal of Hydrogen Energy*, 2001, **26**, 653-659.
9. N. L. Garland, D. C. Papageorgopoulos and J. M. Stanford, *Energy Procedia*, 2012, **28**, 2-11.
10. C. Jiang, S. J. Moniz, A. Wang, T. Zhang and J. Tang, *Chemical Society Reviews*, 2017, **46**, 4645-4660.
11. J. O. M. Bockris, B. E. Conway and E. Yeager, Plenum Press, New York, 1981, 595.
12. R. Foulkes, C. Jiang and J. Tang, in *Solar Fuel Generation*, CRC Press, Taylor & Francis Group, New York, 2017.
13. S. Trasatti, *Journal of Electroanalytical Chemistry and Interfacial Electrochemistry*, 1972, **39**, 163-184.
14. B. Hinnemann, P. G. Moses, J. Bonde, K. P. Jørgensen, J. H. Nielsen, S. Horch, I. Chorkendorff and J. K. Nørskov, *Journal of the American Chemical Society*, 2005, **127**, 5308-5309.
15. I. Roger, M. A. Shipman and M. D. Symes, *Nature Reviews Chemistry*, 2017, **1**,

0003.

16. N.-T. Suen, S.-F. Hung, Q. Quan, N. Zhang, Y.-J. Xu and H. M. Chen, *Chemical Society Reviews*, 2017, **46**, 337-365.
17. R. Van de Krol, M. Grätzel, M. Grätzel and M. Grätzel, *Photoelectrochemical hydrogen production*, Springer, Switzerland, 2012.
18. X. Zhang, H. Li, S. Wang, F.-R. F. Fan and A. J. Bard, *The Journal of Physical Chemistry C*, 2014, **118**, 16842-16850.
19. S. Licht, A. J. Bard and M. Stratmann, Semiconductor Electrodes and Photoelectrochemistry, John Wiley & Sons, Hoboken, New Jersey, 2002.
20. Z. Zhang and J. T. Yates, *Chemical reviews*, 2012, **112**, 5520-5551.
21. D. Li, H. Baydoun, C. N. Verani and S. L. Brock, *Journal of the American Chemical Society*, 2016, **138**, 4006-4009.
22. S. J. A. Moniz, S. A. Shevlin and D. J. Martin, *Energy & Environmental Science*, 2015, **8**,731-759.
23. F. F. Abdi, L. Han, A. H. Smets, M. Zeman, B. Dam and R. van de Krol, *Nat. Commun.*, 2013, **4**, 2195.
24. O. Khaselev, *Science*, 1998, **280**, 425-427.
25. J. Luo, J.-H. Im, M. T. Mayer, M. Schreier, M. K. Nazeeruddin, N.-G. Park, S. D. Tilley, H. J. Fan and M. Grätzel, *Science*, 2014, **345**, 1593-1596.
26. J. Y. Jia, L. C. Seitz, J. D. Benck, Y. J. Huo, Y. S. Chen, J. W. D. Ng, T. Bilir, J. S. Harris and T. F. Jaramillo, *Nature Communications*, 2016, **7**, 6.
27. Y. Qiu, Z. Wen, C. Jiang, X. Wu, R. Si, J. Bao, Q. Zhang, L. Gu, J. Tang and X. Guo, *Small*, 2019, **15**, 1900014.
28. D. V. Esposito, S. T. Hunt, A. L. Stottlemyer, K. D. Dobson, B. E. McCandless, R. W. Birkmire and J. G. Chen, *Angewandte Chemie International Edition*, 2010, **49**, 9859-9862.
29. S. Wang, X. Gao, X. Hang, X. Zhu, H. Han, W. Liao and W. Chen, *Journal of the American Chemical Society*, 2016, **138**, 16236-16239.
30. D. V. Esposito, S. T. Hunt, Y. C. Kimmel and J. G. Chen, *Journal of the American Chemical Society*, 2012, **134**, 3025-3033.
31. S. Saha, B. Martin, B. Leonard and D. Li, *Journal of Materials Chemistry A*, 2016, **4**, 9253-9265.
32. J. Zhang, Y. Zhao, X. Guo, C. Chen, C.-L. Dong, R.-S. Liu, C.-P. Han, Y. Li, Y. Gogotsi and G. Wang, *Nature Catalysis*, 2018, **1**, 985-992.

33. S. Ye, F. Luo, Q. Zhang, P. Zhang, T. Xu, Q. Wang, D. He, L. Guo, Y. Zhang and C. He, *Energy & Environmental Science*, 2019, **12**, 1000-1007.
34. T. F. Jaramillo, K. P. Jørgensen, J. Bonde, J. H. Nielsen, S. Horch and I. Chorkendorff, *Science*, 2007, **317**, 100-102.
35. J. Kibsgaard, Z. Chen, B. N. Reinecke and T. F. Jaramillo, *Nature materials*, 2012, **11**, 963.
36. P. C. K. Vesborg, B. Seger and I. Chorkendorff, *The Journal of Physical Chemistry Letters*, 2015, **6**, 951-957.
37. X. Zou and Y. Zhang, *Chemical Society Reviews*, 2015, **15**, 5184-5180.
38. H. Vrubel and X. Hu, *Angewandte Chemie International Edition*, 2012, **51**, 12703-12706.
39. J. R. McKone, B. F. Sadtler, C. A. Werlang, N. S. Lewis and H. B. Gray, *ACS Catalysis*, 2013, **3**, 166-169.
40. E. J. Popczun, C. G. Read, C. W. Roske, N. S. Lewis and R. E. Schaak, *Angewandte Chemie International Edition*, 2014, **53**, 5427-5430.
41. R. Frydendal, E. A. Paoli, B. P. Knudsen, B. Wickman, P. Malacrida, I. E. L. Stephens and I. Chorkendorff, *ChemElectroChem*, 2014, **1**, 2075-2081.
42. Y. Lee, J. Suntivich, K. J. May, E. E. Perry and Y. Shao-Horn, *The Journal of Physical Chemistry Letters*, 2012, **3**, 399-404.
43. R. Kötz, H. Lewerenz and S. Stucki, *Journal of The Electrochemical Society*, 1983, **130**, 825-829.
44. R. Kötz, H. Neff and S. Stucki, *Journal of The Electrochemical Society*, 1984, **131**, 72-77.
45. T. Audichon, T. W. Napporn, C. Canaff, C. Morais, C. Comminges and K. B. Kokoh, *The Journal of Physical Chemistry C*, 2016, **120**, 2562-2573.
46. M. Escudero-Escribano, A. F. Pedersen, E. A. Paoli, R. Frydendal, D. Friebel, P. Malacrida, J. Rossmeisl, I. E. L. Stephens and I. Chorkendorff, *The Journal of Physical Chemistry B*, 2018, **122**, 947-955.
47. Y. Yao, S. Hu, W. Chen, Z.-Q. Huang, W. Wei, T. Yao, R. Liu, K. Zang, X. Wang, G. Wu, W. Yuan, T. Yuan, B. Zhu, W. Liu, Z. Li, D. He, Z. Xue, Y. Wang, X. Zheng, J. Dong, C.-R. Chang, Y. Chen, X. Hong, J. Luo, S. Wei, W.-X. Li, P. Strasser, Y. Wu and Y. Li, *Nature Catalysis*, 2019, **2**, 304-313.
48. P. Li, M. Wang, X. Duan, L. Zheng, X. Cheng, Y. Zhang, Y. Kuang, Y. Li, Q. Ma, Z. Feng, W. Liu and X. Sun, *Nature Communications*, 2019, **10**, 1711.

49. M. W. Kanan and D. G. Nocera, *Science (New York, N.Y.)*, 2008, **321**, 1072-1075.
50. M. W. Kanan, J. Yano, Y. Surendranath, M. Dinca, V. K. Yachandra and D. G. Nocera, *Journal of the American Chemical Society*, 2010, **132**, 13692-13701.
51. J. G. McAlpin, Y. Surendranath, M. Dincă, T. A. Stich, S. A. Stoian, W. H. Casey, D. G. Nocera and R. D. Britt, *Journal of the American Chemical Society*, 2010, **132**, 6882-6883.
52. Y. Surendranath, M. W. Kanan and D. G. Nocera, *Journal of the American Chemical Society*, 2010, **132**, 16501-16509.
53. J. Wang, W. Cui, Q. Liu, Z. Xing, A. M. Asiri and X. Sun, *Advanced Materials*, 2016, **28**, 215-230.
54. L. Han, S. Dong and E. Wang, *Advanced Materials*, 2016, **28**, 9266-9291.
55. L. Xu, Q. Jiang, Z. Xiao, X. Li, J. Huo, S. Wang and L. Dai, *Angewandte Chemie International Edition*, 2016, **55**, 5277-5281.
56. J. Huang, J. Chen, T. Yao, J. He, S. Jiang, Z. Sun, Q. Liu, W. Cheng, F. Hu, Y. Jiang, Z. Pan and S. Wei, *Angewandte Chemie International Edition*, 2015, **54**, 8722-8727.
57. S.-H. Hsu, S.-F. Hung, H.-Y. Wang, F.-X. Xiao, L. Zhang, H. Yang, H. M. Chen, J.-M. Lee and B. Liu, *Small Methods*, 2018, **2**, 1800001.
58. X. Han, C. Yu, S. Zhou, C. Zhao, H. Huang, J. Yang, Z. Liu, J. Zhao and J. Qiu, *Advanced Energy Materials*, 2017, **7**, 1602148.
59. S.-H. Ye, Z.-X. Shi, J.-X. Feng, Y.-X. Tong and G.-R. Li, *Angewandte Chemie International Edition*, 2018, **57**, 2672-2676.
60. B. Qiu, L. Cai, Y. Wang, Z. Lin, Y. Zuo, M. Wang and Y. Chai, *Advanced Functional Materials*, 2018, **28**, 1706008.
61. X. Zheng, B. Zhang, P. De Luna, Y. Liang, R. Comin, O. Voznyy, L. Han, F. P. García de Arquer, M. Liu, C. T. Dinh, T. Regier, J. J. Dynes, S. He, H. L. Xin, H. Peng, D. Prendergast, X. Du and E. H. Sargent, *Nature Chemistry*, 2017, **10**, 149.
62. Z.-F. Huang, J. Song, Y. Du, S. Xi, S. Dou, J. M. V. Nsanzimana, C. Wang, Z. J. Xu and X. Wang, *Nature Energy*, 2019, **4**, 329-338.
63. F. Song and X. Hu, *Journal of the American Chemical Society*, 2014, **136**, 16481-16484.
64. J. Nai, B. Y. Guan, L. Yu and X. W. Lou, *Science Advances*, 2017, **3**, e1700732.

65. L. Liardet and X. Hu, *ACS Catalysis*, 2018, **8**, 644-650.
66. K. Chakrapani, G. Bendt, H. Hajiyani, T. Lunkenbein, M. T. Greiner, L. Masliuk, S. Salamon, J. Landers, R. Schlögl, H. Wende, R. Pentcheva, S. Schulz and M. Behrens, *ACS Catalysis*, 2018, **8**, 1259-1267.
67. J. Bao, Z. Wang, J. Xie, L. Xu, F. Lei, M. Guan, Y. Zhao, Y. Huang and H. Li, *Chemical Communications*, 2019, **55**, 3521-3524.
68. K. Fan, Y. Ji, H. Zou, J. Zhang, B. Zhu, H. Chen, Q. Daniel, Y. Luo, J. Yu and L. Sun, *Angewandte Chemie International Edition*, 2017, **56**, 3289-3293.
69. K. Fan, H. Chen, Y. Ji, H. Huang, P. M. Claesson, Q. Daniel, B. Philippe, H. Rensmo, F. Li and Y. Luo, *Nature Communications*, 2016, **7**,11981.
70. J. Huang, J. Chen, T. Yao, J. He, S. Jiang, Z. Sun, Q. Liu, W. Cheng, F. Hu and Y. Jiang, *Angewandte Chemie*, 2015, **127**, 8846-8851.
71. S. Wan, J. Qi, W. Zhang, W. Wang, S. Zhang, K. Liu, H. Zheng, J. Sun, S. Wang and R. Cao, *Advanced Materials*, 2017, **29**, 1700286.
72. M. Chauhan, K. P. Reddy, C. S. Gopinath and S. Deka, *ACS Catalysis*, 2017, **7**, 5871-5879.
73. P. Cai, J. Huang, J. Chen and Z. Wen, *Angewandte Chemie International Edition*, 2017, **56**, 4858-4861.
74. B. Zhang, X. Zheng, O. Voznyy, R. Comin, M. Bajdich, M. García-Melchor, L. Han, J. Xu, M. Liu, L. Zheng, F. P. García de Arquer, C. T. Dinh, F. Fan, M. Yuan, E. Yassitepe, N. Chen, T. Regier, P. Liu, Y. Li, P. De Luna, A. Janmohamed, H. L. Xin, H. Yang, A. Vojvodic and E. H. Sargent, *Science*, 2016, **352**, 333-337.
75. P.-P. Liu, Y.-Q. Zheng, H.-L. Zhu and T.-T. Li, *ACS Applied Nano Materials*, 2019, **2**, 744-749.
76. M.-R. Gao, Y.-F. Xu, J. Jiang, Y.-R. Zheng and S.-H. Yu, *Journal of the American Chemical Society*, 2012, **134**, 2930-2933.
77. X. Li, H. Liu, Z. Chen, Q. Wu, Z. Yu, M. Yang, X. Wang, Z. Cheng, Z. Fu and Y. Lu, *Nature Communications*, 2019, **10**, 1409.
78. S. Zhao, Y. Wang, J. Dong, C.-T. He, H. Yin, P. An, K. Zhao, X. Zhang, C. Gao, L. Zhang, J. Lv, J. Wang, J. Zhang, A. M. Khattak, N. A. Khan, Z. Wei, J. Zhang, S. Liu, H. Zhao and Z. Tang, *Nature Energy*, 2016, **1**, 16184.
79. F. Song and X. Hu, *Nature Communications*, 2014, **5**, 4477.
80. J. Wang, L. Gan, W. Zhang, Y. Peng, H. Yu, Q. Yan, X. Xia and X. Wang, *Science*

Advances, 2018, **4**, eaap7970.

81. Y. Yang, L. Dang, M. J. Shearer, H. Sheng, W. Li, J. Chen, P. Xiao, Y. Zhang, R. J. Hamers and S. Jin, *Advanced Energy Materials*, 2018, **8**, 1703189.
82. M. Dincă, Y. Surendranath and D. G. Nocera, *Proceedings of the National Academy of Sciences of the United States of America*, 2010, **107**, 10337-10341.
83. D. K. Bediako, B. Lassalle-Kaiser, Y. Surendranath, J. Yano, V. K. Yachandra and D. G. Nocera, *Journal of the American Chemical Society*, 2012, **134**, 6801-6809.
84. L. Trotochaud, S. L. Young, J. K. Ranney and S. W. Boettcher, *Journal of the American Chemical Society*, 2014, **136**, 6744-6753.
85. D. Friebel, M. W. Louie, M. Bajdich, K. E. Sanwald, Y. Cai, A. M. Wise, M.-J. Cheng, D. Sokaras, T.-C. Weng, R. Alonso-Mori, R. C. Davis, J. R. Bargar, J. K. Nørskov, A. Nilsson and A. T. Bell, *Journal of the American Chemical Society*, 2015, **137**, 1305-1313.
86. M. Görlin, P. Chernev, J. Ferreira de Araújo, T. Reier, S. Dresp, B. Paul, R. Krähnert, H. Dau and P. Strasser, *Journal of the American Chemical Society*, 2016, **138**, 5603-5614.
87. M. Görlin, J. Ferreira de Araújo, H. Schmies, D. Bernsmeier, S. Dresp, M. Gliech, Z. Jusys, P. Chernev, R. Kraehnert, H. Dau and P. Strasser, *Journal of the American Chemical Society*, 2017, **139**, 2070-2082.
88. A. Murphy, P. Barnes, L. Randeniya, I. Plumb, I. Grey, M. Horne and J. Glasscock, *International journal of hydrogen energy*, 2006, **31**, 1999-2017.
89. H. Xu, S. Ouyang, L. Liu, P. Reunchan, N. Umezawa and J. Ye, *Journal of Materials Chemistry A*, 2014, **2**, 12642-12661.
90. S. Piskunov, O. Lisovski, J. Begens, D. Bocharov, Y. F. Zhukovskii, M. Wessel and E. Spohr, *The Journal of Physical Chemistry C*, 2015, **119**, 18686-18696.
91. X. Chen, L. Liu, P. Y. Yu and S. S. Mao, *Science*, 2011, **331**, 746-750.
92. K. Sivula, F. L. Formal and M. Gratzel, *Chemsuschem*, 2011, **4**, 432-449.
93. D. A. Wheeler, G. Wang, Y. Ling, Y. Li and J. Z. Zhang, *Energy & Environmental Science*, 2012, **5**, 6682-6702.
94. Q. Yu, X. Meng, T. Wang, P. Li and J. Ye, *Advanced Functional Materials*, 2015, **25**, 2686-2692.
95. L. Steier, I. Herraiz-Cardona, S. Gimenez, F. Fabregat-Santiago, J. Bisquert, S. D. Tilley and M. Grätzel, *Advanced Functional Materials*, 2014, **24**, 7681-7688.

96. P. Peerakiatkhajohn, J.-H. Yun, H. Chen, M. Lyu, T. Butburee and L. Wang, *Advanced Materials*, 2016, **28**, 6405-6410.
97. A. Kudo, K. Ueda, H. Kato and I. Mikami, *Catalysis Letters*, 1998, **53**, 229-230.
98. Y. Park, K. J. McDonald and K.-S. Choi, *Chemical Society Reviews*, 2013, **42**, 2321-2337.
99. S. K. Pilli, T. E. Furtak, L. D. Brown, T. G. Deutsch, J. A. Turner and A. M. Herring, *Energy & Environmental Science*, 2011, **4**, 5028-5034.
100. S. J. a. Moniz, J. Zhu and J. Tang, *Advanced Energy Materials*, 2014, 4, 1301590.
101. T. W. Kim and K.-S. Choi, *Science*, 2014, **343**, 990-994.
102. Y. Qiu, W. Liu, W. Chen, W. Chen, G. Zhou, P.-C. Hsu, R. Zhang, Z. Liang, S. Fan, Y. Zhang and Y. Cui, *Science Advances*, 2016, **2**, e1501764.
103. R. Liu, Z. Zheng, J. Spurgeon and X. Yang, *Energy & Environmental Science*, 2014, **7**, 2504-2517.
104. M. F. Lichterman, A. I. Carim, M. T. McDowell, S. Hu, H. B. Gray, B. S. Brunschwig and N. S. Lewis, *Energy & Environmental Science*, 2014, **7**, 3334-3337.
105. A. Pareek, P. Paik and P. H. Borse, *Langmuir*, 2014, **30**, 15540-15549.
106. G. Ai, H. Li, S. Liu, R. Mo and J. Zhong, *Advanced Functional Materials*, 2015, **25**, 5706-5713.
107. S. Hu, M. R. Shaner, J. a. Beardslee, M. Lichterman, B. S. Brunschwig and N. S. Lewis, *Science*, 2014, **344**, 2547-2552.
108. K. Sun, F. H. Saadi, M. F. Lichterman, W. G. Hale, H.-P. Wang, X. Zhou, N. T. Plymale, S. T. Omelchenko, J.-H. He and K. M. Papadantonakis, *Proceedings of the National Academy of Sciences*, 2015, **112**, 3612-3617.
109. A. Paracchino, N. Mathews, T. Hisatomi, M. Stefik, S. D. Tilley and M. Grätzel, *Energy & Environmental Science*, 2012, **5**, 8673.
110. K. Sun, S. Shen, Y. Liang, P. E. Burrows, S. S. Mao and D. Wang, *Chemical reviews*, 2014, 17, 8662-8719.
111. A. Paracchino, V. Laporte, K. Sivula, M. Grätzel and E. Thimsen, *Nature materials*, 2011, **10**, 456-461.
112. L. Gao, Y. Cui, J. L. Wang, A. Cavalli, A. Standing, T. T. T. Vu, M. A. Verheijen, J. E. M. Haverkort, E. P. A. M. Bakkers and P. H. L. Notten, *Nano Letters*, 2014, **14**, 3715-3719.

113. M. M. May, H.-J. Lewerenz, D. Lackner, F. Dimroth and T. Hannappel, *Nature Communications*, 2015, **6**, 8286.
114. L. Ji, M. D. Mcdaniel, S. Wang, A. B. Posadas, X. Li, H. Huang, J. C. Lee, A. A. Demkov, A. J. Bard and J. G. Ekerdt, *Nature Nanotechnology*, 2015, **10**, 84-90.
115. M. T. Koper, *Journal of Electroanalytical Chemistry*, 2011, **660**, 254-260.
116. M. G. Walter, E. L. Warren, J. R. McKone, S. W. Boettcher, Q. Mi, E. a. Santori and N. S. Lewis, *Chemical Reviews*, 2010, **110**, 6446-6473.
117. C. C. L. McCrory, S. Jung, J. C. Peters and T. F. Jaramillo, *Journal of the American Chemical Society*, 2013, **135**, 16977-16987.
118. C. C. L. McCrory, S. Jung, I. M. Ferrer, S. M. Chatman, J. C. Peters and T. F. Jaramillo, *Journal of the American Chemical Society*, 2015, **137**, 4347-4357.
119. M. Gao, W. Sheng, Z. Zhuang, Q. Fang, S. Gu, J. Jiang and Y. Yan, 2014, 136, 7077-7084.
120. W. Luo, C. Jiang, Y. Li, S. A. Shevlin, X. Han, K. Qiu, Y. Cheng, Z. Guo, W. Huang and J. Tang, *Journal of Materials Chemistry A*, 2017, **5**, 2021-2028.
121. C. Jiang, S. J. a. Moniz, M. Khraisheh and J. Tang, *Chemistry- A European Journal*, 2014, **20**, 12954-12961.
122. M. J. Kenney, M. Gong, Y. Li, J. Z. Wu, J. Feng, M. Lanza and H. Dai, *Science*, 2013, **342**, 836-840.
123. F. Malara, A. Minguzzi, M. Marelli, S. Morandi, R. Psaro, V. Dal Santo and A. Naldoni, *ACS Catalysis*, 2015, **5**, 5292-5300.
124. W. D. Chemelewski, H. Lee, J. Lin, A. J. Bard and C. B. Mullins, *Journal of the American Chemical Society*, 2014, **136**, 2843-2850.
125. Y. Kuang, Q. Jia, H. Nishiyama, T. Yamada, A. Kudo and K. Domen, *Advanced Energy Materials*, 2016, **6**, 1501645.
126. R. H. Coridan, M. Shaner, C. Wiggenhorn, B. S. Brunschwig and N. S. Lewis, *The Journal of Physical Chemistry C*, 2013, **117**, 6949-6957.
127. P. Bornoz, F. F. Abdi, S. D. Tilley, B. Dam, R. Van De Krol, M. Graetzel and K. Sivula, *The Journal of Physical Chemistry C*, 2014, **118**, 16959-16966.
128. N.Gaillard, Y.Chang, J.Kaneshiro, A.Deangelis, and E. L. Miller, Status of research ontungsten oxide-based photoelectrochemical devices at the University of Hawaii, August,2010.
129. J. Brillet, J.-H. Yum, M. Cornuz, T. Hisatomi, R. Solarska, J. Augustynski, M.

Graetzel and K. Sivula, *Nature Photonics*, 2012, **6**, 824-828.

130. S. Y. Reece, J. A. Hamel, K. Sung, T. D. Jarvi, A. J. Esswein, J. J. H. Pijpers and D. G. Nocera, 2011, **4**, 645-648.
131. C. R. Cox, J. Z. Lee, D. G. Nocera and T. Buonassisi, *Proceedings of the National Academy of Sciences*, 2014, **111**, 14057-14061.
132. O. Khaselev, A. Bansal and J. Turner, *International Journal of Hydrogen Energy*, 2001, **26**, 127-132.
133. Y. Hou, F. Zuo, A. P. Dagg, J. Liu and P. Feng, *Advanced materials*, 2014, 26, 5043-5049.
134. Y. Hou, F. Zuo, A. P. Dagg, J. Liu and P. Feng, *Advanced materials*, 2014, 26, 5043-5049.
135. J. Tauc, *Materials Research Bulletin*, 1968, **3**, 37-46.
136. TSUNEKAWA, Shin, SAHARA, Ryoji, KAWAZOE, Yoshiyuki, KASUYA and Atsuo, 2000, 233.
137. Y. Ma, S. R. Pendlebury, A. Reynal, F. Le Formal and J. R. Durrant, *Chemical Science*, 2014, **5**, 2964-2973.
138. F. Settle, *Handbook of Instrumental Techniques for Anlytical Chemistry*, Prentice Hall PTR, Upper Saddle River, New Jersy, 1997.
139. G. S. Bumbrah and R. M. Sharma, *Egyptian Journal of Forensic Sciences*, 2016, **6**, 209-215.
140. D. A. Skoog, F. J. Holler and S. R. Crouch, *Principles of instrumental analysis*, Cengage learning, Boston, 2017.
141. J. M. Chalmers, H. G. Edwards and M. D. Hargreaves, *Infrared and Raman spectroscopy in forensic science*, John Wiley & Sons, Hoboken, New Jersey, 2012.
142. S. Hofmann, *Auger-and X-ray photoelectron spectroscopy in materials science: a user-oriented guide*, Springer Science & Business Media, Berlin, 2012.
143. D. Koningsberger and R. Prins, X-ray absorption: principles, applications, techniques of EXAFS, SEXAFS, and XANES, 1988.
144. G. Bunker, *Introduction to XAFS: a practical guide to X-ray absorption fine structure spectroscopy*, Cambridge University Press, Cambridge, 2010.
145. J. J. Rehr and R. C. Albers, *Reviews of modern physics*, 2000, **72**, 621.
146. F. Boscherini, in *Characterization of Semiconductor Heterostructures and Nanostructures*, Elsevier, 2008, **11**, 289-330.

147. M. Wang, L. Árnadóttir, Z. J. Xu and Z. Feng, *Nano-Micro Letters*, 2019, **11**, 47.
148. M. Barroso, C. A. Mesa, S. R. Pendlebury, A. J. Cowan, T. Hisatomi, K. Sivula, M. Grätzel, D. R. Klug and J. R. Durrant, *Proceedings of the National Academy of Sciences*, 2012, **109**, 15640-15645.
149. F. M. Pesci, A. J. Cowan, B. D. Alexander, J. R. Durrant and D. R. Klug, *The Journal of Physical Chemistry Letters*, 2011, **2**, 1900-1903.
150. K. Gelderman, L. Lee and S. Donne, *Journal of chemical education*, 2007, **84**, 685.
151. T. Shinagawa, A. T. Garcia-Esparza and K. Takanabe, *Scientific reports*, 2015, **5**, 13801.
152. J. Reichman, *Applied physics letters*, 1980, **36**, 574-577.
153. L. Peter, J. Li and R. Peat, *Journal of electroanalytical chemistry and interfacial electrochemistry*, 1984, **165**, 29-40.
154. R. Memming, *Semiconductor electrochemistry*, John Wiley & Sons, New York, 2008.
155. W. Q. Fang, Z. Huo, P. Liu, X. L. Wang, M. Zhang, Y. Jia, H. Zhang, H. Zhao, H. G. Yang and X. Yao, *Chemistry-A European Journal*, 2014, **20**, 11439-11444.
156. K. Appavoo, M. Liu, C. T. Black and M. Y. Sfeir, *Nano Letters*, 2015, **15**, 1076-1082.
157. C. Ding, J. Shi, D. Wang, Z. Wang, N. Wang, G. Liu, F. Xiong and C. Li, *Physical Chemistry Chemical Physics*, 2013, **15**, 4589-4595.
158. W. Li, P. Da, Y. Zhang, Y. Wang, X. Lin, X. Gong and G. Zheng, *ACS nano*, 2014, **8**, 11770-11777.
159. X. Qi, G. She, M. Wang, L. Mu and W. Shi, *Chemical Communications*, 2013, **49**, 5742-5744.
160. P. M. Chee, P. P. Boix, H. Ge, Y. Fang, J. Barber and L. H. Wong, 2015, **7,** 6852-6859.
161. D. Sharma, S. Upadhyay, V. R. Satsangi, R. Shrivastav, U. V. Waghmare and S. Dass, *The Journal of Physical Chemistry C*, 2014, **118**, 25320-25329.
162. S. Hu, C.-Y. Chi, K. T. Fountaine, M. Yao, H. A. Atwater, P. D. Dapkus, N. S. Lewis and C. Zhou, *Energy & Environmental Science*, 2013, **6**, 1879-1890.
163. L. Gao, Y. Cui, J. Wang, A. Cavalli, A. Standing, T. T. T. Vu, M. a. Verheijen, J. E. M. Haverkort, E. P. a. M. Bakkers and P. H. L. Notten, *Nano Letters*, 2014,

14, 3715-3719.

164. Y. Zhao, N. C. Anderson, K. Zhu, J. A. Aguiar, J. A. Seabold, J. v. d. Lagemaat, H. Branz, N. Neale and J. Oh, *Nano Letters*, 2015, **15**, 2517-2525.
165. Z. Chen, T. F. Jaramillo, T. G. Deutsch, A. Kleiman-Shwarsctein, A. J. Forman, N. Gaillard, R. Garland, K. Takanabe, C. Heske, M. Sunkara, E. W. McFarland, K. Domen, E. L. Miller, J. a. Turner and H. N. Dinh, *Journal of Materials Research*, 2011, **25**, 3-16.
166. H. Kung, H. Jarrett, A. W. Sleight and A. Ferretti, *Journal of applied physics*, 1977, **48**, 2463-2469.
167. M. Etman, *Electrochimica Acta*, 1990, **35**, 1195-1199.
168. X. Shi, I. Y. Choi, K. Zhang, J. Kwon, D. Y. Kim, J. K. Lee, S. H. Oh, J. K. Kim and J. H. Park, *Nature communications*, 2014, **5**, 4775.
169. R. L. Grob and E. F. Barry, *Modern practice of gas chromatography*, John Wiley & Sons, New York, 2004.
170. D. Hughes, *Journal of Chemical Education*, 1965, **42**, 450.
171. K. Kadoya, N. Matsunaga and A. Nagashima, *Journal of physical and chemical reference data*, 1985, **14**, 947-970.
172. A. H. FUJISHIMA, KENICHI, *Nature*, 1972, **238**, 37-38.
173. A. Wolcott, W. A. Smith, T. R. Kuykendall, Y. Zhao and J. Z. Zhang, *Small*, 2009, **5**, 104-111.
174. X. Y. Yang, A. Wolcott, G. M. Wang, A. Sobo, R. C. Fitzmorris, F. Qian, J. Z. Zhang and Y. Li, *Nano Letters*, 2009, **9**, 2331-2336.
175. V. Chakrapani, J. Thangala and M. K. Sunkara, *International Journal of Hydrogen Energy*, 2009, **34**, 9050-9059.
176. Y. Park, K. J. McDonald and K. S. Choi, *Chemical Society Reviews*, 2013, **42**, 2321-2337.
177. K. Sivula, R. Zboril, F. Le Formal, R. Robert, A. Weidenkaff, J. Tucek, J. Frydrych and M. Grätzel, *Journal of the American Chemical Society*, 2010, **132**, 7436-7444.
178. N. Serpone, D. Lawless, R. Khairutdinov and E. Pelizzetti, *The Journal of Physical Chemistry*, 1995, **99**, 16655-16661.
179. D. W. Bahnemann, M. Hilgendorff and R. Memming, *The Journal of Physical Chemistry B*, 1997, **101**, 4265-4275.
180. X. B. Cao, P. Chen and Y. Guo, *J Phys Chem C*, 2008, **112**, 20560-20566.

181. E. Hendry, M. Koeberg, B. O'Regan and M. Bonn, *Nano letters*, 2006, **6**, 755-759.
182. D.-K. Hwang, H.-S. Kim, J.-H. Lim, J.-Y. Oh, J.-H. Yang, S.-J. Park, K.-K. Kim, D. C. Look and Y. Park, *Applied physics letters*, 2005, **86**, 151917.
183. M. Liu, C.-Y. Nam, C. T. Black, J. Kamcev and L. Zhang, *The Journal of Physical Chemistry C*, 2013, **117**, 13396-13402.
184. M. Shi, X. Pan, W. Qiu, D. Zheng, M. Xu and H. Chen, *International journal of hydrogen energy*, 2011, **36**, 15153-15159.
185. N. Chouhan, C. L. Yeh, S.-F. Hu, R.-S. Liu, W.-S. Chang and K.-H. Chen, *Chemical Communications*, 2011, **47**, 3493-3495.
186. G. Wang, X. Yang, F. Qian, J. Z. Zhang and Y. Li, *Nano Letters*, 2010, **10**, 1088-1092.
187. S. Xie, X. Lu, T. Zhai, W. Li, M. Yu, C. Liang and Y. Tong, *Journal of Materials Chemistry*, 2012, **22**, 14272-14275.
188. J. Sun, D. K. Zhong and D. R. Gamelin, *Energy & Environmental Science*, 2010, **3**, 1252-1261.
189. L. Shi, Y. Xu, S. Hark, Y. Liu, S. Wang, L.-m. Peng, K. Wong and Q. Li, *Nano Letters*, 2007, **7**, 3559-3563.
190. S. J. a. Moniz, J. Zhu and J. Tang, *Advanced Energy Materials*, 2014, 4, 1301590.
191. L. E. Greene, M. Law, J. Goldberger, F. Kim, J. C. Johnson, Y. Zhang, R. J. Saykally and P. Yang, *Angewandte Chemie International Edition*, 2003, **42**, 3031-3034.
192. L. E. Greene, M. Law, D. H. Tan, M. Montano, J. Goldberger, G. Somorjai and P. Yang, *Nano letters*, 2005, **5**, 1231-1236.
193. F. Dong, S. Guo, H. Wang, X. Li and Z. Wu, *The Journal of Physical Chemistry C*, 2011, **115**, 13285-13292.
194. S. K. Choi, W. Choi and H. Park, *Physical Chemistry Chemical Physics*, 2013, **15**, 6499-6507.
195. Q. Li, J. Bian, J. Sun, J. Wang, Y. Luo, K. Sun and D. Yu, *Applied Surface Science*, 2010, **256**, 1698-1702.
196. T. Makino, Y. Segawa, A. Tsukazaki, A. Ohtomo and M. Kawasaki, *Applied Physics Letters*, 2005, **87**, 022101.
197. J. W. Sun, Y. M. Lu, Y. C. Liu, D. Z. Shen, Z. Z. Zhang, B. H. Li, J. Y. Zhang,

B. Yao, D. X. Zhao and X. W. Fan, *Applied Physics Letters*, 2006, **89**, 232101.

198. A. Tsukazaki, A. Ohtomo, T. Onuma, M. Ohtani, T. Makino, M. Sumiya, K. Ohtani, S. F. Chichibu, S. Fuke and Y. Segawa, *Nature materials*, 2005, **4**, 42-46.
199. G. D. Yuan, W. J. Zhang, J. S. Jie, X. Fan, J. A. Zapien, Y. H. Leung, L. B. Luo, P. F. Wang, C. S. Lee and S. T. Lee, *Nano Letters*, 2008, **8**, 2591-2597.
200. H. M. Chen, C. K. Chen, Y.-C. Chang, C.-W. Tsai, R.-S. Liu, S.-F. Hu, W.-S. Chang and K.-H. Chen, *Angewandte Chemie*, 2010, **122**, 6102-6105.
201. R. Cai, Y. Du, W. Zhang, H. Tan, T. Zeng, X. Huang, H. Yang, C. Chen, H. Liu, J. Zhu, S. Peng, J. Chen, Y. Zhao, H. Wu, Y. Huang, R. Xu, T. M. Lim, Q. Zhang, H. Zhang and Q. Yan, *Chemistry- A European Journal*, 2013, **19**, 1568-1572.
202. E. M. Steinmiller and K.-S. Choi, *Proceedings of the National Academy of Sciences*, 2009, **106**, 20633-20636.
203. M. J. Kenney, M. Gong, Y. Li, J. Z. Wu, J. Feng, M. Lanza and H. Dai, *Science*, 2013, **342**, 836-840.
204. B. Klahr, S. Gimenez, F. Fabregat-Santiago, J. Bisquert and T. W. Hamann, *Journal of the American Chemical Society*, 2012, **134**, 16693-16700.
205. K. J. McDonald and K.-S. Choi, *Chemistry of Materials*, 2011, **23**, 1686-1693.
206. D. K. Zhong, S. Choi and D. R. Gamelin, *Journal of the American Chemical Society*, 2011, **133**, 18370-18377.
207. J. A. Seabold and K. S. Choi, *Chemistry of Materials*, 2011, **23**, 1105-1112.
208. S. Y. Reece, J. A. Hamel, K. Sung, T. D. Jarvi, A. J. Esswein, J. J. H. Pijpers and D. G. Nocera, *Science*, 2011, **334**, 645-648.
209. H. M. Chen, C. K. Chen, C. C. Lin, R.-S. Liu, H. Yang, W.-S. Chang, K.-H. Chen, T.-S. Chan, J.-F. Lee and D. P. Tsai, *The Journal of Physical Chemistry C*, 2011, **115**, 21971-21980.
210. Y. Hou, F. Zuo, A. P. Dagg, J. Liu and P. Feng, *Advanced Materials*, 2014, **26**, 5043-5049.
211. M. W. Kanan, Y. Surendranath and D. G. Nocera, *Chemical Society Reviews*, 2009, **38**, 109-114.
212. Y. Wang, Y. Wang, R. Jiang and R. Xu, *Industrial & Engineering Chemistry Research*, 2012, **51**, 9945-9951.
213. D. L. Felker and P. M. Sherwood, *Surface Science Spectra*, 2003, **9**, 106-113.
214. R. K. Brow, *Journal of non-crystalline solids*, 1996, **194**, 267-273.

215. J. R. Bolton, S. J. Strickler and J. S. Connolly, *Nature*, 1985, **316**, 495-500.
216. T. G. Deutsch, C. A. Koval and J. A. Turner, *The Journal of Physical Chemistry B*, 2006, **110**, 25297-25307.
217. O. Khaselev and J. A. Turner, *Science*, 1998, **280**, 425-427.
218. L. Kornblum, D. Fenning, J. Faucher, J. Hwang, A. Boni, M. Han, M. Morales-Acosta, Y. Zhu, E. Altman and M. Lee, *Energy & Environmental Science*, 2017, **10**, 377-382.
219. S. Hu, M. R. Shaner, J. A. Beardslee, M. Lichterman, B. S. Brunschwig and N. S. Lewis, *Science*, 2014, **344**, 1005-1009.
220. K. Sun, Y. Kuang, E. Verlage, B. S. Brunschwig, C. W. Tu and N. S. Lewis, *Advanced Energy Materials*, 2015, **5**, 1402276.
221. A. J. Henegar, A. J. Cook, P. Dang and T. Gougousi, *ACS Applied Materials & Interfaces*, 2016, **8**, 1667-1675.
222. H. Kuhr, W. Ranke and J. Finster, *Surface Science*, 1986, **178**, 171-178.
223. S. K. Choi, W. Choi and H. Park, *Physical chemistry chemical physics*, 2013, **15**, 6499-6507.
224. T. Jin, P. Diao, D. Xu and Q. Wu, *Electrochimica Acta*, 2013, **114**, 271-277.
225. M. Dincă, Y. Surendranath and D. G. Nocera, *Proceedings of the National Academy of Sciences*, 2010, **107**, 10337-10341.
226. E. Janik, P. Dluzewski, S. Kret, A. Presz, H. Kirmse, W. Neumann, W. Zaleszczyk, L. T. Baczewski, A. Pietruczik, E. Dynowska, J. Sadowski, W. Caliebe, G. Karczewski and T. Wojtowicz, *Catalytic growth of ZnTe nanowires by molecular beam epitaxy: Structural studies*, 2007, 18, 475606.
227. C. Dong, X. Yuan, X. Wang, X. Liu, W. Dong, R. Wang, Y. Duan and F. Huang, *Journal of Materials Chemistry A*, 2016, **4**, 11292-11298.
228. X. Zhang, R. Liu, Y. Zang, G. Liu, G. Wang, Y. Zhang, H. Zhang and H. Zhao, *Chemical Communications*, 2016, **52**, 5946-5949.
229. Y. Zhang, F. Ding, C. Deng, S. Zhen, X. Li, Y. Xue, Y.-M. Yan and K. Sun, *Catalysis Communications*, 2015, **67**, 78-82.
230. Y. Liang, H. Wang, J. Zhou, Y. Li, J. Wang, T. Regier and H. Dai, *Journal of the American Chemical Society*, 2012, **134**, 3517-3523.
231. H. Zhang, B. Chen, H. Jiang, X. Duan, Y. Zhu and C. Li, *Nanoscale*, 2018, **10**, 12991-12996.
232. A. Aijaz, J. Masa, C. Rösler, W. Xia, P. Weide, A. J. R. Botz, R. A. Fischer, W.

Schuhmann and M. Muhler, 2016, **55**, 4087-4091.

233. A. Grimaud, K. J. May, C. E. Carlton, Y.-L. Lee, M. Risch, W. T. Hong, J. Zhou and Y. Shao-Horn, *Nature Communications*, 2013, **4**, 2439.

234. B. S. Yeo and A. T. Bell, *Journal of the American Chemical Society*, 2011, **133**, 5587-5593.

235. R. Wei, M. Fang, G. Dong, C. Lan, L. Shu, H. Zhang, X. Bu and J. C. Ho, *ACS Applied Materials & Interfaces*, 2018, **10**, 7079-7086.

236. L. Zhuang, L. Ge, Y. Yang, M. Li, Y. Jia, X. Yao and Z. Zhu, *Advanced Materials*, 2017, **29**, 1606793.

237. J. Wang, R. Gao, D. Zhou, Z. Chen, Z. Wu, G. Schumacher, Z. Hu and X. Liu, *ACS Catalysis*, 2017, **7**, 6533-6541.

238. F.-C. Shen, Y. Wang, Y.-J. Tang, S.-L. Li, Y.-R. Wang, L.-Z. Dong, Y.-F. Li, Y. Xu and Y.-Q. Lan, *ACS Energy Letters*, 2017, **2**, 1327-1333.

239. X. Wang, P. Sun, H. Lu, K. Tang, Q. Li, C. Wang, Z. Mao, T. Ali and C. Yan, 2019, **11**,1804886.

240. M. Yang, Y. Li, Y. Yu, X. Liu, Z. Shi and Y. Xing, 2018, **24**, 13002-13008.

241. I. L. Júnior, J.-M. M. Millet, M. Aouine and M. do Carmo Rangel, *Applied Catalysis A: General*, 2005, **283**, 91-98.

242. K. Fan, Y. Ji, H. Zou, J. Zhang, B. Zhu, H. Chen, Q. Daniel, Y. Luo, J. Yu and L. Sun, *Angew Chem Int Ed Engl*, 2017, **56**, 3289-3293.

243. T. M. Masikhwa, J. K. Dangbegnon, A. Bello, M. J. Madito, D. Momodu and N. Manyala, *Journal of Physics and Chemistry of Solids*, 2016, **88**, 60-67.

244. W. Wang and J. Xu, *ACS Applied Materials & Interfaces*, 2015, **7**, 415-421.

245. J. Yang, H. Cheng and R. L. Frost, *Spectrochimica Acta Part A: Molecular and Biomolecular Spectroscopy*, 2011, **78**, 420-428.

246. J. Zhang, W. Gao, M. Dou, F. Wang, J. Liu, Z. Li and J. Ji, *Analyst*, 2015, **140**, 1686-1692.

247. S. Huanhuan, L. Hanfeng, M. Fangwang and W. Zhoucheng, *Angewandte Chemie*, 2017, **129**, 588-592.

248. J. C., N. G. A. and B. O., *physica status solidi (b)*, 1997, **201**, 319-326.

249. S. Lee, *Solid State Ionics*, 2003, **165**, 111-116.

250. L. Frost Ray, A. Henry Dermot, L. Weier Matt and W. Martens, *Journal of Raman Spectroscopy*, 2006, **37**, 722-732.

251. C. Julien, M. Massot and C. Pérez-Vicente, *Materials Science and Engineering:*

B, 2000, **75**, 6-12.

252. Y. Ji, Z. Zhao, A. Duan, G. Jiang and J. Liu, *The Journal of Physical Chemistry C*, 2009, **113**, 7186-7199.
253. A. Parmaliana, F. Arena, F. Frusteri, G. Martra, S. Coluccia and V. Sokolovskii, in *Studies in Surface Science and Catalysis*, eds. R. K. Grasselli, S. T. Oyama, A. M. Gaffney and J. E. Lyons, 1997, **110**, 347-356.
254. J. Pritchard, L. Morris, D. Walsh, S. Sadasivan, H. Ménard, R. M. Bellabarba, M. T. Weller and R. P. Tooze, *Catalysis Letters*, 2018, **148**, 235-245.
255. S. Li, S. Peng, L. Huang, X. Cui, A. M. Al-Enizi and G. Zheng, *ACS Applied Materials & Interfaces*, 2016, **8**, 20534-20539.
256. C.-T. Wang, M.-T. Chen and D.-L. Lai, *Applied Surface Science*, 2011, **257**, 5109-5114.
257. D. C. Frost, C. A. McDowell and I. S. Woolsey, *Chemical Physics Letters*, 1972, **17**, 320-323.
258. D. C. Frost, C. A. McDowell and I. S. Woolsey, *Molecular Physics*, 1974, **27**, 1473-1489.
259. H. Liu, X. Liu, Z. Mao, Z. Zhao, X. Peng, J. Luo and X. Sun, *Journal of Power Sources*, 2018, **400**, 190-197.
260. W. G. Hardin, D. A. Slanac, X. Wang, S. Dai, K. P. Johnston and K. J. Stevenson, *The Journal of Physical Chemistry Letters*, 2013, **4**, 1254-1259.
261. J. Suntivich, H. A. Gasteiger, N. Yabuuchi, H. Nakanishi, J. B. Goodenough and Y. Shao-Horn, *Nature Chemistry*, 2011, **3**, 546.
262. J. Suntivich, K. J. May, H. A. Gasteiger, J. B. Goodenough and Y. Shao-Horn, 2011, **334**, 1383-1385.
263. Y. Zhan, G. Du, S. Yang, C. Xu, M. Lu, Z. Liu and J. Y. Lee, *ACS Applied Materials & Interfaces*, 2015, **7**, 12930-12936.
264. X. Peng, L. Wang, L. Hu, Y. Li, B. Gao, H. Song, C. Huang, X. Zhang, J. Fu, K. Huo and P. K. Chu, *Nano Energy*, 2017, **34**, 1-7.
265. M. Xing, L.-B. Kong, M.-C. Liu, L.-Y. Liu, L. Kang and Y.-C. Luo, *Journal of Materials Chemistry A*, 2014, **2**, 18435-18443.
266. J. Zhang, B. Yuan, S. Cui, N. Zhang, J. Wei, X. Wang, D. Zhang, R. Zhang and Q. Huo, *Dalton Transactions*, 2017, **46**, 3295-3302.
267. Y. Sun, S. Gao, F. Lei and Y. Xie, *Chemical Society Reviews*, 2015, **44**, 623-636.
268. T. Maiyalagan, K. A. Jarvis, S. Therese, P. J. Ferreira and A. Manthiram, *Nature*

Communications, 2014, **5**, 3949.

269. J. Rosen, G. S. Hutchings and F. Jiao, *Journal of the American Chemical Society*, 2013, **135**, 4516-4521.
270. Y. Sun, S. Gao, F. Lei, J. Liu, L. Liang and Y. Xie, *Chemical Science*, 2014, **5**, 3976-3982.
271. M. S. Burke, M. G. Kast, L. Trotochaud, A. M. Smith and S. W. Boettcher, *Journal of the American Chemical Society*, 2015, **137**, 3638-3648.
272. M. S. Burke, L. J. Enman, A. S. Batchellor, S. Zou and S. W. Boettcher, *Chemistry of Materials*, 2015, **27**, 7549-7558.
273. L. Wang, C. Lin, F. Zhang and J. Jin, *ACS Nano*, 2014, **8**, 3724-3734.
274. J. Haber, M. Witko and R. Tokarz, *Applied Catalysis A: General*, 1997, **157**, 3-22.
275. J. Jiang, F. Sun, S. Zhou, W. Hu, H. Zhang, J. Dong, Z. Jiang, J. Zhao, J. Li, W. Yan and M. Wang, *Nature Communications*, 2018, **9**, 2885.
276. T. Chun, Z. Rong, L. Wenbo, H. Liangbo, J. Xiue, A. A. M. and S. Xuping, *Advanced Materials*, 2017, **29**, 1602441.
277. B. S. Yeo, *Nature Catalysis*, 2019, **2**, 284-285.
278. C. Wei, Z. Feng, G. G. Scherer, J. Barber, Y. Shao-Horn and Z. J. Xu, *Advanced Materials*, 2017, **29**, 1606800.
279. J. R. Petrie, H. Jeen, S. C. Barron, T. L. Meyer and H. N. Lee, *Journal of the American Chemical Society*, 2016, **138**, 7252-7255.
280. H. Liu, X. Liu, Z. Mao, Z. Zhao, X. Peng, J. Luo and X. Sun, *Journal of Power Sources*, 2018, **400**, 190-197.
281. M. Pramanik, C. Li, M. Imura, V. Malgras, Y.-M. Kang and Y. Yamauchi, *Small*, 2016, **12**, 1709-1715.
282. Z. Xu, S.-c. Yan, Z. Shi, Y.-f. Yao, P. Zhou, H.-y. Wang and Z.-g. Zou, *ACS Applied Materials & Interfaces*, 2016, **8**, 12887-12893.
283. A. Bergmann, E. Martinez-Moreno, D. Teschner, P. Chernev, M. Gliech, J. F. de Araújo, T. Reier, H. Dau and P. Strasser, *Nature Communications*, 2015, **6**, 8625.
284. X. Miao, L. Wu, Y. Lin, X. Yuan, J. Zhao, W. Yan, S. Zhou and L. Shi, *Chemical Communications*, 2019, **55**, 1442-1445.
285. Y. Tong, Y. Guo, P. Chen, H. Liu, M. Zhang, L. Zhang, W. Yan, W. Chu, C. Wu and Y. Xie, *Chem*, 2017, **3**, 812-821.
286. Y.-Z. Jin, Z. Li, J.-Q. Wang, R. Li, Z.-Q. Li, H. Liu, J. Mao, C.-K. Dong, J. Yang,

S.-Z. Qiao and X.-W. Du, *Advanced Energy Materials*, 2018, **8**, 1703469.

287. T. Pauporté, L. Mendoza, M. Cassir, M. Bernard and J. Chivot, *Journal of the Electrochemical Society*, 2005, **152**, C49-C53.

288. Y.-C. Liu, J. A. Koza and J. A. Switzer, *Electrochimica Acta*, 2014, **140**, 359-365.

289. Z. Chen, C. X. Kronawitter, Y.-W. Yeh, X. Yang, P. Zhao, N. Yao and B. E. Koel, *Journal of Materials Chemistry A*, 2017, **5**, 842-850.

290. W. Chen, L. Mai, J. Peng, Q. Xu and Q. Zhu, *Journal of Solid State Chemistry*, 2004, **177**, 377-379.

291. N. Van Landschoot, E. M. Kelder and J. Schoonman, *Solid State Ionics*, 2004, **166**, 307-316.

292. R. L. Frost, D. A. Henry, M. L. Weier and W. Martens, *Journal of Raman Spectroscopy: An International Journal for Original Work in all Aspects of Raman Spectroscopy, Including Higher Order Processes, and also Brillouin and Rayleigh Scattering*, 2006, **37**, 722-732.

293. J. Chen, W. Shi, S. Yang, H. Arandiyan and J. Li, *The Journal of Physical Chemistry C*, 2011, **115**, 17400-17408.

294. C.-J. Chang, Y.-C. Chu, H.-Y. Yan, Y.-F. Liao and H. M. Chen, *Dalton Transactions*, 2019, **48**, 7122-7129.

295. S. Zhang, L. Zhang, H. Li, J. Li, Z. Jiang, W. Chu, Y. Huang, J. Wang and Z. Wu, *Journal of synchrotron radiation*, 2010, **17**, 600-605.

296. J. Liu, Y. Ji, J. Nai, X. Niu, Y. Luo, L. Guo and S. Yang, *Energy & Environmental Science*, 2018, **11**, 1736-1741.

297. J. Yang, H. Liu, W. N. Martens and R. L. Frost, *The Journal of Physical Chemistry C*, 2010, **114**, 111-119.

298. K.-L. Yan, J.-F. Qin, J.-H. Lin, B. Dong, J.-Q. Chi, Z.-Z. Liu, F.-N. Dai, Y.-M. Chai and C.-G. Liu, *Journal of Materials Chemistry A*, 2018, **6**, 5678-5686.

299. H. Yang, Y. Long, Y. Zhu, Z. Zhao, P. Ma, J. Jin and J. Ma, *Green Chemistry*, 2017, **19**, 5809-5817.